Friction and Wear Reduction via Ultrasonic Lubrication

Dissertation

Presented in Partial Fulfillment of the Requirements for the Degree
Doctor of Philosophy in the Graduate School of The Ohio State
University

By

Sheng Dong, B.S, M.S.

Graduate Program in Mechanical Engineering

The Ohio State University

2015

Dissertation Committee:

Professor Marcelo Dapino, Advisor

Professor Karl Graff

Doctor Timothy Krantz

Professor Rebecca Dupaix

Professor Vishnu Baba Sundaresan

Abstract

It has been shown that the coefficient of dynamic friction and the surface wear between two surfaces decrease when ultrasonic vibrations are superimposed on the macroscopic sliding velocity. This phenomenon is often referred to as ultrasonic lubrication. This research experimentally and analytically investigates the fundamental principles and potential applications of friction and wear reduction using ultrasonic lubrication.

An experiment is conducted on ultrasonic friction reduction, using vibrations generated by Poisson effect (ratio of lateral strain to longitudinal strain). A motor effect region is identified, in which the effective friction force becomes negative as the vibratory waves drive the motion of the interface. Outside of the motor region, friction reduction is observed to be between 30% and 60%. A flextensional actuator is tested for friction reduction by sliding it between two steel plates in a sandwich structure. Friction reduction of up to 70% is achieved when ultrasonic vibrations are applied. A modified pin-on-disk tribometer is designed and built, with the addition of a piezoelectric actuator to the pin to generate vibrations in the direction perpendicular to the disc. A protocol is developed to conduct friction testing using this tribometer, and to characterize wear using optical profilometry. Indexes such as volume loss, surface roughness, friction forces and stick-slip phenomenon are chosen for comparison before and after application of ultrasonic vibrations. Experimental studies are conducted to

investigate the influence of linear velocity, normal stress, vibrational amplitude, and material combinations on friction and wear reduction.

An elastic-plastic cube model is formulated by using a cube to represent all the contacting asperities of two surfaces. Friction force is considered as the product of the tangential contact stiffness and the deformation of the cube. Ultrasonic vibrations are projected onto three orthogonal directions, separately changing the contact parameters and deformations, and hence, the overall friction forces. The cube model is also applied to explain wear reduction by correlating the volume loss in the disc to the volume of the cube. Furthermore, a multi-scale model is proposed to take into consideration the system dynamics, electromechanics, and surface contact of ultrasonic lubrication systems. Parameters such as driving voltage, macroscopic velocity, driving frequency, and signal waveform are studied. Experimental data were compared with the computational results from all the models and good matches were found in all cases, with errors less than 15%.

Several practical considerations are also taken into account, in order to utilize ultrasonic lubrication in real-life applications. The relationship between friction reduction and power consumption under various velocities and normal stresses is studied. Contour plots of the relationship are made to guide the design of ultrasonic lubrication systems. A comparison between different lubrication methods is conducted, including ultrasonic, traditional, and a combination of both. Different lubrication regimes are identified based on linear velocity and normal stress. Temperature is measured at the interface where ultrasonic vibrations are applied. Ultrasonic vibrations can cause a rise in temperature by increasing the actual vibratory velocity. On the other hand, they can lead to a drop in temperature by reducing the friction. The actual temperature change is affected by both factors. Preliminary work on the application of ultrasonic lubrication in consumer products proves that ultrasonic vibrations are also effective in reducing friction between metal and soft non-metal materials. Finally, a collar element with variable friction is designed, analyzed, built, and tested for the application of ultrasonic lubrication in damper rods.

To my parents

Acknowledgments

I would not have been able to complete this work without the support of many individuals. First, I would like to express the deepest appreciation to my advisor, Professor Marcelo Dapino, who gave me a life-changing opportunity to work in his lab when I decided to switch the major for my Ph.D. Over the years, I have been very grateful to receive his excellent guidance and generous support. His professional insights and technical knowledge have been invaluable for me to develop as a researcher.

I also want to thank my committee, Professors Karl Graff, Rebecca Dupaix, Vishnu Baba Sundaresan, and Dr. Timothy Krantz, for their input and comments on this research.

I want to thank Honda R&D Americas, Inc., NASA Glenn Research Center, and NSF I/UCRC Smart Vehicle Concepts Center for the financial and technical support to this research, as well as Dr. Bill Post, Andrew Fox, Duane Detwiler, Dr. Ryan Hahnlen and Dr. Timothy Krantz for being the mentors of this project. I also want to thank Allen Sheldon and Kishore Pydimarry for the internship opportunity at Honda R&D in the summer of 2014. It was a great experience and a pleasure working with both of them.

I was most fortunate to receive the Presidential Fellowship from the Graduate School of the Ohio State University for the recognition of research achievements. This would have never happened without the recommendation and help from Professors Dapino, Graff, Ahmet Kahraman, Dr. Krantz, and Allen Sheldon.

Thanks to my colleagues in the Smart Materials and Structures Laboratory for their friendship and companionship. The interaction with Dr. Leon Headings, Dr. John Larson, Justin Scheidler, Paul Wolcott, Adam Hehr, and Zhangxian Deng over the years was very enjoyable. Special thanks to Dr. Ryan Hahnlen, who gave me the tour to the lab when I first contacted Professor Dapino. His insightful input as a colleague and, later on, as a mentor of the project, has propelled this research forward.

I owe a lot to my friends who gave me support and encouragements during difficult times, especially Xiaolu Jiang, Biye Gong, Jamie and Terracina Maxwell. I also want to thank my tennis friends with whom I had great times. Tennis kept me physically and mentally tough, and gave me a good place to recharge when my batteries were running low in research. Special thanks to my doubles partner Brian Conrad, who not only shared a lot of memorable moments with me on court, but also gave me tremendous help and support in English writing off court.

This work would have never been possible without the unconditional love and support that my parents have given me. I am deeply indebted to them for raising me to be who I am and allowing me to chase my dreams.

Vita

September 26, 1986	Born – Wuhu, China
July, 2007	B.S., Civil Engineering, Southeast University, Nanjing, China
June, 2010	M.S., Bridge Engineering, Tongji University, Shanghai, China
2010–2011	French Fellow, The Ohio State University.
2011–2012	Graduate Research Associate, The Ohio State University.
2012–2015	NSF I/UCRC Smart Vehicle Concepts Center Fellow, The Ohio State University.
2015–present	Presidential Fellow, The Ohio State University.

Publications

Dong, S. and Dapino, M.J., "Piezoelectrically-induced ultrasonic lubrication by way of Poisson effect," *Proc. SPIE 8343*, Industrial and Commercial Applications of Smart Structures Technologies, San Diego, CA, March 11–15, 2012.

Dong, S. and Dapino, M.J., "Elastic-plastic cube model for ultrasonic friction reduction via Poisson effect," *Ultrasonics*, **54**, 343-350, 2014.

Dong, S. and Dapino, M.J., "Wear reduction through piezoelectrically-assisted ultrasonic lubrication," *Proc. ASME SMASIS*, Snowbird, UT, September 16–18, 2013.

Dong, S. and Dapino, M.J., "Wear reduction through piezoelectrically-assisted ultrasonic lubrication," *Smart Materials and Structures,* **23**, 104005, 2014.

Dong, S. and Dapino, M.J., "Model for friction and wear reduction through piezoelectrically-assisted ultrasonic lubrication" *Proc. SPIE 9059*, Industrial and Commercial Applications of Smart Structures Technologies, San Diego, CA, March 9–12, 2014.

Dong, S. and Dapino, M.J., "Mapping of power consumption and friction reduction in piezoelectrically-assisted ultrasonic lubrication," *Proc. SPIE 9433*, Industrial and Commercial Applications of Smart Structures Technologies, San Diego, CA, March 8–11, 2015.

Fields of Study

Major Field: Mechanical Engineering

Studies in:

Ultrasonic Lubrication   Prof. Marcelo J Dapino

Table of Contents

List of Tables

List of Figures

Chapter 1: Introduction

1.1 Overview and Motivation

Friction can be observed in all mechanical systems [1]. In some cases, such as vehicle brakes, tires, and clutches, high friction is critical for functionality. However, in many other instances, low friction is desirable for efficiency. Reducing friction, whether through improved designs, use of better suited materials, or various ways of lubrication, is an extremely important topic in modern technology.

Materials near the surfaces undergo plastic deformation and break away from the body of the material, resulting in surface wear [2]. This takes place in concert with friction at the interface. Although wear can be useful for producing surfaces, writing, and preserving sharp edges, it is usually considered a harmful phenomenon. Reducing wear can prevent mechanical failures and elongate the lifetime of critical components.

Ultrasonic lubrication is an innovative approach to reduce friction and wear. Since the 1960s [3], it has been shown that the application of ultrasonic vibrations at the interface of two surfaces in sliding contact reduces the effective friction force. Ultrasonic vibrations are usually generated by piezoelectric materials, which are a class of "smart" materials that are widely used as actuators or sensors. Furthermore, friction force can be controlled by applying various voltages to the piezoelectric stacks, which is termed as ultrasonic friction control.

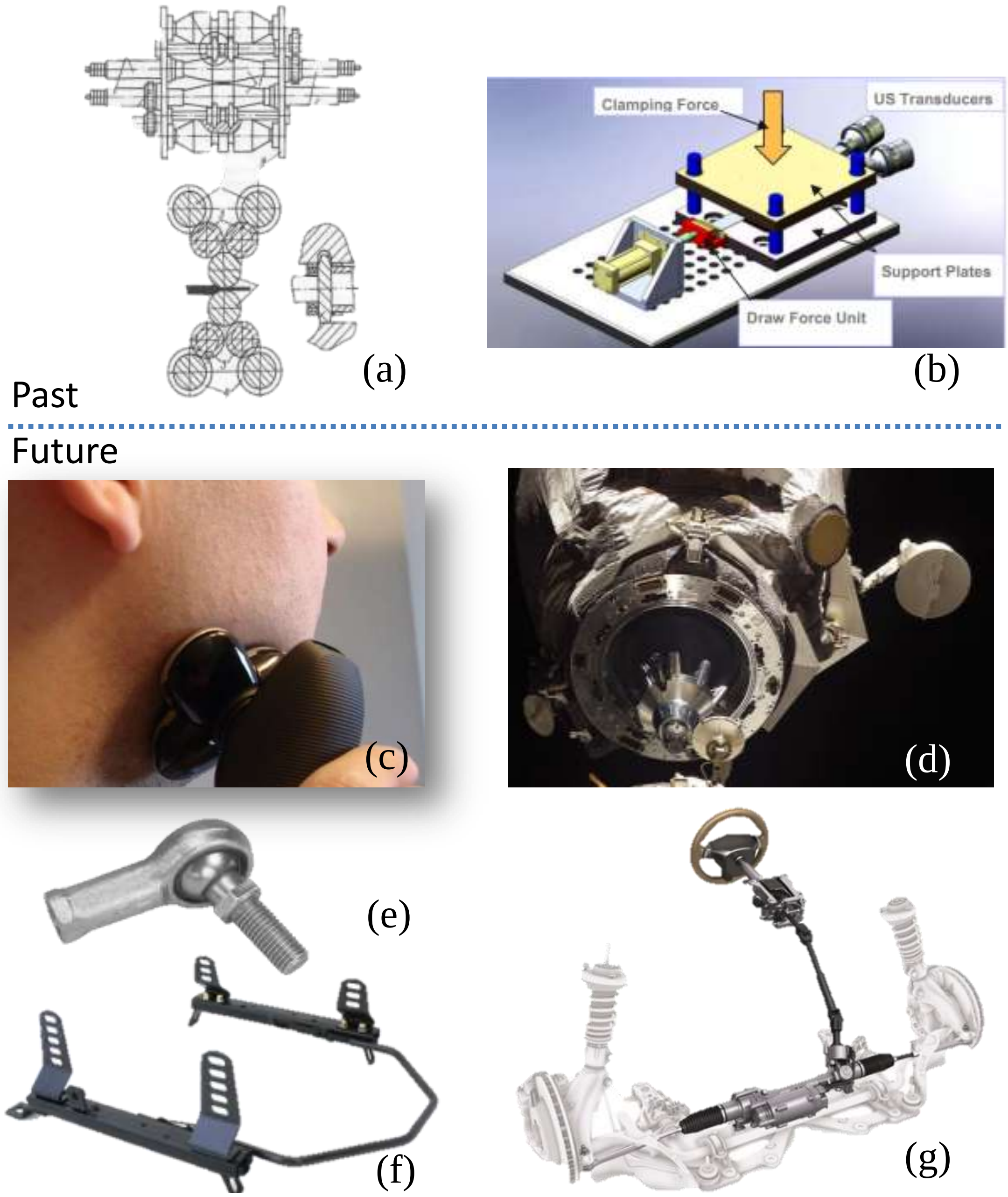

Figure 1.1: Applications of ultrasonic lubrication: (a) metal sheet rolling [4]; (b) EWI test bed [5]; (c) consumer product [6]; (d) space mechanism [7]; (e) ball joints [8]; (f)vehicle seat rail [9]; (g) vehicle steering mechanism [10].

Ultrasonic lubrication has been successfully applied in metal forming processes, such as sheet rolling, extrusion, compressing, and wire drawing (Fig. 1.1 (a)). Reduction of friction force results in less heat generation, smaller input forces, and improved surface finishes. Also, this technology requires no additional detergents to remove lubricants from the final products, which is more environmentally friendly [4]. In other processes such as friction stir welding, friction exists between the workpiece and the containment plates. The reduction of friction facilitates the process and prevents production defects (Fig. 1.1 (b)) [5].

Some potential applications for this technology are under investigation, as shown in Fig. 1.1 (c)–(g). In consumer products, friction reduction between the skin and the product can substantially enhance the user experience by requiring no additional lubricants or coatings. In automobile applications, modulating the friction can improve the motion control of ball joints. Friction reduction between vehicle seats and rails facilitates seat movement, saving room that would otherwise be occupied by traditional components and mechanisms. Ultrasonic lubrication can also help to improve fuel efficiency by reducing friction in powertrain and suspension systems in cars. It can also be integrated into suspension joints to automatically adapt themselves to various road conditions [11]. In space vehicles, where traditional lubricants cannot be used, ultrasonic lubrication can help reduce wear and extend the life of critical components.

1.2 Background

1.2.1 Friction

Friction is the resistance to the motion between two contacting surfaces when they slide or roll relative to each other [2]. It acts directly opposite to the direction of the relative motion. Early findings of friction by Amontons and Coulomb [12, 13] can be summarized into three quantitative laws.

First, friction force (F_t) is linearly proportional to normal load (F_N), that is

$$F_t = F_N \mu, \tag{1.1}$$

where μ is known as the coefficient of friction, and has been widely used as an indicator of the magnitude of friction between different surfaces. This law applies to most materials unless they are extremely hard or extremely soft, such as diamonds or polymers.

The second law states that friction is independent of the nominal area. This is due to the fact that real contact between two surfaces actually takes place on the asperities, which only comprise a small portion of the nominal surface [14]. The real contact area is determined by parameters such as normal force, surface roughness, and material properties.

Finally, the third law maintains that friction is independent of velocity, although this law is not always as valid as the first two [2]. Some studies indicate that the relationship between dynamic friction and velocity is positive at low velocities but negative at high velocities [15].

Another empirical law states that the static friction force is generally greater than dynamic friction. One commonly observed phenomenon related to this law is stick-slip: sliding of one object over another under a constant pulling force and relative constant velocity may undergo some jerky motion, causing fluctuation of the linear velocity as well as the pulling force. Stick-slip takes place because during the sliding, the nominally constant pulling force does not remain constant all the time. Once pulling force varies to a value that is not sufficient to overcome the dynamic friction, the velocity of the motion drops and the resistance increases. Therefore, a greater pulling force is required to maintain the motion speed. Once the pulling force is increased to resume the motion, the resistance drops, leading to a sudden increase in the motion velocity. This fluctuation of the pulling force results in the observed jerky motion, or stick-slip [16].

In terms of friction models, Coulomb [12] proposed a simple equation to calculate dynamic friction at steady-state velocity,

$$F_c = F_N \mu \mathrm{sgn}(v_r), \tag{1.2}$$

where F_c is the Coulomb friction, μ is the coefficient of friction, v_r is the macroscopic velocity, and F_N is the normal force. The Coulomb model does not capture the transition between static friction to dynamic friction due to the discontinuity at zero velocity, making it problematic for determining the friction at zero sliding velocity, both at start-up and during a change of direction.

Dahl's model [17] solves this problem by describing the relationship between friction force and pre-sliding displacement, which can be expressed as

$$\frac{dF_t}{dx} = K_t(1 - \frac{F}{F_c}\mathrm{sgn}(v_r)), \tag{1.3}$$

where F_t is the friction force, K_t is the contact stiffness, and x is the displacement. The model maintains that friction is zero when the displacement is zero. It increases to the value of the Coulomb friction F_c as the displacement increases to its maximum before sliding occurs. After that, at a steady state when $F = F_c$, $dF/dx = 0$, Dahl's model becomes the Coulomb model. Dahl's model is widely used for modelling friction in dynamic systems. However, both models base friction only on displacement and the direction of the velocity, thus excluding commonly observed viscous friction and the Stribeck effect. The Stribeck effect classifies variation in friction force for sliding lubricated surfaces [18].

The LuGre model [103] takes into consideration velocity-dependent viscous friction and the Stribeck effect. It defines friction as the deflection force of elastic springs when a tangential force is applied. The model is expressed as

$$\frac{dz}{dt} = v - K_t \frac{v}{g(v)} z, \tag{1.4}$$

$$F = K_t z + c(v)\frac{dz}{dt} + f_v. \tag{1.5}$$

where z is the deflection of the springs, v is the velocity, K_t is the contact stiffness, $c(v)$ is the micro-damping coefficient, f_v is the viscous friction, and $g(v)$ is a function used to explain the Stribeck effect. This equation is often used in modeling friction between lubricated surfaces.

1.2.2 Wear

Wear is the plastic deformation, removal, or displacement of materials from surfaces during sliding [1]. Some commonly observed wear mechanisms are abrasive wear, adhesive wear, corrosive wear, and fatigue wear [2]. Abrasive wear takes place when a hard surface, or a soft surface with hard particles, slides over a soft surface, and ploughs grooves in the opposing soft surface. Material from the surfaces is removed and forms loose particles [19]. Adhesive wear occurs between smooth surfaces sliding relative to each other. Materials from both surfaces are pulled off and adhere to each other, or are displaced at a later time as loose particles [20]. Corrosive wear is observed when sliding takes place in a corrosive environment. The sliding wears away the film formed on the surfaces by corrosion, thus repeating the corrosion process on the newly formed surfaces [21]. Finally, fatigue wear occurs with repeated sliding or rolling between surfaces. The repeated loading and unloading cycles result in the deformation and cracking of the substrates, which eventually leads to the removal of a large amount of material and the formation of big fragments [22]. These four main types of wear are not exclusive to each other: two or more of them may occur concurrently with one type dominating.

Different configurations can be adopted to conduct wear tests. National standards give standard procedures for the following wear tests: block-on-ring (ASTM G77), crossed cylinder (ASTM G83), pin-on-disc (ASTM G99), sphere-on-disc (DIN 50324) and rotating pin-on-flat (ASTM G98) [23]. There are several ways to quantify wear. The simplest way is to properly clean the sample and weigh it before and after testing. Another way is to measure the volume loss of the sample. According to different resolution requirements, one can choose mechanical gauging or optical measurements to calculate volume loss, and derive the wear rate as an index for the severity of wear. For adhesive wear with very small volume loss, the change of surface roughness can be used as an index for wear.

Archard's wear equation is most commonly used for sliding wear, expressed as,

$$Q = \frac{KW}{H} \tag{1.6}$$

where Q is the volume loss per sliding distance, W is the normal load, K is a dimensionless coefficient of wear, which is dependent on the material, and H is the hardness of the softer material [24]. Parameter K, usually smaller than 1, is used to demonstrate the severity of wear between materials.

1.2.3 Lubrication

Lubrication is a process employed to reduce friction, wear, adhesion, or heating between two contacting surfaces. Traditional methods rely on lubricants or coatings. In principle, they can be divided into three different types: solid film lubricants, chemical coatings, and liquid lubricants [2].

For solid film lubricants, graphite-molybdenum disulfide in a binder is most widely used. The thickness of film when applied is generally about 15 μm, which provides the longest life. Chemical coatings are usually used for limited protection against server surface damages and are very often applied in combination with other lubricants [25].

Liquid lubricants likewise have many types, and their uses can be divided into regimes depending on the level of asperity contacts [18]. The curve of the lubrication regimes is shown in Fig. 1.2. The division of regimes is based on the normal load applied, the viscosity of the lubricant, and the relative velocity between the two sliding surfaces. In boundary lubrication, the contact is partially on the asperities but mostly on the lubricants. Therefore, the friction coefficient in this regime is lower than dry friction but much higher than other regimes. In between boundary and hydrodynamic, there is a mixed regime, where the friction coefficient drops dramatically. Hydrodynamic lubrication takes place when the normal load is fully supported

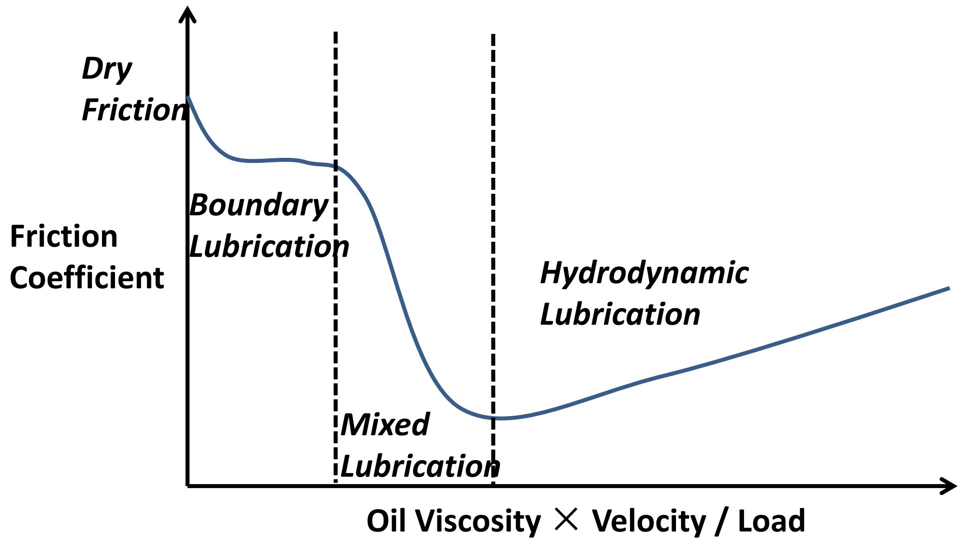

Figure 1.2: Regimes of liquid lubricants.

by the lubricated film and solid-solid contact is avoided. Friction increases again in this regime as the velocity or normal load increases.

1.2.4 Piezoelectric Materials

Piezoelectric materials are a class of “smart” materials that can generate electrical energy when mechanically stressed, or mechanically deform when electrical voltage is applied [26]. These two phenomena are often called direct and inverse piezoelectric effects, and make piezoelectric materials useful both as sensors and actuators. Compared to other smart materials, they have fast response, so they can handle frequencies higher than 20 kHz. Also, once poled, they have a large range of linear response between stroke and voltage, which enables modulation of the amplitude of the vibration by changing the voltage.

The governing equations of piezoelectricity are expressed as [27]

$$\mathbf{D} = \epsilon^{\mathbf{T}}\mathbf{E} + \mathbf{d}\mathbf{T}, \tag{1.7}$$

and

$$\mathbf{S} = \mathbf{d}\mathbf{E} + \mathbf{s}^{\mathbf{E}}\mathbf{T}, \tag{1.8}$$

where $\mathbf{D}$ is the electric displacement, $\mathbf{T}$ is the stress, $\mathbf{E}$ is the electric field, and $\mathbf{S}$ is the strain, $\epsilon^{\mathbf{T}}$ is the permittivity under constant stress, $\mathbf{s}^{\mathbf{E}}$ is the mechanical compliance with constant electric field, and $\mathbf{d}$ is the piezoelectric constant.

The average power consumption of a piezoelectric actuator driven by sinusoid voltages can be estimated as

$$P_a \approx C U_{max} U_{pp} f \tag{1.9}$$

where C is the capacitance, U_{max} is the maximum voltage, U_{pp} is the peak-to-peak voltage, and f is the driving frequency [28].

1.2.5 Ultrasonics

Ultrasonics is a branch of acoustics that deals with the generation and use of acoustic waves with frequencies higher than 20 kHz [29]. The applications of ultrasonics can be divided into two broad areas: low power (in the range of milliwatts) with high frequency (in the range of megawatts); and high power (typically but not strictly in the range from 10s to kilo watts) with low frequency (less than 100 kHz). Low power applications include ultrasonic range finder, ultrasound imaging (medical use), surface ultrasonic waves, and ultrasonic non-destructive testing.

High power applications, to which ultrasonic lubrication belongs, change the physical, chemical, and biological properties of materials and systems [30]. For example, ultrasonic additive manufacturing incorporates the principles of ultrasonic metal welding to create metal parts with artificial shapes and seamless embedded materials [31]. Piezoelectric materials, the transducer elements that typically drive ultrasonic lubrication systems, have been incorporated into ultrasonic motors smaller than 1 cm^3 and with higher energy density than conventional motors. This makes ultrasonic vibrations of great interest, especially in applications where miniaturized motion control is desired [32]. Acoustic levitation has been studied and utilized as a method to suspend particles. The suspension forces can be increased when the waves reach ultrasonic frequencies along with high energy intensity [33].

1.3 Literature Review

1.3.1 Ultrasonic Friction Reduction

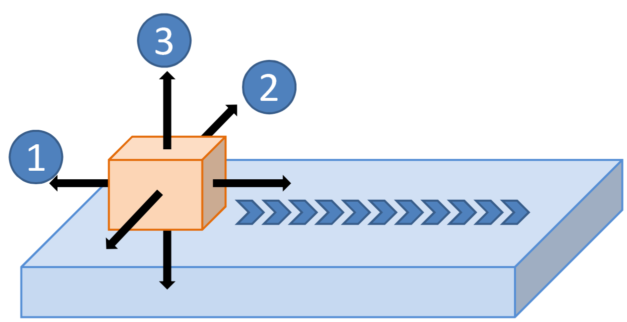

Figure 1.3: Ways to apply ultrasonic vibrations.

The earliest studies of ultrasonic friction reduction were conducted by Mason [3] to reduce wear in relays, and related phenomena were further investigated by many scholars. Ultrasonic vibrations are usually applied only to one of the two contacting surfaces and may be applied in one of three directions relative to the macroscopic sliding velocity: perpendicular, longitudinal or transverse, as shown in Fig. 1.3. Numerous studies have been devoted to each of the three directions and combinations thereof. Figure 1.4 shows a summary of the friction reduction results for the experiments conducted in all three directions. The results are plotted against two other critical parameters that could influence the effectiveness of ultrasonic lubrication: normal stress and linear velocity.

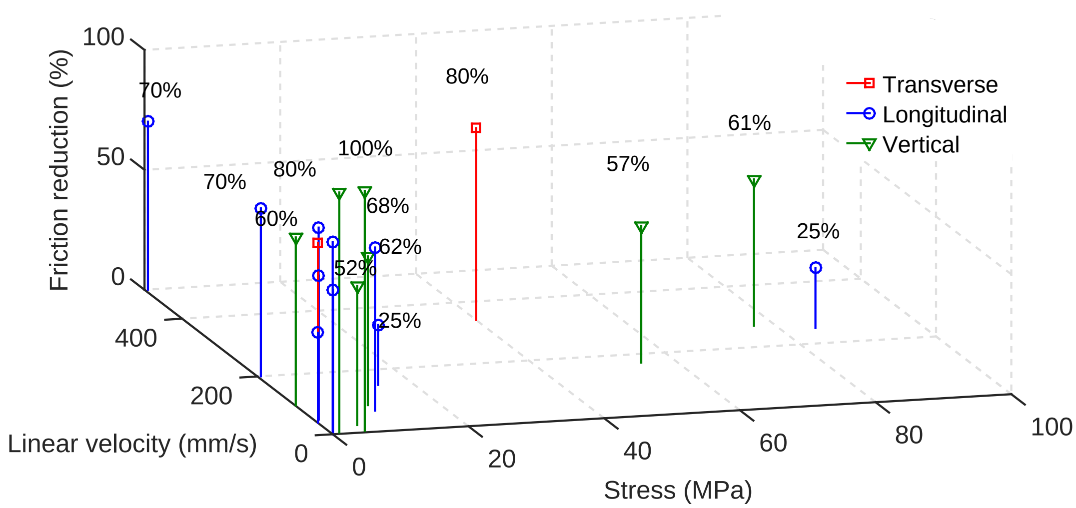

Figure 1.4: Map of ultrasonic friction reduction, linear velocity, and normal stress from previous studies.

For example, Littmann et al. [34, 35] connected a piezoelectrically-driven actuator to a slider, on which a force sensor and a frame were installed for measuring friction forces and applying normal loads. A pneumatic actuator was employed to push the slider together with the actuator along a guide rail. Ultrasonic vibrations were applied in the direction longitudinal to the sliding velocity. The piezoelectric actuator generated vibrations at 60 kHz, the sliding velocity ranged from 0 to 0.5 m/s, and the velocity of the ultrasonic vibration was up to 0.26 m/s. They achieved friction reduction up to 70%, and found that friction reduction decreases as the velocity increases.

Kumar and Hutchings [36] experimentally studied the influence of in-plane longitudinal and transverse vibrations on friction reduction at low normal stresses. They installed a pin on a sonotrode which was energized by an ultrasonic transducer. Ultrasonic vibrations were generated and transmitted to the pin, which was placed in contact with a tool steel surface. Normal force was applied by a pneumatic cylinder and measured by a load cell. The relative motion between the pin and the disc was created by a reciprocating table. They experimentally studied the influence of in-plane longitudinal and transverse vibrations on friction reduction. A pin-on-disc set-up was employed, where the pin was made of aluminum, copper, and stainless steel while the disc was held by a table with reciprocating motion. They determined that longitudinal vibrations were more effective at reducing friction force than transverse vibrations, and confirmed that the velocity ratio greatly influences the degree of friction reduction.

Popov et al. [37] studied ultrasonic friction reduction under low loads and low speeds for different material combinations using a pin-on-disc tribometer. They utilized an actuator with conical waveguides. The actuator was placed in contact with a rotating base plate. Cones made of nine materials with various hardnesses were adopted to study the influence of material hardness on ultrasonic friction reduction.

It was shown that ultrasonic vibrations create less friction reduction on softer materials than harder ones. They argued that contact stiffness influences the degree of friction force reduction. Due to the low normal force applied in their test, the amplitude of vibrations was relatively low as well (less than 1 μm), which may explain why they did not find any friction reduction in materials like rubber and aluminum.

Teidelt et al. [38] extended the work of Popov et al. [37] using the same experimental set-up, but they applied ultrasonic vibrations in the vertical direction. They varied both the vibrational amplitude for various vibrational velocity and reach friction reduction up to 60%.

Gutowski and Leus [39] measured friction force between a slider and a base with and without longitunidal ultrasonic vibrations applied to the base. The normal stress (0.031 MPa) and linear velocity (0.62 mm/s) were set at low range. Friction reduction up to 90% were achieved by increasing the vibrational velocity to 6.64 mm/s, which is more than ten times of the macroscopic velocity.

Pohlman and Lehfeldt [40] also implemented a pin-on-disc experiment. Unlike other studies, they employed a magnetostrictive transducer to generate ultrasonic vibrations. To study the optimum direction for ultrasonic friction reduction, the transducer was carefully aligned so that the vibrational direction was longitudinal, transverse, and vertical to the macroscopic velocity. They studied ultrasonic friction reduction on both dry and lubricated surfaces. Molykote was used as lubricant at the interface, which makes it different from the dry friction condition in this paper. They observed good friction reduction with ultrasonic vibrations applied tangentially and transversely to the sliding velocity. However, they found very little friction reduction when ultrasonic vibrations were vertical to the disc surface. The major reason is that, ultrasonic vibrations are constantly changing relative velocity when they are applied in-plane with the disc surface. This results in changing lubrication regimes, which leads to a friction reduction. However, when ultrasonic vibrations are applied vertically, the separation between the surfaces that created by the lubricant dwarfs the ultrasonic vibrations, which leaves the friction unchanged.

Oiwa [41] studied the influence of ultrasonic vibrations on rolling friction. Tests were conducted on linear-motion guides for precision positioning, the accuracy of which may have been substantially reduced by the presence of friction and the resulting stick-slip phenomenon caused by it. Both the rail and the carriage were ultrasonically excited in the tests, and an overall 25% friction reduction was achieved. They also reported that the reduction of static friction can only be reduced at a very low velocity. Tsai et al. [42] studied ultrasonic friction reduction using vibrations applied in angles with the macroscopic velocity. They concluded that vibrations in longitudinal direction are more effective than those in transverse direction.

Bharadwaj and Dapino [43, 44, 45] conducted similar experiments using a piezoelectric stack actuator connected to a conical waveguide at either end of the stack. Contacts took place between the spherical edges of the cones and the surface of the guide rail. The effects of system parameters such as contact stiffness, normal load, and global stiffness were studied. They developed experiments in which longitudinal vibrations where used to investigate the effect of macroscopic sliding velocity, normal load, contact stiffness, and global stiffness on friction reduction. They experimentally demonstrated a decrease of up to 68% in effective friction coefficient. They also experimentally investigated ultrasonic lubrication for creating adaptive seat belts with controllable force at the interface between the D-ring and webbing. Proof-of-concept experiments were conducted under normal loads up to 670 N by using out-of-plane ultrasonic vibrations. Friction was reduced by up to 60%.

1.3.2 Ultrasonic Wear Reduction

Most previous studies in friction reduction did not carry on into wear reduction. However, some scholars have attempted to utilize vibrations to reduce wear between two contacting surfaces. Chowdhury and Helali [46] vibrated a rotating disc in a pin-on-disc setup. The vibrations were generated by a supporting structure of two parallel plates located under the rotating disc. The top plate has a spherical ball installed off-center on the bottom surface, which slides in a slot that was engraved at the top surface of the bottom plate. The slot was machined with a periodically variable depth so that the top plate moves vertically during rotation. The frequencies ranged around 100 Hz according to the rotational speed. They studied the correlation between wear reduction and vibration frequency, relative humidity, and sliding velocity. Their results showed that higher frequency leads to lower wear rates, and the relative velocity does not have an evident influence on wear reduction.

Bryant and York [47, 48] studied the effect of micro-vibrations on wear reduction. They inserted a carbon cylinder through a holder with one end rested on a spinning steel disc and the other end connected to a coil spring. In one case, the cylinder was snug fitted in the holder so that there was no space for vibration. In other cases, clearances were left to allow micro-vibrations of the cylinder while the cylinder was in contact with the spinning disc. The weight loss of the cylinder was measured to calculate the wear rate. They created a carbon slider that vibrates at an amplitude of 10 to 100 μm at frequencies ranging from 10 to 100 Hz against a steel disc, achieving wear reduction of up to 50%. They found that the change of wear rate correlated well with the corresponding change of kinetic energy of the vibration of the slider.

Goto and Ashida [49, 50] also adopted a pin-on-disc experiment. They connected pin samples with a transducer via a tapered cone and a horn. The pin vibrated in the direction perpendicular to the disc surface. A mass was connected to the transducer on its top for applying normal loads. Friction forces were translated from the torque that was applied to rotate the disc. Wear was identified as adhesive because both pin and disc were made of carbon steel. Wear rates were calculated from volume loss measurements. They conducted tests at frequencies in the ultrasonic range. Applying vibrations normal to the surface of the disc, they studied the relationship between wear rate and normal loads. Their findings show that ultrasonic vibrations can reduce wear under various normal loads. In these tests, the amplitude of the ultrasonic vibrations was 8 μm and the normal load was up to 88 N. They also studied the contact time between two surfaces while ultrasonic vibrations were applied, and showed when the amplitude of ultrasonic vibration is large enough, contact time between two surfaces will be reduced as one surface moves away from the other.

1.3.3 Modeling of Ultrasonic Lubrication

To explain the experimental data of ultrasonic friction reduction, Littmann et al. [34, 35] developed a mathematical relationship between velocity ratio and friction ratio, which indicates that a higher vibration velocity results in a greater friction reduction. In their study, the velocity ratio ζ was defined as the macroscopic velocity over the velocity of the ultrasonic vibrations. The friction ratio μ_i was defined as the friction force with ultrasonic vibrations over friction force without ultrasonic

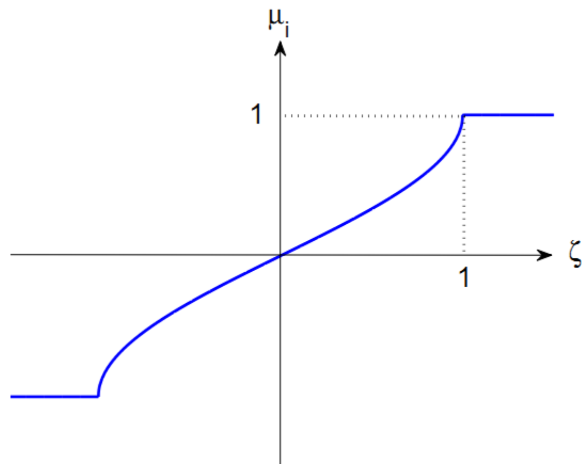

Figure 1.5: The relationship between friction ratio and velocity ratio proposed by Littmann et al [34, 35].

vibrations (Fig. 1.5). It was proposed that a small velocity ratio leads to a low friction ratio, and hence effective friction reduction. As the velocity ratio increases, so does the friction ratio until a value of 1 is achieved and no further benefit from the ultrasonic vibrations is possible. Therefore, an increase in sliding velocity moves the system towards a friction ration of 1 and reduces the effectiveness of the ultrasonic vibrations. Conversely, to maintain high friction reduction for high sliding velocities, a high vibration frequency is necessary. Due to the nature of piezoelectricity, achieving high frequency of operation requires an actuator capable of handling high output power.

Kumar and Hutchings [36] studied the mechanisms of friction reduction with ultrasonic vibrations applied longitudinally and transversely, respectively, relative to the macroscopic velocity. Coulomb friction was also employed in their study, which assumes a constant coefficient of friction during sliding. The superimposition of ultrasonic vibrations both in longitudinal and transverse directions, changed the direction of instantaneous velocity so that the overall magnitude of the friction was reduced. Similar explanations were also proposed by Popov et al. [37] and Tsai et al. [42].

Instead of the Coulomb friction model, Bharadwaj and Dapino [43, 44, 45] and Gutowski and Leus [39] adopted Dahl's [17] friction model and built it into their dynamic systems. Bharadwaj and Dapino [43, 44, 45] analyzed the influence of contact stiffness, global stiffness, mass, coefficient of friction, and signal waveform on friction reduction. Gutowski and Leus [39] simulated time-dependent friction as the output of a dynamic system, and obtained good agreement between the simulation and experimental data. However, in both studies, they treated contact stiffness as a constant value as opposed to a changing parameter when ultrasonic vibrations are present. They neither provided any physical explanation for the calculation of the contact stiffness, but presented it as a manipulated value for matching the experimental data. Despite the issues these models have, they were successful in explaining ultrasonic friction reduction with vibrations applied longitudinally to the sliding direction.

In follow-up work done by Teidelt et al. [38], they extended Popov's modeling work from in-plane to out-of-plane. The pin-on-disc set-up was adopted, and ultrasonic vibrations were applied on the pin in a direction perpendicular to the disc surface. They employed the Coulomb friction model, and explained the friction reduction as a result of reduced normal load. The change of the normal load was calculated as the product of the contact stiffness and the deformation in the vertical direction.

1.4 Research Objectives and Outline

Literature review shows that there has been significant work in ultrasonic lubrication. Experiments on ultrasonic friction reduction, both sliding and rolling, were conducted with various material combinations at different velocities. Each study took into consideration some of the parameters that could possibly influence the reduction effect, such as the vibrational direction, normal load, and vibrational amplitudes among others. However, there still exists a gap between the existing studies and understanding this phenomenon systematically and comprehensively. For example, most normal loads applied were relatively low, and inherently, the vibration amplitudes were kept low as well. Likewise, some important parameters, such as power consumption have not been studied at all.

Previous modeling efforts, accompanied by the experimental work, were mostly based on the classic Coulomb friction model, which assumes friction force is only proportional to the normal load. This assumption is not always valid, especially when ultrasonic vibrations change the surface properties. Dahl's model was used to build dynamic systems to study various parameters and to simulate friction reduction. However, the calculation of some parameters, such as contact stiffness was poorly-defined in physics and the coefficient of friction was still assumed to be constant. A more comprehensive analytical model, one that incorporates surface contacts, material properties, electromechanics of the transducer, and system dynamics is required to explain ultrasonic lubrication systematically and in-depth.

In terms of wear reduction, there were some successful precedents showing that vibrations, both at low frequencies and ultrasonic frequencies, can reduce wear. However, not many material combinations have been tested. Also, important variables such as surface roughness and normal load have not yet been studied. Almost none of the previous wear reduction studies developed analytical models to explain their experimental data. Therefore, I propose a study of ultrasonic wear reduction with more materials combinations, including the formulation of an analytical model to explain the experimental data.

Many practical considerations need to be investigated as this study intends to move ultrasonic lubrication further into applications. These considerations include the relationship between friction reduction and power consumption under various running conditions, the temperature change at the interface and the factors that influence that change, whether ultrasonic lubrication is still effective if it is used when traditional lubrication methods are present, and whether ultrasonic lubrication is able to work between different materials, even soft materials.

Finally, a collar element with variable friction is proposed to demonstrate the design, analysis, manufacturing, and testing of a ultrasonic lubrication component that can be used in real-life applications.

To summarize, the key objectives of this research, along with each chapter's structure, are listed below:

- Experimental investigation of friction and wear reduction using different actuators under various normal loads/stresses, linear velocities, and material combinations (Chapter 1).

- A comprehensive analytical model that incorporates parts that representing surface contacts, material properties, transducer electromechanics, and system dynamics to explain ultrasonic lubrication (Chapter 2).

- Studies on practical considerations of ultrasonic lubrication applications and the demonstration of a collar element with variable friction (Chapter 3).

Chapter 2: Experiments

2.1 Ultrasonic Friction Reduction via Poisson Effect

2.1.1 Introduction

In a previous study conducted at EWI [51], vibrations created by the Poisson effect under ultrasonic vibrations were, for the first time, adopted as the means for achieving friction reduction. Due to the Poisson effect, the longitudinal vibration of the horn induces vibration through the thickness of the vibrating object. The study was to reduce the friction between workpiece and containment plates in thermal stir welding processes. Experimental data showed friction reduction averaging over 70% for clamping loads up to 2,500 lbs, and demonstrated the possibility of using this method for conditions with clamping forces up to 5,000 lbs.

The first experiment of this research was inspired by the work done by EWI. It was desired that the ultrasonic vibration created by the Poisson effect be perpendicular to the sliding plane. The combination of vibrations in two orthogonal directions leads to elliptical movement of points located at the interface between the sliding objects, creating a different type of friction reduction mechanism. This mechanism is potentially more effective than the conventional in-plane modes of vibration, as in most prior art. This section shows how Poisson-effect ultrasonic vibrations affect the dynamic friction coefficient between surfaces under various conditions including different material combinations and normal loads.

2.1.2 Experimental Set-up

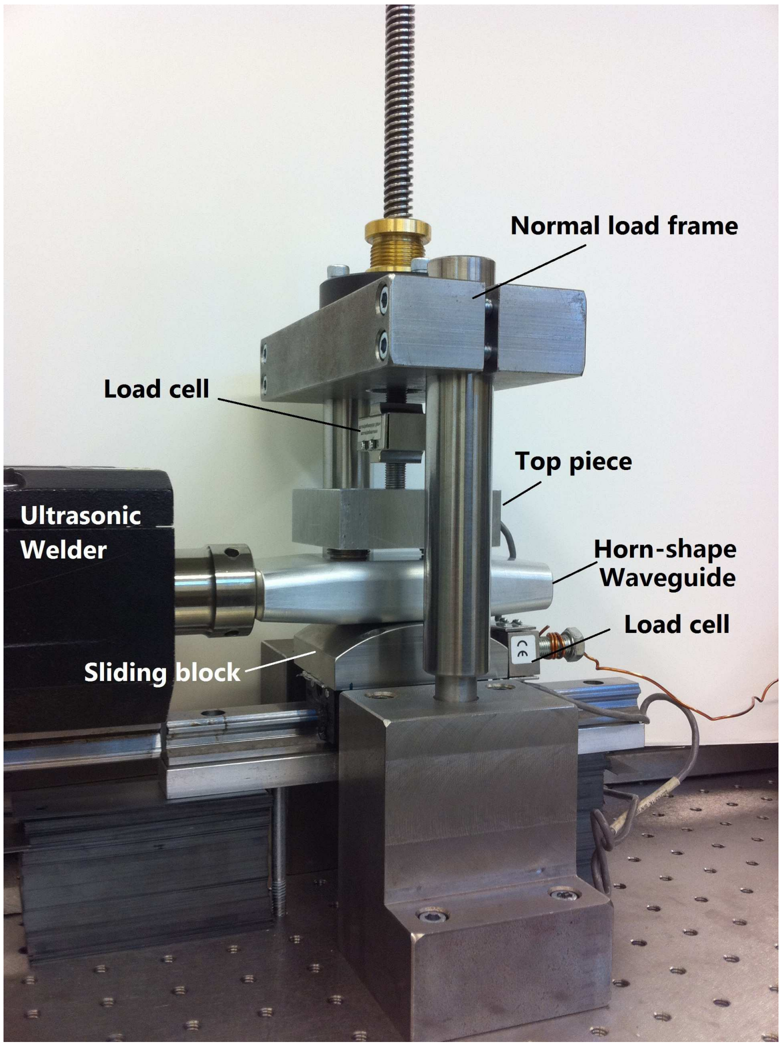

Figure 2.1: Experimental set-up of ultrasonic friction reduction via Poisson effect.

An experiment was developed using a commercial ultrasonic welder (Dukane 220) as the source of vibrations. When connected to its dedicated power supply, this welder reliably supplies 20 kHz sinusoidal signals at various discrete power levels (25, 50, 75, and 100% of the full 8.5 μm amplitude, 2.2 kW power machine limit). As shown in Fig. 2.1, vibrations from the welder are transmitted to a waveguide with dimensions 5 in. (127 mm) by 2.4 in. (60.96 mm) by 1 in. (25.4 mm). The dimensions of the waveguide is shown in Fig. 2.2. A block with a curved top surface slides underneath the horn, creating a line contact with the bottom surface of the horn. Two different materials were chosen for the horn and sliding block, stainless steel and aluminum. Tests were conducted for three material combinations (aluminum horn on stainless steel block, stainless steel horn on aluminum block, and stainless steel horn on stainless steel block).

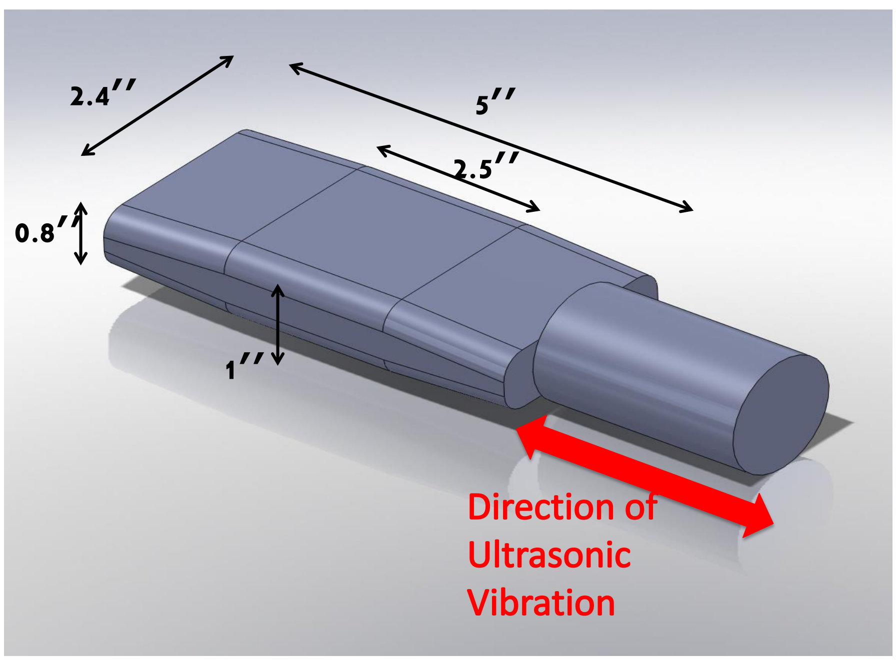

Figure 2.2: Dimensions of the waveguide.

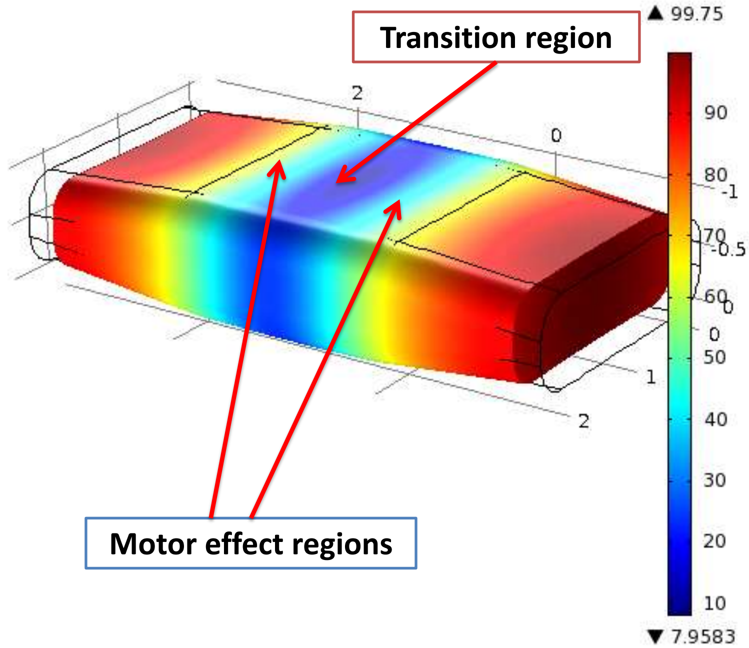

Figure 2.3: FEA simulation of the vibrations of the waveguide.

In order to investigate the Poisson-effect ultrasonic lubrication, which is expected to be most effective around the half-wavelength node region, the system was tested with the interface between the horn and sliding block within ±1 in (±25.4 mm) of the centerline of the horn. In this manner, both the transition and motor effect regions are characterized. The block is given a sliding velocity of 0.2 in/s (5 mm/s) under normal loads from 60 N to 240 N supplied by a screw connected to a load frame. Low-friction pads located between the "top piece" and the horn minimize the tangential force created by friction between these two components. Load cells measure the normal force exerted by the screw and tangential force required to displace the sliding block.

2.1.3 Finite Element Analysis

A finite element simulation was implemented in COMSOL Multiphysics 4.2 to calculate the Poisson-effect vibration of the horn subjected to force excitation on one side face. The first axial modes for the aluminum and stainless steel horns are 20.6 kHz and 20.8 kHz, respectively. Since the drive frequency for the welder is 20 kHz, the first axial modes this dominate the vibration of both horns. The axial strain from horizontal vibration of the horn causes lateral strain, which makes the vibration at the bottom surface of the horn follow an elliptical pattern.

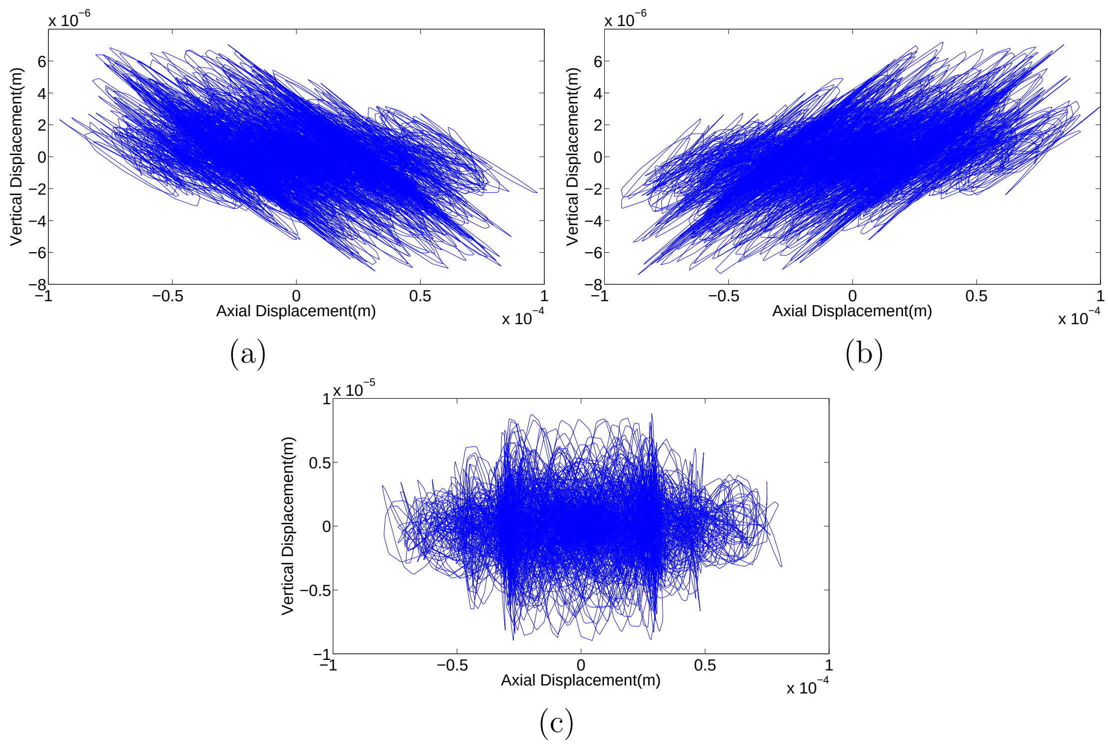

Figure 2.4: Locus curves of the vibrations at points on the horn surface [(a) point -1; (b) point +1; (c) point 0].

The locus curves of the vibration are shown in Fig. 2.4 for three different locations: Point 0 (centerline of the bottom surface of the horn), Point -1 (1 in to the left of the centerline), and Point +1 (1 in to the right of the centerline). The motion at locations -1 and +1 follows an overall elliptical trend. Such motion generates contact forces which push points on the horn surface towards the centerline. We refer to this phenomenon as *motor effect*, and we consider it similar to the motor force encountered in piezoelectric ultrasonic motors. Theoretically, the entire flat surface of the bottom of the horn should be subjected to symmetric motor forces pushing points towards the centerline. However, it is observed experimentally that around the centerline the motor force is negligible due to the small vibration amplitude associated with the half-wavelength node. We refer to this region with negligible motor effect as *transition region*, as shown in Fig. 2.3. In this region the motion of points on the surface of the horn is random. The approximate dimensions of the motor effect regions and transition regions measured experimentally for aluminum and stainless steel are shown in Table 2.1.

Table 2.1: Approximate dimensions of the transition and motor effect regions for the aluminum and stainless steel horns.

Horn	Transition region	Motor effect (left)	Motor effect (right)
Aluminium	-0.25 in to +0.25 in	-1.5 in to -0.25 in	+0.25 in to +1.5 in
Stainless steel	+0.1 in to +0.2 in	-1.5 in to +0.1 in	+0.2 in to +1.5 in

2.1.4 Friction Reduction in Motor Effect Regions

The first group of tests was conducted at location -1 with no externally applied tangential force acting on the sliding block. The sliding block was observed to experience a net contact force from the piezoelectric vibrations which creates macroscopic motion toward the centerline of the horn. The motor force thus overcomes the static friction coefficient, giving an effective friction reduction of more than 100%. Similar results were obtained from the tests conducted at location +1. The motor force was quantified from the reading of the tangential load cell with the sliding block fixed at either the -1 or +1 position (Fig. 2.5). This measurement was conducted for the aluminum horn and stainless steel block. As shown in Fig. 2.6, the net motor force increases linearly as the normal force increases.

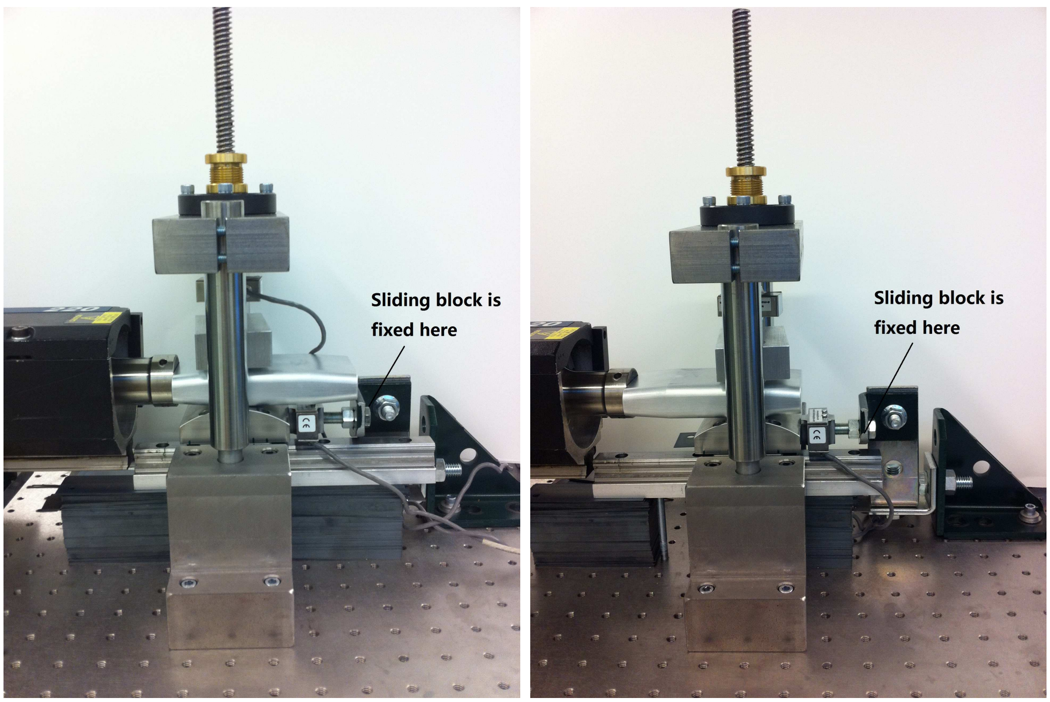

(a) (b)

Figure 2.5: Test set-up for quantifying the net motor force: (a) point -1 and (b) point +1.

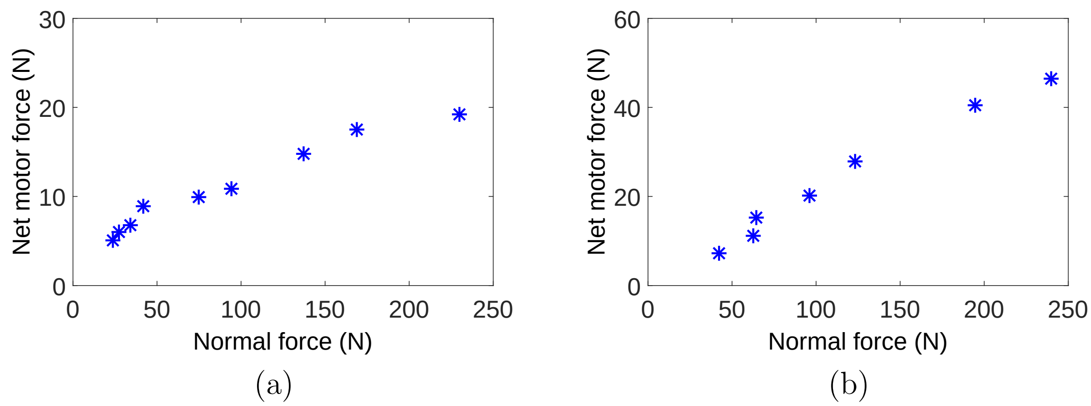

Figure 2.6: Relationship between normal force and net motor force: (a) point -1 and (b) point +1.

2.1.5 Friction Reduction in Transition Region

Tests conducted in the transition region for the aluminum horn and stainless steel sliding block are shown in Fig. 2.7 (a). The data shows a relatively linear relationship between tangential and normal forces both without and with ultrasonic power applied. In order to calculate the effective friction coefficients, points were extracted from the data as shown in panel (a). The dynamic friction coefficients are reduced from approximately 0.55 without ultrasonic vibration to approximately 0.35 with ultrasonic power applied. The percent friction reduction, shown in panel (c), hovers around 40% for all normal forces.

The measurements and calculated friction reduction curves for the other two material combinations are presented in Fig. 2.8 and 2.9. For the combination of stainless steel horn and aluminium block, the dynamic friction is reduced by 25 to 48%. For the combination of stainless steel horn and stainless steel block, the friction is reduced

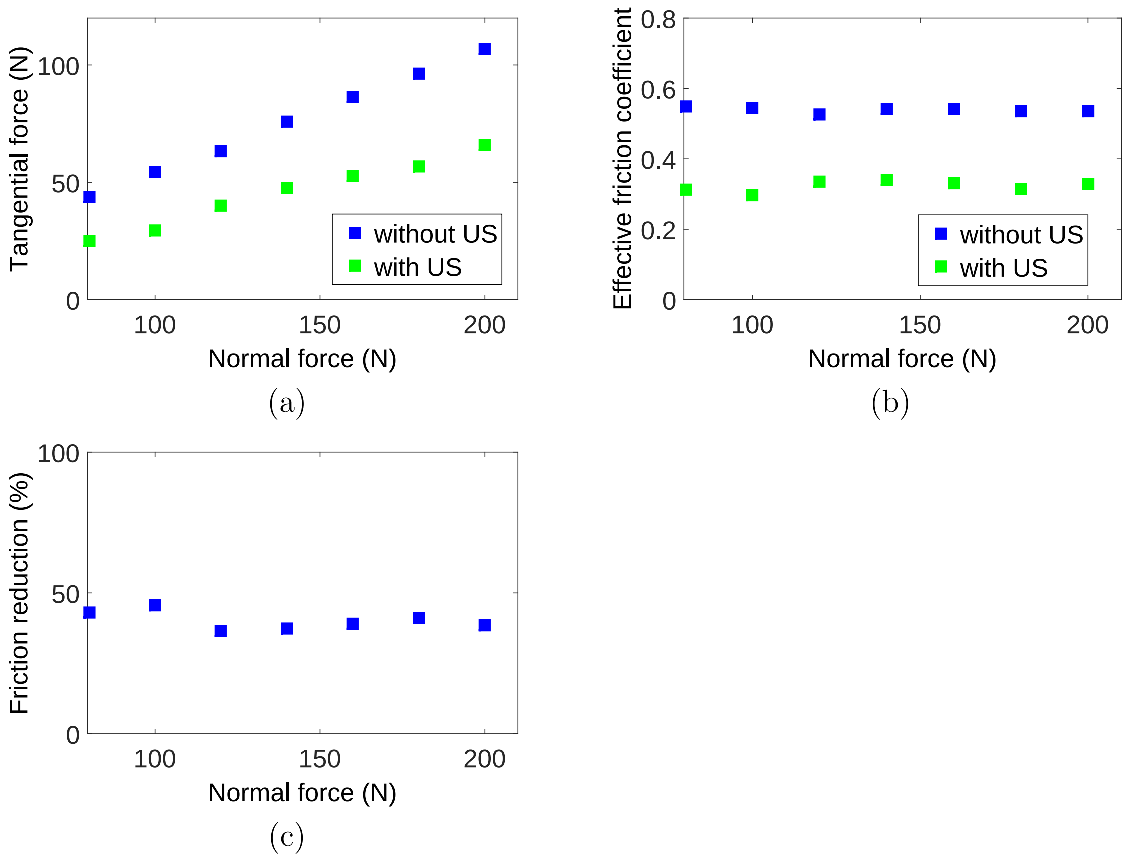

Figure 2.7: Transition region data for the aluminium horn and stainless steel block. (a) Measured normal forces and tangential forces; (b) Relationship between normal forces and friction coefficients calculated from the points in panel (a); (c) Friction reduction percentage as a function of normal load.

by 50 to 56%. The stiffer material combination gives greater friction reduction, as expected in general.

2.1.6 Discussion

In the motor effect regions, the vibrations drive the slider to move towards the centerline. However, measurements show that the driving forces at point -1 are much

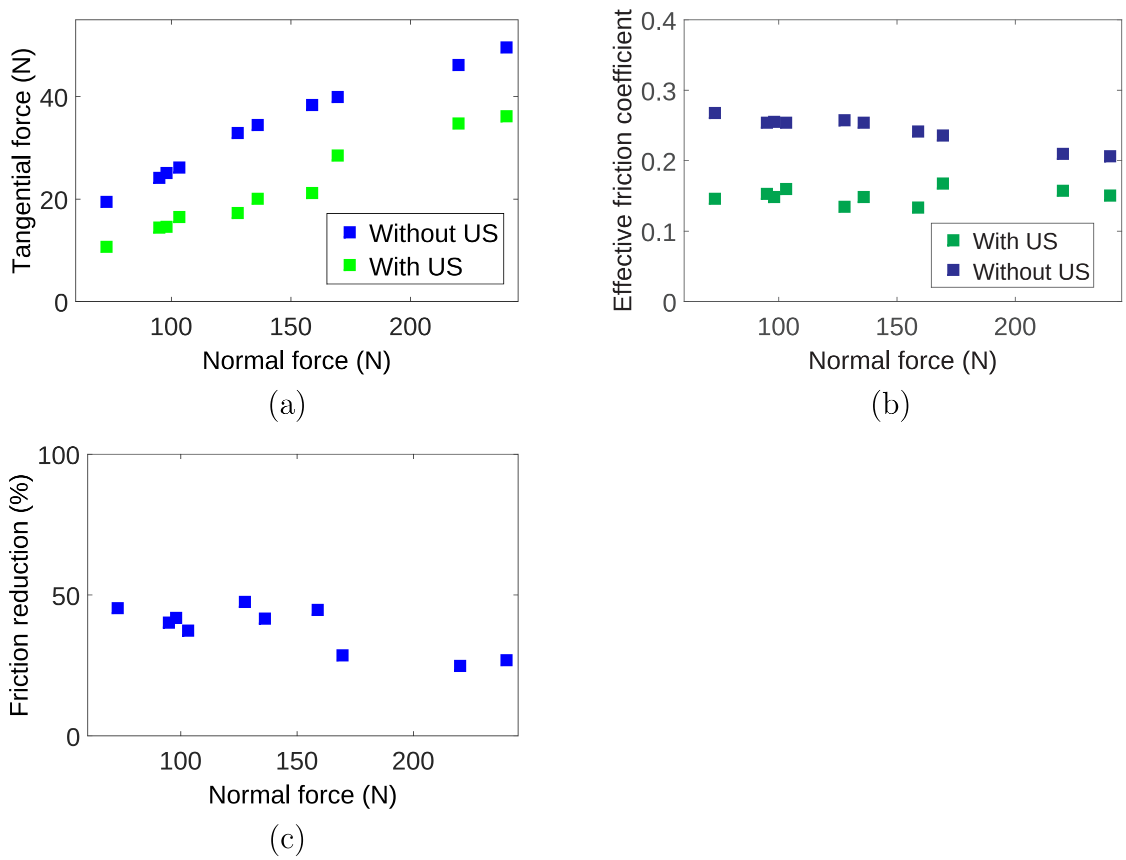

Figure 2.8: Measured friction, calculated friction coefficients, and calculated friction reduction for the stainless steel horn and aluminum block.

smaller than those at point +1. The reason for this is because the vibration amplitude at point -1 is smaller than that of point +1.

For friction in the transition region, it is evident that intrinsic friction measured between the stainless steel horn with an aluminum slider was smaller than that between the aluminum horn with a stainless slider, despite identical material combinations. This was due to the design of the experimental set-up. Normal force was applied through two low-friction pads on to the waveguide. Given the distance between the two pads, bending deformation was able to occur on the waveguide. Despite the low

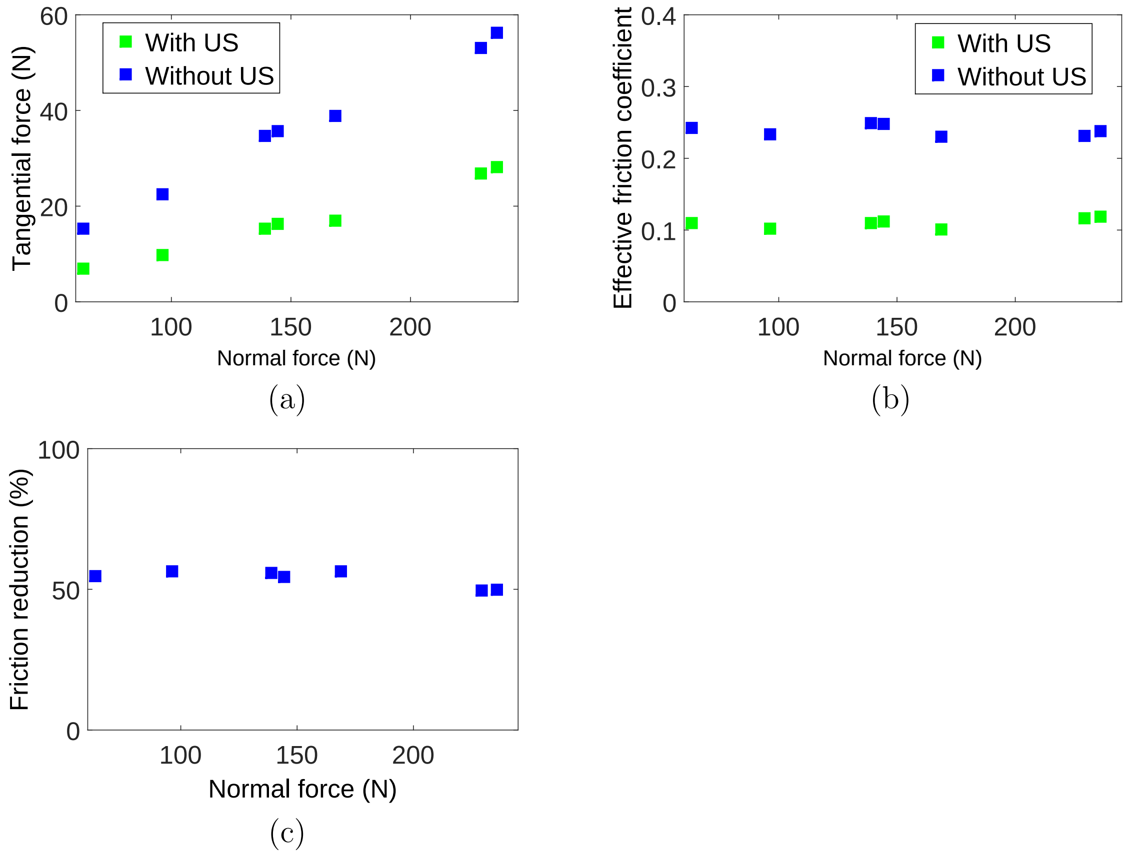

Figure 2.9: Measured friction, reduced data, calculated friction coefficients, and calculated friction reduction for the stainless steel horn and stainless steel block.

magnitude, the deformation created additional resistance to the sliding block. The deformation was larger for the aluminum waveguide than the stainless steel version since aluminum is less stiff. This leads to a larger intrinsic friction measured between the aluminum waveguide and the stainless steel slider.

2.1.7 Summary

This section presents an experimental study of ultrasonic lubrication created by Poisson-effect excitation. The ultrasonic horn was designed to exhibit two distinct regions. In the motor effect regions, the friction forces are fully cancelled by the motor force generated by the ultrasonic vibrations. The friction reduction in this region is 100%. In the transition region, the friction reduction percentages vary with different material combination and normal loading, in the range from 30% to 60%. The net motor forces increase when the normal load increases and the relationship follows a linear trend.

2.2 Friction Reduction using Flextensional Piezoelectric Actuator

2.2.1 Introduction

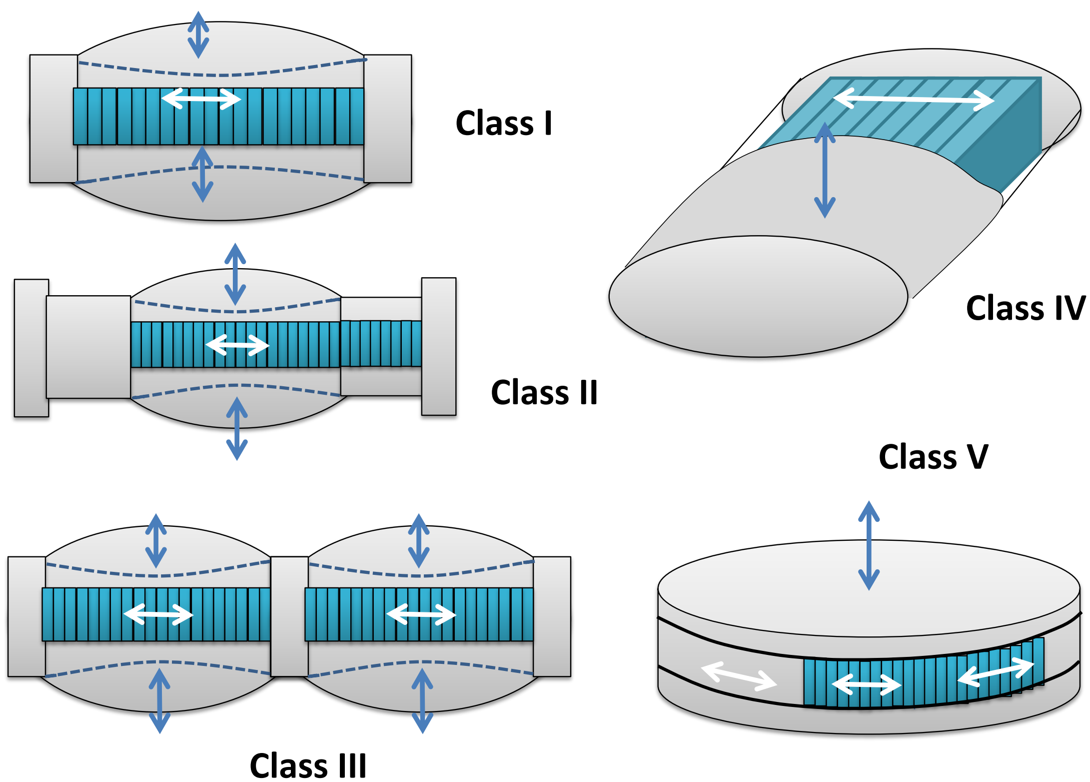

Figure 2.10: Different classes of flextensional transducers [52].

The second experimental study was conducted using a flextensional piezoelectric actuator. Flextensional transducers are a class of transducers capable of significantly amplifying the motion of the driver through a flexural-extensional behavior. Drivers can be piezoelectric or magnetostrictive [52]. The types of flextensional transducers can be divided into several major classes, as shown in Fig. 2.10.

2.2.2 Experimental Set-up

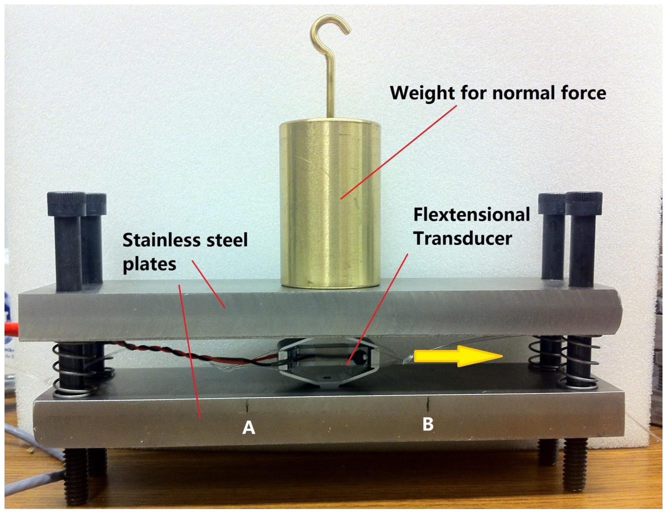

Figure 2.11: Experimental set-up of ultrasonic friction reduction using miniature transducer.

The experimental set-up is shown in Fig. 2.11. The flextensional actuator is a Cedrat APA40sm (Fig. 3.47), with a maximum stroke of 52 μm at the highest driving voltage of 150 V, a resonance frequency at 16 kHz, and a capacitance of 1.53 μF. The dimensions of the actuator is 14.9 mm by 27.1 mm by 10.5 mm. It was placed between two stainless steel plates, with the bottom plate set on a table top. The top plate was placed on four springs and guided by four pins. The actuator was pulled manually in the longitudinal direction indicated by the yellow arrow from point A to B at constant velocities. Between point A and B, the normal force was kept constant. Normal force was applied by placing different weights on the top plate. A load cell was connected to the actuator by fishing line to measure the pulling force, which is two times the friction force.

Figure 2.12: Flextensional actuator used in the experiment.

2.2.3 Friction Reduction vs. Driving Voltage

Two groups of tests were conducted under this set-up. The first studied the relationship between friction reduction and driving voltage under different normal loads. Peak-to-peak voltages were chosen to be 0 V, 2-6 Vpp, 4-8 Vpp, and 6-10 Vpp. Normal loads were 2.6 N, 4.6 N, and 6.6 N. Figure 2.13 (a)–(c) show the friction measurements under the three normal loads, respectively. In each plot, different colors denote different driving voltages. Intrinsic friction was measured when voltage was at 0 V and shown in black curves. Each test lasted approximately 10 seconds, with a linear velocity of approximately 5 mm/s. For all measurements, friction increased in the beginning of the sliding and decreased slightly afterward. This is due to the fact that static friction is higher than dynamic friction.

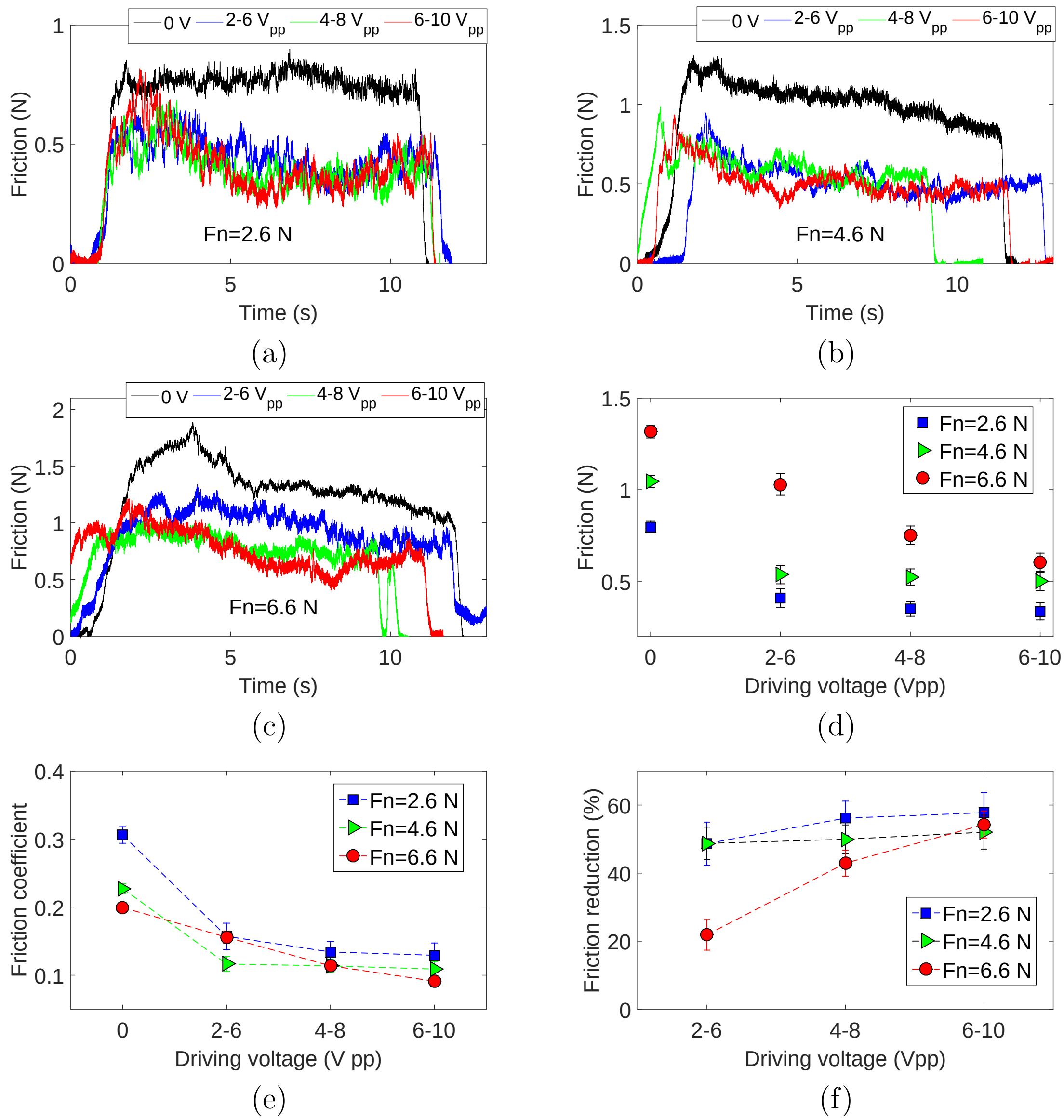

Figure 2.13: Relationship between friction reduction and driving voltage under various normal loads.

Evident friction reduction can be observed at all three loads. Steady state friction, friction coefficients, and friction reduction percentages are calculated and plotted against the driving voltage in Fig. 2.13 (d)-(f), where the markers and error bars represent the mean values and standard deviations of the measured data, respectively.

Plots show that higher voltage results in better friction reduction, however, saturation appears at higher voltages. Normal load has little effect in friction reduction, especially at higher voltages.

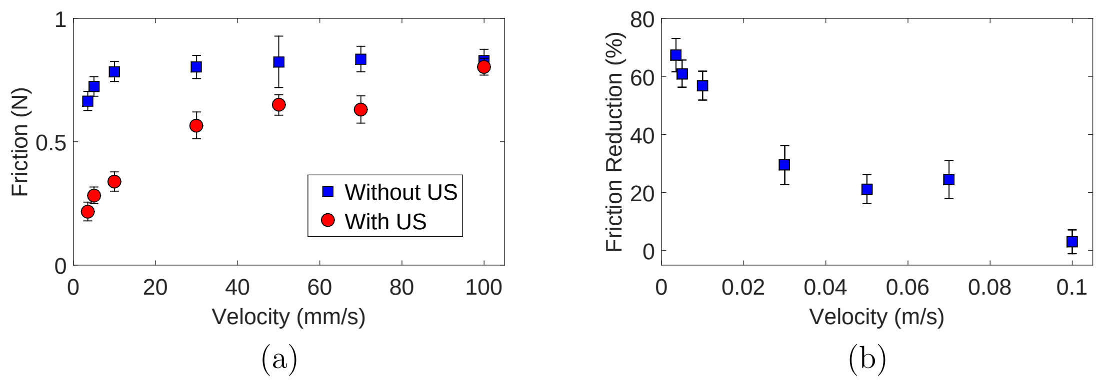

Figure 2.14: Relationship between friction reduction and linear velocity.

2.2.4 Friction Reduction vs. Linear Velocity

The second group of tests using this set-up investigated the relationship between friction reduction and linear velocity. Linear velocities were 3.5, 5, 10, 30, 50, 70, and 100 mm/s. Normal force was 2.6 N, and driving voltage was 2-6 Vpp.

Measured friction and calculated friction reduction is plotted against linear velocity in Fig. 2.14. In figure (a), intrinsic friction is plotted in blue markers and the reduced friction in red. Intrinsic friction increases rapidly as linear velocity increases, when under 10 mm/s. However, once the linear velocity is greater than 10 mm/s, it remains constant. Maximum friction reduction of approximately 70% was achieved at 3.5 mm/s of linear velocity. Friction reduction decreases as the linear velocity increases (One data point off the trend at 70 mm/s is possibly due to some experimental artifacts).

2.2.5 Discussion

Experimental data show that higher driving voltage results in greater friction reduction, however, friction reduction saturates as the driving voltage continues to increase. It should be pointed out that higher maximum voltage was applied to the actuator instead of peak-to-peak voltage, which is 4 V for all cases. Increasing maximum voltage results in more power to drive the actuator (0.59, 0.78, and 0.98 W, respectively). However, it is the peak-to-peak voltage that decides the vibrational amplitude, which greatly influences the effect of friction reduction. Therefore, friction reduction was not improved accordingly, even though more power was applied to the actuator.

Experimental data also show that friction reduction decreases when linear velocity increases. This finding is in line with previous studies by Littmann et al. [34, 35]. In their papers, it was concluded that when the ratio of vibrational and macroscopic velocities are close to 1, the friction reduction is nearly 0. Therefore, since vibrational velocity is approximately 150 mm/s in the second group of tests, the velocity ratio approaches 1 when macroscopic velocity is 100 mm/s. Thus, friction reduction decreases to a level close to none.

It should be noted that Littmann et al. employed ultrasonic vibrations in the direction longitudinal to the macroscopic velocity, while vibrations were employed in the vertical direction in this study. Although the relationship between friction reduction and linear velocity follows the same trend in both approaches, the mechanisms behind the phenomenon are different. Further investigation is required.

2.2.6 Summary

Ultrasonic friction reduction was achieved by sliding a flextensional actuator between two stainless steel plates in a sandwich structure. The friction between the flat surfaces of the actuator and the plates were reduced by up to 70% at different levels of driving power, normal loads, and linear velocities. Higher driving voltage results in higher friction reduction, but the effect saturates due to the fact that peak-to-peak voltage was not increased. Normal force has little effect on friction reduction. Higher linear velocity leads to lower friction reduction. When linear velocity increases close to the vibrational velocity of the actuator, friction reduction diminishes.

2.3 Friction and Wear Reduction using Modified Pin-on-disc Tribometer

2.3.1 Modified Pin-on-disc Tribometer

The experimental set-up used in this study is a modified pin-on-disc tribometer, as shown in Fig. 2.15 (A). This tribometer applies a specified force between a still pin and a rotating disc for the purpose of studying the characteristics of friction and wear on the disc surface. The pin has been modified with the addition of a piezoelectric actuator and an acorn nut with a rounded end (Fig. 2.15 (E)). The actuator imparts ultrasonic vibrations to the rotating disc along the direction perpendicular to the disc. The tribometer is held by a lever which is part of a gymbal assembly that has been installed on the frame (Fig. 2.15 (D)). Weights connected to the gymbal assembly are used to apply a force normal to the surface of the disc. The normal force is measured by a load sensor pad placed between the pin and the disc. The resistance of the sensor pad changes as a function of the applied force, resulting in a change of output voltage. The gymbal assembly is instrumented to measure friction forces using a load cell. The load cell is installed on one side of the assembly frame and pretensioned horizontally by a weight located on the other side. A schematic is shown in Fig. 2.16.

The piezoelectric actuator generates vibrations with amplitude of 2.5 μm at a frequency of 22 kHz. The temperature of the actuator can increase rapidly from the heat generated and accumulated during the test. To maintain even temperatures, air flow and a thermocouple are employed to cool down the actuator and monitor the temperature, respectively. The disc is 76.2 mm (3 in.) in diameter and held in place by a lathe chuck. The chuck, which is placed on a platform, is driven by a DC motor and variable speed controller.

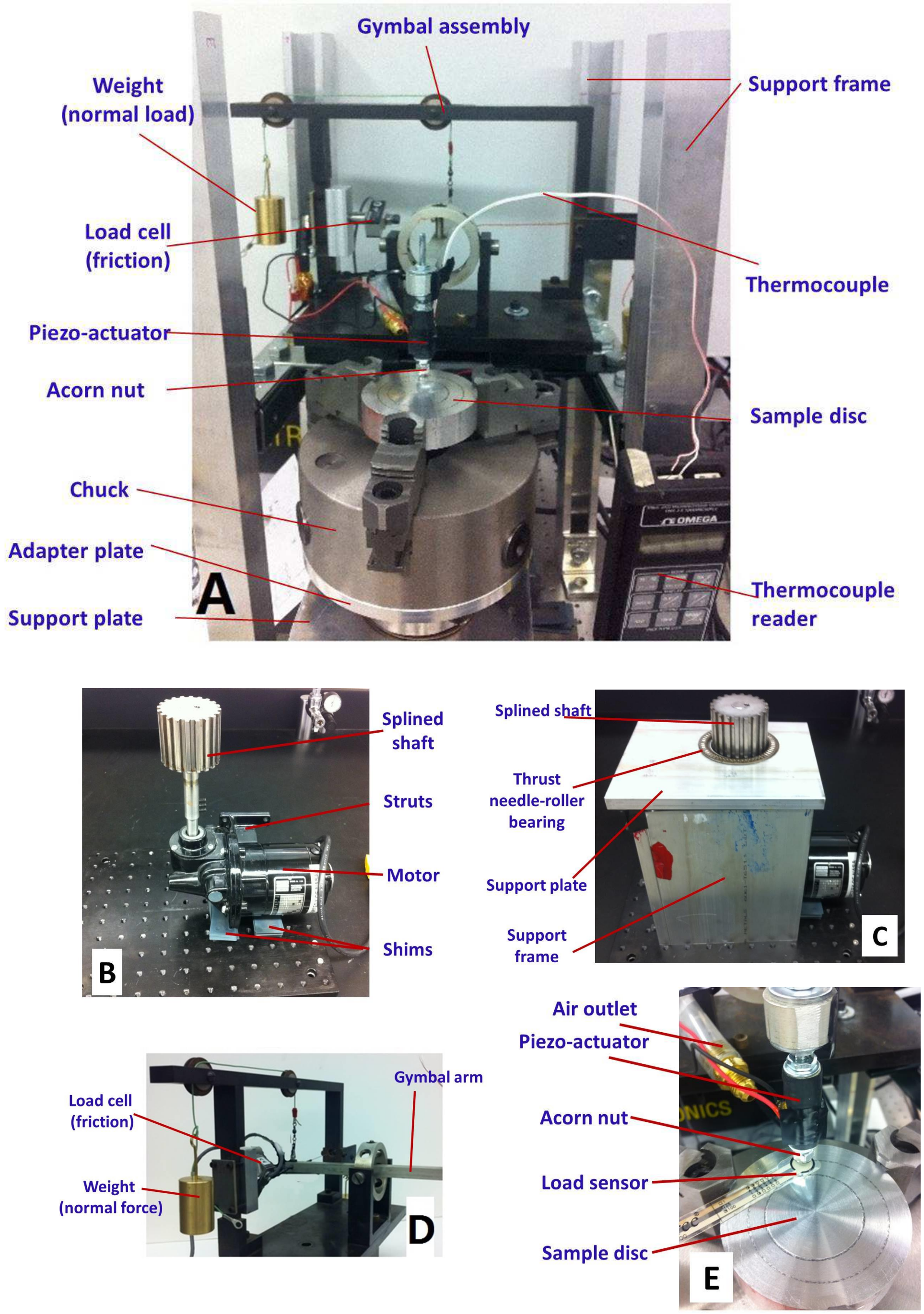

Figure 2.15: Experimental set-up for low stress and low velocity tests: (A) overall (B) gymbal assembly (C) piezo-actuator in detail.

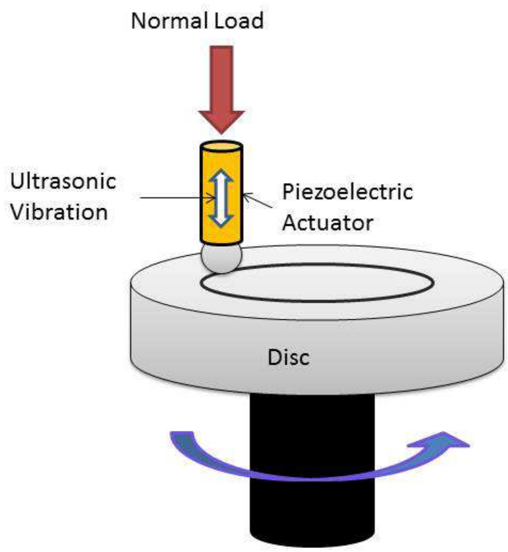

Figure 2.16: Schematic of modified pin-on-disc tribometer.

2.3.2 Parameters, schematics and procedures

Two studies were conducted using the tribometer to study the dependence of friction and wear reduction on linear speed and revolution, respectively. In study I, three groups of tests were conducted at linear speeds of 20.3, 40.6, and 87 mm/s. The distance traveled by the pin and the number of revolutions were kept constant by changing the duration of the test. For each speed, tests were conducted with and without ultrasonic vibrations. The remaining test parameters were fixed as shown in Table 2.2.

Each pin-on-disc test was conducted following the procedures suggested by ASTM G99 [53] with modifications:

Table 2.2: Parameters utilized in the tribometer tests of study I.

Parameter	Value		
Linear speed (mm/s)	20.3	40.6	87
Running time (h)	4	2	0.93
Distance traveled by pin (m)	292.5		
Revolutions	1600		
Pin material	Stainless steel 316		
Disc material	Aluminum 2024		
Nominal normal force (N)	3		
Disc run out (mm)	± 0.0286		
US frequency (kHz)	22		
US amplitude (μm)	2.5		
Nominal Groove diameter (mm)	50		
Nominal temperature (°C)	21 ± 1		
Nominal actuator temperature (°C)	31 ± 1		
Environment	Laboratory air		
Sampling frequency (Hz)	400		

(a) Clean and dry the acorn nut and disc specimens immediately prior to testing. Ethanol and acetone were used to remove all foreign matter.

(b) Insert the sample securely into the chuck so that the disc is perpendicular to the axis of revolution in order to minimize wobbling

(c) Install the acorn nut and compress it tightly against the piezoelectric actuator

(d) Adjust the position of the pin, making sure that it is perpendicular to the disc surface

(e) Add weight for application of normal loads

(f) Start the motor and adjust the speed to the desired value while preventing the pin from making contact with the disc, then stop the motor.

(g) Record the temperature and ambient environment of the tests. Prepare the data acquisition system for testing.

(h) Put the pin in contact with the disc. Start the motor and the piezoelectric actuator (when applicable). Stop the motor when the desired running time is reached.

(i) Clean the specimens and measure the volume loss and roughness parameters using a profilometer.

A more detailed protocol for conducting ultrasonic lubrication tests can be found in Appendix A.

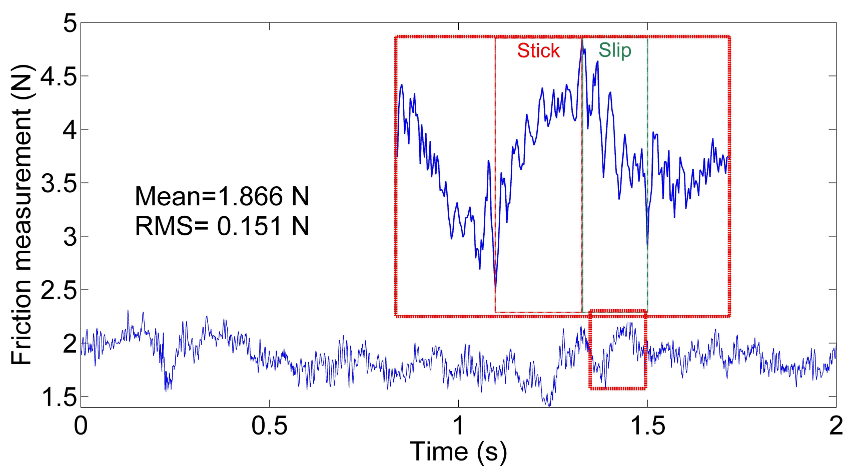

Figure 2.17: Time trace of the measured friction force showing the stick-slip effect.

Friction force was sampled at a frequency of 400 Hz and each sampling window was 2 seconds. Typical data from a single sampling window appears in Fig. 2.17, in which stick-slip is observed. The mean value and root mean square value (RMS) of the variation were calculated for each sampling window. A profilometer was then employed to measure the volume loss of the discs and the roughness parameters of the disc surfaces.

2.3.3 Friction Reduction vs. Linear Speed

Friction without ultrasonic vibrations

Mean friction values for three linear speeds are plotted against pin travel distance in Fig. 2.18 (a). In each case, the friction force increases rapidly initially, reaches steady state after a certain travel distance, and remains at that level for the remainder of the test. There is fluctuation of friction force after it reaches steady state. Unlike the fluctuation observed in Fig. 2.17, which is due to stick-slip, the fluctuation here is caused disc runout. The disc wobbles a small amount while rotating. The inertia from the up and down pin movement causes fluctuation of the normal force, and accordingly, fluctuation of the tangential friction force. The data confirms that higher speed results in a higher steady state value for the friction force.

Table 2.3 lists the steady state friction forces, their RMS values and the stabilization distance. As expected, the intrinsic friction force (force without ultrasonic vibrations) increases as the speeds increase. For metals, the friction-speed curve has a positive slope when speeds are low and a negative slope when speeds are high [54]. The speeds adopted in this study are relatively low.

Friction reduction

The mean value of the measured friction force with applied ultrasonic vibrations is plotted versus sliding distance in Fig. 2.18 (b) for three linear speeds. As with the intrinsic friction force, the measurement in each of these cases reaches steady state after the pin has traveled a certain distance over the surface of the disc. As in

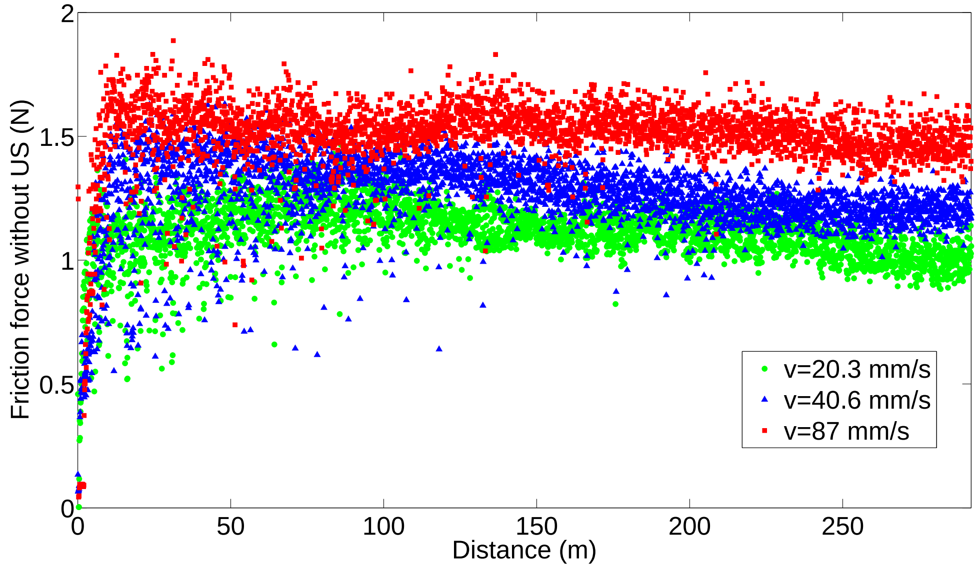

(a)

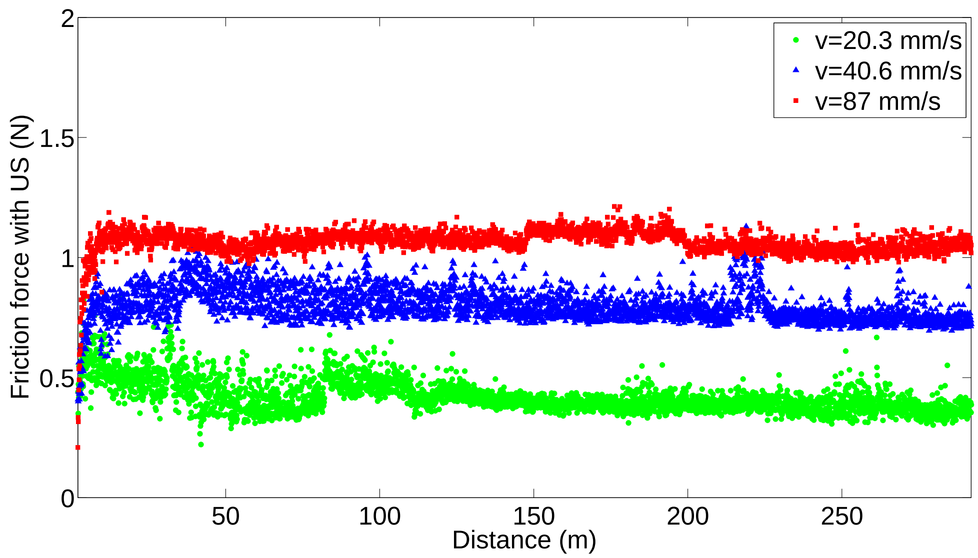

(b)

Figure 2.18: Steady state friction forces: (a) without ultrasonic vibrations; (b) with ultrasonic vibrations.

the previous case, the friction force fluctuates because of disc run out. However, the fluctuation amplitudes are smaller because the inertial forces on the pin are reduced when ultrasonic vibrations are present.

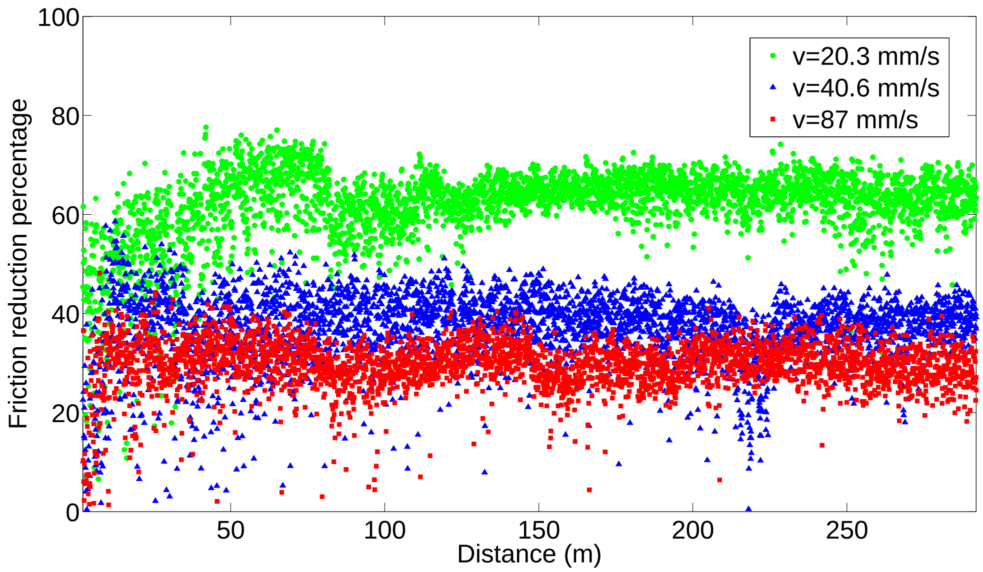

Figure 2.19: Friction reduction percentage vs. distance that pin travels.

The friction reduction percentage is defined as

$$P_f = \frac{f_0 - f_1}{f_0} \times 100, \tag{2.1}$$

where f_0 is the intrinsic friction force and f_1 is the friction force when ultrasonic vibrations are applied. The friction reduction percentages for each linear speed are plotted in Fig. 2.19. All three linear speeds give consistent friction reduction at steady state; a lower sliding speed results in greater friction force reduction.

Table 2.3 lists the steady-state friction forces, their RMS values, and the distances needed to reach steady state. As is the case with the intrinsic friction force, the friction force when ultrasonic vibrations are applied increases as the linear speed increases.

Table 2.3: Comparison of steady state friction forces and distances to achieve steady state.

Group	Linear speed (mm/s)	US	Steady-state friction (N)	Distance to achieve steady state (m)	RMS of steady-state friction (N)	Distance to achieve steady state (m)
1	20.3	No	1.024±0.063	4.17	0.197±0.039	3.11
		Yes	0.379±0.041	2.78	0.081±0.020	35.71
2	40.6	No	1.201±0.055	11.61	0.251±0.034	7.97
		Yes	0.748±0.035	7.21	0.096±0.033	45.44
3	87	No	1.472±0.064	8.94	0.249±0.033	3.22
		Yes	1.041±0.056	4.64	0.188±0.021	31.53

The trend is shown in Fig. 2.20, where the markers indicate the mean values and the error bars are the RMS of the steady state values.

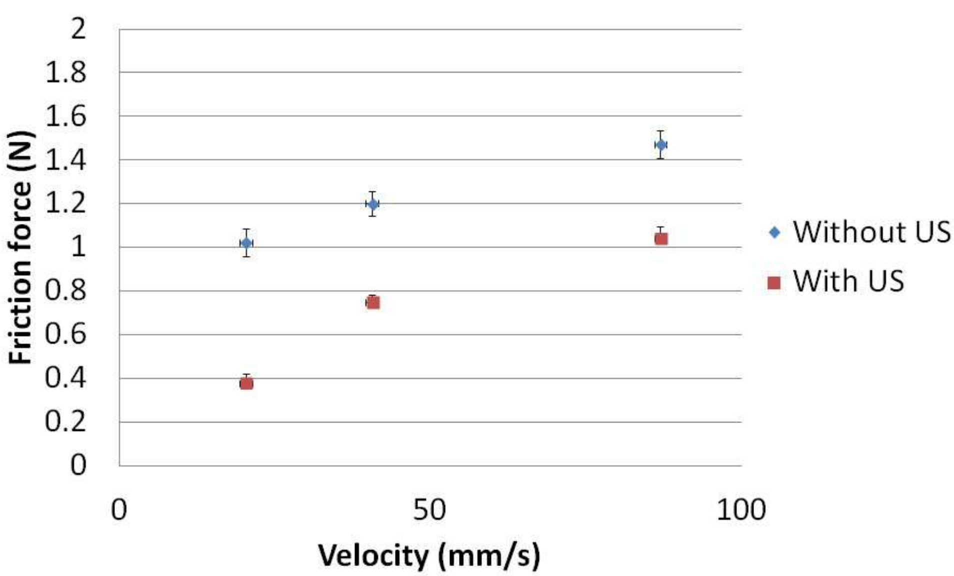

Figure 2.20: Relationship between measured friction force and linear speed.

It is emphasized that it takes a shorter distance for the force to stabilize when ultrasonic vibrations are applied, for the three linear speeds tested. The ultrasonic vibrations make it easier for the oxide layer of the pin and disc to break down and build up a steady contact while it takes a longer time for that to occur without ultrasonic vibrations. At the intermediate speed (40.6 mm/s) the force takes longer to stabilize both with and without ultrasonic vibrations.

RMS of friction force variation

As shown in Fig. 2.17 (inset), the instantaneous friction force fluctuates due to stick-slip. Stick is the stage when two objects stay relatively still and friction increases. Slip happens when the friction increases to such an extent that the two surfaces release to slide relative to each other. A commonly accepted explanation for stick-slip is that the effective friction coefficient varies during sliding over a range covering the static and dynamic coefficients [54]. Another cause of stick-slip can be the waviness of the surface, which results in an inconsistent effective friction coefficient [2]. In this study, the average amplitude of the stick-slip fluctuation is found from the RMS value of the measured force. This calculation is performed over consecutive 2-second boxcar windows. The RMS friction force is plotted versus travel distance for each of the tests groups without ultrasonic vibrations and with ultrasonic vibrations (Fig. 2.21).

In both cases, the RMS values reach steady state after a certain distance is reached. Contrary to the mean values, however, it takes significantly longer for the stick-slip to stabilize when the ultrasonic vibrations are on than when they are off. The stick-slip amplitudes are nearly the same for the three speeds when the ultrasonic vibrations are absent. When the vibrations are applied, all three cases show amplitude reductions with different levels. The steady state values of friction force and distances to achieve

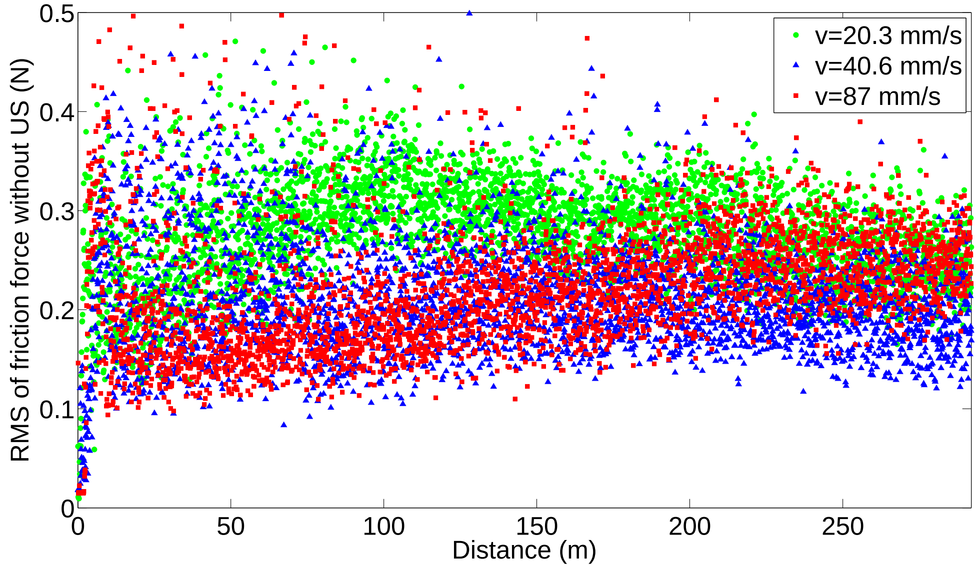

(a)

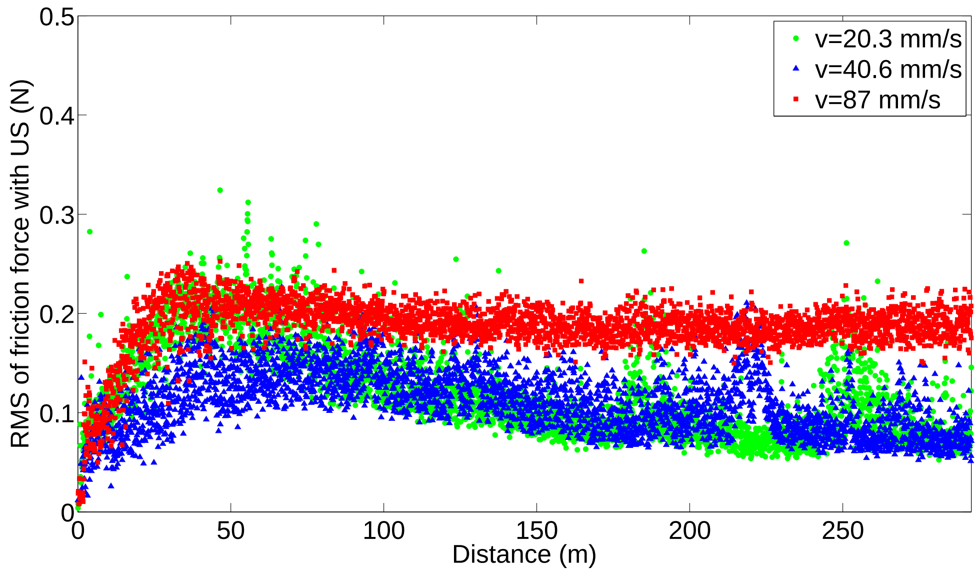

(b)

Figure 2.21: RMS of friction force: (a) without ultrasonic vibrations; (b) with ultrasonic vibrations.

steady state friction are presented in Table 2.3; Fig. 2.22 shows the RMS value of friction force with the markers indicating the average value of the RMS force over the entire test and the error bars represent one standard deviation of the RMS values.

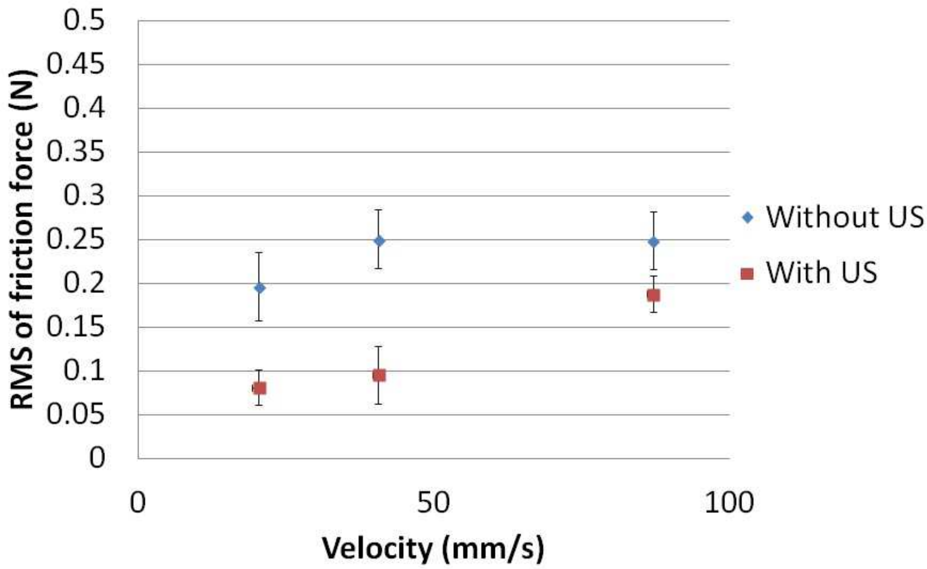

Figure 2.22: Relationship between RMS of friction force and linear speed.

2.3.4 Wear Reduction vs. Linear Velocity

The materials in this study, stainless steel and aluminum, exhibit hardnesses ranging from 700 to 950 kg/mm^2 and from 45 to 50 kg/mm^2, respectively. Due to the difference in hardness, the type of wear between them is abrasive: the harder material digs into the softer one, removing material and creating grooves [55].

Images of the wear grooves from all test groups are shown in Fig. 2.23. Each image shows approximately one quarter of the whole groove. It can be observed that the grooves from tests with ultrasonic vibrations (images A, C, E) appear more uneven and non-reflective than the ones without it (images B, D, F).

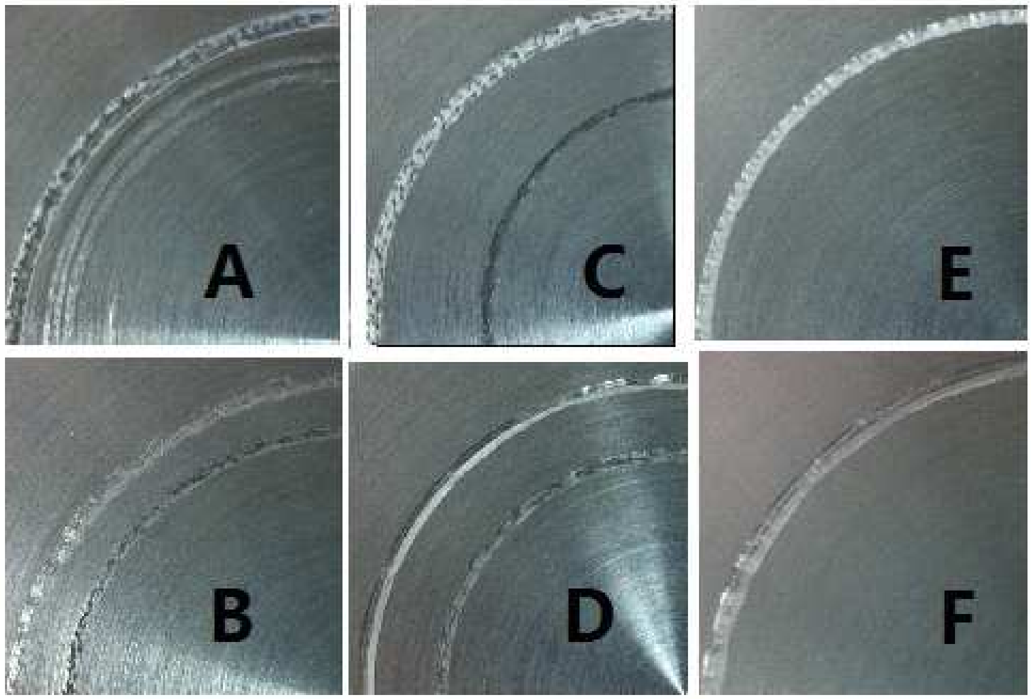

Figure 2.23: Wear grooves obtained with ultrasonic vibrations (A, C, and E) and without ultrasonic vibrations (B, D, and F). Each column corresponds to a linear speed: 20.3 mm/s (A, B); 40.6 mm/s (C, D); and 87 mm/s (E, F).

A 3D profilometer was employed to quantify the wear volume loss and obtain the profiles of the wear grooves along with roughness parameters of the scanned surface. Eight spots along the path of each wear ring were scanned. Each scan was conducted over an area of 1.8 mm by 2.4 mm with a scan stroke of ±100 μm. The 3-D profiles of the grooves from all linear speeds are shown in Fig. 2.25. The groove topology changes when ultrasonic vibrations are applied by becoming narrower and less smooth. This explains why the grooves appear uneven in Fig. 2.23. Round dents are observed in B, C and F, becoming more distinct as linear speed increases. This effect is not observed without ultrasonic vibrations. The color coding representing the depth of the grooves shows that the grooves are shallower when ultrasonic vibrations are applied. In addition, the surface roughness parameters are consistently lower when ultrasonic vibrations are applied, as shown in Table 2.4. In combination, these measurements suggest that ultrasonic vibrations reduce wear.

To quantify the degree of wear reduction, wear rate is defined as

$$W = \frac{V}{D}, \tag{2.2}$$

where V is disc volume loss in mm^3 and D is the distance travelled by the pin in meters. The disc volume loss is calculated from data of groove volume obtained with the profilometer. The wear reduction percentage is defined as

$$P_w = \frac{W_0 - W_1}{W_0} \times 100, \tag{2.3}$$

where W_0 is the wear rate without ultrasonic vibrations applied and W_1 is the wear rate with ultrasonic vibrations applied. The wear rates and wear reduction percentages are listed in Table 2.5. The results show that the wear rate is nearly constant for the three linear speeds, both with and without ultrasonic vibrations. The wear reduction percentage slightly increases as the speed increases. Few previous studies focused on the relationship between abrasive wear and sliding speed, but the effect of sliding distance on friction has been investigated in depth [56, 57]. Studies have shown that when there is unlimited abrasive material (harder material), the wear rate is initially low and subsequently increases until it reaches a steady state value. However, if the abrasive material is limited, the wear rate will decrease as the test continues. In both cases, the wear rate was found not to depend on the sliding velocity.

There is a close correlation between the observed stick-slip and the topology of the grooves. The segment of the groove in Fig. 2.25 (F) shows two indentations

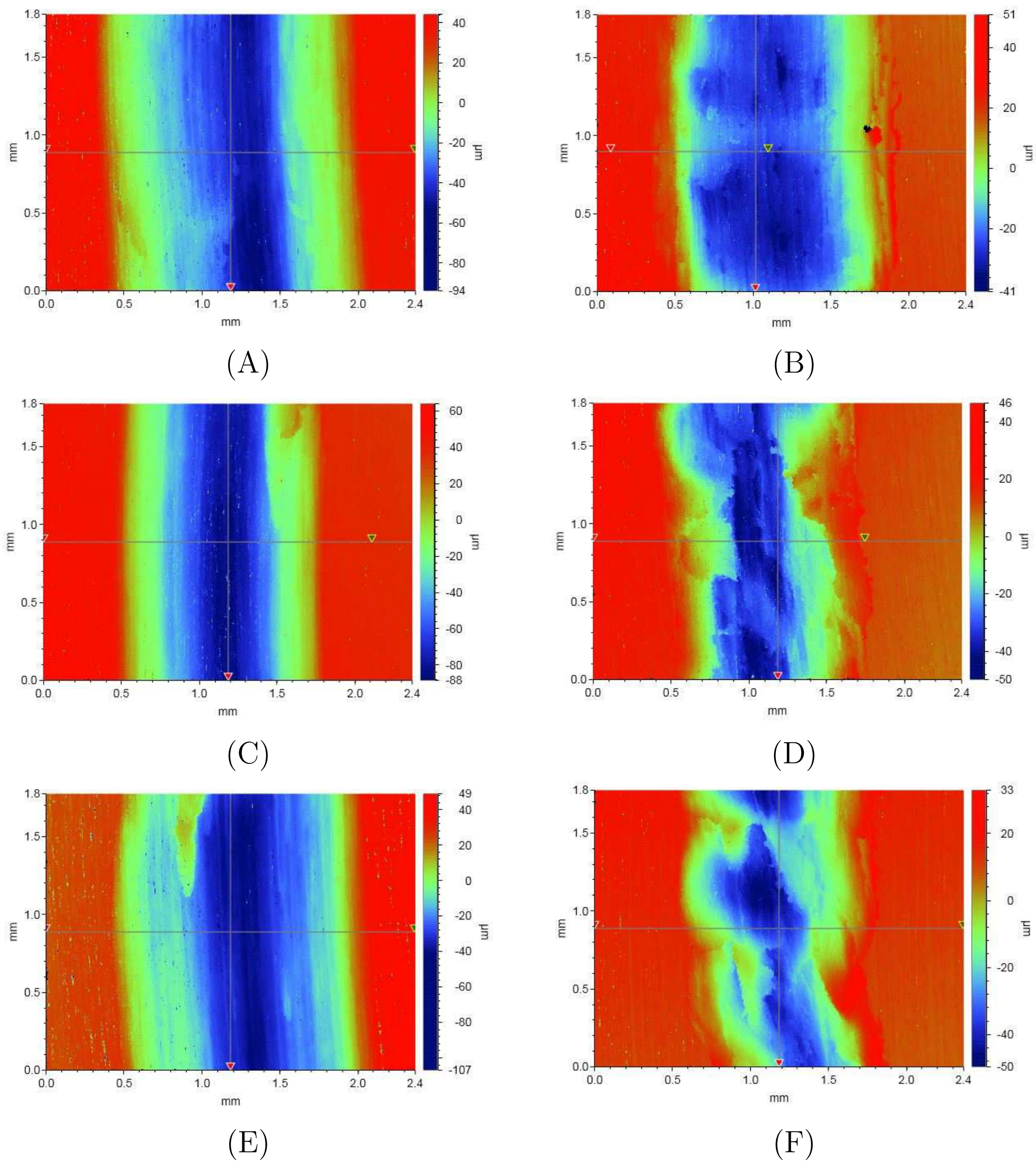

Figure 2.24: 2D profiles of wear grooves obtained without ultrasonic vibrations (A, C, and E) and with ultrasonic vibrations (B, D, and F). Each represents a linear speed: 20.3 mm/s (A, B); 40.6 mm/s (C, D); and 87 mm/s (E, F).

which were created by the contact between pin and disc during the stick phase. The measured distance between the two indentations is 0.869 mm. It is noted that the

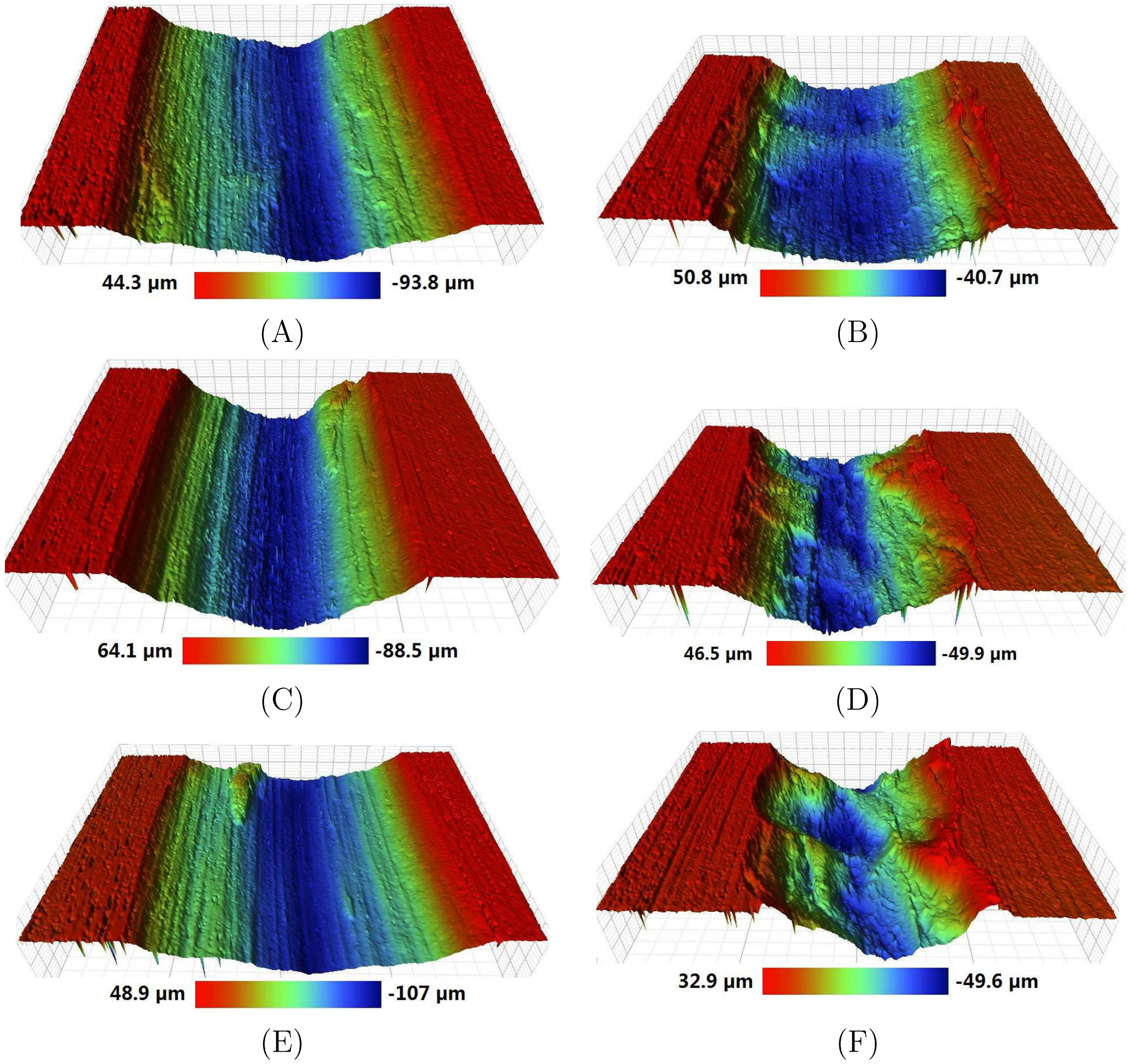

Figure 2.25: 3D profiles of wear grooves obtained without ultrasonic vibrations (A, C, and E) and with ultrasonic vibrations (B, D, and F). Each represents a linear speed: 20.3 mm/s (A, B); 40.6 mm/s (C, D); and 87 mm/s (E, F).

scale on the plane of the surface is different than the scale along the depth direction. The distance between the indentation centers can be estimated by

$$s = \Delta t \times v, \tag{2.4}$$

where $\Delta t = 0.01$ sec is the period of stick-slip (high frequency component in the inset of Fig. 2.17) and v is the linear speed. The calculated distances are 0.213 mm, 0.426 mm, and 0.853 mm for the three linear speeds of 20.3 mm/s, 40.6 mm/s, and 87 mm/s, respectively. The data and calculation match well for the speed of 87 mm/s. However, the individual indentations are not as evident in the other two cases because at these lower speeds the indentations overlap one another. When no ultrasonic vibrations are applied, the pin and disc make contact during both the stick and slip phases, creating little waviness along the grooves.

Scanning electron microscopy was employed to observe in detail various wear features and quantify key dimensions of wear patterns. Images (A) and (B) in Fig. 2.26 were taken of the grooves created without and with ultrasonic vibrations at a speed of 87 mm/s, respectively. The wear pattern without ultrasonic vibrations shows a uniform shade of gray and straight white lines, while the one with ultrasonic vibrations has curved white lines and various darker irregularities. Image (C) shows a magnified view of the groove in image (B). The groove surface includes voids (black), deposits of foreign materials from the pin (gray), and oxide layers (white), which are marked with triangular, rectangular, and circular shapes, respectively. The white dotted lines are the traces of the contact points between pin and disc asperities. Image (D) shows a close-up of those lines. The visible white dots are attributed to a punching action of the pin on the disc as the piezoelectric actuator cyclically increases and decreases the contact pressure between the two. This punching action is observed in the round indentations shown in Fig. 2.25 (B, D, F). The nominal distance between the dots is measured as 3.6 μm, which is close to the value of 3.9 μm calculated from the ratio of linear speed and frequency of ultrasonic vibrations. It is proposed that the contact between the pin and disc takes place only on groups of asperities instead of the whole nominal area of contact. This observation motivates one of the assumptions made to develop the cube model for wear, explained in the following section.

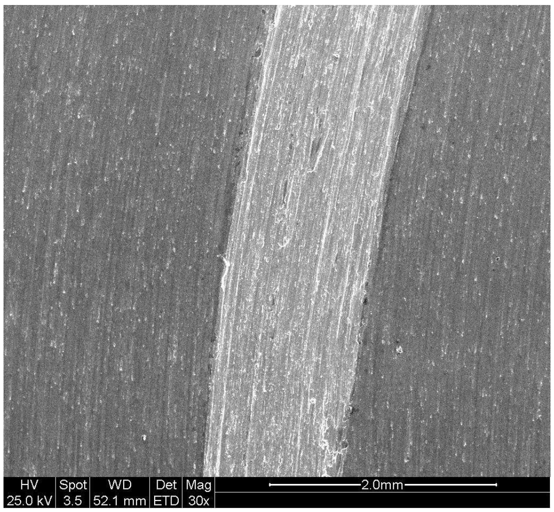

(A)

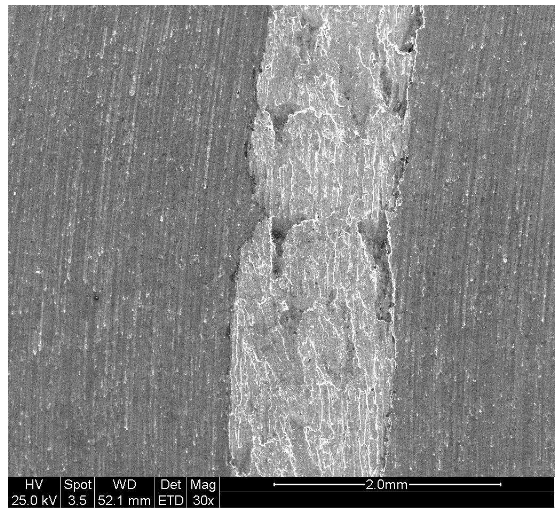

(B)

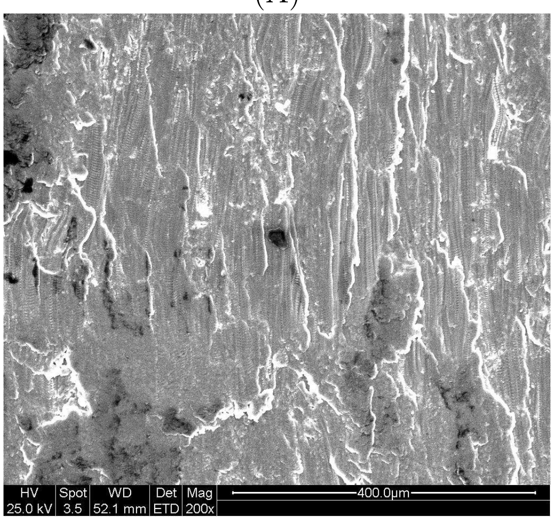

(C)

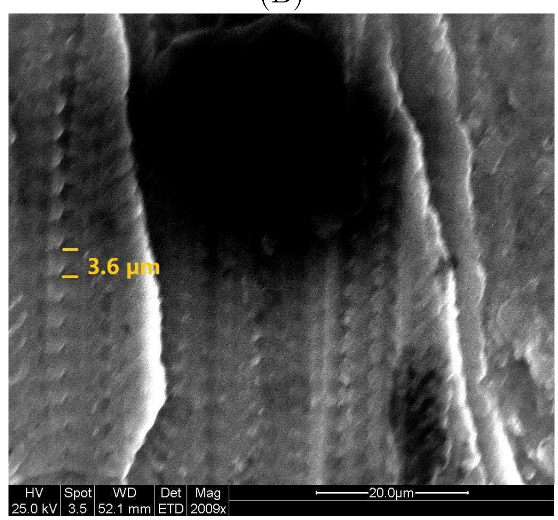

(D)

Figure 2.26: SEM images of wear grooves: (A) without ultrasonic vibrations, and (B) with ultrasonic vibrations. Image (C) is a close-up of (B), whereas further magnification of the same image is shown in (D).

Table 2.4: Comparison of surface roughness parameters: R_a arithmetic average; R_p maximum peak height; R_q root mean squared; R_t maximum height of the profile; and R_v maximum valley depth.

Speed (mm/s)	US	R_a (μm)	R_p (μm)	R_q (μm)	R_t (μm)	R_v (μm)
No wear		0.45	10.071	0.58	18.887	8.816
20.3	N	18.829	48.440	21.421	124.35	75.906
	Y	17.238	38.458	18.975	87.011	48.554
40.6	N	21.647	46.646	22.673	109.28	62.638
	Y	17.289	42.469	19.922	106.42	63.947
87	N	19.825	48.910	21.921	130.52	81.612
	Y	17.606	44.245	20.126	111.25	66.877

Table 2.5: Reduction percentages as a function of linear speed for friction force, wear, and stick-slip measurements.

Linear speed (mm/s)	Wear rate without US (mm^3/m)	Wear rate with US (mm^3/m)	Wear reduction (mm^3/m)	Wear reduction (%)	Number of contacts	Friction reduction (%)
20.3	2.237×10^{-2}	1.214×10^{-2}	1.023×10^{-2}	45.76	3.17×10^{8}	62.22
40.6	2.581×10^{-2}	1.338×10^{-2}	1.243×10^{-2}	48.18	1.58×10^{8}	36.11
87	2.430×10^{-2}	1.248×10^{-2}	1.182×10^{-2}	48.63	7.39×10^{7}	29.32

2.3.5 Discussion

The measurements indicate that ultrasonic vibrations are effective to reduce friction, stick-slip, and wear at all three linear speeds (see Fig. 2.27).

With increasing speed, the degree of friction reduction decreases from 62.2% for 20.3 mm/s to 29.3% for 87 mm/s. This observation is in line with Littmann et al. [34], who studied the relationship between velocity ratio and friction ratio. In

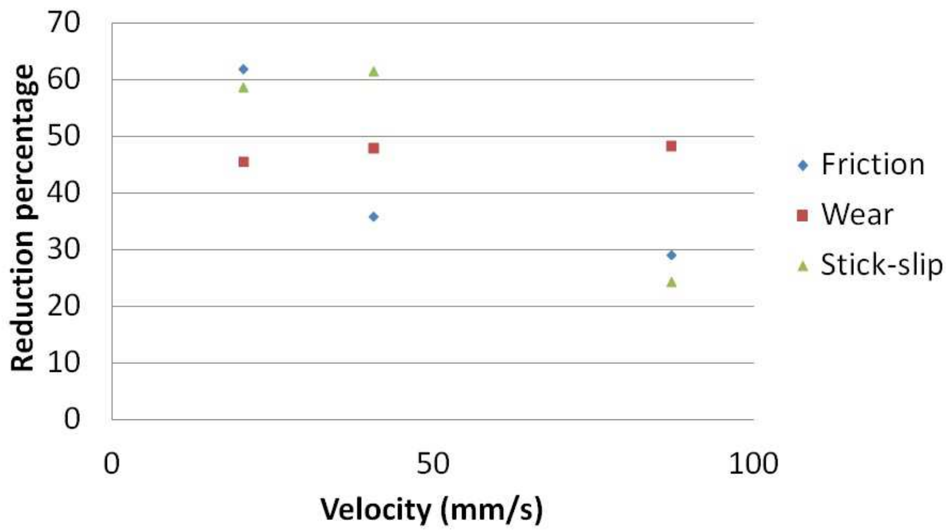

Figure 2.27: Relationship between reduction results and linear speeds.

their study, the velocity ratio was defined as the macroscopic velocity over the velocity of the ultrasonic vibrations. The friction ratio was defined as the friction force with ultrasonic vibrations over friction force without ultrasonic vibrations. It was proposed that a small velocity ratio leads to a low friction ratio, and hence effective friction reduction. As the velocity ratio increases, so does the friction ratio until a value of 1 is achieved and no further benefit from the ultrasonic vibrations is possible. Therefore, an increase in sliding velocity moves the system towards a friction ration of 1 and reduces the effectiveness of the ultrasonic vibrations. Conversely, to maintain high friction reduction for high sliding velocities, a high vibration frequency is necessary. Due to the nature of piezoelectricity, achieving high frequency of operation requires an actuator capable of handling high output power.

In our measurements, wear reduction varies over a narrow range with changing linear speed (45.8% to 48.6%). Surprisingly, a higher velocity results in a slightly higher wear reduction. One explanation is that as speed increases the actual contact between the pin and the disc decreases. Studies showed that when the amplitude of ultrasonic vibrations is large enough, the contact time between two sliding surfaces is reduced as one surface moves away from the other [49, 50]. Assuming that the pin makes one contact with the disc and then moves away from it in one cycle of ultrasonic vibration, the number of contacts between the disc and the pin over the duration of a test can therefore be estimated. These values are presented in Table 2.5.

The relationship between stick-slip reduction and linear speed does not follow the same trend. As shown in Fig. 2.27, the percentage reduction of stick-slip first increases with linear speed and then decreases. It has been shown that the amplitude of vibration caused by stick-slip is related to the stiffness and damping of the system and that increasing the stiffness can greatly reduce the amplitude of vibration [2]. The reason is that stick-slip can be considered as an excitation to the system, and linear speeds in addition to the waviness of the surface can change the frequency of the excitation. At certain speeds, the system is excited at its resonance frequency, which results in a magnification of the stick-slip vibration. The system resonance frequency can be increased if the system is stiffer. Therefore, the possibility of magnifying the vibration is reduced when the surfaces slide at the same range of speeds [57].

2.3.6 Wear Reduction vs. Revolution

In study II, stainless steel acorn nuts and aluminum discs were tested for wear reduction for 900, 1600, and 1900 revolutions at a constant angular speed, which results in different pin travel distances, as shown in Table 2.6. For each revolution, tests were conducted with and without ultrasonic vibrations. The remaining test parameters were kept the same as the ones from friction reduction experiments, shown in Table 2.2. Wear in these tests is abrasive due to the fact that stainless steel is harder than aluminum. This experiment is designed to investigate the relationship between abrasive wear reduction and the number of revolutions traveled by the pin relative to the disc.

Table 2.6: Parameters utilized in ultrasonic wear reduction tests of study II.

Parameter	Value		
Running time (h)	1	1.68	2
Distance traveled by pin (m)	75.2	126.4	150.5
Revolutions	960	1600	1900
Linear speed (mm/s)	20.3		

Table 2.7: Wear reduction data with and without ultrasonic vibrations.

Parameter	Value		
Revolutions	950	1600	1900
Volume loss without US (mm^3)	1.815	3.229	3.839
Wear rate without US (mm^3/m)	2.414×10^{-2}	2.554×10^{-2}	2.551×10^{-2}
Volume loss with US (mm^3)	1.134	1.745	2.094
Wear rate with US (mm^3/m)	1.509×10^{-2}	1.381×10^{-2}	1.392×10^{-2}
Wear reduction (%)	37.50	45.95	45.45

2.3.7 Summary

In this study, a modified pin-on-disc tribometer was built for investigating the effect of ultrasonic vibrations on friction and abrasive wear between stainless steel pins and aluminum discs under a normal load of 3 N. Ultrasonic vibrations generated by a piezoelectric actuator had an amplitude of 2.5 μm and a frequency of 22 kHz. Three different linear speed were considered (20.3 mm/s, 40.6 mm/s, and 87 mm/s) while keeping other parameters unchanged throughout the testing.

The friction measurements show that ultrasonic vibrations reduce the effective friction force up to 62 %. Consistent with previous studies, the benefit of ultrasonic vibrations diminishes with increasing speed, though 20 % friction force reduction was still achieved at 87 mm/s. Other parameters such as contact stiffness, surface roughness, and materials hardness are known to participate in ultrasonic lubrication. Those parameters will be the subject of a future study. Further, characterization of ultrasonic lubrication will be performed at higher speeds and normal pressures. According to theory, higher ultrasonic power is required to achieve the same degree of ultrasonic lubrication achieved at lower speeds and pressures.

The wear measurements show a consistent reduction in volume loss of up to 49%, with little dependency on velocity at the speeds considered. A slight increase in the effectiveness of wear reduction at 87 mm/s is attributed to a decrease in the number of contacts over the duration of the test. The SEM images of wear grooves show abrasive mode with small scale features located 3.6 μm apart that appear to be created by a punching action of the pin as it vibrates at 22 kHz over the surface of the disc. Larger scale indentations located approximately 0.9 mm apart appear to be created by stick-slip at a frequency of approximately 100 Hz. The measurements show that stick-slip amplitudes decrease up to 61% when ultrasonic vibrations are applied. However, no clear trend is found in the relationship between stick-slip reduction and linear speeds. Future work will focus on the relationship between system stiffness and stick-slip amplitudes.

2.4 Friction and Wear Reduction Studies for Metal Forming

2.4.1 Introduction

Experiments on the modified tribometer were conducted with normal stress smaller than 5 MPa and velocity smaller than 100 mm/s. In this section, modifications are made to the tribometer so that tests with higher linear velocities and higher normal stresses can be conducted. This was a preliminary study for ultrasonic lubrication in metal forming processes, such as sheet rolling, sheet drawing, wire drawing, press forming, and drilling among others. It included two parts: a literature review on the role of ultrasonics in metal forming, and an experimental study of ultrasonic friction and wear reduction with high stress and high velocity.

Previous studies [58, 59, 60, 61] have shown that ultrasonic lubrication can help:

- Reducing the drawing/pressing force [62, 63]
- Reducing the damage of the work piece: wrinkling and cracking from pressing work [64]
- Overcoming difficulties in achieving desired tolerance [65]
- Improving final shape of products [66, 67]
- Elongating tool life [68]

Studies have been conducted to investigate the mechanisms behind the effects. Major findings from the literature are summarized in Fig. 2.28. Four major benefits of using ultrasonics in metal forming can be related to the reduction of three items: drawing force, surface wear, and friction. Five mechanisms were proposed, with detailed descriptions of each elaborated below.

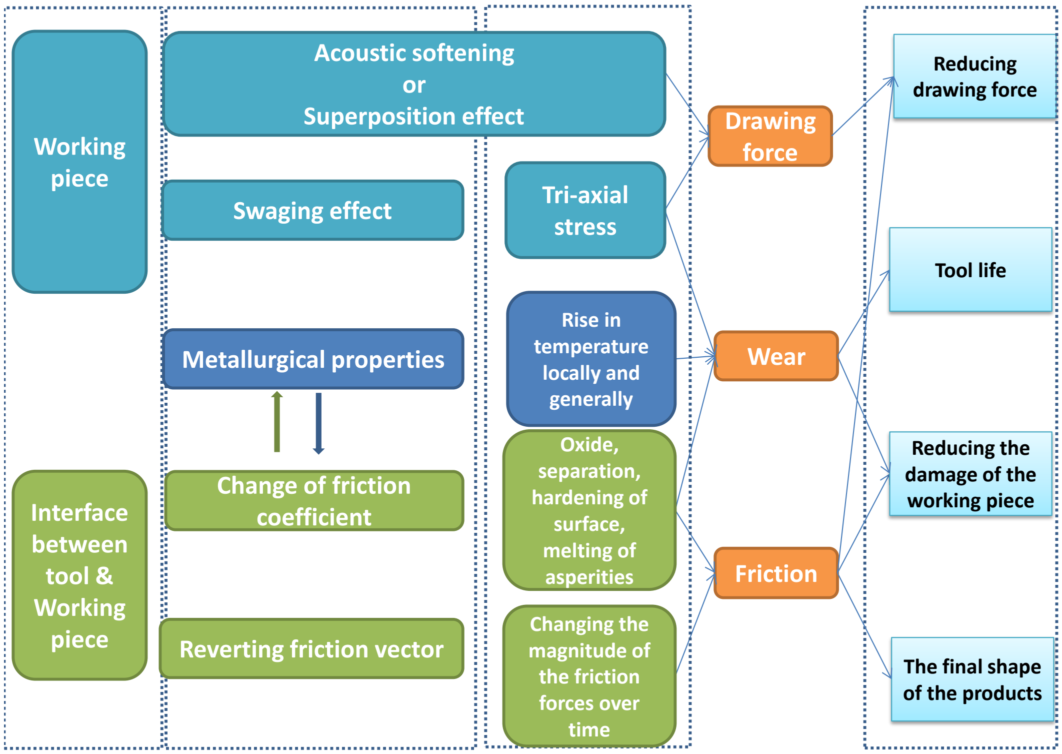

Figure 2.28: Mechanisms of ultrasonics in metal forming.

Acoustic softening vs. superposition effect

It was first found by Blaha and Langenecker [69] that the force to deform zinc single crystal can be reduced by 40% by applying ultrasound. Since then, numerous experimental studies have been devoted to explaining the mechanisms behind the phenomenon. However, the exact mechanisms are still unclear, due in part to the lack of agreement between those supporting the acoustic softening theory and the superposition effect theory. The acoustic softening theory is based on that ultrasonic vibrations reduce the yield strength of metals, in a similar fashion to heat weakening of metals. However, the difference is that the ultrasonic energy is used in localized regions along the metal piece, while heat energy is distributed evenly over the piece [70]. Severdenko et al. [4] tested material strength with ultrasonic vibrations between 15 kHz to 1.5 MHz. It was shown that the effect depends on the intensity of vibrations rather than their frequency, and that plasticity can be realized by a high intensity input of ultrasonic vibrations at room temperature. Acoustic softening can be explained using dislocation theory. Energy is needed to overcome the hindrance of dislocations. Ultrasound helps to activate retarded dislocations. In some cases, the introduction of ultrasound can also result in temperature rise, which may also help reduce the stress. In the superposition effect theory, the force reduction is due to the superposition of steady and alternating stresses [71].

Swaging effect

In drawing processes, deformation is achieved by the axial tensile stress working together with the two lateral compressive stresses. The majority of industrial processes for working metals by pressure occur in the presence of contact friction between the surfaces of the metals. The contact friction forces cause a tri-axial stress state, an increase in the mechanical work done in deformation, an increase in the total force for deformation, and increased wear of the working tool.

Change of friction coefficient

The change in the friction coefficient when ultrasound is applied can be due to (a) pumping of the lubricant, (b) chemical activation of the lubricant, (c) separation of the surfaces, and (d) softening or melting of the asperities. From previous results, (a) and (d) are the greatest contributors to friction reduction (without lubricant, (d) is the major reason). Bunget and Ngaile [65] reported a better surface finish was achieved by applying ultrasonic vibration on dies for micro-extrusion processes. They proposed that higher instantaneous sliding velocities help shifting a boundary lubrication regime to a mixed-film regime, which gave better lubrication at the contact.

Reverting friction vector

For this effect, the coefficient of friction between two surfaces is not changed. The friction vector is varied by changing the relative motion between surfaces. Thus, the overall magnitude of friction force is reduced. This has been summarized in literature review in Chapter 1.

Surface metallurgical properties

Metallurgical changes occur either locally or globally when ultrasonics is applied, as a result of a local or global rise in temperature. The rise in temperature is a consequence of the degeneration of vibrational energy to heat. Hung et al. [66] conducted compression tests on aluminum rings and claimed that the friction force at the interface between the die and the sample piece plays an important role in the deformation and final shape of the sample. They monitored the temperature at the interface and observed a significant temperature rise when ultrasonic vibrations were applied.

Modeling of ultrasonic metal forming

There have also been many studies dedicated to the modeling of the mechanisms in ultrasonic metal forming from different angles, as shown in Fig. 2.29.

Hayashi et al [67] used finite element analysis (FEA) to simulate the ultrasonically-assisted wire drawing process. They calculated the drawing forces of several cases, including conventional drawing, axial ultrasonic vibration drawing, and radial ultrasonic vibration drawing. This model helped to explain tri-axial stress state at the

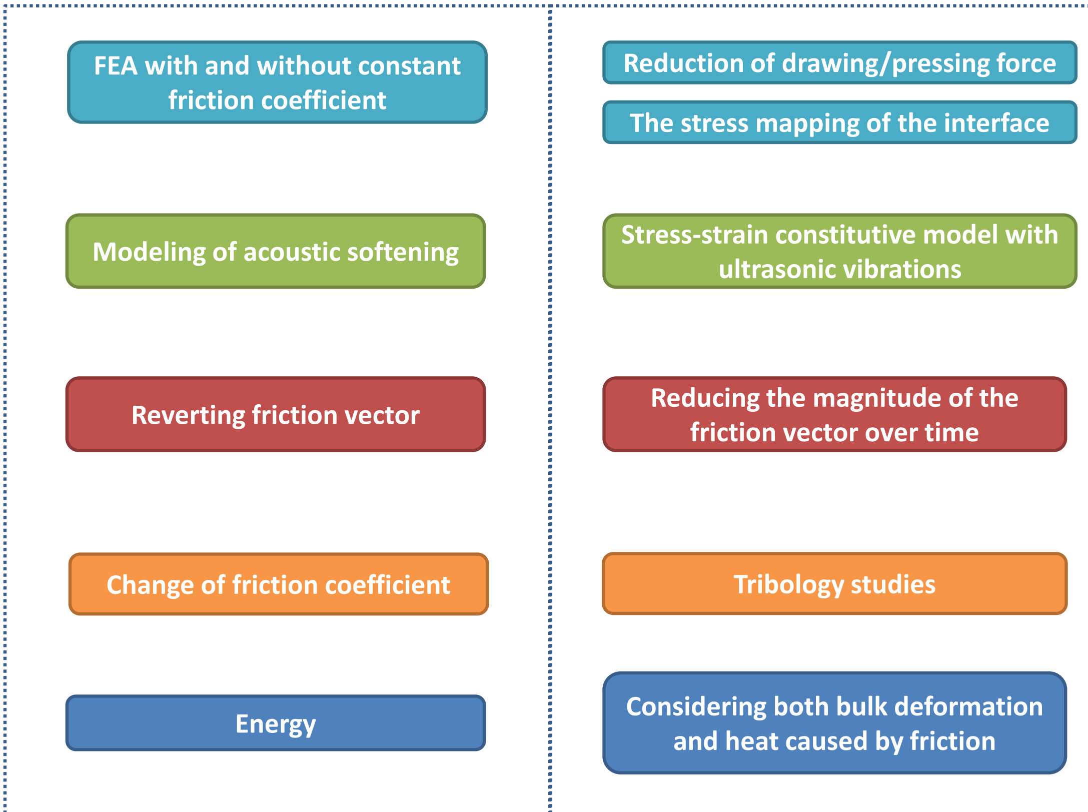

Figure 2.29: Modeling of ultrasonics in metal forming.

neck of the die. However, they only used a constant coefficient of friction throughout the simulation without considering the change of boundary and friction due to ultrasonic vibrations. Also, the acoustic softening phenomenon was not addressed in this modeling. Hung et al. [66] conducted upsetting tests on aluminum samples and used a constant shear friction model in FEA simulations. Lucas and Daud [72, 73, 74] simulated ultrasonic extrusion of aluminum using a conventional material model with varying coefficients of friction to explain the application of ultrasonic energy. They started at using μ=0.1 for the static deformation and then changed to μ=0.06 and 0 with the application of ultrasonic vibrations.

Siddiq and Sayed [76] proposed a constitutive model based on energy to simulate the stress and strain relationship with and without ultrasonic vibrations. They simulated in a ABAQUS/Explicit and compared the computational results with the experimental data from Duad et al. [74].

Dinelli et al. [75] observed friction reduction using ultrasonic vibration at low amplitude. They proposed a model that considers the interface as a solid-like thin film that consists of water and other contaminants. As the ultrasonic vibrations are applied, the fast motion between the two surfaces eliminates the solid-like film and results in a change in the coefficient of friction, hence, the friction force.

Siddiq and Ghassemieh [76] analyzed thermal and acoustic softening of metals within a conventional plasticity framework. They pointed out that in order to simulate the ultrasonic forming process, both volume (acoustic softening) and surface (heating due to friction) effects should be considered.

2.4.2 Experimental Set-up

Experimental set-up is shown in Fig. 2.30, which adopted a similar pin-on-disc concept as the modified tribometer in previous section. Similar to the tribometer, the disc was held by a chuck driven by a DC motor, but the motor can provide higher rotational speeds. The chuck rested on a support frame through a turntable thrust bearing. Unlike the gymbal assembly with the piezo-actuator, in this set-up, ultrasonic vibrations were generated by a commercial plastic welder (Dukane 220). The welder, which offers high power ultrasonic vibrations up to 2.2 kW, was previously utilized in section 2.1 for the study of friction reduction via Poisson effect. An acorn nut was connected to the bottom of the waveguide and placed in contact with the

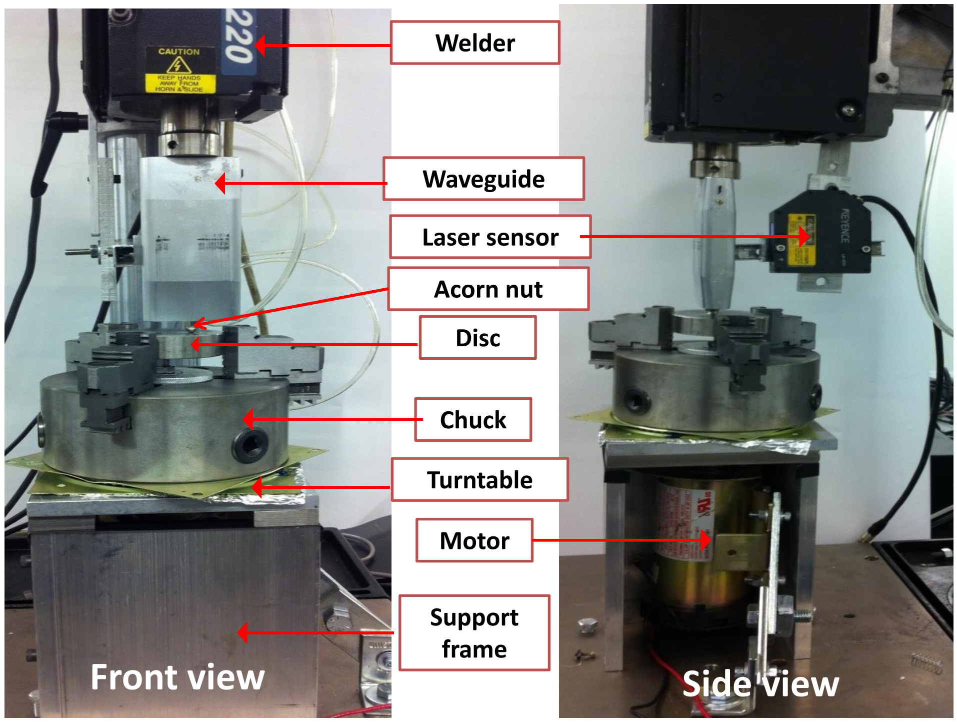

Figure 2.30: Experimental set-up for ultrasonic lubrication study with high stress and high velocity.

disc. The pneumatic system of the welder can provide normal force up to 600 N at the interface. By keeping the contact area relative small, the stress at the interface can reach a level of 100 MPa, which is sufficient for the simulation of processes such as metal forming. Instead of a direct measurement of friction by a load cell, a laser displacement sensor was employed to measure the deflection of the waveguide. The correlation between the horn deflection and friction force was calibrated before measurements.

There are two types of acorn nuts used in this study: flat tip and round tip. They corresponded to two groups of tests, respectively. Although the normal load adopted in both tests is the same, 70 N, the normal stress ranges were different due to different

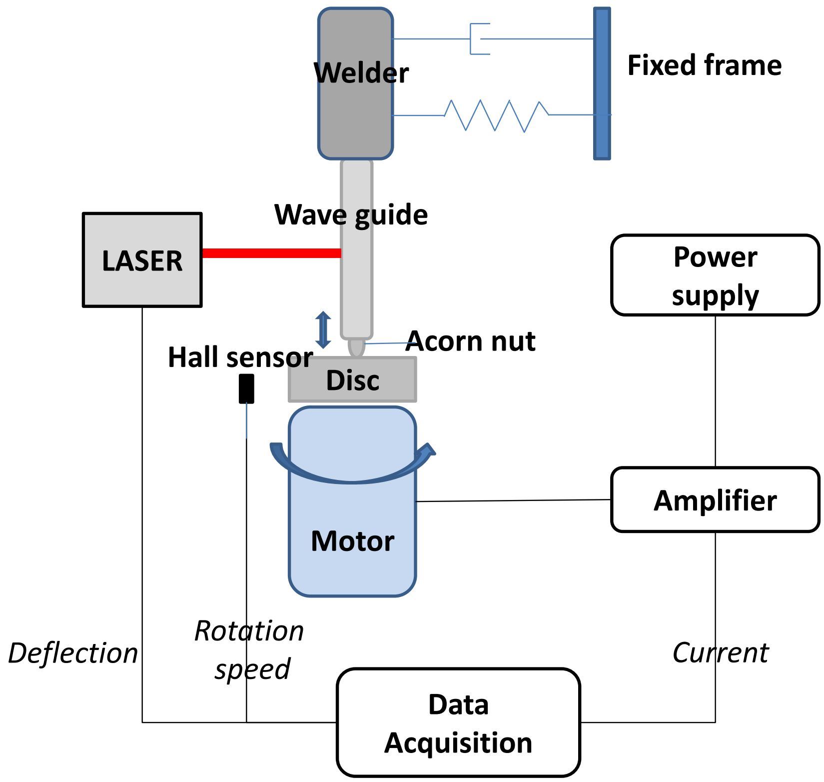

Figure 2.31: Experimental schematic for ultrasonic lubrication under high stress and high velocity.

nominal areas of contact. The acorn nut with the flat tip had a contact area of 2 mm^2 before the test and 2.25 mm^2 after due to wear. Correspondingly, the normal stress was 31 MPa at the beginning of the test and 35 MPa after. The stress was distributed evenly over the contact area.

For the acorn nut with a round tip, the contact area was much smaller, in the range of 1-1.27 mm^2. The nominal stress was between 55 MPa to 70 MPa before and after the test. Due to the shape of the tip, the actual stress was even higher at the center of the tip (2 times the nominal stress according to FEA simulations). Other parameters of the tests are listed in Table 2.8.

Table 2.8: Experimental parameters.

Parameter	Value	
	Test 1: round tip nut	Test 2: flat tip nut
Normal load	70 N	
Nominal area of contact	1-1.27 mm^2	2-2.25mm^2
Nominal normal stress	55-70 MPa	31-35 MPa
Rotation speed	54.9-76.7 rpm	51.2-76.9 rpm
Groove diameter	60 mm	66.04 mm
Rounds pin travels	11	11
Distance pin travels	2.0734 m	2.2814 m
Linear speed	172.5 mm/s, 240.9 mm/s	177 mm/s, 265.9 mm/s
Materials	Stainless steel vs. stainless steel	
US amplitude	11.46 μm	
US frequency	20 kHz	
Driving voltage	8 V	
Disc run-out	0.0286 mm	

A hall sensor chip was employed to measure the rotational speed of the disc by recording the change of magneto fields. A magnet was placed at the rim of the disc and generated different readings by the hall sensor depending on the distance between it and the sensor. The motor was powered by an electrical amplifier. The angular speed of the motor was set at a fixed value by keeping the driving voltage of the motor constant (8 V in this study). The current was adjusted automatically by the amplifier according to the torque of the motor. The rotational speed was set to be approximately 50 rpm for both tests. When ultrasonic vibrations were turned on during the tests, the sudden decrease of torque, due to the reduction in friction, caused the rotational speed jump to 77 rpm.

2.4.3 Calibration

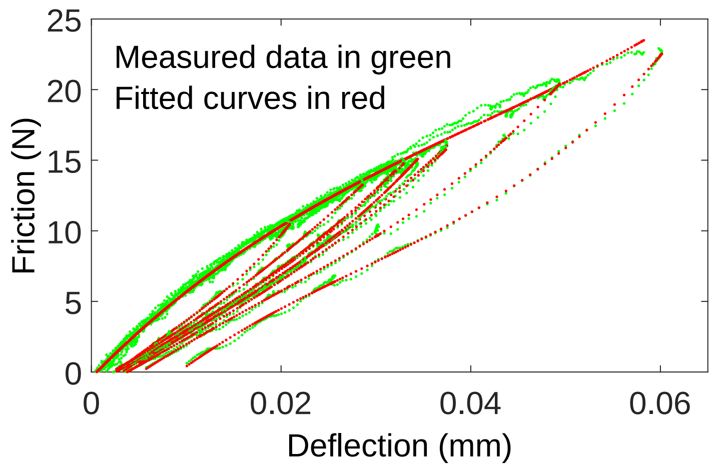

Figure 2.32: Calibration of friction force and waveguide deformation.

Prior to the tests, a calibration was made to determine the relationship between friction and waveguide deflection. A load cell was connected to the acorn nut by a fishing line and the laser displacement sensor was engaged to measure the deflection of the waveguide. By manually pulling and releasing the load cell horizontally, the pulling force and the deflection of the horn were measured concurrently by the load cell and laser sensor, respectively.

It was found that the relationship is not linear, but with hysteresis loops, as shown in Fig. 2.32. Depending on the position where the unloading begins, the curve follows different routes back to the point of origin. Therefore, multiple measurements were conducted to map the hysteresis loops so that the correlation between friction and deflection can be more precise.

Tests were conducted after the calibration. Each test followed the procedures as shown below:

- Install the waveguide and check the working condition of the welder (Look for any overloading that may occur if installed incorrectly).
- Turn on the signal generator, the amplifier, and the welder.
- Start the data acquisition. Set the voltage output at 8 V.
- Turn on ultrasonic welder, hold it for a few seconds, and then turn it off. After a few seconds, turn off the motor.
- End data acquisition.
- Scan the groove using an optical profilometer and analyze data.

2.4.4 Friction Reduction

Measurements of waveguide deflection and calculated friction force with flat tip and round tip acorn nuts are shown in Fig. 2.33. Steady-state intrinsic friction between the flat tip and the disc was approximately 18 N. It was greater than that between round tip and the disc, which was 12 N. Evident friction reduction can be observed in both cases when ultrasonic vibrations are applied. Data of friction and friction reduction for both cases can be found in Table 2.9. Despite the different levels and distribution of normal stresses on the tips, friction reduction was at the same level for both cases.

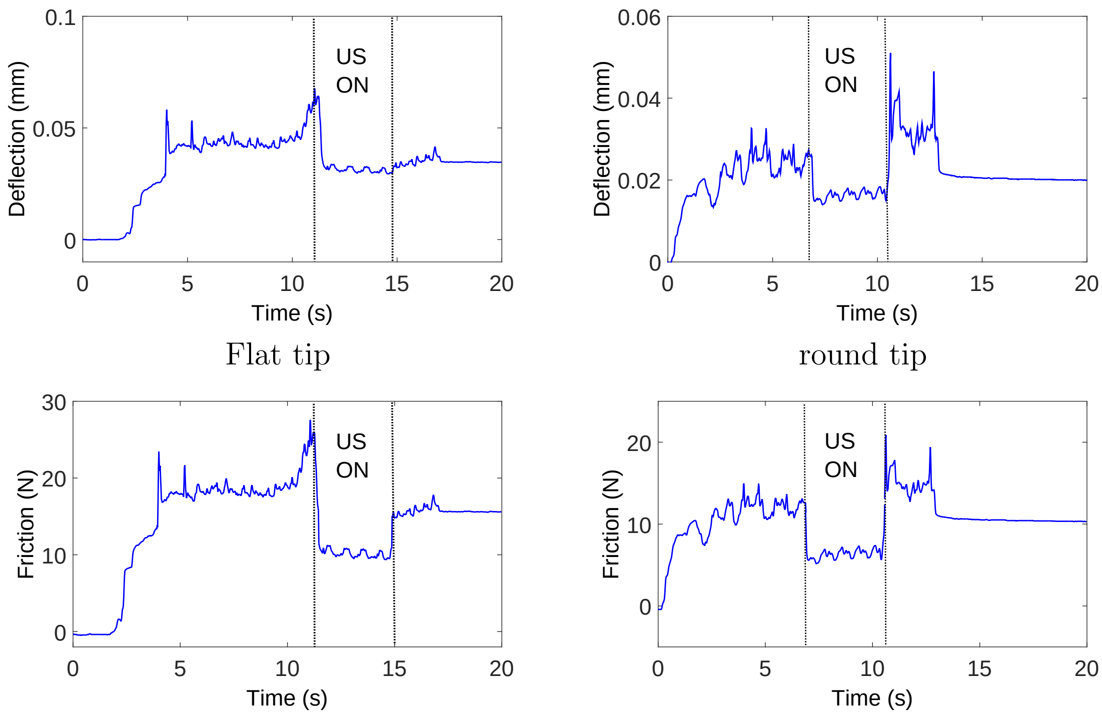

Figure 2.33: Friction reduction: first row shows the deflection measurements, second row shows the converted friction, left column is the flat tip, and right column is the round tip.

When ultrasonic vibrations are applied, the driving current for the motor dropped by approximately 0.4 A in both tests. This was due to the reduction of torque of the motor when the friction was reduced. A similar decrease in current also indicated the reduction of friction for two cases were close. The sudden drop in current resulted in an increase in linear velocity, which may be the reason for the sharp increase of friction in the flat tip case.

2.4.5 Wear Reduction

Optical profilometry was employed to characterize wear created on the discs. The scan area was 1.8 mm by 2.4 mm. Two- and three-dimensional profiles were generated

Table 2.9: Friction reduction data with and without ultrasonic vibrations.

Parameter	Value	
	Round tip	Flat tip
Linear velocity	172.5 -240.9 mm/s	177- 265.9 mm/s
Friction without US	10.73-13.02 N	16.88-19.52 N
Friction with US	5.323-6.845 N	9.93-10.71 N
Friction reduction	47.4-50.4%	46.8-51.1%
Current without US	1.427 A	1.208 A
Current with US	1 A	0.801 A

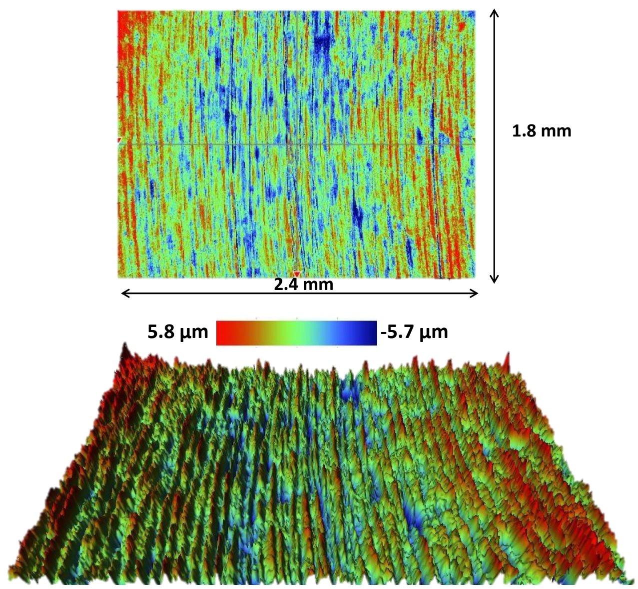

Figure 2.34: 2D and 3D profiles of the original surface without wear.

for both the tip of the acorn nuts and the disc. Figure 2.34 shows the profiles of the unworn surfaces, and Fig. 2.35 and 2.36 show the profiles from the round and flat tip tests, respectively.

All the images use the same color code. However, values in legend indicate that the wear groove created by round tip is wider and deeper, while the one created by

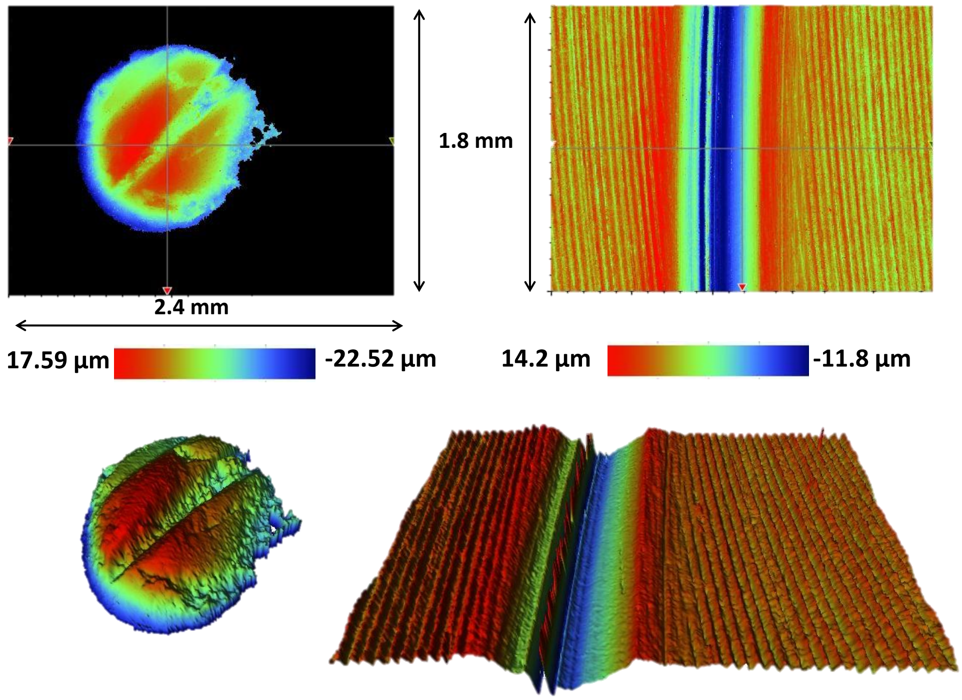

Figure 2.35: 2D and 3D profiles of the round tip acorn nut and the corresponding wear groove.

Table 2.10: Wear reduction data with and without ultrasonic vibrations.

	No wear	Round tip	Flat tip
Ra (Arithmetic average)	0.671	1.786	0.677
Rq (root mean square)	0.857	2.54	0.87
Total volume loss of the groove	/	0.335 mm^3	0.013 mm^3
Volume loss per turn	/	0.03 mm^3	0.0012 mm^3
Total distance pin travels		2.0734 m	2.2814 m
Volume loss per meter		0.162 mm^3/m	0.005 mm^3/m

flat tip is much narrower – despite the fact that the contact area is much bigger for the flat tip.

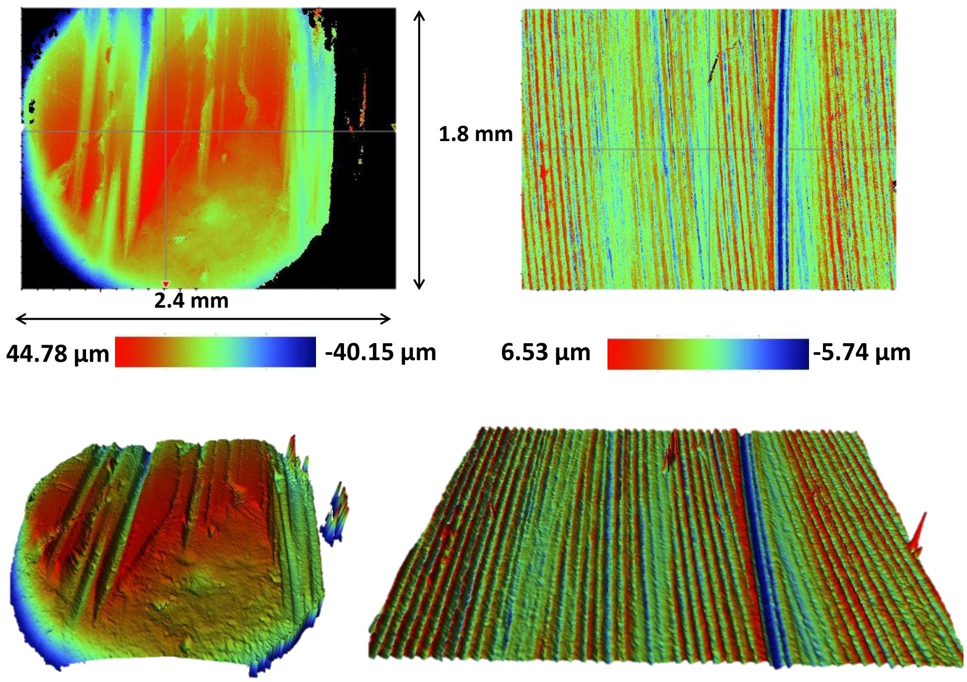

Figure 2.36: 2D and 3D profiles of the flat tip acorn nut and the corresponding wear groove.

Wear rates of flat and round tips were calculated based on the volume loss of the discs and the distances that the pins traveled, listed in Table 2.10. It should be noted that the wear rate of the flat tip is only 3% of the rate of the round tip. Although both cases share the same normal force, the difference in normal stress made a huge impact in wear generation.

To study wear reduction under high stress and high velocity conditions, an additional group of tests was conducted. The tests followed the same procedures previously described. There was no ultrasonic vibrations applied during the first test, while ultrasonic vibrations were applied all the time during the second test. Round tip was chosen since it can create more wear.

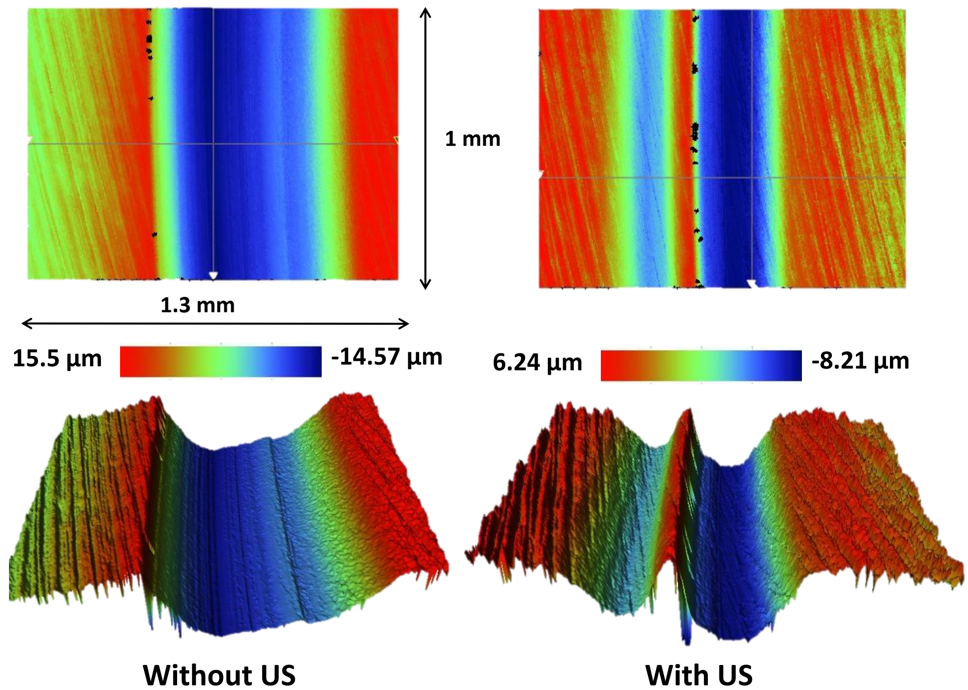

Figure 2.37: 2D and 3D profiles of the wear groove created by the round tip, with and without ultrasonic vibrations.

A comparison of profiles of the wear grooves was conducted with images shown in Fig. 2.37. This time, the profilometry scans are conducted in a 1 mm by 1.3 mm area. Likewise, by comparing the numbers in the legends, it is evident that wear was greatly reduced with the application of ultrasonic lubrication. In fact, by calculating the wear rates, wear reduction reached 72.6%.

2.4.6 Summary

This section presents a literature review on the role of ultrasonics in metal forming, as well as an experimental study on ultrasonic friction and wear reduction with normal stress up to 70 MPa and linear velocity up to 250 mm/s. Tests were conducted with flat tip acorn nuts and round tip acorn nuts to simulate contacts with evenly distributed stress and concentrated stress. It was found that stress plays little role in friction reduction but makes a large difference in wear generation. By applying ultrasonic vibrations, friction was reduced up to 51% for both tips, and wear was reduced by 72.6% on round tip.

2.5 Wear Reduction between Various Materials

2.5.1 Introduction

Aluminum and stainless steel were the adopted pin and disc materials in the previous experiments. This section presents experimental data of ultrasonic wear reduction for other material combinations. Materials include metals such as titanium, M50 tool steel, and stainless steel, as well as non-metals like ceramic.

Titanium alloys have very high tensile strength and toughness (even at extreme temperatures) [77]. They are light in weight, have extraordinary resistance to corrosion and can withstand extreme temperatures. The two most useful properties of the metal are its corrosion resistance and the highest strength-to-density ratio of any metal. In its unalloyed condition, titanium is as strong as some steels, but less dense. In this study, the titanium tested is grade 5 (Ti6Al4V), which is the most commonly used titanium alloy.

Tool steel [78] refers to a variety of carbon and alloy steels that are particularly well-suited to be made into tools due to their distinctive hardness, resistance to abrasion and deformation, and their ability to hold a sharp edge even at elevated temperatures. M-type tool steels are used for cutting tools, where strength and hardness must be retained at temperatures up to, or exceeding, 760 °C (1,400 °F) [79]. The type of tool steel used in this study is M50.

The ceramic type for this study is aluminum oxide. Aluminium oxide is a chemical compound of aluminium and oxygen represented by the chemical formula Al_2O_3. It is the most commonly occurring of several aluminium oxides, and specifically identified as aluminium(III) oxide. Aluminium oxide is favored for its hardness and strength. It is widely used as an abrasive, including as a much less expensive substitute for industrial diamond. Many types of sandpaper use aluminium oxide crystals. In addition, its low heat retention and low specific heat make it widely used in grinding operations, particularly cutoff tools. [80]

2.5.2 Stainless Steel Pin on Titanium Disc

Table 2.11: Parameters for ultrasonic wear tests between stainless steel pin on titanium disc.

Parameter	Value
Normal force (N)	3
US frequency (kHz)	22
US amplitude (μm)	2.5
Nominal groove diameter (mm)	25.4
Linear speed (mm/s)	16.9
Running time (h)	3
Distance (m)	182.5
Revolutions	2298

Four wear tests were conducted utilizing stainless steel pins and titanium discs. Tests 1 and 2 were conducted without ultrasonic vibrations. Tests 3 and 4 were conducted with ultrasonic vibrations present. Other parameters remained unchanged for all four tests, as listed in Table 2.11. The testing procedures followed the testing procedures of the modified tribometer.

Photos of the tip of the acorn nuts and disc surfaces are shown in Fig. 2.38 and Fig. 2.39. Contrary to expectations, more wear occurred to the disc and the acorn nuts. The wear surfaces of the acorn nuts without ultrasonic vibration have diameters averaging 2.1 mm, while the ones with ultrasonic vibrations averages 3.4 mm. Correspondingly, the widths of the wear grooves on the discs with ultrasonic vibrations are wider than those on the discs without ultrasonic vibrations.

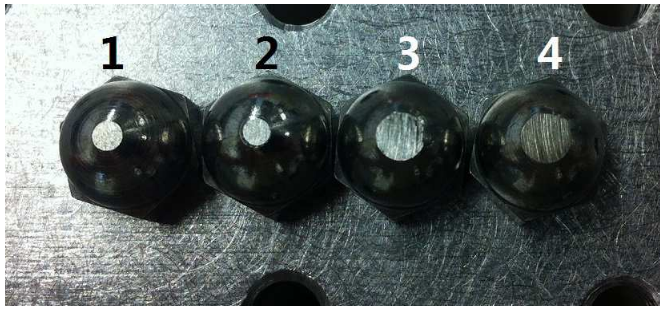

Figure 2.38: Stainless steel acorn nuts after the tests: 1 and 2 without US; 3 and 4 with US.

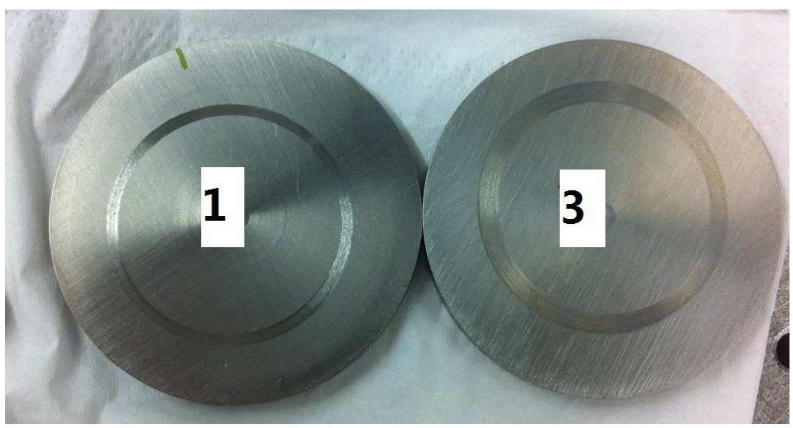

Figure 2.39: Titanium discs after the tests: 1 is without US; 3 is with US.

To quantify the difference in surface wear, the optical profilometer was again employed to scan the wear grooves. 2D and 3D profiles are shown in Fig. 2.40. The wear groove with ultrasonic vibrations is not only wider but also deeper than the one without ultrasonic vibrations. Surface roughness changes from 0.45 μm (unworn)

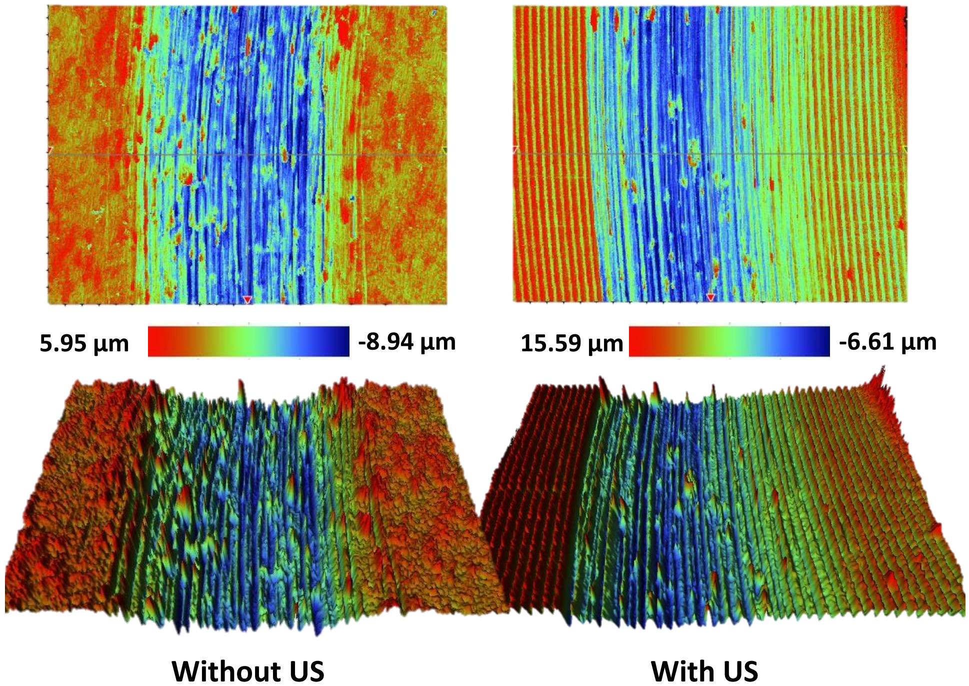

Figure 2.40: Profilometry of wear grooves on titanium discs (tested with stainless steel pins).

to 1.5 μm (worn) without ultrasonic vibrations. With vibrations, the roughness is 1.8 μm, which is another indicator of ultrasonics creating more wear in this case.

Moreover, it is evident that there are projections on the surface of both grooves. Their presence is due to the material exchange between the pin and disc, indicating that adhesive wear between the two surfaces exists.

In terms of friction, friction force without ultrasonic vibrations is 1.33±0.1 N, while, friction with ultrasonic vibrations is 0.61±0.03 N. The average friction reduction is 53%. Therefore, although ultrasonic vibrations are not effective in reducing wear between stainless steel pins and titanium discs, they are still effective in reducing friction.

2.5.3 Titanium Pin on Titanium Disc

An additional group of tests was conducted between titanium pins on titanium discs. Three different distances were achieved by running tests for varying durations at a constant linear velocity. Two vibrational amplitudes were selected. Likewise, time-dependent friction forces were measured and recorded. The profilometer was used to scan the surface of the wear grooves.

Table 2.12: Parameters for ultrasonic wear tests between titanium pin on titanium disc.

Parameter	Value
Normal force (N)	3
US frequency (kHz)	21
US amplitude (μm)	2.5, 1
Nominal groove diameter (mm)	25.4
Linear speed (mm/s)	16.9
Running time (h)	2, 4, 6
Distance (m)	122, 244, 366
Revolutions	1532, 3064, 4596

Experimental data show the following findings:

- Ultrasonic vibrations reduced friction between titanium pin and titanium disc by up to 60%.
- Friction reduction dropped from 60% to 40% when vibrational amplitude decreases from 2.5 μm to 1 μm.
- Ultrasonic vibrations were not effective in reducing adhesive wear. There was more wear observed when ultrasonic vibrations were applied.

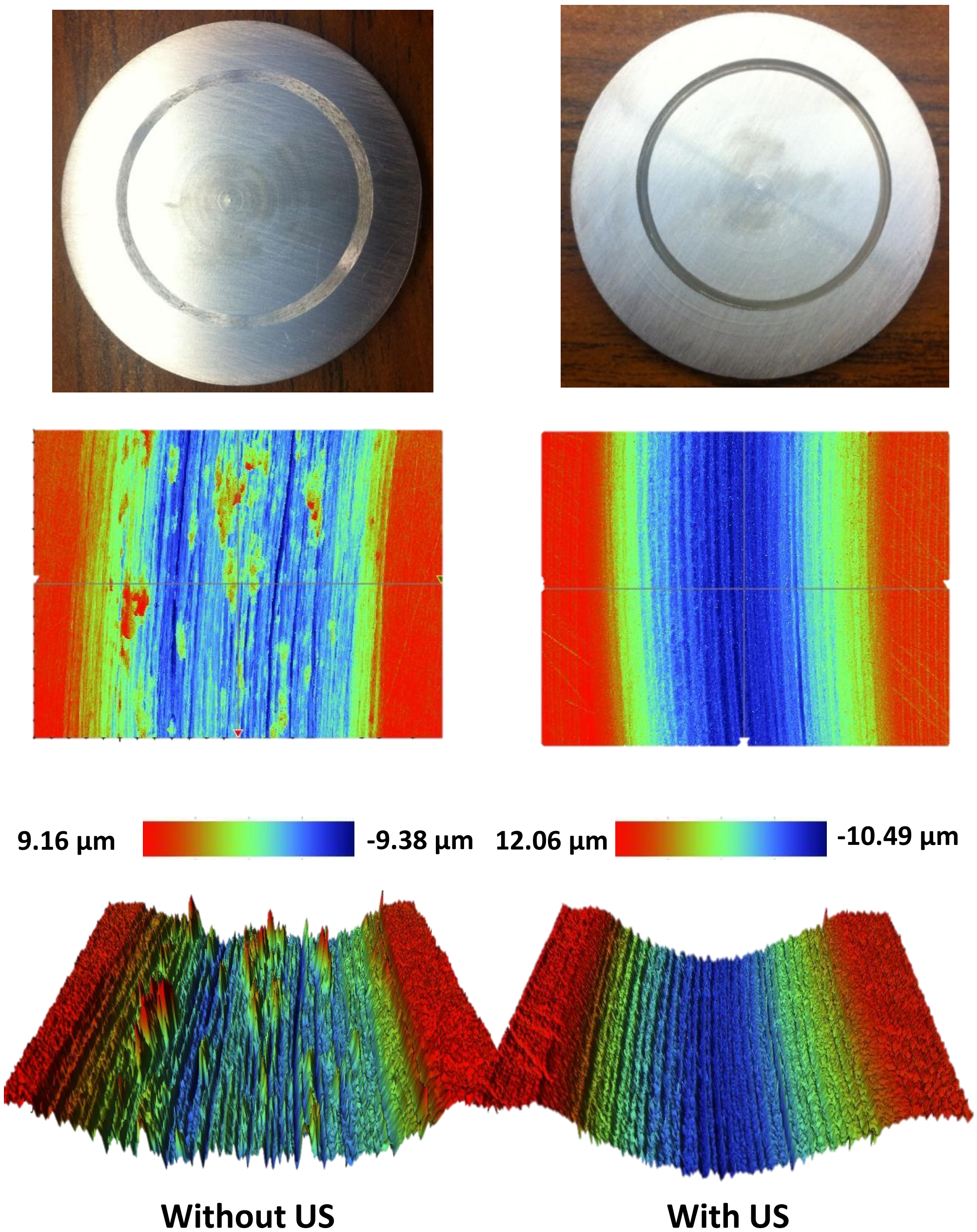

Figure 2.41: Profilometry of wear grooves on titanium discs (tested with titanium pins).

- Higher vibrational amplitude resulted in more adhesive wear.

- Ultrasonic vibrations helped to create smoother wear grooves.
- The wear grooves only became wider, but not deeper, when the sliding distance increased, which is different from the result between the stainless steel pin and aluminum disc (section 2.3).

Figure 2.41 shows photos of the grooves left on the titanium discs and their profilometry scans. Dissimilar to the stainless steel pin and titanium disc test, the widths of the grooves are not evidently larger when ultrasonic vibrations are applied. However, the legends indicate that the grooves with ultrasonics are slightly deeper. The wear groove without ultrasonic vibrations has significant projections on the surface, which was also observed in the case of stainless steel pin and titanium disc. However, when ultrasonic vibrations are applied, there are no projections on the surface of the groove, leaving a smooth profile. This is different from the stainless pin and titanium disc with ultrasonic vibrations results(Fig. 2.40). Possible reasons for this phenomenon will be discussed later.

2.5.4 Ceramic Pin on M50 Tool Steel Disc

Two more materials, which are much harder than the previous ones, were tested: ceramic and M50 tool steel. The procedures for each test were identical as in previous tests and the testing parameters are listed in Table 2.13.

The disc is made of M50 tool steel with a mirror-like surface finish. Pin materials are ceramic (Al_2O_3) and M50 tool steel in two groups of tests, respectively. The photos of the wear grooves, microscopy, and profilometry for the ceramic pin and M50 disc are shown in Fig. 2.42 and 2.43. Photos show obvious wear grooves on both discs with and without ultrasonic vibrations. Microscope scans clearly show

Table 2.13: Parameters for ultrasonic wear tests between ceramic pin and M50 tool steel disc.

Parameter	Value
Pin material	M50 tool steel, ceramic(Al_2O_3)
Disc material	M50
Nominal normal force (N)	3
Nominal pressure (MPa)	300*
US frequency (kHz)	22
US amplitude (μm)	2.5
Nominal groove diameter (mm)	34.3
Linear speed (mm/s)	13.5
Running time (h)	3
Distance (m)	145.8
Revolutions	1350

* Pressure is estimated by the initial contact area. The pressure decreases as the contact area enlarges during the test.

that the wear groove with ultrasonic vibrations is significantly narrower than the one without ultrasonic vibrations. Furthermore, profiles indicate no volume loss of the disc surface, but rather more material attached to the surfaces.

Microscope images of the tip of the pins are also shown in Fig. 2.42. Without ultrasonic vibrations, the wear at the pin tip is in a round shape, while, with ultrasonic vibrations, the wear is apparently in smaller area. There exists a white ring around the worn area which could be in contact intermittently during the test. The mechanism is that, as the pin vibrates vertically, the contact area is constantly changing between big and small. The center dark area has always been in contact, therefore it has same level of wear as the round area in the case without ultrasonic vibrations. Big contact area includes the white ring, which is not always in contact and did not undergo the same level of wear as in the center.

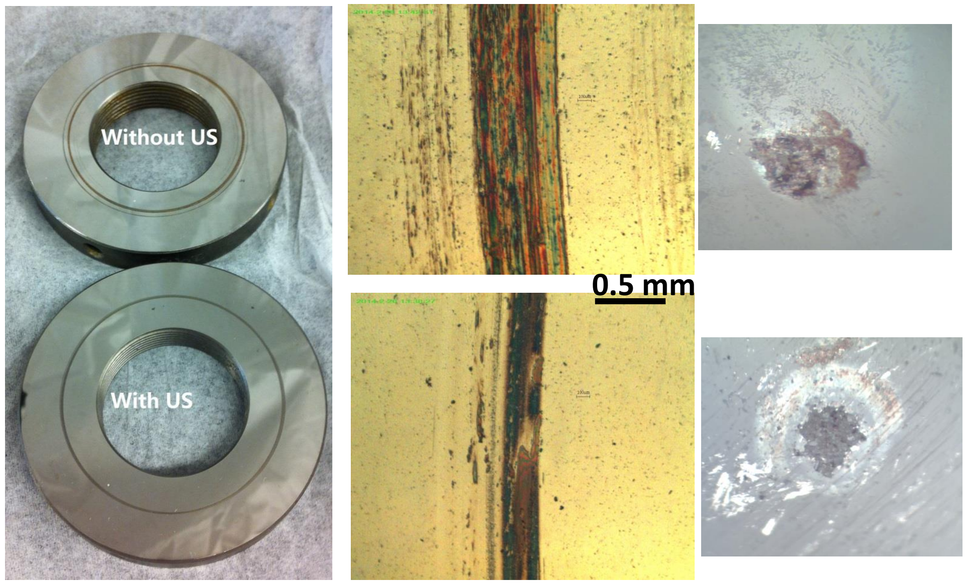

Figure 2.42: Photos and microscopy images of M50 discs and ceramic pins.

In terms of friction reduction, friction force drops from 0.665±0.1 N to 0.224±0.02 N by 66.3% when ultrasonic vibrations are applied.

2.5.5 M50 Tool Steel Pin on M50 Tool Steel Disc

An additional group of tests were conducted between an M50 tool steel pin and M50 tool steel disc using the same testing parameters listed in Fig. 2.13. Again, photos, microscopy scans, and profilometry scans were taken to characterize the wear reduction. Unlike the case of ceramic pin and M50 steel, the photos of wear grooves shown in Fig. 2.44 indicate that wear was almost eliminated when ultrasonic vibrations were applied. In fact, the wear groove is barely visible. The microscopy and profilometry images (Fig. 2.45) also prove that not only the width of groove is smaller, but the severity of the wear is greatly reduced as well.

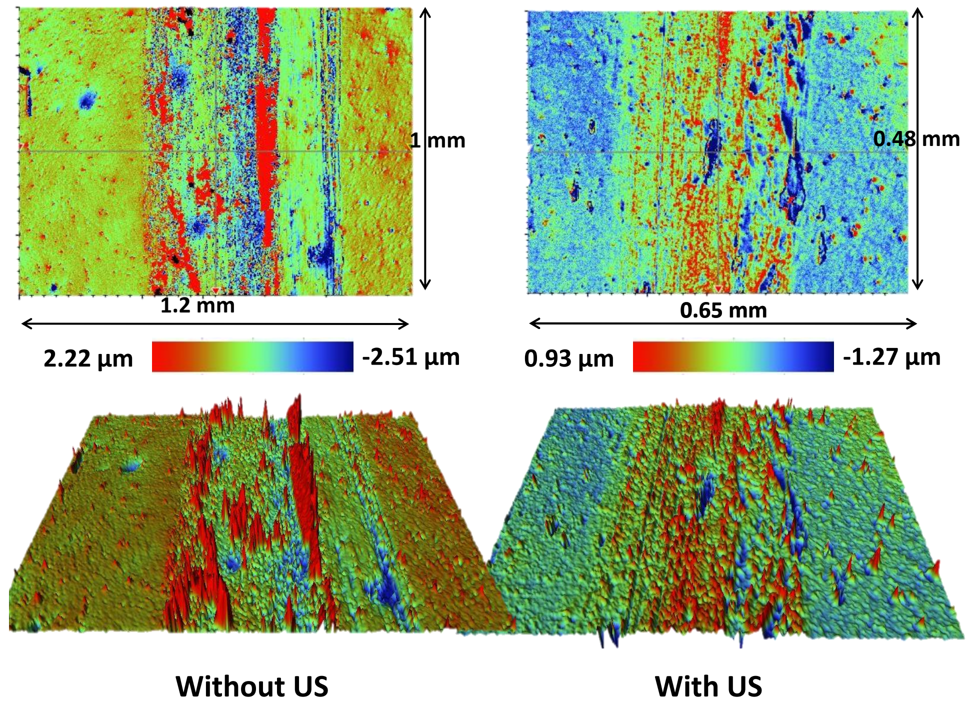

Figure 2.43: Profilometry images of M50 discs (tested with ceramic pins).

Similar to the previous cases with Titanium, evident projections on the grooves exist, due to material exchanges. This indicates that the type of wear between the M50 materials is adhesive. Ultrasonic vibrations are not able to prevent the material adhesion. In terms of friction reduction, friction force drops from 0.769±0.05 N to 0.769±0.02 N by 80.1% when ultrasonic vibrations are applied.

2.5.6 Discussion

A summary of wear reduction tests conducted between all the different material combinations is listed in Table 2.14. Among all the combinations, only the wear between stainless steel and aluminum can be categorized as mainly abrasive due to the difference in hardness. Hardness of all the materials are listed in Table 2.15. Although a hardness difference exists in some of the other combinations, their wear

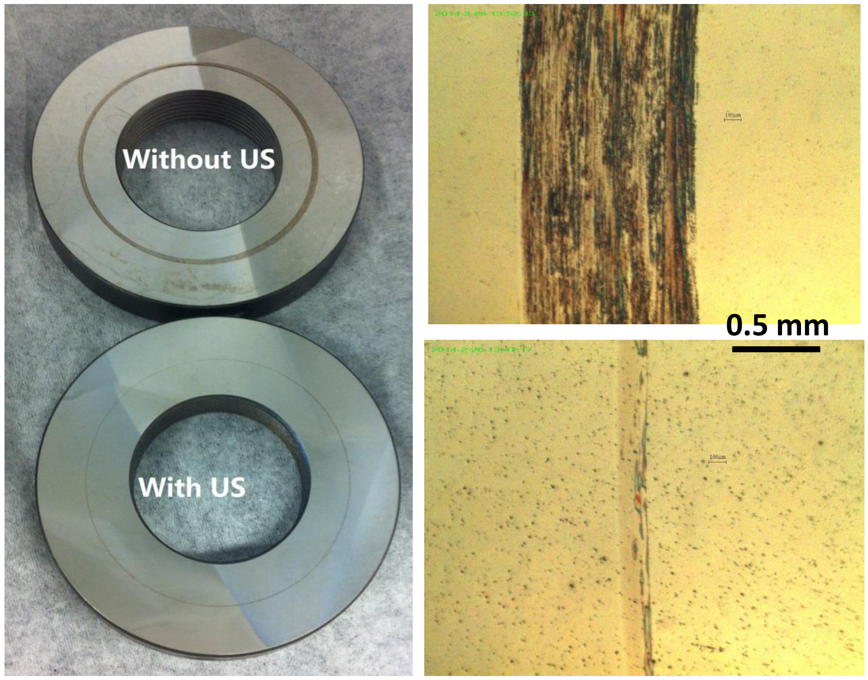

Figure 2.44: Photos and microscopy images of M50 discs.

types are identified as mainly adhesive, due to the evident material exchanges and adhesion. Note that abrasive and adhesive wear take place concurrently between two surfaces. The identification of one type does not deny the existence of the other.

Table 2.14: Summary on ultrasonic wear reduction between various materials.

Pin	Disc	Wear type	Wear reduction	Friction reduction
Stainless steel	Aluminum	Abrasive	49%	62%
Stainless steel	Stainless steel	Adhesive	72%	51%
Stainless steel	Titanium	Adhesive	No reduction	53%
Titanium	Titanium	Adhesive	No reduction	60%
Ceramic	M50	Adhesive	53%	66%
M50	M50	Adhesive	73%	80%

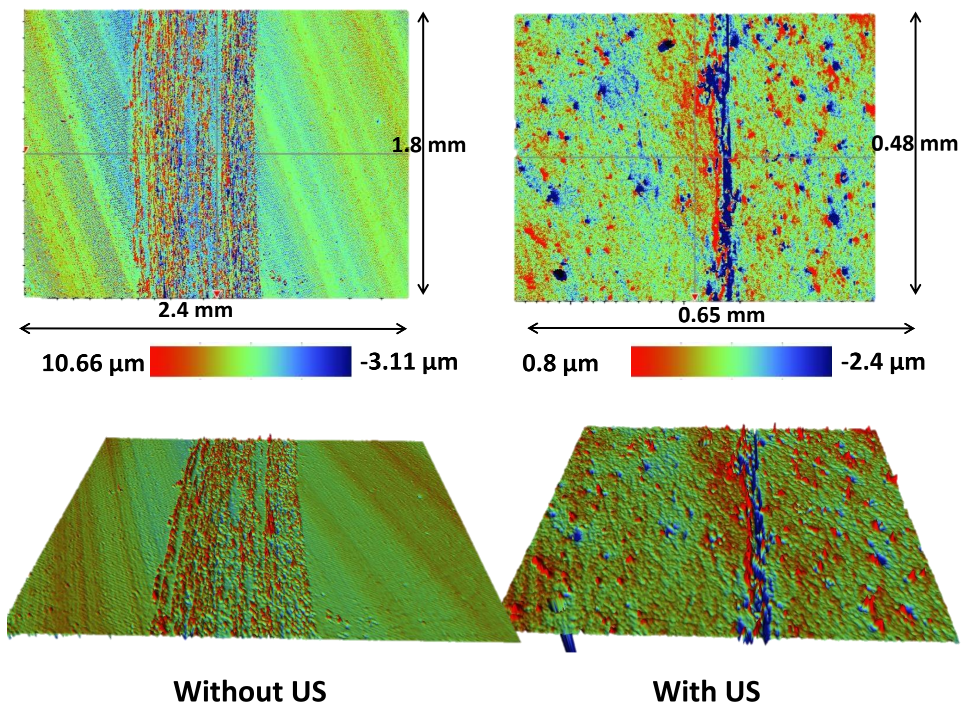

Figure 2.45: Profilometry images of M50 discs (tested with M50 pins).

In the case of stainless steel and titanium pins sliding against titanium discs, ultrasonic vibrations were not able to reduce wear. Instead, ultrasonic vibrations introduced more wear on both the discs and the pins. The cause for titanium behaving differently may have to do with its physical or metallurgical properties. Titanium is a highly ductile metal, compared to the other materials used in this study. Among the metals studied here, only the crystal structure of titanium is hexagonal close packed (hcp). Others are either face centered cubic or body centered cubic. The hcp structure provides a great ability for the atoms to roll over each other into new positions without breaking the metallic bond. Atoms are packed closer in titanium than in other materials, which makes it more capable to extend without fracture. It is more likely to react this way when the temperature at the interface increases, due to the heat generated either from friction or ultrasonic vibrations. Properties such as solubility and others may also have influence on the behavior of titanium alloys with the present of ultrasonic vibrations.

Aluminum is another very ductile material in the group. At the same time, aluminum is very soft, making it easy to be removed from bulky material when in contact with a harder material. Titanium, on the other hand, is both hard and ductile. Therefore, ultrasonic vibrations could not separate the contacting surfaces and reduce the interaction like in other cases.

Table 2.15: Hardnesses and crystal structures of different materials used in the experiments.

Material	Vicker hardness	crystalline structure
Aluminum 2024	137	face-centered cubic
Stainless steel 316	217	face-centered cubic
Stainless steel 303	262	face-centered cubic
Titanium 5	349	hexagonal close packed
M50 tool steel	960	body-centered cubic
Ceramic	1601	non-metal

Another interesting observation in the tests with titanium was how the wear groove on titanium disc had projections with ultrasonic vibrations when the pin was stainless steel. However, there were no projections at all on the groove surface when the pin material was changed to titanium. The reason could be due to the adhesion between Titanium and Titanium is not as strong as that between stainless and Titanium. Therefore, ultrasonic vibrations are more likely to shake off any Titanium than stainless steel particles that may have adhered to the disc.

2.5.7 Summary

This section presents experimental data from ultrasonic wear reduction tests using additional material combinations other than stainless steel pin on aluminum steel. These combinations include stainless steel on titanium, titanium on titanium, ceramic on M50 tool steel, and M50 on M50. Adhesive wear is the primary type at the interfaces of these material combinations. Abrasive wear only takes place between stainless steel pin and aluminum disc. Ultrasonic vibrations were effective in reducing friction for all cases and reduced wear between all material combinations except in cases where titanium was involved. Maximum friction reduction was 73% and wear reduction was 80%. Both results were achieved in the tests between M50 pin and M50 disc.

Chapter 3: Models

3.1 Elastic-plastic Cube Model for Ultrasonic Lubrication

Nominal flat surfaces have asperities [1], as shown in Fig. 3.11 (a). Real contacts between two surfaces take place on asperities so that the actual contact area is much smaller than the nominal contact area. This model utilizes the concept that a cube model is used to represent asperities in contact. As shown in Fig. 3.11 (b), the area of the top surface of the cube is equal to the real area of two surfaces in contact, which is denoted as A_{r0}. The height of the cube is equal to the distance between the two surfaces, which is denoted d_0.

The cube model consists of three parts: contact, friction and friction reduction. Contact model examines the contact of two surfaces from the level of asperities and calculates the contact parameters. Friction model examines the relationship between friction force and deformation of contacting asperities. Friction reduction model provides explanations about how ultrasonic vibrations change the contact parameters and microscopic deformations, and therefore, the friction force.

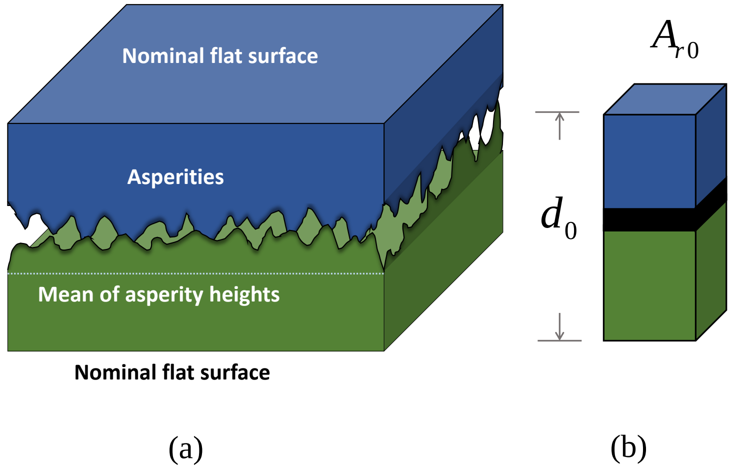

Figure 3.1: (a) Asperities between two nominally flat surfaces; (b) the cube.

3.1.1 Contact Model

This paper employs assumptions widely adopted in surface contact studies [14]. The contact between two rough surfaces can be replaced by one rough surface contacting a smooth surface. Surfaces in contact are assumed isotropic. No bulk deformation is taken into consideration, but bulk displacement is examined when ultrasonic vibrations are applied. Asperity peaks have a spherical shape with a uniform radius R_s.

First asperity contacts form when two surfaces contact each other with normal force applied. These contacts remain elastic only under very special conditions, such as very smooth surfaces with asperities having even heights or under very low normal loads [81]. In more common cases, where asperities are uneven and normal loads are high, the first asperity contacts have plastic deformations and new pairs of asperities come into contact until normal loads are balanced. By analyzing the contact of a single asperity pair, a critical interference ω_c is used to determine whether the asperity contact is elastic or plastic [82]

$$\omega_c = \left[\frac{C_\nu \pi (1-\nu^2) Y_0}{2E^*}\right]^2 R_s, \tag{3.1}$$

where C_v is a hardness coefficient related to Poisson's ratio of the softer material ($C_v = 1.234 + 1.256\nu$), ν is the Poisson's ratio, Y_0 is the failure strength of the softer material, R_s is the average radius of asperity summits, and E^* is the combined Young's modulus of two materials ($1/E^* = (1-\nu_1^2)/E_1 + (1-\nu_2^2)/E_2$). When the height of the asperity is smaller than ω_c, the contact is elastic, otherwise it is plastic.

The heights of the asperities follow a Gaussian distribution. An exponential probability distribution ϕ is used instead of a Gaussian distribution [82]

$$\phi(z) = ce^{-\lambda z}, \tag{3.2}$$

where z is the normalized distance between the asperity summit and the mean of asperity heights, and c and λ are constants. It was shown in [82] that when c and λ are equal to 17 and 3, respectively, the exponential distribution makes the best approximation to the Gaussian distribution, while being simpler to implement.

When two surfaces slide relative to each other through a tangential force, contacting asperity pairs deform longitudinally as a whole until the bonds are broken. Plastically deformed asperities may come off from the main body if weak bonds exist in the asperities rather than at the interfaces. This is one of the explanations for wear. New asperity contacts take place as old ones are separated during sliding. Overall, there are always sufficient asperities in contact to balance the normal force. Meanwhile, the tangential force that permits sliding to continue is balanced by the deformations of the asperity contacts. This tangential force is considered as the overall dynamic friction force.

Total normal force F_n is the summation of elastic and plastic contributions [105],

$$F_n = F_e + F_p. \tag{3.3}$$

Following the method in [82], the total normal force from the elastically deformed asperities is an integral of the normal force of asperity contact pairs over the range of asperity heights, from the lowest to the critical interference. The integral has a closed form solution as

$$\begin{aligned} F_e \quad &= \quad \frac{4c\beta(R_q/R_s)^{1/2}}{3\lambda^{5/2}} \Bigg[\frac{3\sqrt{\pi}}{4}\mathrm{erf}\Big(\sqrt{\lambda\omega_c/R_q}\Big) \\ &\quad - \frac{(\lambda\omega_c/R_q)^{3/2} + \frac{3}{2}\sqrt{\lambda\omega_c/R_q}}{e^{\lambda\omega_c/R_q}}\Bigg] e^{-\lambda d/R_q}\ , \end{aligned} \tag{3.4}$$

where β is the roughness parameter ($\beta = \eta R_q R_s$), η is the areal density of asperities, R_q is the standard deviation of surface roughness, and erf is the error function used to get the closed form solution ($\mathrm{erf}(x) = \frac{2}{\sqrt{\pi}}\int_0^x e^{-t^2}dt$).

Similarly, the total normal force from the plastically deformed asperities is calculated as

$$F_p = \frac{c\pi\beta C_v(1-\nu^2)Y_0}{E^*\lambda^2}\Big(2+\lambda\frac{\omega_c}{R_q}\Big)e^{-\lambda(d+\omega_c)/R_q}. \tag{3.5}$$

It is noted that F_e, F_p, and F_n are functions of d. The cube height d corresponding to a normal load F_n can be calculated from (3.3)–(3.5).

The actual contact area A_r is calculated as

$$A_r = A_e + A_p. \tag{3.6}$$

The actual contact area of the elastically deformed asperities is

$$A_e = \frac{c\pi\beta A_n}{\lambda^2}\Big[1-\Big(1+\lambda\frac{\omega_c}{R_q}\Big)e^{\lambda\omega_c/R_q}\Big]e^{-\lambda d/R_q}, \tag{3.7}$$

where A_n is the nominal contact area. The actual contact area of the plastically deformed asperities is

$$A_p = \frac{c\pi\beta A_n}{\lambda^2}\Big(2 + \lambda\frac{\omega_c}{R_q}\Big)e^{-\lambda(d+\omega_c)/R_q}. \tag{3.8}$$

3.1.2 Friction Model

The cube deforms when two surfaces slide relative to each other. Since asperities are connected to the body of the material, it can be assumed that two ends of the cube are fixed and the cube itself can be treated like a bending beam, as shown in Fig. 3.11. The plastic region works as a plastic hinge (it provides no higher moment when its maximum moment is reached). The tangential contact stiffness Kt can be derived from the bending stiffness of a beam with two fixed ends [83]. Given the geometry of the cube, K_t has the form

$$K_t = \frac{E^* A_r^2}{d^3}. \tag{3.9}$$

Friction has been studied extensively [106]. Many friction models have been proposed, and this study adopts Dahl's model. Dahl [17] supplies an ordinary differential equation to calculate time-dependent microscopic deformation δ as

$$\frac{d\delta}{dt} = v_{rel}\Big[1 - \frac{K_t\delta}{F_{t0}}\mathrm{sgn}(v_{rel})\Big], \tag{3.10}$$

where v_{rel} is the relative sliding velocity between two surfaces, which is equal to 5 mm/s in this paper, and F_{t0} is the static friction between two surfaces measured from experiments.

Dynamic friction is calculated as the product of microscopic deformation and tangential contact stiffness,

$$F_t = K_t\delta. \tag{3.11}$$

3.1.3 Friction Reduction Model

As described in the introduction, ultrasonic vibrations can be applied in different ways. Vibrations can be projected in three orthogonal directions: in-plane parallel, in-plane perpendicular, and out-of-plane perpendicular to the sliding direction, denoted as u, v, and w, respectively. The deformations are functions of coordinates x, y, z, and time t. For δ, d, A_r, and K_t, prime symbols are employed to denote changed parameters after the application of ultrasonic vibrations.

It is assumed in the cube model that projection w has little influence on friction reduction and the projection u is directly added to the longitudinal microscopic deformation δ. Hence, in the presence of ultrasonic vibrations, the new deformation (denoted δ') is the sum of the initial deformation and the longitudinal projection of the vibrations,

$$\delta' = \delta + u. \tag{3.12}$$

The out-of-plane perpendicular projection v changes distance between two surfaces, which is equal to the height of the cube. The new cube height is calculated as

$$d' = d + v. \tag{3.13}$$

The actual contact area changes with the new distance and its value A_r' can be calculated using Eqs. (3.6), (3.7) and (3.8). Therefore, the new tangential contact stiffness K_t' is calculated as

$$K_t' = \frac{E^* A_r'^2}{d'^3} = \frac{E^* A_r'^2}{(d+v)^3}. \tag{3.14}$$

Vibrations add relative vertical movements between two surfaces. When the surfaces move towards each other, friction increases so that the sliding pauses. The two surfaces are now in stick phase. When two surfaces move away from each other, friction is reduced and the sliding resumes, defined as slip phase. The sliding process consists of stick and slip phases alternating at an ultrasonic frequency. The overall dynamic friction is the average friction at the slip phase.

Assuming that each slip and stick phase takes place in half of one ultrasonic vibration period, T, the overall dynamic friction is the integration of the time-dependent friction over the slip phase,

$$F_t' = \frac{2}{T}\int_0^{T/2} K_t'\delta' dt = \frac{2}{T}\int_0^{T/2} \frac{E^* {A_r'}^2(\delta + u)}{(d+v)^3} dt. \tag{3.15}$$

Note that the parameters K_t', A_r', u, v, d', and δ' are all time-dependent. This friction is considered as reduced friction by ultrasonic vibrations.

This model is applicable to various cases of ultrasonic lubrication because it does not depend on the pattern of applying ultrasonic vibrations. It breaks the vibrations down into projections in three orthogonal directions and evaluates them separately.

3.1.4 Model Validation and Discussion

Contact parameters

Experimental data from Section 2.1 is employed to validate the model. The parameters used in the cube model simulations are listed in Table 3.1. The surface roughness parameters R_q, R_s, and η are estimated using surface roughness comparison standards. These standards give prevalent surface roughness values for different surface finishes. The model simulation gives the same contact parameters for test 1 (aluminum waveguide with stainless steel block) and test 2 (stainless steel waveguide and aluminum block). Cube heights under different normal loads are calculated using elastic-plastic equations (Eqs. (3.4) and (3.5)) and plotted in Fig. 3.2 (a). Cube

Table 3.1: Parameters used in model simulations.

Symbol	Parameter	Value	Unit
R_q	Asperity heights deviation	6	μm
R_s	Asperity summits radius	1.7	μm
A_n	Nominal contact area	1×10^{-4}	m^2
η	Areal asperity density	47×10^9	/m^2
E_1	Young's modulus of aluminum	73	GPa
ν_1	Poisson ratio of Aluminum	0.33	$--$
E_2	Young's modulus of stainless steel	200	GPa
ν_2	Poisson ratio of stainless steel	0.29	$--$
Y_0	Failure strength of the softer material	410	MPa

heights calculated using elastic equations are also plotted in this figure for comparison. A similar comparison about real contact areas is conducted and shown in Fig. 3.2 (b).

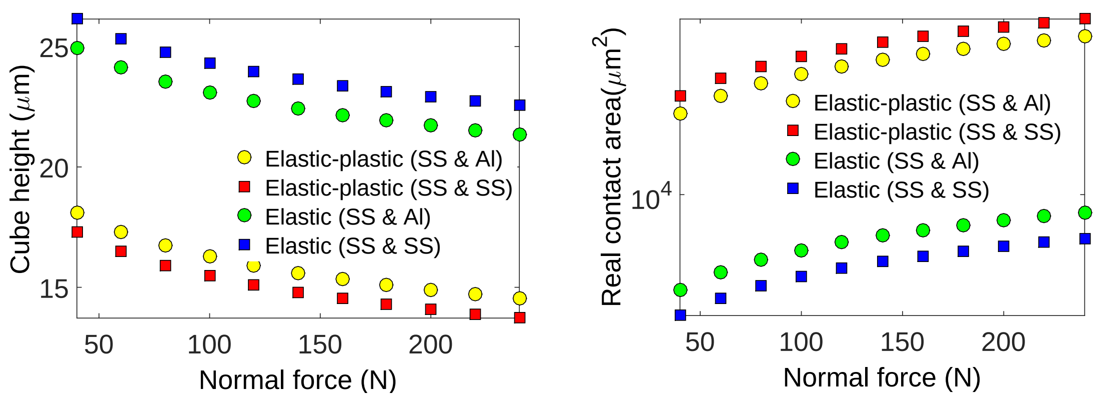

(a) (b)

Figure 3.2: Comparison of calculated parameters from elastic and elastic-plastic models: (a) cube heights; (b) real contact area.

It is observed in Fig. 3.2 (a) that the elastic-plastic assumption leads to a smaller cube height and associated smaller separation between surfaces. The elasticplastic model predicts less separation between stainless steel surfaces than between aluminum and stainless steel, while the opposite is true for the purely elastic model. For the aluminum and stainless steel combination, at 40 N normal load, the separation is around 25 μm using the purely elastic model but 18 μm using the elasticplastic model; the difference between the two models is around 7 μm under the range of normal loads considered. For the stainless steel and stainless steel combination, the discrepancy between the models is larger, close to 9 μm on average.

A smaller separation indicates a greater real contact area. When the first contacting asperities start to undergo plastic deformation, the plastic regions continue growing but contribute no additional resisting force. Therefore, as the normal force increases, more asperity contacts are formed and a larger real contact area is generated. As shown in Fig. 3.2 (b), there is up to a sevenfold increase in contact area as the normal force varies over the range. The discrepancy between the elastic and elasticplastic models is about 10^2 μm^2.

Friction

Friction forces at various normal loads obtained from all three test groups are plotted in Fig. 3.3 (a), and the corresponding dynamic friction coefficients are plotted in Fig. 3.3 (b). In different test groups, the normal loads adopted are different. As shown in the figures, test 1 uses 11 normal loads from 40 N to 240 N with an interval of 20 N. Due to the test operation changes, the other two groups use 10 and 8 normal loads, respectively, which cover the same range but without an even distribution of forces.

Results from all three test groups show good linearity between the normal loads and the tangential forces, which presents relatively constant friction coefficients within the different groups. However, test 1 gives higher friction forces than test 2. The average coefficients are respectively 0.54 and 0.26. It is emphasized that those two test groups give different results even though they are from the same two types of materials. The different behavior may be caused by the way normal forces are applied onto the contact interface of the two materials. For the stainless steel waveguide (tests 2 and 3), the results show that the friction forces are approximately the same regardless of sliding block material.

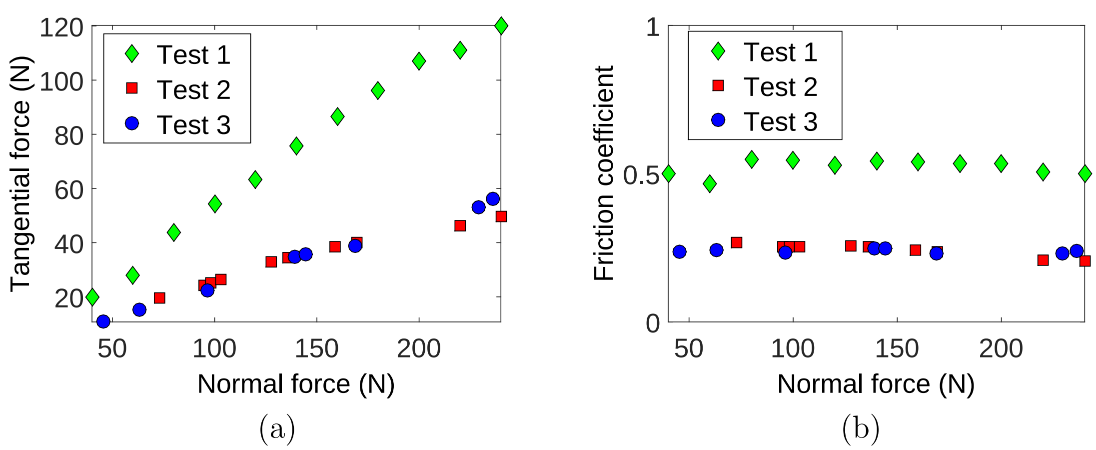

Figure 3.3: Comparison of dynamic friction coefficients measured from tests.

Friction reduction

A comparison of test results and model simulations for all three test groups is shown in Fig. 3.4. Each figure plots three sets of data, two of which are from tests and one from model simulations. The red squares denote natural friction forces. The blue circles indicate friction forces with ultrasonic vibrations measured from tests. The green diamonds are friction forces with ultrasonic vibrations predicted by the cube model. The model parameters used for calculation are listed in Table 3.1.

All three sets of data show good linearity between friction forces and normal forces, which indicate constant dynamic friction coefficients. But in test 2, at three points when normal loads are larger than 160 N, reduced friction forces measure larger than the linearity indicates, which may be caused by experimental error.

Friction forces are substantially reduced in all three cases when ultrasonic vibrations are employed. Percentages from both tests and simulations are plotted in Fig. 3.4 for comparison.

Tests 1 and 2 have friction reduction in the range of 30–50% and show trends that higher normal loads provide lower reduction percentages. Test 3 has higher reduction percentage, in the range of 50–60%, but results show no evident decreasing trend when the normal load goes up.

Note that both the waveguide and sliding block used in test 3 are all stainless steel, which is different from tests 1 and 2, which mix aluminum and stainless steel. Since stainless steel is a harder than aluminum, it can be hypothesized that the harder the materials of the contacting surfaces, the higher the friction reduction. However, this hypothesis requires more testing using materials with a wider range of hardness.

Another observation is that test 3 reveals less wear than tests 1 and 2, which may also be explained by the fact that stainless steel is harder than aluminum. In tests 1 and 2, fretting wear mostly occurs on aluminum parts but much less on stainless steel parts.

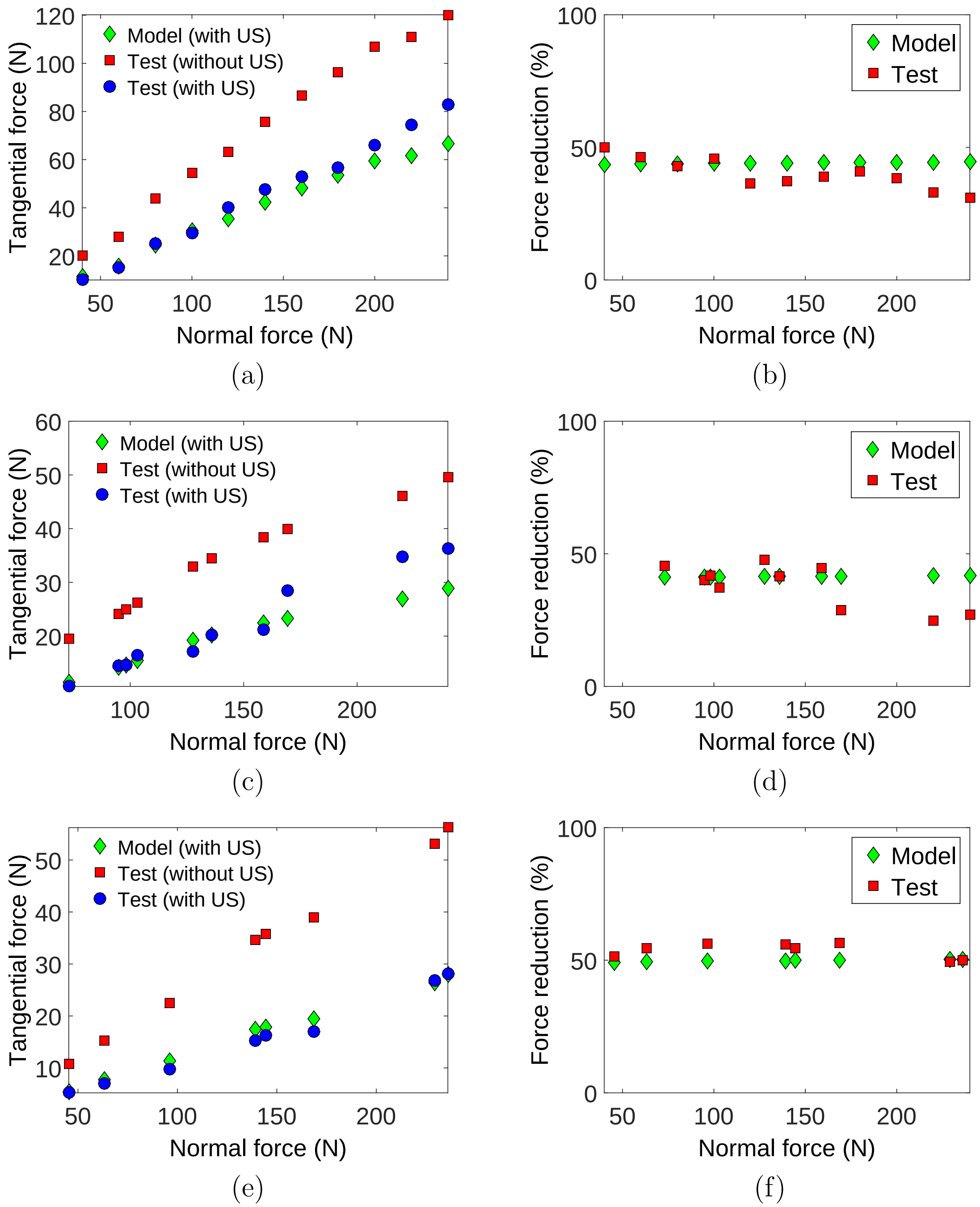

Figure 3.4: Comparison of friction reduction percentage between tests and model simulations.

Comparison of model simulation and experimental data

The results show that the model predictions closely match the experimental data. However, there are some discrepancies between the test and model, as seen in each figure. In tests 1 and 2, the discrepancy becomes evident when normal load is increased. Despite possible test errors, another reason for that could be the asperity heights distribution model, an exponential function used to approximate the Gaussian distribution for ease of calculation. The discrepancy between those two functions becomes greater as normal loads increase.

The relative error between test and simulation is defined as

$$e = \frac{|\text{test} - \text{model}|}{\text{test}} \times 100. \tag{3.16}$$

Most errors from all three tests are below 20%, showing good agreement.

Waveguide kinematics

Waveguide kinematics helps to understand the generation and propagation of ultrasonic vibrations in the waveguide. In this study, the influence of the tapering and rounded edges of the waveguide is neglected for simplicity, and the vibrations of the waveguide are treated as a superposition of the motion of all modes,

$$u(x,t) = \sum_{n=1}^{\infty} (a_n \sin \omega_n t + b_n \cos \omega_n t) U_n(x), \tag{3.17}$$

where ω_n is the nth order frequency and $U_n(x)$ is the function of nth order normal mode shape, which has the form

$$U_n(x) = c_n \sin(\omega_n x / c_0) + d_n \cos(\omega_n x / c_0), \tag{3.18}$$

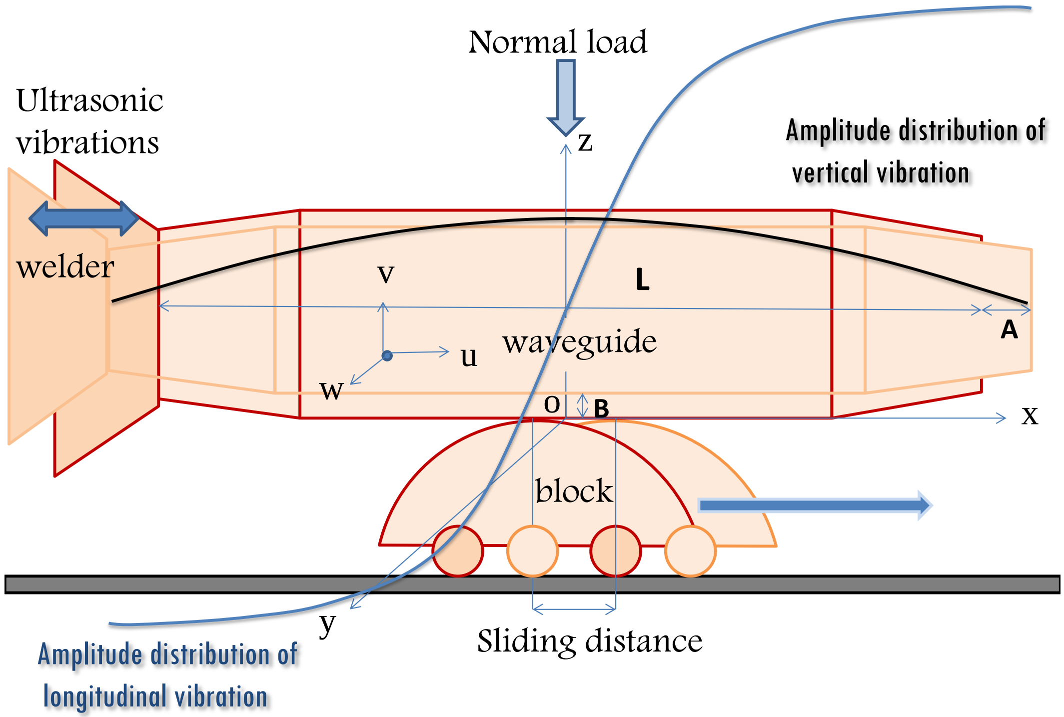

Figure 3.5: Schematic of waveguide vibration.

where c_0 is the axial speed of wave propagation. For each mode n, there exists a wave equation[84]

$$\frac{\partial^2 U_n}{\partial x^2} + \frac{{\omega_n}^2 U_n}{{c_0}^2} = 0. \tag{3.19}$$

It is deduced that $d_n = 0$; using the boundary conditions $\partial u(-L/2, t)/\partial x = 0$ and $\partial u(L/2, 0)/\partial x = 0$, it is obtained that $\cos(\omega_n L/2c_0) = 0$, thus

$$\omega_n = n\pi c_0/L \ (n = 0, 1, 2...). \tag{3.20}$$

Given that the frequency and the waveguide length in this paper are respectively 20 kHz and 0.127 m, the order of the vibration, therefore, is equal to 1, which means that the vibration is at the half-wavelength frequency and its corresponding normal mode function can be written as

$$U_1 = c_1 \sin(\omega_1 x/c_0) = c_1 \sin(\pi x/L). \tag{3.21}$$

Thus, the longitudinal vibration function is written as

$$u(x,t) = b_1 \cos(2\pi f t) U_1 = b_1 c_1 \cos(2\pi f t) \sin(\pi x/L). \tag{3.22}$$

Letting $A = b_1 c_1$, the function of longitudinal displacement Eq. (3.22) is derived. The vertical strain is caused by longitudinal strain, known as Poisson's effect. The longitudinal strain is calculated as

$$\varepsilon_x = \frac{\partial u(x,t)}{\partial x} = \frac{A\pi}{L} \cos(2\pi f t) \cos(\pi x/L). \tag{3.23}$$

Therefore, the vertical strain is

$$\varepsilon_y = \nu \varepsilon_\chi = \frac{A\pi\nu}{L} \cos(2\pi f t) \cos(\pi x/L), \tag{3.24}$$

The vertical displacement of the point at the bottom surface of the waveguide is the integration of the strain over half of the thickness of the waveguide, which is expressed as

$$v(x,t) = \frac{DA\pi\nu}{2L} \sin(2\pi f t) \cos\left(\frac{\pi x}{L}\right), \tag{3.25}$$

where D is the thickness of the waveguide. Letting $B = DA\pi\nu/2L$, the function of vertical displacement Eq. (3.25) is derived. In this study, the values of A and B are determined by Doppler laser-vibrometer measurements.

3.1.5 Summary

In this work, an cube model is presented which describes ultrasonic lubrication under a range of conditions. Ultrasonic vibrations are projected on three orthogonal directions and the influence of each projection on friction reduction is calculated. An overall reduction result summarizes all three projections. The calculation of contact parameters takes into consideration plastic deformation, which gives smaller distances between two surfaces and larger real contact areas.

The cube model is used to describe the reduction in friction force using parameters from the tests and contact model. These simulations show good agreement with the test results, reflecting average relative errors below 20% despite the fact that small discrepancies exist with normal loads above 160 N. Future work may be able to address this issue by employing a Gaussian distribution for asperity heights instead of an exponential distribution.

Furthermore, the cube model can be applied to model dynamical systems with ultrasonic lubrication devices. The results are of great interest in predicting system outputs, thus aiding in system design. Through in-depth analysis of stress, strain and plastic deformations of asperities, the cube model may be used in modeling wear reduction.

3.2 Cube Model for Wear Reduction

3.2.1 Concept

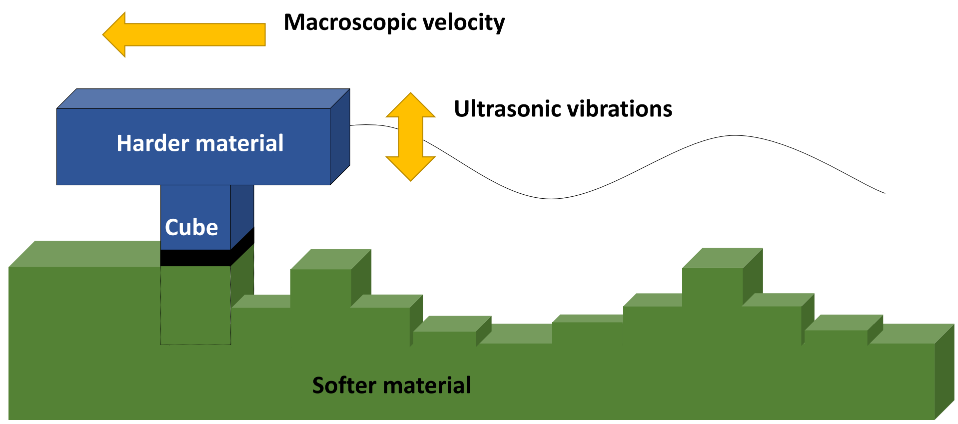

Figure 3.6: Mechanics of ultrasonically-induced wear reduction.

Based on the cube concept, a description for ultrasonic wear reduction is proposed. It can be seen in Fig. 3.6 that as the top surface moves along the bottom surface, contact asperity pairs deform and break, bringing new asperities into contact. As addressed previously, wear in this study is abrasive in nature due to the fact that stainless steel is much harder than aluminum. Breakage of the contacting asperity pairs is assumed to take place at the roots of the asperities of the softer material, i.e. the aluminum disc. The broken asperities correspond to half of the cube's volume; this removed volume accounts for abrasive wear in the aluminum disc. When ultrasonic vibrations are applied, the contact between the two surfaces is reduced resulting in a reduction of wear.

An approach to quantify wear reduction is illustrated in Fig. 3.7. The geometry considered is that of the stainless steel acorn nut used in the experiments as it slides relative to the aluminum disc. Over the sliding distance D, the total volume of material removed is calculated as

$$Vol = \frac{A_r d}{2}, \tag{3.26}$$

where Vol is the volume loss of the aluminum disc, A_r is the actual area of contact between the two surfaces, and d is the height of the cube. Distance D can be calculated from the nominal area A_n as

$$D = \frac{4\sqrt{A_n}}{\pi}. \tag{3.27}$$

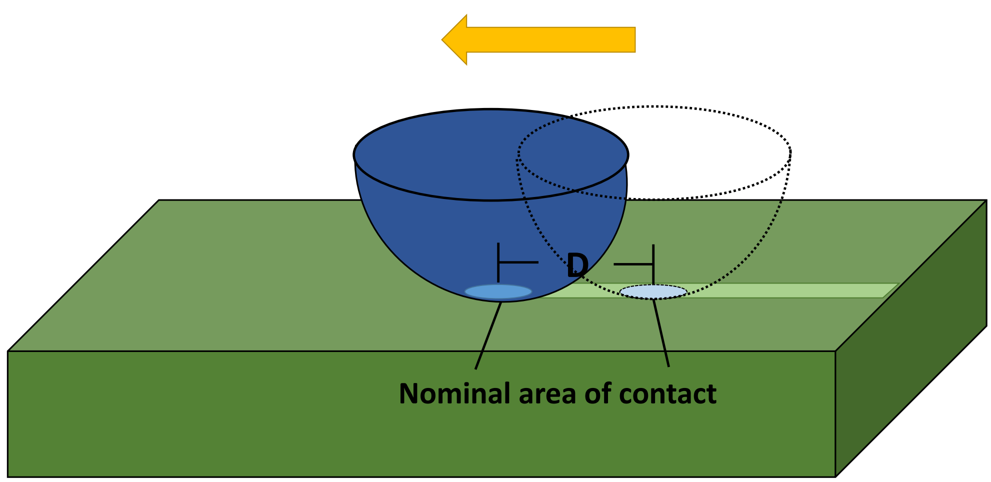

Figure 3.7: Schematic of wear rate calculation.

When ultrasonic vibrations are applied, the acorn nut vibrates in the direction perpendicular to the disc surface. The contact area and the separation between the two surfaces change accordingly. We denote A_r' the area of the top of the cube and

Table 3.2: Parameters used in the cube model for wear reduction.

Symbol	Meaning	Value
F_n	Normal force	3 N
E^*	Combined Young's modulus	59.6 GPa
A_n	Nominal contact area	2.25 mm^2
R_q	RMS of asperity heights	6 μm
R_s	Summit radius of single asperity	1.5 μm
η	Areal density of asperities	4.7×10^{10} /m^2
Y_0	Yield strength of softer material	410 MPa

d' the height of the cube when ultrasonic vibrations are applied. The volume loss of the aluminum disc over the sliding distance D is

$$Vol' = \frac{1}{2T}\int_0^T A'_r d' dt, \tag{3.28}$$

where T is the period of ultrasonic vibrations, A'_r is the time-dependent actual area of contact when ultrasonic vibrations are applied, and d' is the time-dependent height of the cube. The wear rate is calculated as

$$W' = \frac{V'}{D} = \frac{1}{2T}\int_0^T \frac{A'_r d'}{D} dt, \tag{3.29}$$

The parameters used to perform these calculates are listed in Table 3.2. Wear reduction percentage is defined as

$$P_w = \frac{W - W'}{W} \times 100\%. \tag{3.30}$$

3.2.2 Model validation

The comparison between the experimental data (from Section 2.3) and model simulations are listed in Table 3.3 and 3.4. The model was able to predict wear rate with and without ultrasonic vibration very well with all errors less than 15%.

Table 3.3: Comparison between experimental data and model calculation of wear rates with various linear velocities.

Linear speed m/s	Wear rate ($\times 10^{-2}$ mm^3/m)					
	With US			Without US		
	test	model	error	test	model	error
20.3	2.237	2.566	14.7%	1.214	1.335	11.6%
40.6	2.581	2.566	0.58%	1.338	1.335	1.27%
87	2.430	2.566	5.6%	1.248	1.335	8.57%

Table 3.4: Comparison between experimental data and model calculation of wear rates with various revolutions.

Revolution	Wear rate ($\times 10^{-2}$ mm^3/m)					
	Without US			With US		
	test	model	error	test	model	error
900	2.414		6.3%	1.509		10.2%
1600	2.554	2.566	0.47%	1.381	1.355	1.89%
1900	2.551		0.59%	1.392		2.66%

3.2.3 Summary

The concept of cube model previously developed to quantify ultrasonic friction reduction was extended and implemented to describe the wear measurements conducted on the modified pin-on-disc tribometer. Without fundamental modifications, the model describes wear reduction well with errors less than 15%.

3.3 Multi-Scale Dynamics System Model for Ultrasonic Lubrication

An ultrasonic lubrication system usually consists of the following components: a contact interface of interest, a transducer for vibration generation, and a structure to hold the transducer in place and maximize the vibration. This model is developed to represent these components in three scale levels: the "cube" model for contact and friction reduction mechanisms, an electromechanical model for the piezoelectric transducer, and a system dynamics model for the entire structure.

3.3.1 System Dynamics

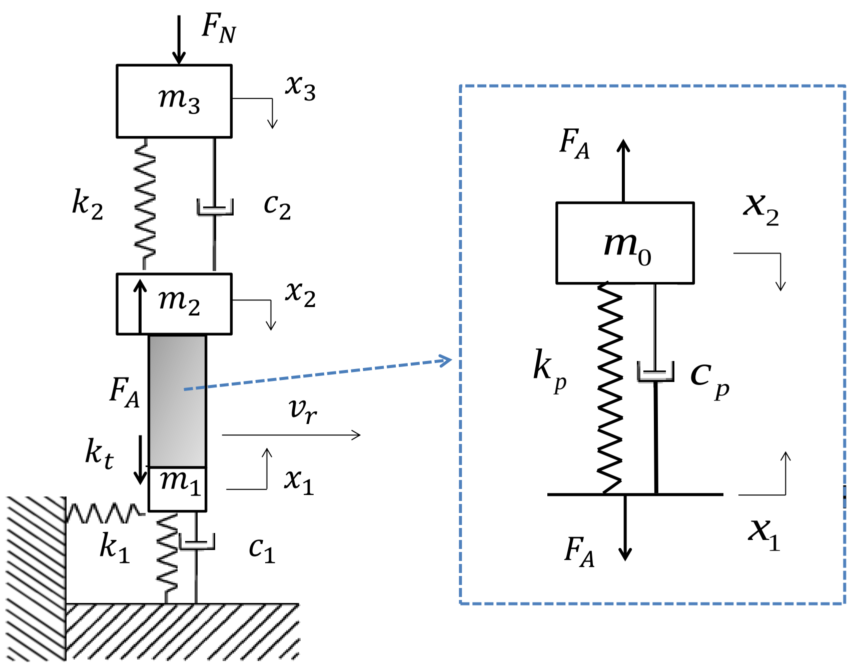

Figure 3.8: Diagram of system dynamics model.

A lumped three degree-of-freedom system dynamics model is shown in Fig. 3.8, which consists of a piezoelectric transducer, three masses, a fixed plane, springs, and dampers. Mass m_1 and the fixed plane represent the two moving objects in contact, between which the friction is of interest and aimed to be reduced. Relative velocity between the two surfaces is denoted as v_r, and normal force at the interface is F_N. Normal force F_N is applied through a structure, the equivalent mass, stiffness, and damping of which are denoted as m_3, k_2 and c_2. The piezoelectric actuator is represented by a spring-mass system, with equivalent dynamic mass, stiffness, and damping coefficient denoted as m_0, k_p, and c_p, respectively.

Mass m_1 is connected to the piezo-actuator, which generates ultrasonic vibrations (x_1) in the direction perpendicular to the macroscopic velocity (v_r). Piezoelectric actuators are usually made of a stack of piezoelectric wafers. Compression is applied to avoid tension in the stack due to the brittle nature of piezoelectric materials.

A second mass m_2 is connected to the other end of the actuator, which is generally selected to be much larger than m_1, so that most of the vibrations created by the actuator can then be distributed at m_1. Mass m_2 is often referred to as the reaction mass.

Equations of motion of the system can be written as

$$\begin{bmatrix} m_1 & 0 & 0 \\ 0 & m_2 + m_0 & 0 \\ 0 & 0 & m_3 \end{bmatrix} \begin{bmatrix} \ddot{x}_1 \\ \ddot{x}_2 \\ \ddot{x}_3 \end{bmatrix} + \begin{bmatrix} c_1 + c_p & c_p & 0 \\ c_p & c_p + c_2 & -c_2 \\ 0 & -c_2 & c_2 \end{bmatrix} \begin{bmatrix} \dot{x}_1 \\ \dot{x}_2 \\ \dot{x}_3 \end{bmatrix} + \begin{bmatrix} k_p + k_1 & k_p & 0 \\ k_p & k_p + k_2 & -k_2 \\ 0 & -k_2 & k_2 \end{bmatrix} \begin{bmatrix} x_1 \\ x_2 \\ x_3 \end{bmatrix} = \begin{bmatrix} F_A \\ F_A \\ F_N \end{bmatrix}, \tag{3.31}$$

where F_A is the actuation force generated by the actuator.

3.3.2 Piezoelectric Actuator

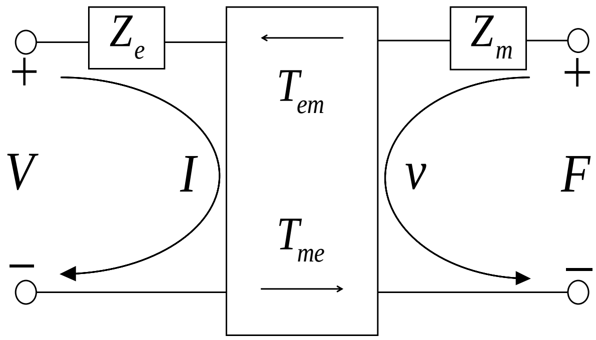

Figure 3.9: Electromechanical coupling of piezoelectric transducers.

The constitutive equations of piezoelectric materials are [27]

$$\mathbf{D} = \epsilon^{\mathbf{T}}\mathbf{E} + \mathbf{dT}, \tag{3.32}$$

and

$$\mathbf{S} = \mathbf{dE} + \mathbf{s}^{\mathbf{E}}\mathbf{T}, \tag{3.33}$$

where $\mathbf{D}$ is the electric displacement, $\mathbf{T}$ is the stress, $\mathbf{E}$ is the electric field, and $\mathbf{S}$ is the strain, $\epsilon^{\mathbf{T}}$ is the permittivity under constant stress, $\mathbf{s}^{\mathbf{E}}$ is the mechanical compliance with constant electric field, and $\mathbf{d}$ is the piezoelectric constant. In this model, only the quantities in the poling direction (33) are taken into consideration.

Electromechanical coupling is shown in Fig. 3.9, where F is the mechanical load, v is the velocity, Z_m is the blocked mechanical impedance, V is the driving voltage, I is the current, Z_e is the blocked electrical impedance, T_{me} and T_{em} are electromechanical transduction coefficients. The coupling equations between electrical and mechanical are

$$V = Z_e I + T_{em} v, \tag{3.34}$$

and

$$F = T_{me} I + Z_m v, \tag{3.35}$$

where Z_e is calculated as

$$Z_e(s) = \frac{1}{Cs}, \tag{3.36}$$

where C is the blocked capacitance of the stack. Z_m is calculated as

$$Z_m(s) = \frac{k_p}{s}, \tag{3.37}$$

T_{em} and T_{em} are calculated as

$$T_{em}(s) = T_{em}(s) = \frac{d_{33}}{sN\epsilon^S S^E}, \tag{3.38}$$

where $\epsilon^S = \epsilon^T(1 - k^2)$, and k is the electromechanical coupling factor.

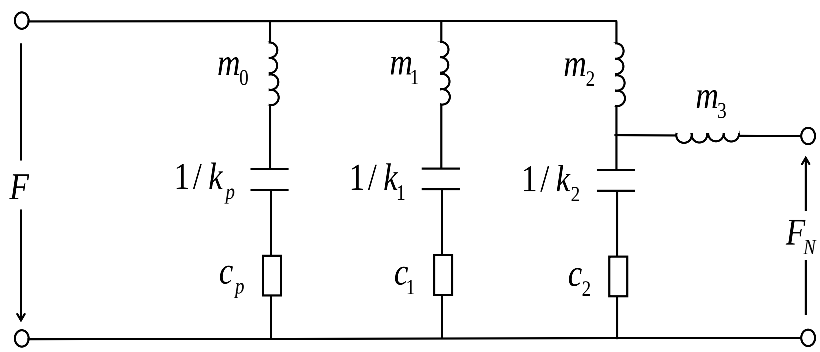

Figure 3.10: Equivalent circuit of the mechanical load.

It is assumed that force F acts on a load of impedance Z_L. The equivalent circuit of the dynamic system is shown in Fig. 3.10. The impedance from the load can be expressed as

$$Z_L(s) = [\frac{1}{m_0 s + c_p + k_p/s} + \frac{1}{m_1 s + c_1 + k_1/s} + \frac{1}{m_2 s + Z_0}]^{-1}, \tag{3.39}$$

where

$$Z_0 = [\frac{1}{m_3 s + F_N/s} + \frac{1}{c_2 + k_2/s}]^{-1}. \tag{3.40}$$

Therefore, the total electrical impedance of the actuator is

$$Z_{ee}(s) = Z_e + \frac{-T_{me}T_{em}}{Z_m + Z_L}, \tag{3.41}$$

and the actuation force generated by the actuator is calculated as

$$F_A = N d_{33} k_p V, \tag{3.42}$$

where N is the number of the wafers in the stack.

3.3.3 The "Cube" Model

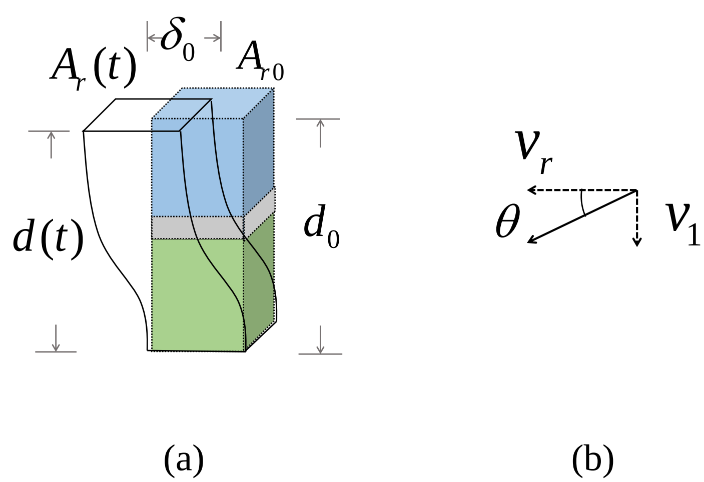

Figure 3.11: The "cube" model: (a) deformation of the "cube"; (b) velocity vector.

The elastic-plastic "Cube" model has been previously proposed and described. The top area of the cube, A_r, is the real contacting area, and the height of the cube,

d, is the distance between the two surface. Detailed calculations of A_r and d can be found in Section 3.1. Deforming asperities provide stiffness in both axial and tangential directions, which are expressed as k_1 and k_t, respectively, in the system dynamics model (Fig. 3.8). Based on the geometry of the cube, axial stiffness, k_1, is calculated as

$$k_1 = \frac{E^* d}{A_r}, \tag{3.43}$$

where E^* is the combined Young's modulus of the two materials in contact. Tangential stiffness, k_t, is calculated as

$$k_t = \frac{E^* A_r^2}{d^3}. \tag{3.44}$$

Under normal load F_N, axial and tangential stiffness at equilibrium ($x_1 = 0$) are denoted as k_{10} and k_{t0}, which are calculated from a cube with A_{r0} and d_0 (Fig. 3.11 (b)). Friction comes from the resistance created by the deformed contacting asperities in the direction opposite to the relative velocity. Intrinsic friction (F_{t0}), tangential deformation (δ_0), and tangential stiffness (k_{t0}) have a relationship as

$$F_{t0} = k_{t0}\delta_0. \tag{3.45}$$

It is assumed that tangential deformation of the asperities (δ_0) is only dependent on the macroscopic velocity (v_r) and remains constant despite the application of ultrasonic vibrations. When ultrasonic vibrations are applied, relative displacement between two surfaces in the vertical direction (x_1) changes the geometry of the cube, hence, the stiffness. When two surfaces move away from each other ($x_1 > 0$), more asperities cease being in contact, which results in a taller cube with smaller top area. On the other hand, when two surfaces move towards each other ($x_1 < 0$), more asperities come into contact, resulting in a shorter cube with larger top area. The time-dependent cube height and top area are denoted as $d(t)$ and $A_r(t)$ (Fig. 3.11 (a)).

Instantaneous velocity is at an angle with the tangential direction (θ) once ultrasonic vibrations are applied (Fig. 3.11 (b)),

$$\theta(t) = \cos^{-1}\big[\frac{v_r}{v_1(t)}\big]. \tag{3.46}$$

Therefore, instantaneous friction force is the projection of the resisting force in the tangential direction,

$$F_t(t) = k_t(t)\delta_0 \cos\big[\theta(t)\big]. \tag{3.47}$$

Overall friction force is the average of the instantaneous friction force over the vibration period T,

$$F_t = \frac{1}{T}\int_0^T F_t(t)dt. \tag{3.48}$$

3.3.4 Computational Results

Total electrical impedance of the piezo-actuator of the modified pin-on-disc tribometer was measured. The measurement was employed to identify of the critical parameters of the model, by matching the computational curve with the measured curve (Fig. 3.12). These parameters, along with others used in the simulation, are listed in Table 3.5. The simulation was conducted using Simulink in MATLAB.

The simulation results of the system vibrations are shown in Fig. 3.13. Plot (a) shows the overall displacement at x_1 and x_2. It takes approximately 0.05 second for the vibrations to reach steady states. Steady-state vibrations consist of vibrations at driving frequency and fluctuations at approximately 100 Hz (plot (b)). Vibrational

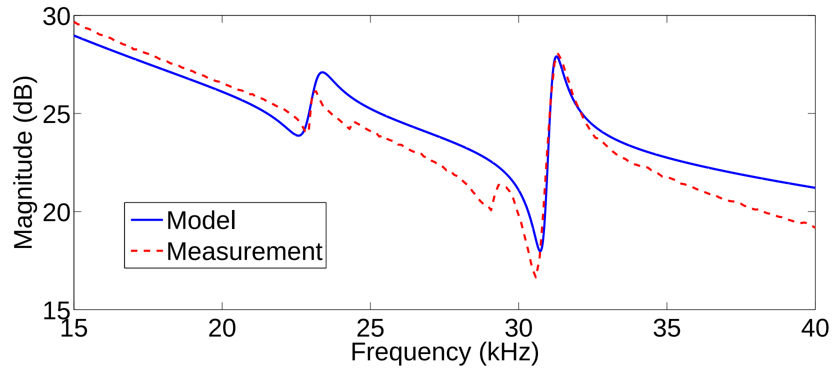

Figure 3.12: Electrical impedance of the piezoelectric actuator.

Table 3.5: Parameters used in the simulation.

Parameter	Symbol	Value
Deviation of asperities heights	R_q	6 μm
Average radius of asperities summits	R_s	1.5 μm
Capacitance of the piezoelectric stack	C	360 nF
Electromechanical coupling factor	k	0.431
Piezoelectric constant	d_{33}	140×10^{-12} mV
Number of layers	N	62
Equivalent stiffness of the piezo-actuator	k_p	2×10^{9} N/m
Equivalent mass of the piezo-actuator	m_0	0.07 kg
Equivalent damping coefficient	c_p	30

amplitude at steady-state (x_1) is approximately 2.5 μm, which is equal to the value measured by a laser vibrometer.

A comparison between the experimental data, presented in section 2.3, and the model prediction regarding reduction of friction is conducted to validate the model.

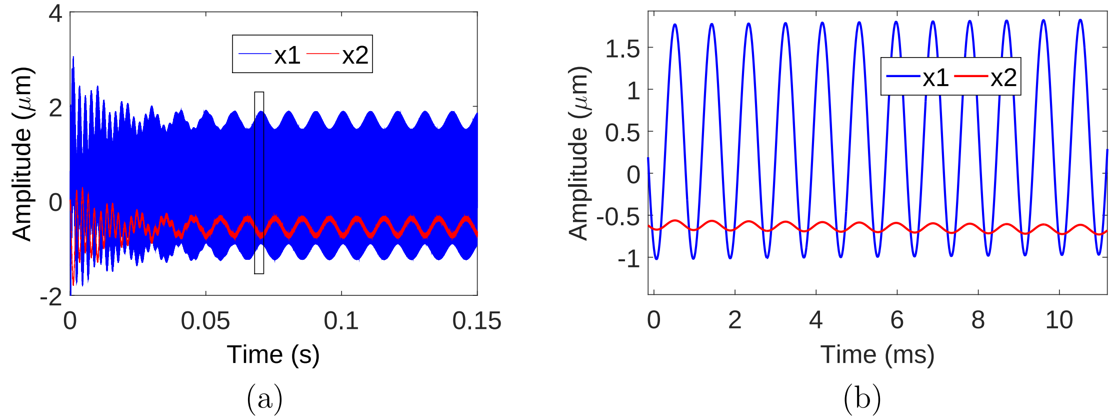

Figure 3.13: Simulation results of system vibrations: (a) displacement; (b) zoomed-in displacement.

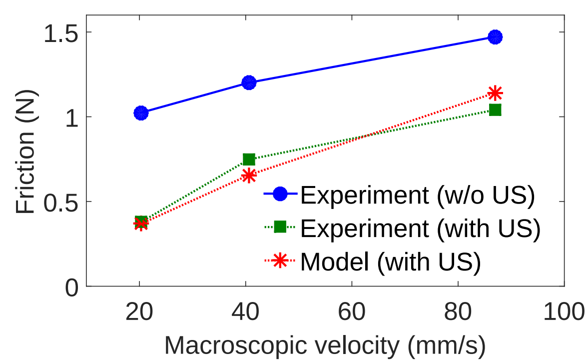

Figure 3.14: Comparison between friction from measurements and simulation.

The friction forces measured at three velocities, with and without ultrasonic vibrations, are plotted as dots and squares in Fig. 3.14. The reduced friction forces calculated from the model are plotted with stars. The comparison shows that the simulation matches the experimental data well at all three velocities, with errors less than 10%.

3.3.5 Parametric Study

Parameters such as driving voltage, macroscopic velocity, driving frequency, and signal waveform are studied. Friction ratio is defined to indicate the effectiveness of the friction reduction, as

$$\gamma = F_t/F_{t0}. \tag{3.49}$$

Lower friction ratio suggests better friction reduction.

Driving voltage

Simulations were conducted at different levels of voltages, from 0 to 200 V peak-to-peak. The displacement x_1, velocity v_1, tangential stiffness, and instantaneous friction in one period of ultrasonic vibration are shown in Fig. 3.15 (a)–(d).

Plots show that both the steady-state displacement and velocity at the interface are sinusoidal. Higher driving voltage results in higher amplitudes of displacement and velocity. When two surfaces move towards each other ($x_1 < 0$), a decrease in the cube height, an increase in the top area, and an increase in tangential stiffness occur. The tangential stiffness and instantaneous friction force reach their peaks when x_1 is at its minimum. The contact between two surfaces is reduced when they move away from each other ($x_1 > 0$). Once the dynamic load introduced by the ultrasonic vibrations overcomes the static normal load, the surfaces separate and hopping takes place. This occurs when x_1 is greater than 3.8 μm (dashed line in Fig. 3.15 (a)) and k_t becomes virtually zero (Fig. 3.15 (c)).

The relationship between friction ratio and driving voltage is plotted in Fig. 3.15 (e). The friction force drops significantly when driving voltage increases from 0 to 20 V, but friction reduction becomes less significant when the voltage continues to increase

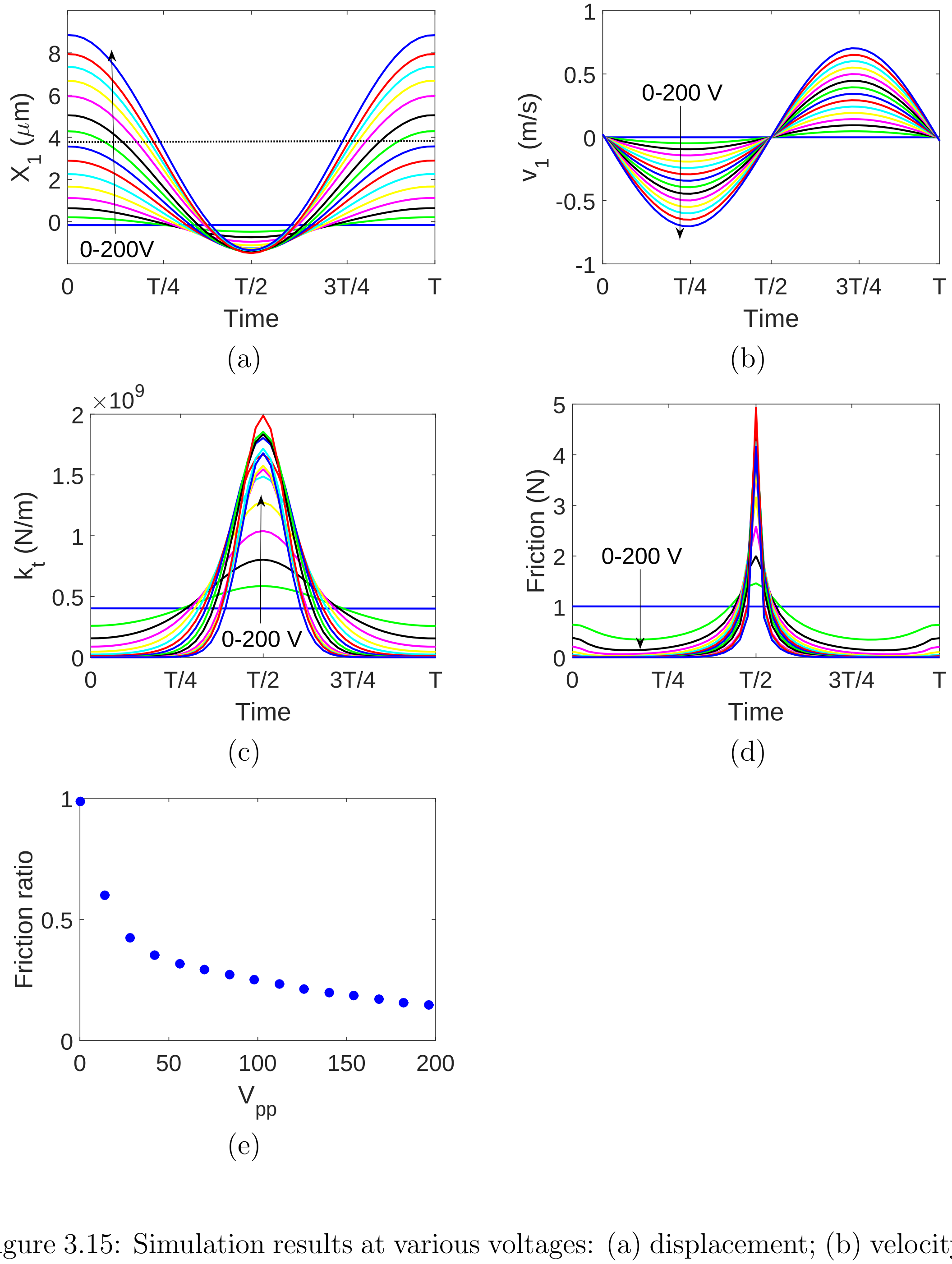

Figure 3.15: Simulation results at various voltages: (a) displacement; (b) velocity; (c) tangential stiffness; (d) instantaneous friction; (e) relationship between voltage and friction ratio.

over 20 V. It is concluded that higher driving voltage results in more friction reduction. However, increasing voltage becomes less effective in gaining friction reduction as the voltage increases.

Macroscopic velocity

Macroscopic velocity is critical to ultrasonic friction reduction. There have been studies in the relationship between friction reduction and velocity when ultrasonic vibrations were applied in the direction longitudinal to the macroscopic velocity. It was proposed that ultrasonic vibrations can change the direction of the friction force, hence, the overall magnitude of friction. Higher macroscopic velocity results in less friction reduction [34].

In this study, ultrasonic vibrations are out-of-plane perpendicular to the macroscopic velocity. Different voltages are employed for the simulation, from 0 V to 200 V peak-to-peak. Different voltages result in a different vibratory velocity. A velocity ratio is defined, as

$$\zeta = v_r/v_1, \tag{3.50}$$

where v_r is the macroscopic velocity (chosen to be 0 m/s to 1 m/s), and v_1 is the vibrational velocity obtained from the simulation. The relationship between the friction ratio and the velocity ratio are plotted in Fig. 3.16.

For all voltages, the trend is that higher macroscopic velocity leads to lower friction reduction, which is in line with the experimental data and previous studies of ultrasonic vibrations in a longitudinal direction. For a certain macroscopic velocity, a higher driving voltage results in a higher friction reduction.

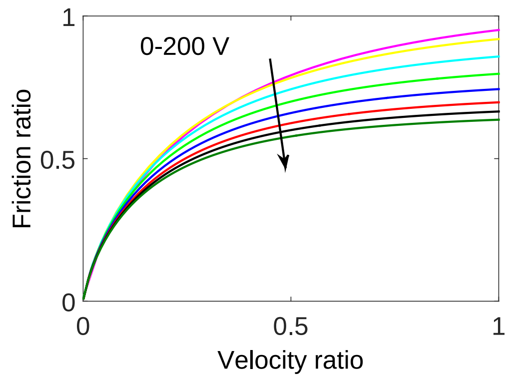

Figure 3.16: Relationship between friction ratio and velocity ratio.

Driving frequency

The driving frequency of the actuator is generally set to be at the resonant frequency of the system in order to maximize the vibration. The relationships between friction ratio and driving frequency (1–100 kHz) at different voltages are plotted in Fig. 3.17 (a).

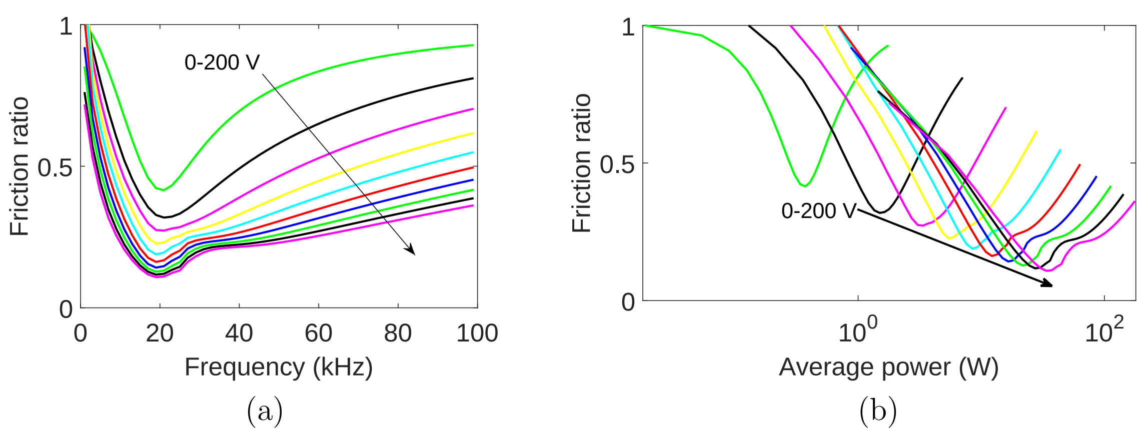

Figure 3.17: (a) Relationship between friction ratio and driving frequency; (b) Relationship between friction ratio and power consumption.

It is evident that, for all voltages, the relationship between friction ratio and frequency has a "v" shape: the maximum friction reduction takes place at the resonance. Higher amplitude results in higher maximum reduction. One observation from this plot is that, to achieve same level of friction reduction, the actuator can be driven either at a lower frequency with a higher amplitude, or at a higher frequency with a lower amplitude. There is no singular solution. However, if the power consumption is taken into consideration, an optimum does exist.

The relationships between the friction ratio and average power at different voltages are plotted in Fig. 3.17 (b). For each voltage, the friction ratio curve remains in a "v" shape. The tips of the "v"s form an envelope curve. It indicates that, to achieve a certain level of friction reduction at a certain given voltage, the solution with the least power consumption is to drive it at the resonance frequency. An equal amount of reduction may be achieved by driving the actuator at a higher voltage and a non-resonant frequency, but more power is then consumed.

Signal waveform

In the experiment, sinusoidal waveform is adopted for driving the piezo-actuator. Here, four types of waveforms are compared: sawtooth, square, triangle, and sinusoid. As shown in Fig. 3.18 (a), the amplitude and the frequency of the signals remain equal: 0-200 V peak-to-peak and 22 kHz. The macroscopic velocity is 20.3 mm/s.

For all four waveforms, the steady-state vibrations in one period are plotted in Fig. 3.18 (b). It can be seen that all vibrations follow sinusoidal patterns, despite the different waveforms of the driving signals. Square waveform generates the highest vibrational amplitude at the interface, and therefore, leads to highest amount of friction reduction (Fig. 3.18 (c)). The remaining waveforms that give the highest to lowest reduction are sinusoid, triangle, and sawtooth.

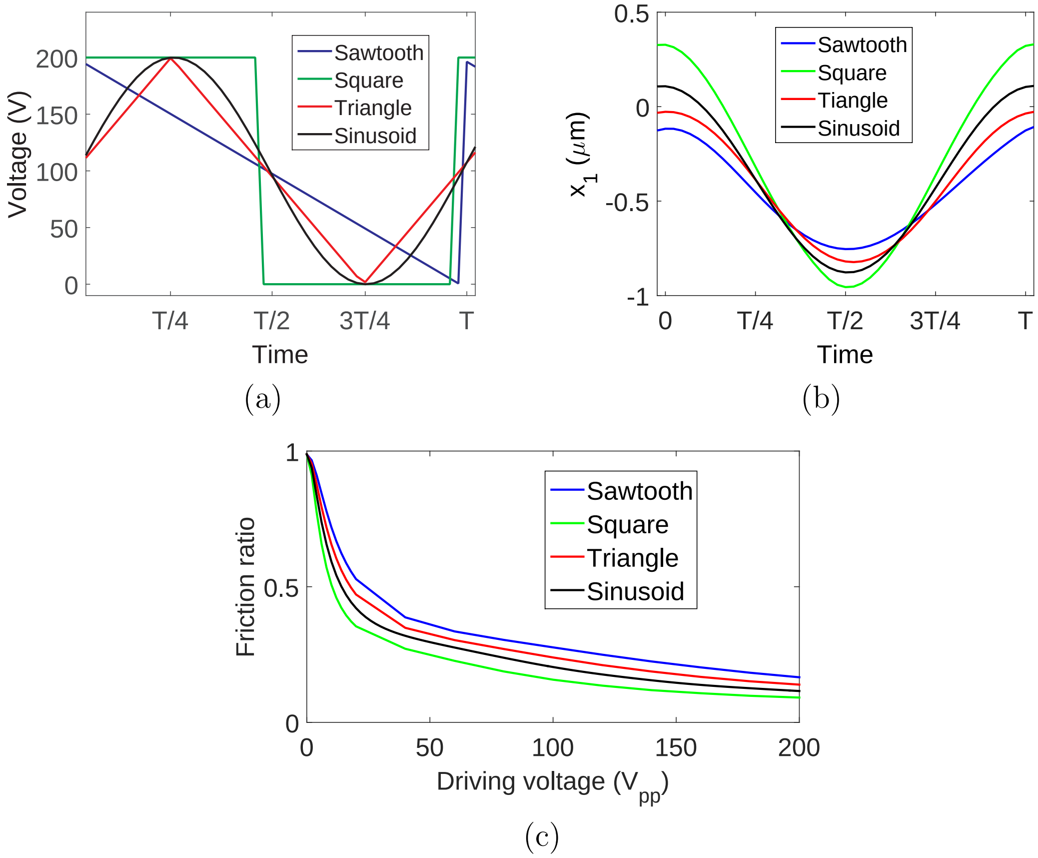

Figure 3.18: Parametric study of waveform: (a) waveforms; (b) steady-state displacement at x_1; (c) relationship between friction ratio and waveform.

3.3.6 Summary

A multi-scale dynamic model was proposed in a general form to represent ultrasonic lubrication systems. The model consists of components at different scale levels. A system dynamics model is employed to represent the structure of the lubrication system. An electromechanical model is utilized for the piezoelectric actuator. The contact between two surfaces, of which the friction is aimed to be reduced, is modeled by the "cube" model.

An electrical impedance measurement was taken to identify critical model parameters. The simulation results were validated by the experimental data taken from the modified tribometer tests. The simulations match well with the measurements, with all errors less than 10%.

The influence of driving voltage, macroscopic velocity, driving frequency, and signal waveform on friction reduction is studied. Higher driving voltage results in greater friction reduction. Higher macroscopic velocity leads to a lower reduction of friction. Driving the actuator at its resonant frequency is the most effective solution and requires the least amount of power. When driving at the same peak-to-peak voltages, all waveforms result in friction reduction, and can be ranked in the following order from highest to lowest: square, sinusoid, triangle, and sawtooth.

Chapter 4: Applications

4.1 Mapping of Friction Reduction and Power Consumption

4.1.1 Experimental Set-up

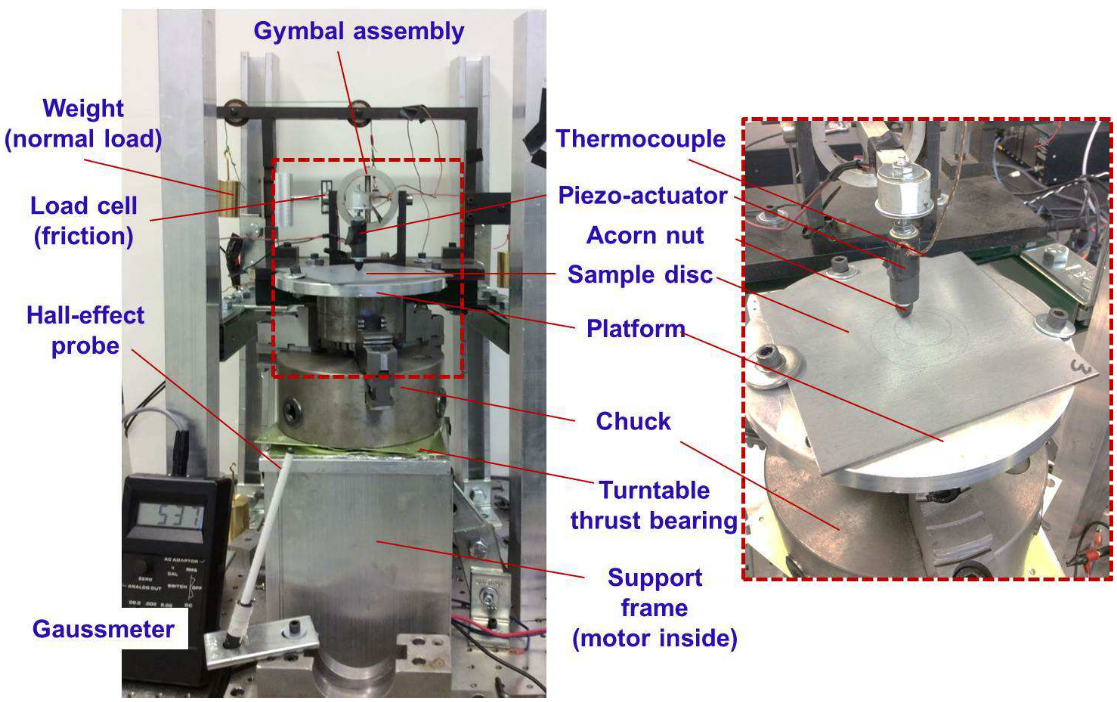

Figure 4.1: Experimental set-up.

The pin-on-disc tribometer was modified for this experiment, as shown in Fig. 4.22. The pin is placed in contact with a 4.8 in. by 4.8 in. square plate, which is clamped on

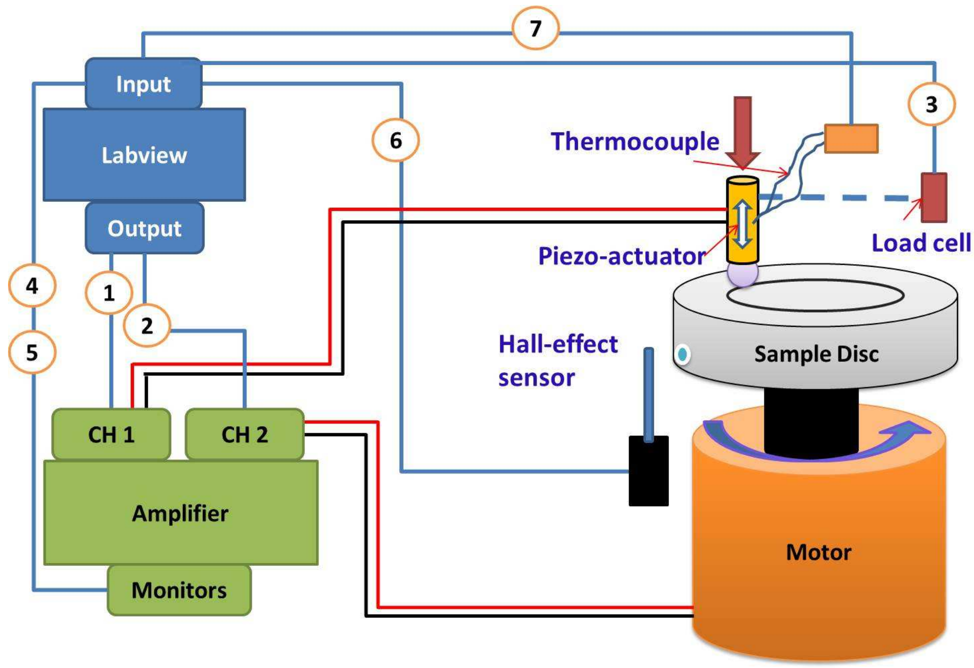

Figure 4.2: Connection diagram of the set-up.

a platform. The platform is held by a chuck and connected to a DC motor through a splined shaft. The weight of the plate, the platform, and the chuck is supported by a frame via a turntable thrust bearing. The DC motor with controllable speeds is used to rotate the plate. A Hall-effect probe is placed next to the turntable and connected to a gaussmeter. A magnet is fixed at the rim of the turntable and creates peaks in the gaussmeter readings when it gets closest to the Hall-effect probe during the rotation. Time-dependent gaussmeter readings provide information of the number of the rotations during the test and the duration of each rotation.

Connection diagram of the experimental set-up is shown in Fig. 4.2. A Labview system was adopted for signal generation and data acquisition. An electrical amplifier magnifies the signals from the Labview and provides them to the actuator and the motor. An AC voltage with adjustable magnitudes (signal 1) is applied to the piezo-actuator to generate vibrations with different amplitudes, while a DC voltage (signal 2) is applied to drive the motor and control the rotational velocity. The data that the Labview system collects includes voltage and current applied to the piezo-actuator (signals 4 and 5), friction force measured by the load cell (signal 3), temperature of the actuator measured by a thermocouple (signal 7), and Hall-effect gaussmeter readings (signal 6).

Table 4.1: Parameters used in the experiment.

Parameter	Value
Normal load (N)	3, 4, 5, 6, 7, 8, 9
Nominal contact area (mm^2)	0.126
Nominal normal stress (MPa)	23, 32, 40, 48, 55, 63, 70
Rotational diameter (mm)	28, 48.3
Linear velocity (mm/s)	50-200
Peak-to-peak voltage (V)	0, 5.1, 10.3, 15.5, 20.7, 25.9
Actuator capacitance (nF)	360
Power consumed by the actuator (W)	0, 0.21, 0.84, 1.9, 3.39, 5.31
Nominal US amplitude (μm)	0, 0.46, 0.92, 1.38, 1.85, 2.31
US frequency (kHz)	22
Pin material	Uncoated steel
Disc materials	Uncoated and powder-coated steel

Two groups of tests were conducting using uncoated steel plates and powder coated plates, respectively. Parameters used in this experiment are listed in Table 4.1. Normal load is set to be in the range of 3 N to 9 N with increments of 1 N. Nominal contact area is 0.126 mm^2 which is calculated from the width of the wear grooves. Correspondingly, nominal normal stresses are between 23 MPa to 70 MPa. Rotational velocity is controlled by the voltage that drives the motor. The voltage remains constant during each test and varies from test to test to reach various rotational velocities. Two rotational diameters, 1.1 in. (28 mm) and 1.9 in. (48.3 mm), are also adopted for different linear velocities. As a result, tests with six rotational velocities are conducted with each rotational diameter. Seven plates are prepared with each of them assigned for one normal load. Therefore, each wear scar can be created by the same amount of interaction between the pin and the plate. Piezo-actuator is driven at five levels of peak-to-peak voltages at 22 kHz, which is the resonance frequency of the actuator. The average power that drives the actuator can be calculated using Eq. 1.9. The corresponding power consumed by the actuator is between 0.21 W and 5.31 W, as listed in Table 4.1.

4.1.2 Experimental Data

Representative results

The measurements of an example test are shown in Fig. 4.3. The test was conducted under 5 N of normal force and the rotational diameter was 1.1 in. Left figure plots the measured friction force against the time, while the right plot is the time-dependent voltage that drives the actuator (blue) and the reading from the gaussmeter (green). The test lasts for approximately 32.5 s and the motor starts rotating at 0.5 s. During the first 12 s of the test, the piezo-actuator is turned off so that the intrinsic friction can be measured. Ultrasonic vibrations are applied starting at 12.5 s, and five levels of voltages are employed, with 4 s duration for each. Average time intervals between two peaks is 1.34 s, therefore, linear velocity in this measurement is 65.5 mm/s.

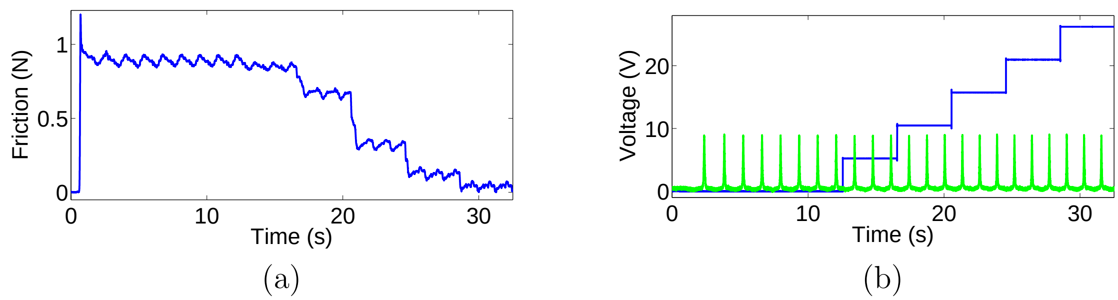

Figure 4.3: Representative results: (a) friction force; (b) voltage (blue) and guassmeter reading (green).

Table 4.2: Representative results of friction and reduction percentage.

Voltage (V_{pp})	Friction (N)	Reduction (%)
0	0.89±0.04	N/A
5.1	0.85±0.03	2.60±1.49
10.3	0.67±0.04	25.36±0.83
15.5	0.32±0.04	66.94±2.45
20.7	0.12±0.04	90.49±3.47
25.9	0.04±0.04	100±3.87

As shown in the friction measurement, the intrinsic friction overcomes the static friction as the rotation initiates, which is around 1.2 N, to become dynamic friction. There exists fluctuation in the dynamic friction, which is due to the wobbling of the plate during the rotation. The intrinsic friction is 0.89±0.04 N at steady state. Friction is reduced when ultrasonic vibrations are applied, and remains at relatively constant levels despite the fluctuation. Friction drops 0.3 N with the initial application of 5.1 V voltage to the actuator. As the voltage increases, friction continues to decrease to greater extents. Friction reduction percentage has been defined previously (Eq. 2.1). Table 4.2 lists the representative results of friction forces and reduction percentages. At the highest voltage (25.9 V), friction force is reduced to a very low level. It was observed in Section 2.1 that, in some cases, the degree of friction reduction surpassed 100%. This was attributed to a "motor effect" created by the pizoelectrically induced vibrations [32]. In this study, friction reduction of 100% (and higher) were measured. Although it is not physically possible for the friction force to be negative, an experimental artifact is created when the string that connects the gymbal arm to the load cell is not taut during the measurements. This happens when the friction force is very low. It is then concluded that the amount of friction reduction at low speeds can be close to 100%.

Friction reduction vs. linear velocity

Tests were conducted following the format of the example test with various normal loads and linear velocities, as listed in Table 4.1. The reduction percentages are plotted against linear velocity in Fig. 4.4 and 4.5. Five plots represent five voltages applied, and measured data under various loads are denoted by different markers (mean value) and error bars (standard deviation) in each plot. At the lowest voltage (5.1 V), ultrasonic vibrations reduce friction by less than 10% for all linear velocities (Fig. 4.4 (a)). As voltage increases to (10.3 V), friction reduction is improved, however, more reduction is achieved at lower velocities than higher velocities (Fig. 4.4 (b)). A clear trend can be observed that higher velocities lead to lower friction reduction. At even higher voltages (15.5 V to 25.9 V), friction reduction continues to improve, and very low levels of friction are achieved at low velocities (Fig. 4.4 (c)-(e)). Although lower velocity results in higher friction reduction, the relationship between reduction

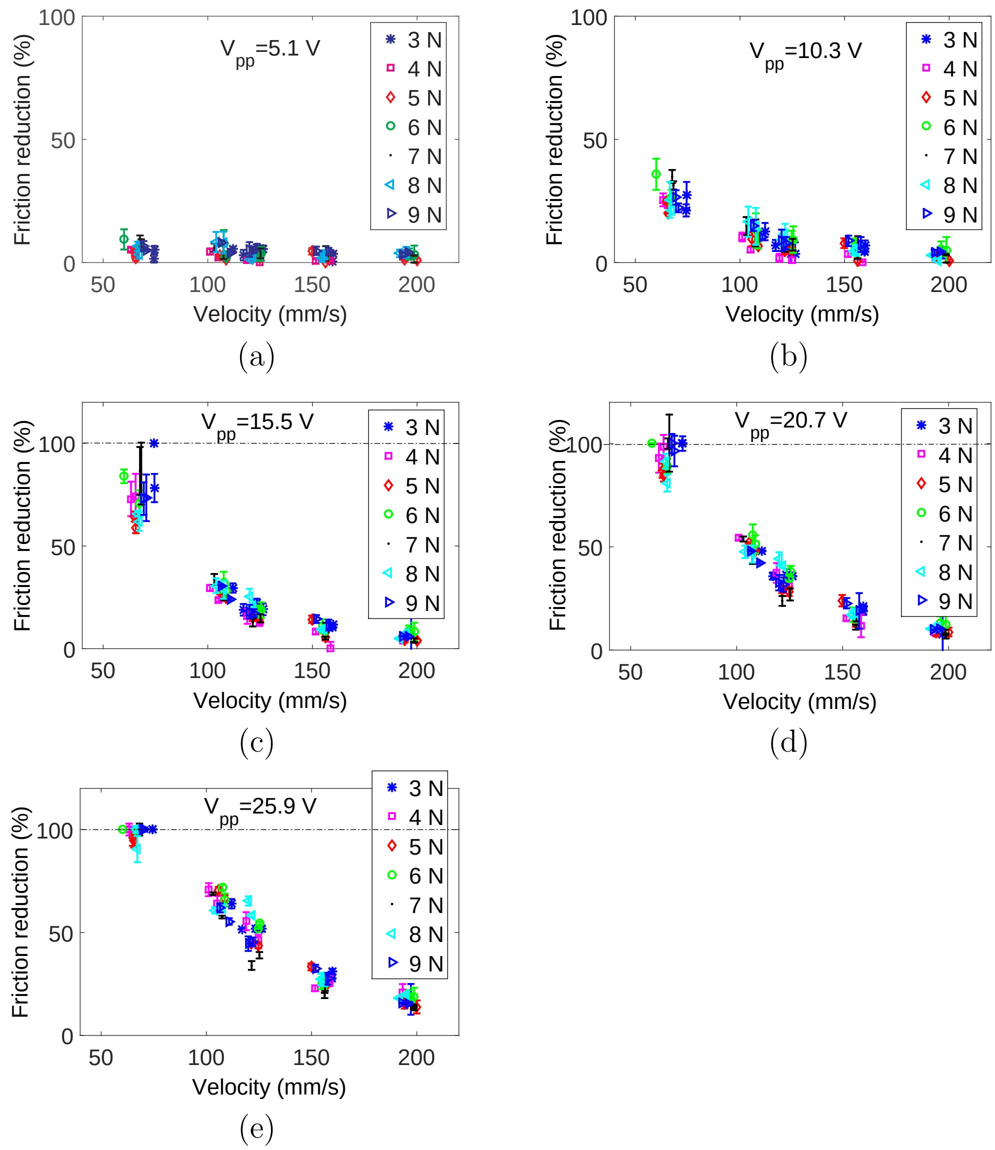

Figure 4.4: Relationship between friction reduction and linear velocity for five applied voltages (uncoated steel).

and velocity is not linear. Friction reduction drops faster at higher velocities. Similar plots on coated plates are plotted in Fig. 4.5.

A comparison of the reduction-velocity curves between coated and uncoated steel plates is shown in Fig. 4.6, in which blue markers denote the data points from the

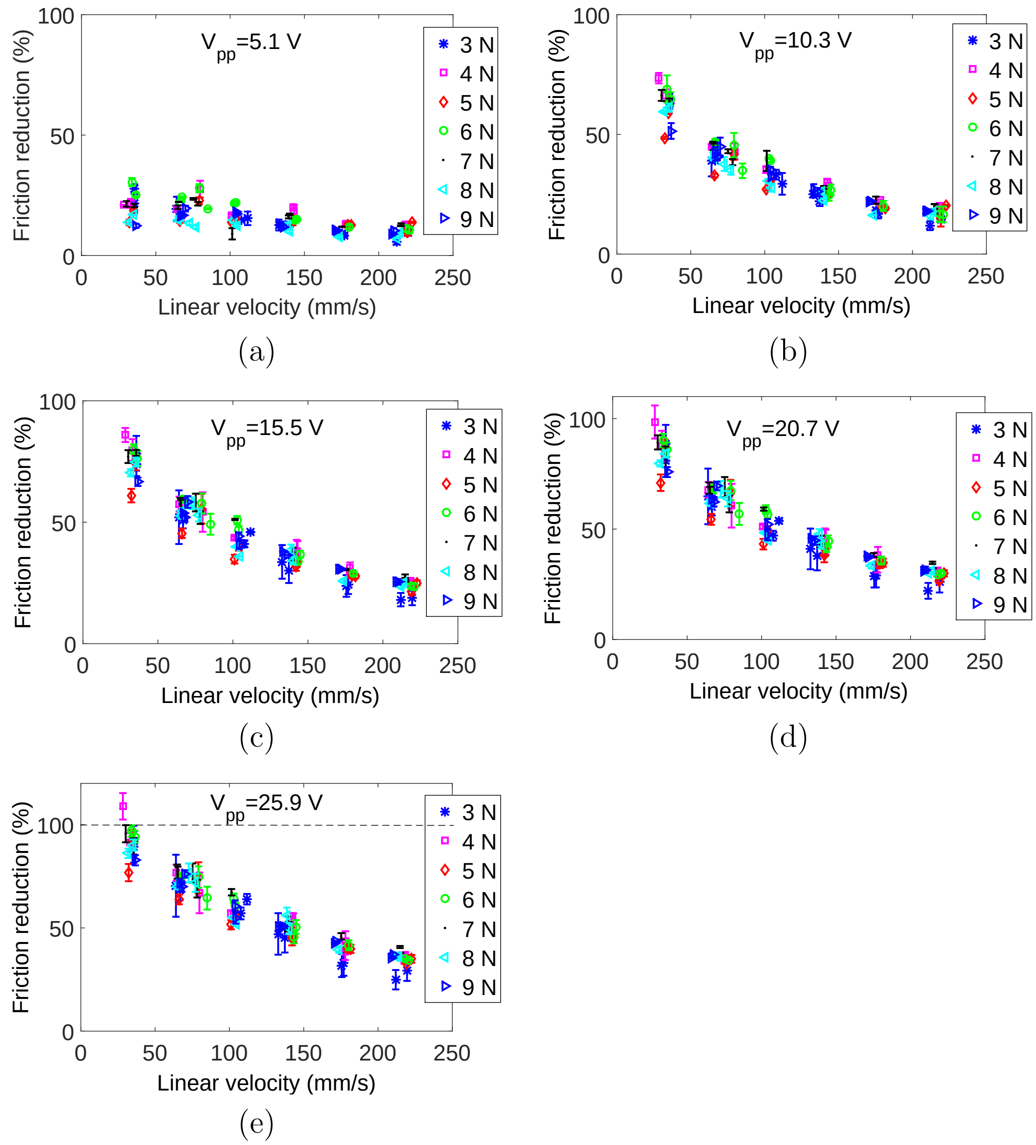

Figure 4.5: Relationship between friction reduction and linear velocity for five applied voltages (coated steel).

uncoated plates while red markers the coated. At low voltages, friction reduction is higher for all velocity cases for coated steel. At higher voltages, the friction reduction on the uncoated plates reaches 100% at a higher velocity than coated plates but drops to a lower level faster than coated plates as the velocities increase.

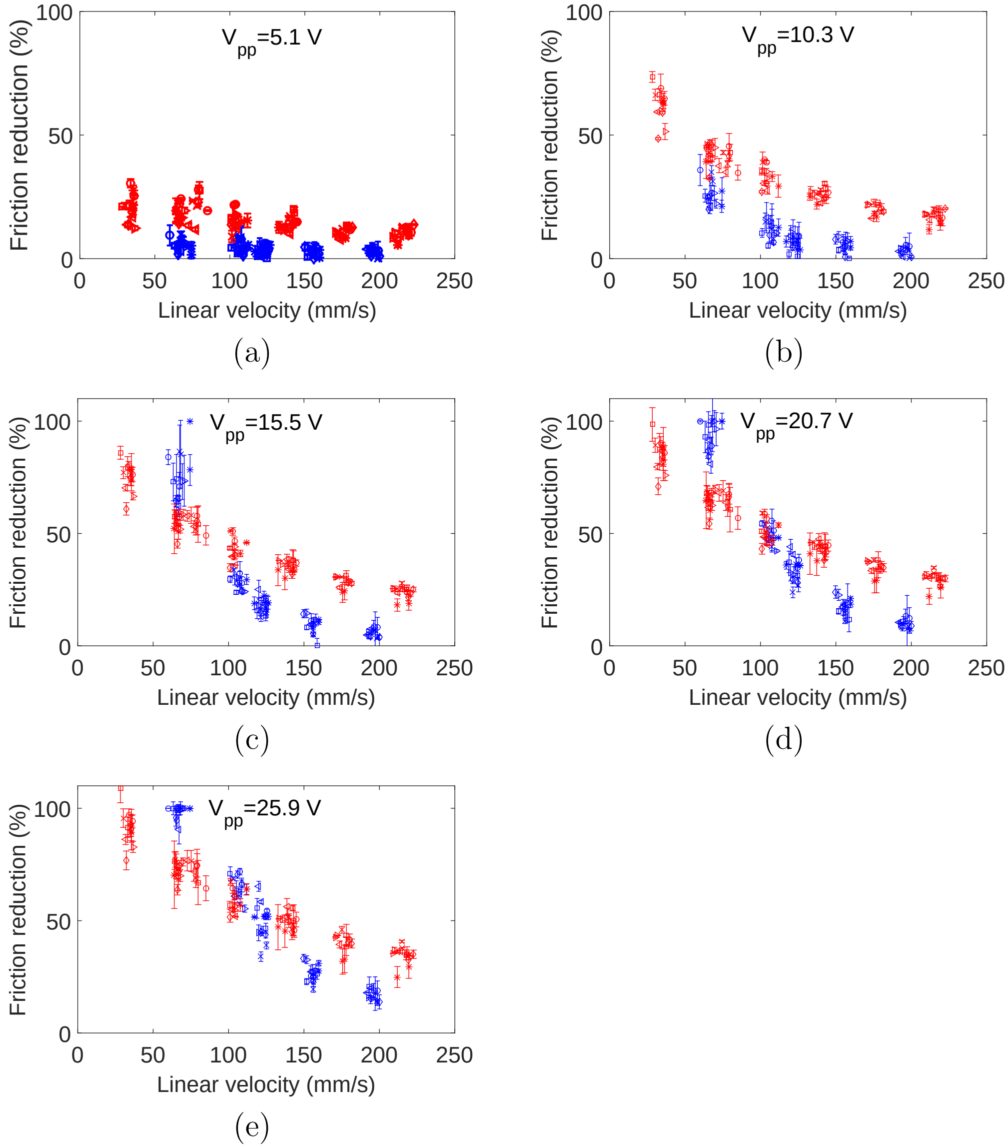

Figure 4.6: Comparison of reduction-velocity curves between coated and uncoated plates: blue–uncoated; red–coated.

Friction reduction vs. normal force

The relationships between friction reduction and normal force on uncoated and coated plates are plotted in Fig. 4.7 and 4.8, respectively. Each plot shows the

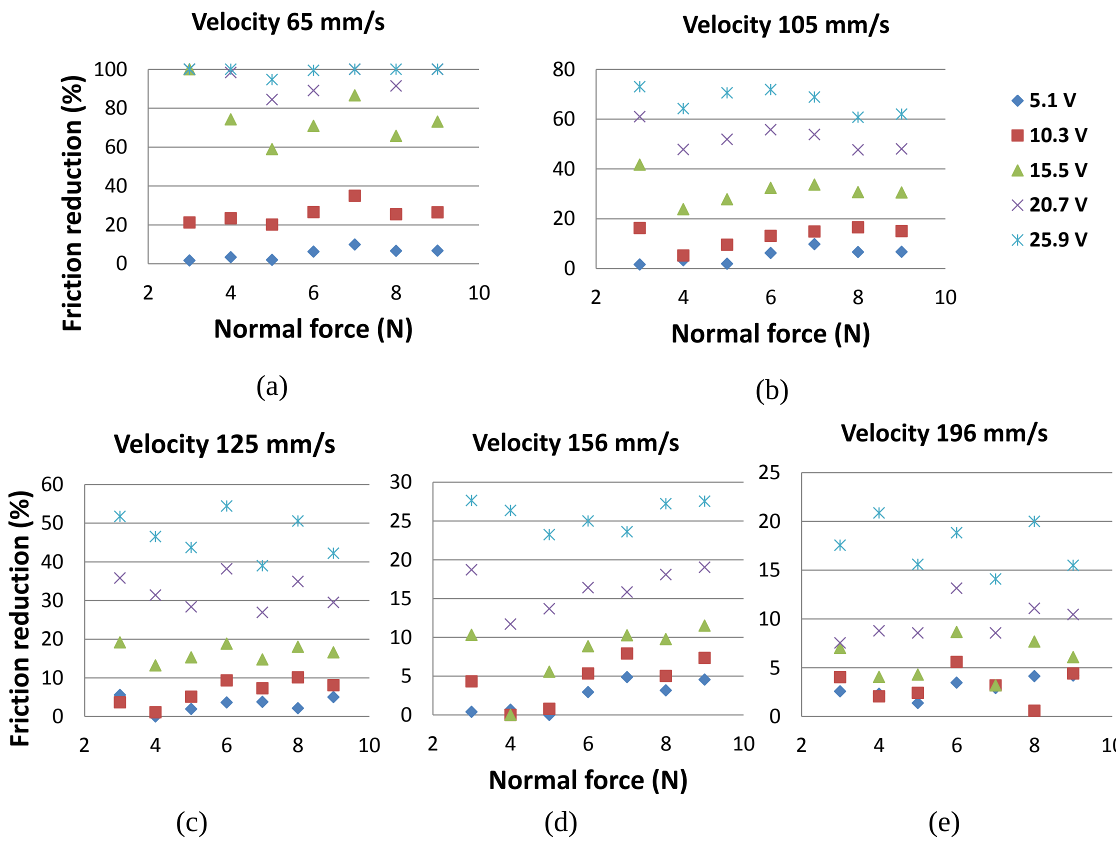

Figure 4.7: Relationship between friction reduction and normal load at five linear velocities (uncoated steel).

data from one linear velocity, and five levels of voltages are represented by different markers.

The relationship between friction reduction and normal force appears relatively flat for most tests. However, there are variations in the curves, with friction reduction peaking at around 6 N or 7 N. This can be explained using the system dynamics of the modified tribometer. As described previously, different weights are connected to the gymbal assembly to apply normal forces. The arm of the gymbal assembly vibrates when ultrasonic vibrations are applied, which affects the total vibrations at

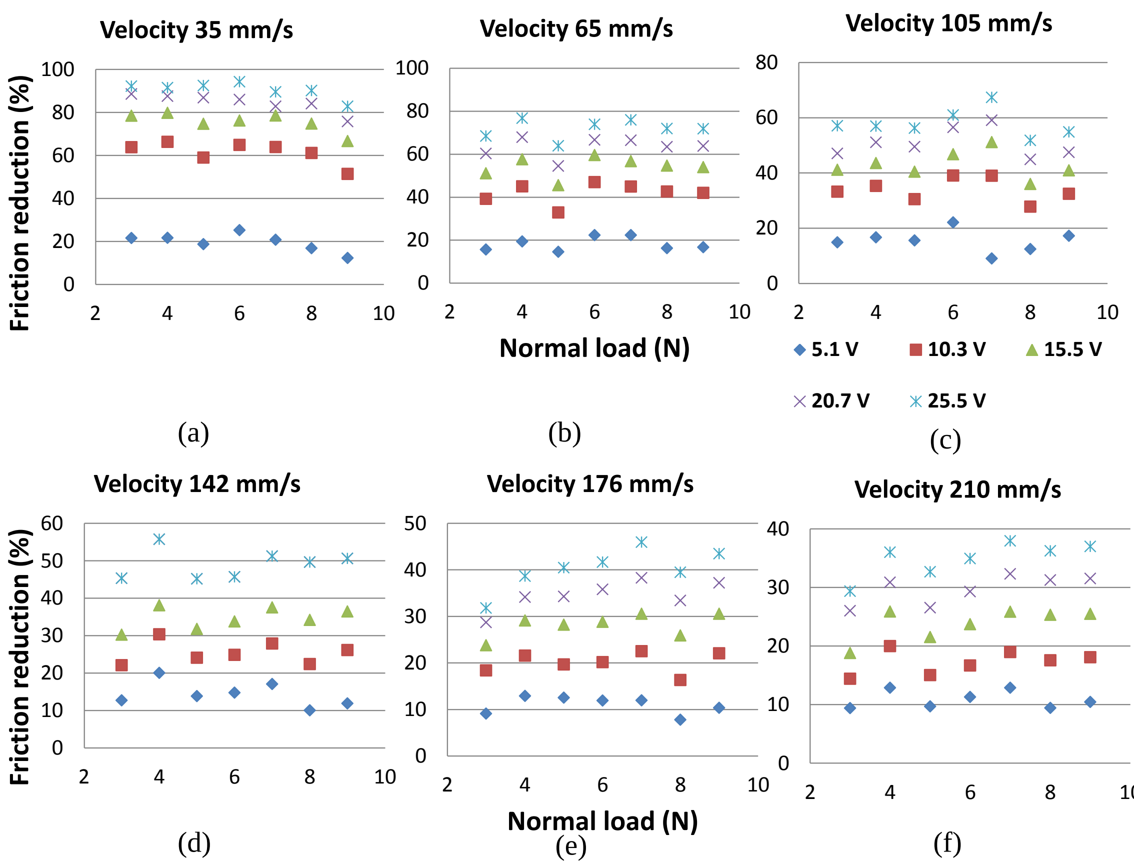

Figure 4.8: Relationship between friction reduction and normal load at six linear velocities (coated steel).

the interface. The vibrational amplitude of gymbal arm changes as different weights (masses) are connected to the gymbal arm.

Higher amplitude of vibration is created at the gymbal arm when weights for 6 N and 7 N normal forces are connected. Although this type of vibration has much lower frequency (around 100 Hz) than the ultrasonic vibrations, it creates additional vertical movement between the pin and the plate, which leads to extra friction reduction. In this experiment, the extra friction reduction is less than 10%, which is not significant. However, this finding is meaningful to ultrasonic lubrication systems design. By carefully choosing the mass and stiffness of the system to match the resonance, the extra friction reduction can be achieved at much higher levels.

In summary, normal stress/load has little influence on ultrasonic friction reduction. However, the structure of the ultrasonic lubrication system may result in extra friction reduction.

Contour plots

Contour plots of friction reduction, linear velocity and normal stress are created by interpolating raw experimental data, shown in Fig. 4.10. At low voltage, there is no clear dependence of friction reduction (Fig. 4.10 (a)). As voltage increases, the dominating influence of friction reduction is from linear velocity, although normal stress creates variations (Fig. 4.10 (b)-(e)). From a design point of view, if an ultrasonic lubrication system is driven at a certain voltage, there exists an optimum friction reduction in terms of the combination of stress and velocity.

Contour plots of friction reduction, power consumption, and linear velocity with various normal stresses are created, as shown in Fig. 4.11 and 4.12. The plots have similar shapes: greater friction reduction takes place at the lowest velocity when power is higher; lower friction reduction is either at higher velocity or with lower power. Neither of those two parameters are dominating the effect of friction reduction.

Same amount of friction reduction can be achieved at a high velocity with higher power or at a low velocity with lower power. To achieve better friction reduction, a trade-off exists between lowering the relative velocity between contacting surfaces and increasing the driving power of the ultrasonic lubrication component. At low

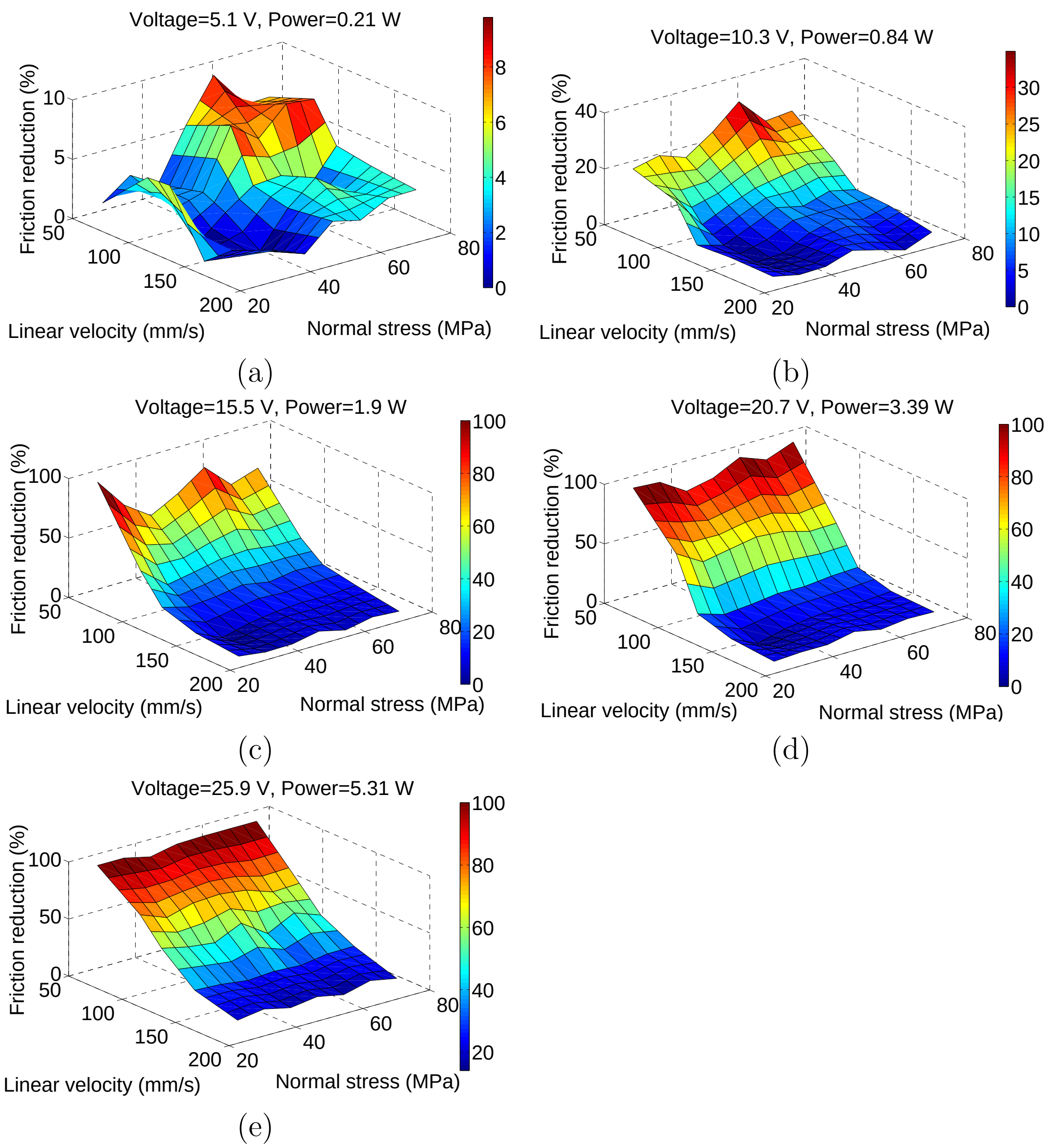

Figure 4.9: Contour plots of friction reduction, linear velocity, and normal stress for five power consumption levels (uncoated steel).

velocities, there is an optimum power level where friction can be reduced to its minimum and remain at a low level. In that case, the extra power consumed does not create additional friction reduction.

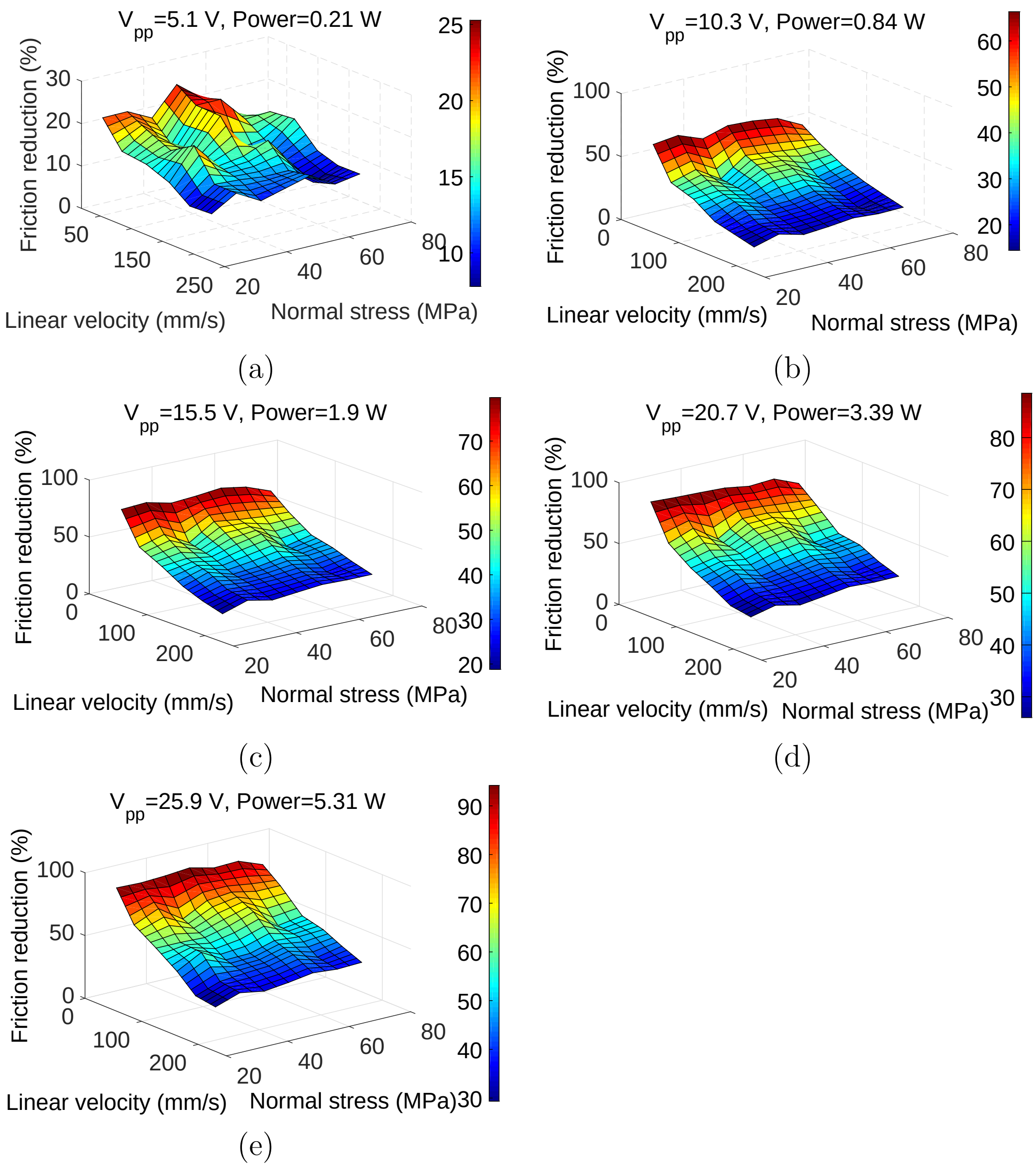

Figure 4.10: Contour plots of friction reduction, linear velocity, and normal stress for five power consumption levels (coated steel).

Higher driving power can be achieved either by increasing the driving voltage to achieve a higher vibratory amplitude, or utilizing a different transducer with a higher resonance frequency, driven at resonance. In either approach, the vibratory velocity

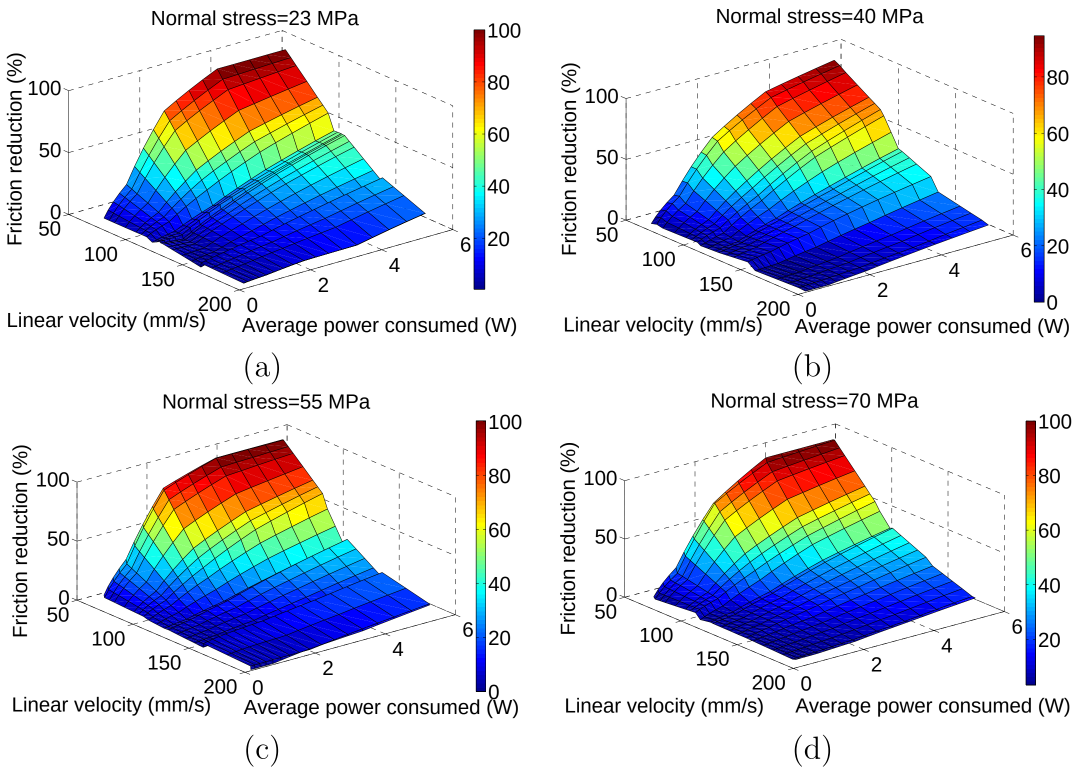

Figure 4.11: Contour plots of friction reduction, linear velocity, and power consumption for four normal stress levels (uncoated steel).

of the transducer is essentially increased, which results in a lower velocity ratio. As stated previously, a lower velocity ratio leads to a lower friction ratio, hence, more friction reduction. It is emphasized that there are limits to how much additional friction reduction is achieved by increasing driving power. As demonstrated previously in modeling, the benefit of increasing power eventually saturates as the driving voltage continues to increase. Another practical limit is that the heat generated by driving a piezoelectric transducer at high power could negatively effect its functionality.

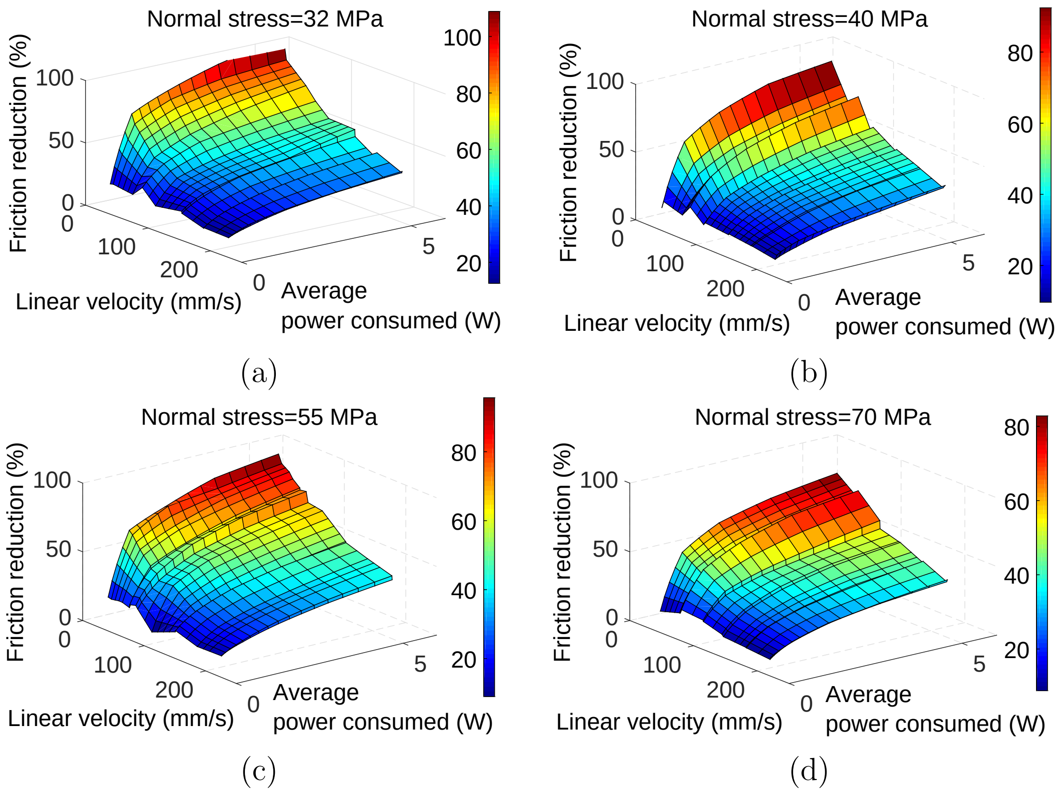

Figure 4.12: Contour plots of friction reduction, linear velocity, and power consumption for four normal stress levels (uncoated steel).

Power, energy, and efficiency metrics

An efficiency coefficient is proposed to utilize the information derived from the contour plots, which is defined as

$$\eta = \frac{(F_{t0} - F_{t1}) v_{rel} A_n}{F_N P_a}, \tag{4.1}$$

where v_{rel} is the relative linear velocity, A_n is the nominal contact area, F_N is the normal force, P_a is the average power consumed by the actuator, which can be calculated from Eq. (1.9). Here, F_N/A_n represents the normal stress, and the product of friction and velocity is frictional energy. Therefore, the efficiency parameter can be

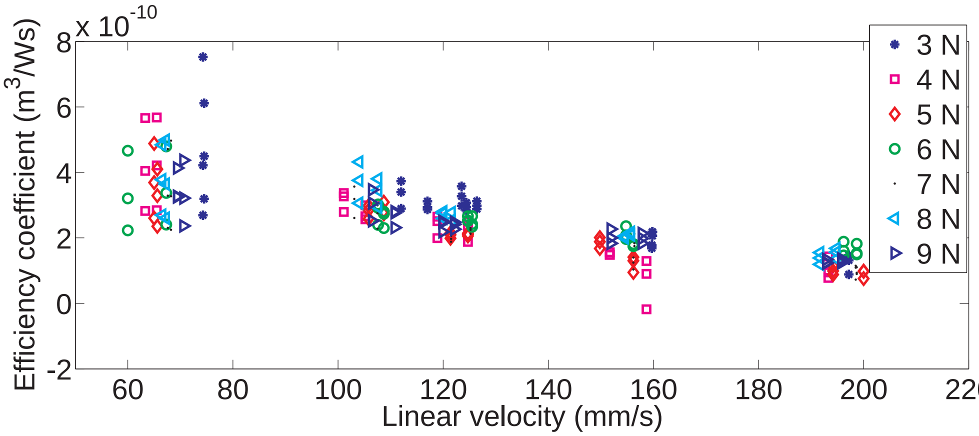

Figure 4.13: Relationship between efficiency coefficient and linear velocity.

interpreted as the amount of frictional energy saved with unit normal stress and unit power consumption.

In this study, normal loads were relatively small although the stress was achieved as high as 70 MPa. In real-world ultrasonic systems, the same level of stress might be reached, but with much higher forces and larger contact areas. It is assumed here that the efficiency coefficient of a certain stress remains its value as long as the stress is the same, even if both normal load and nominal contact area are at higher levels.

Figure 4.13 plots the values of all the efficiency coefficients against linear velocity. Each marker represents the value derived from one measurement regardless of the conditions of normal stress or linear velocity. It is evident that markers concentrate at higher velocities and scatter at low velocity. The reason is that, at low velocities, there exists optimum power consumption. The extra power applied to the actuator does not result in any additional friction reduction, which leads to a drop in efficiency. Those markers should concentrate if the power used for calculation was at its optimum. Nevertheless, a linear relationship can be found between the efficiency coefficient and the velocity. This relationship can be expressed as

$$\eta = av_{rel} + b, \tag{4.2}$$

where a and b are the constants for the fitted line, which are equal to -2.93 and 0.672, respectively (v_{rel} in m/s). Therefore, the power required for reducing friction from F_{t0} to F_{t1} can be calculated as

$$P_a = \frac{(F_{t0} - F_{t1})v_{rel}A_n}{F_N(av_{rel} + b)}. \tag{4.3}$$

Similarly, the new (reduced) friction can be calculated as

$$F_{t0} = F_{t1} - \frac{F_N(av_{rel} + b)P_a}{v_{rel}A_n}. \tag{4.4}$$

The efficiency coefficient and equations (4.3) and (4.4) can be employed to realize ultrasonic friction control, which is to modulate friction between high and low by driving the actuator with different levels of power. It should be noted that the values of the metric and the constants of the equations are only measured for the experimental set-up in this study. Each ultrasonic lubrication system has its unique design and the metric values should be calibrated for each system. This is only one example of how metrics can be utilized.

4.1.3 Wear Observation

Wear takes place in concert with friction between two surfaces that slide relative to each other. In this experiment, wear is identified as mainly adhesive, when pin and plates were both made from uncoated steel. The wear between the uncoated pin and coated steel is mainly abrasive due to the fact that the powder coating is softer than the pin. Micro-indentation hardness tests show that the Vicker hardness

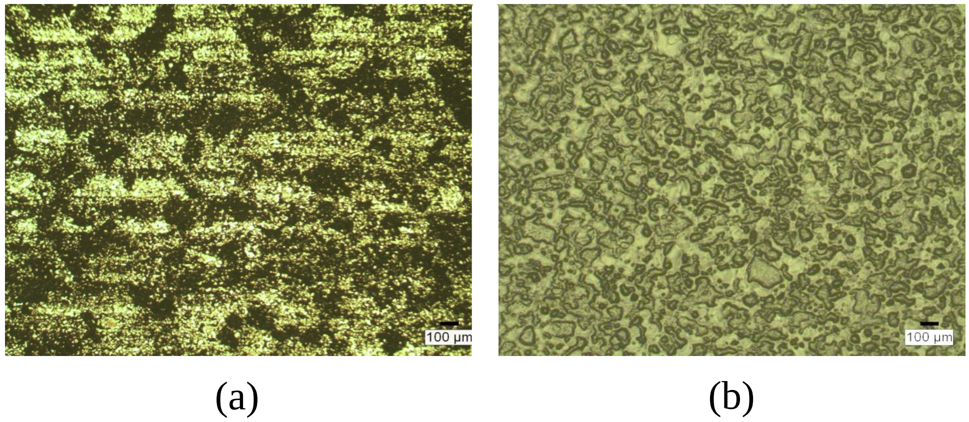

Figure 4.14: Microscopy of unworn surfaces (50X): (a) uncoated; (b) coated.

of the uncoated steel and coating are 274 and 39 HV (Vicker hardness at 25 g load), respectively. The coating thickness is 0.00235±0.00015 in.

The focus of this study was not to quantify wear reduction, but to investigate the differences between the wear on coated and uncoated steel plates. Measurements were conducted using optical profilometry and microscopy.

Unworn surfaces

First, unworn surfaces were scanned using a microscope, as shown in Fig. 4.14. The patterns of the uncoated and coated steel plates are very different. The surface of uncoated steel shows some horizontal marks left from the forming process, while the powder-coated plates show some roundish patterns on a much smaller scales. Profilometry images of the two surfaces are shown in Fig. 4.15. It is evident that the uncoated steel has asperities much smaller in size. Contrary to expectation, the uncoated surface has a slightly smaller roughness than the coated surface (1.69 μm

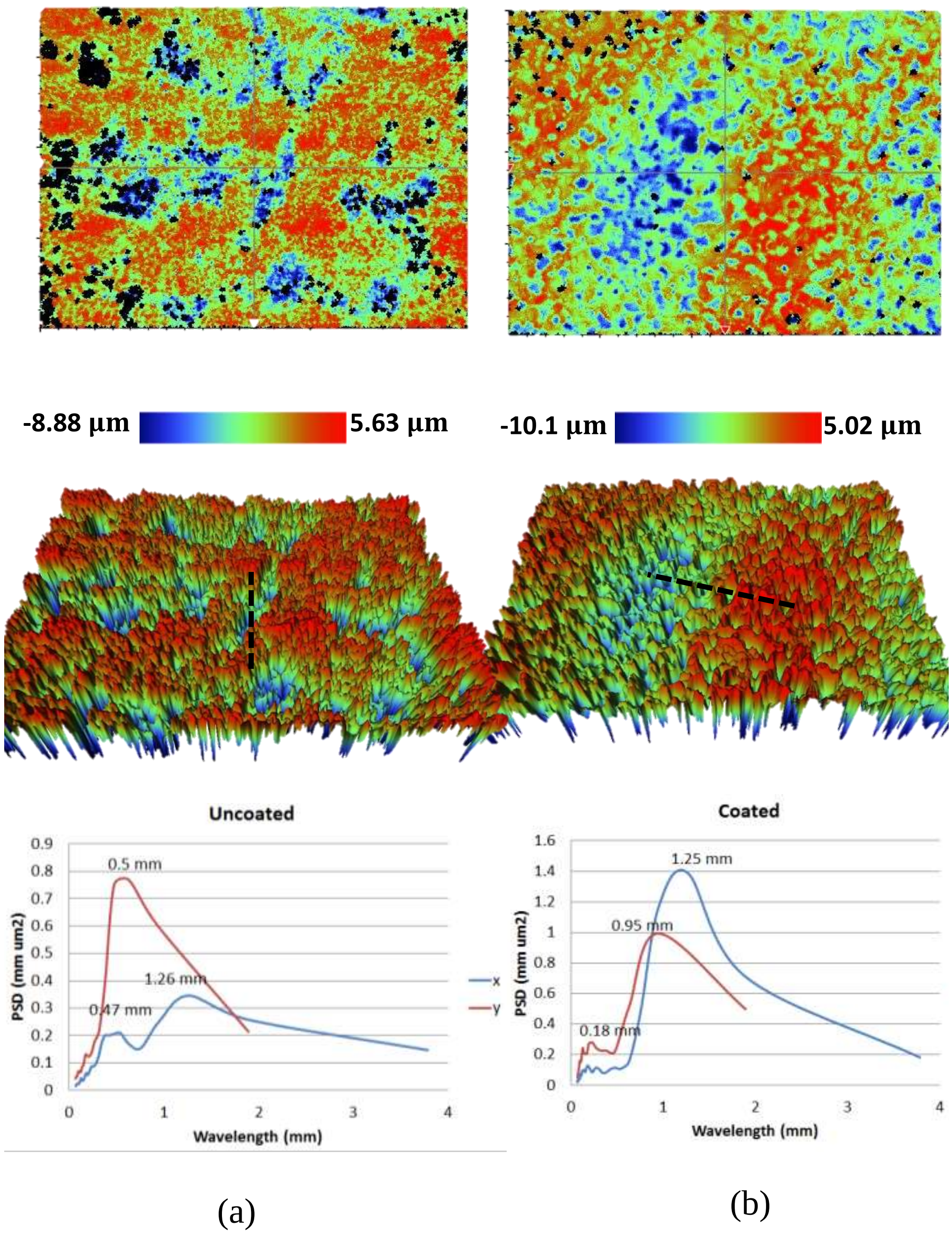

Figure 4.15: Profilometry of unworn surfaces: (a) uncoated; (b) coated.

versus 1.73 μm), despite the fact that intrinsic friction on uncoated steel is much higher than that on coated steel (0.17–0.2 N versus 0.67–0.1 N).

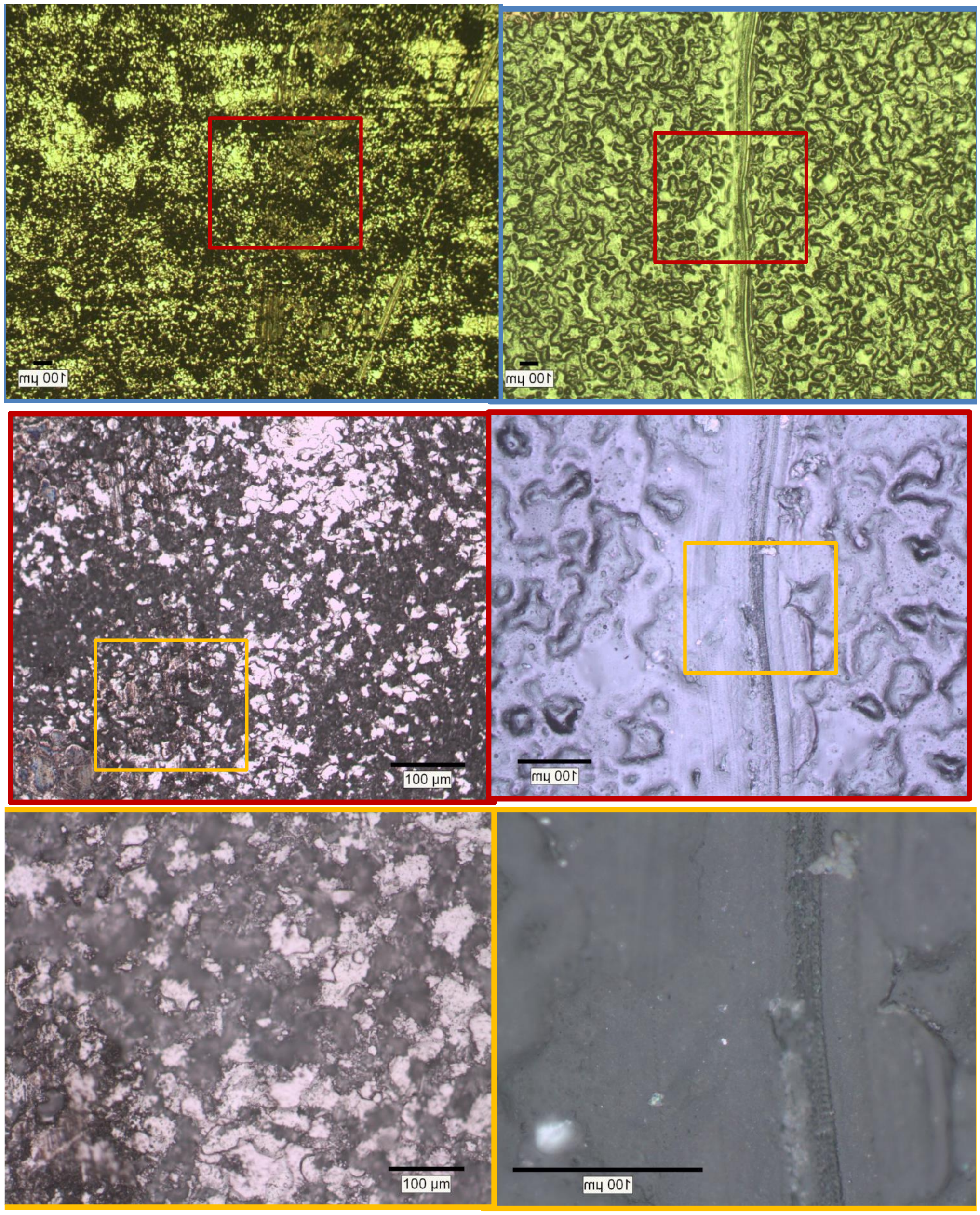

(a) (b)

Figure 4.16: Microscopy of wear grooves (50X, 200X, and 500X row 1 to 3): (a) uncoated; (b) coated.

By conducting FFT scans of the surface heights, the waviness of the two surfaces can be obtained (last row of Fig. 4.15). For the uncoated surfaces, the main waviness is in y-direction, which is equal to the distance between the horizontal marks. For the coated surfaces, the waviness occurs at two levels: one is 0.18 mm in both directions, which equals the size of the roundish pattern observed in Fig. 4.14 (b); the other is the distance between the red and blue areas in profilometry images (1.25 mm in x-direction and 0.95 mm in y-direction).

Wear grooves

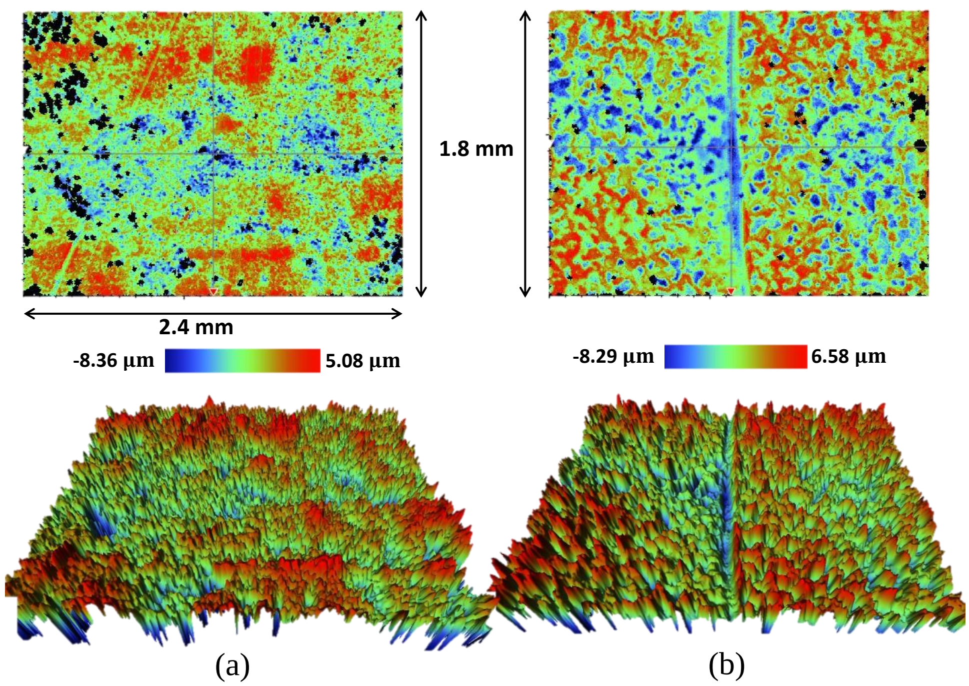

Figure 4.17: Photos and microscope images of wear grooves on the plates with different normal loads.

As described previously, each plate was assigned for tests conducted under one loading condition. Two wear scars were created on each plate, with diameters of

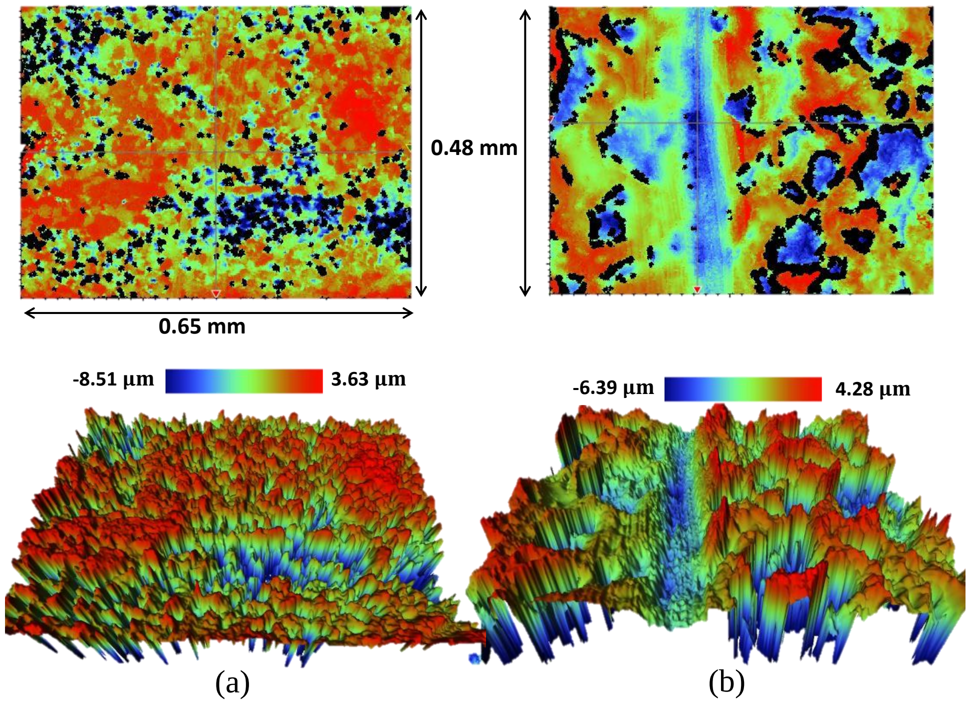

Figure 4.18: Photos and microscope images of wear grooves on the plates with different normal loads.

1.1 inch and 1.9 inches, respectively. Each scar was created by the same amount of interaction between the pin and the plate. Therefore, the only varying parameter to be taken into consideration is normal stress. Higher stress results in more severe surface wear for both plates. The wear grooves under the normal load of 7 N were studied for both coated and uncoated plates.

Microscopy images at different resolution levels are shown in Fig. 4.16. There is an evident wear groove observed on the coated plate, while there is only a barely visible mark on the uncoated plate. Profilometry images are shown in Fig. 4.17 to 4.19. Clear wear groove can be observed on the coated steel. The maximum depth is approximately 5 μm. On the uncoated plate, a change of the shapes of the asperities

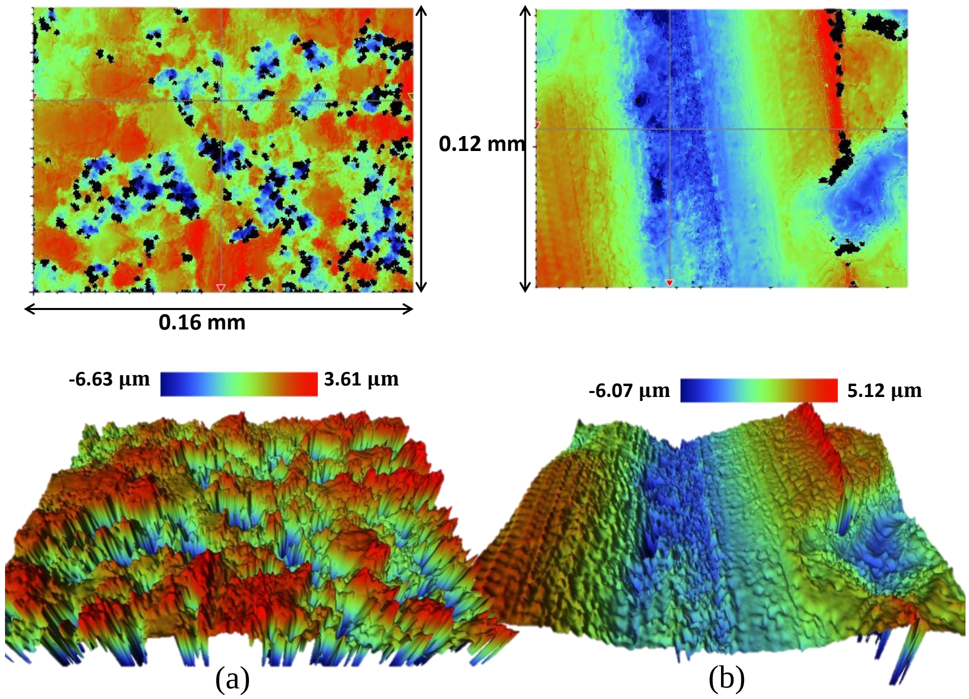

Figure 4.19: Photos and microscope images of wear grooves on the plates with different normal loads.

can be observed at the spots where wear occurred, but no evident volume loss can be observed.

4.1.4 Model Prediction

The multi-scale model was used to calculate friction reduction. Contour plots of the relationship between friction reduction, linear velocity, and power consumption are created using data from the model calculations, as shown in Fig. 4.20. The model prediction used parameters from tests on uncoated steel plates. It successfully captured the trends that have been observed in the experimental data: higher power consumption and lower velocity result in higher friction reduction.

A comparison between experimental data and model simulation was conducted. The reduction-velocity relationship is plotted in Fig. 4.21, where the star markers represent the data points from simulations and squares stand for the experimental data. Different colors denote different normal stresses. The model is able to predict the experimental data at low velocities at all voltages. However, there exist discrepancies at higher velocities.

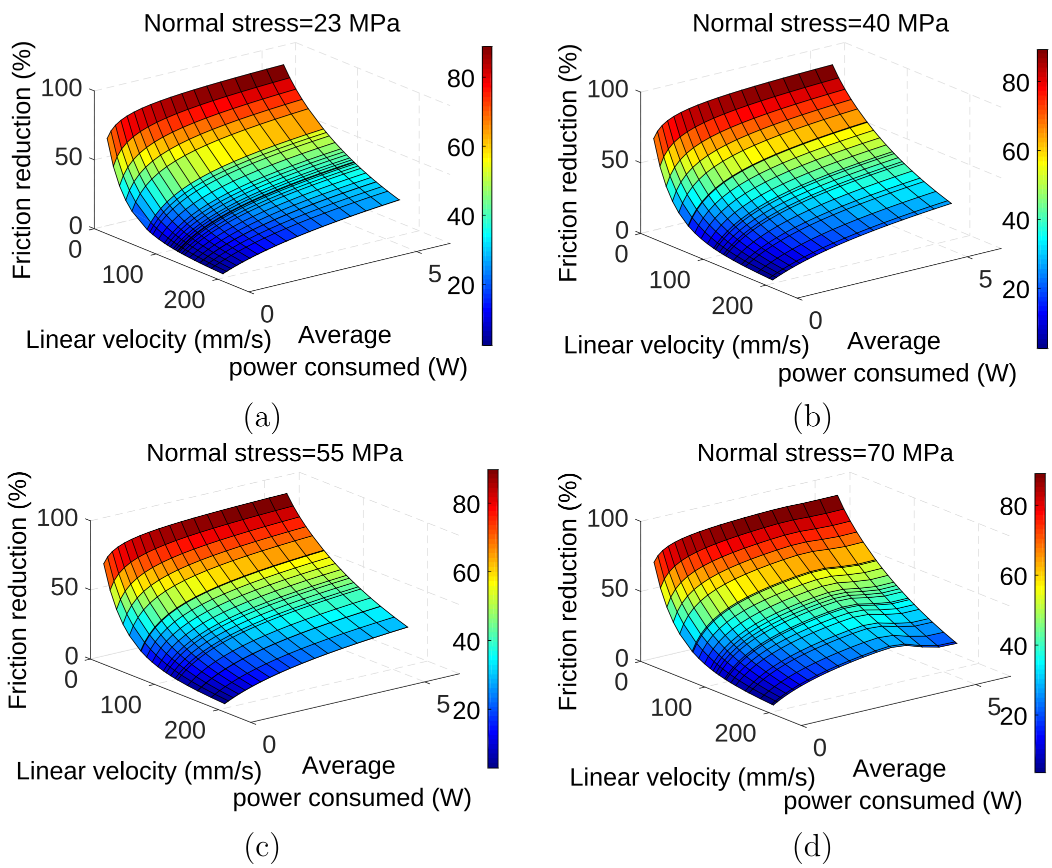

Figure 4.20: Model prediction on the relationship between friction reduction, linear velocity, and power consumption for four normal stress levels (uncoated steel).

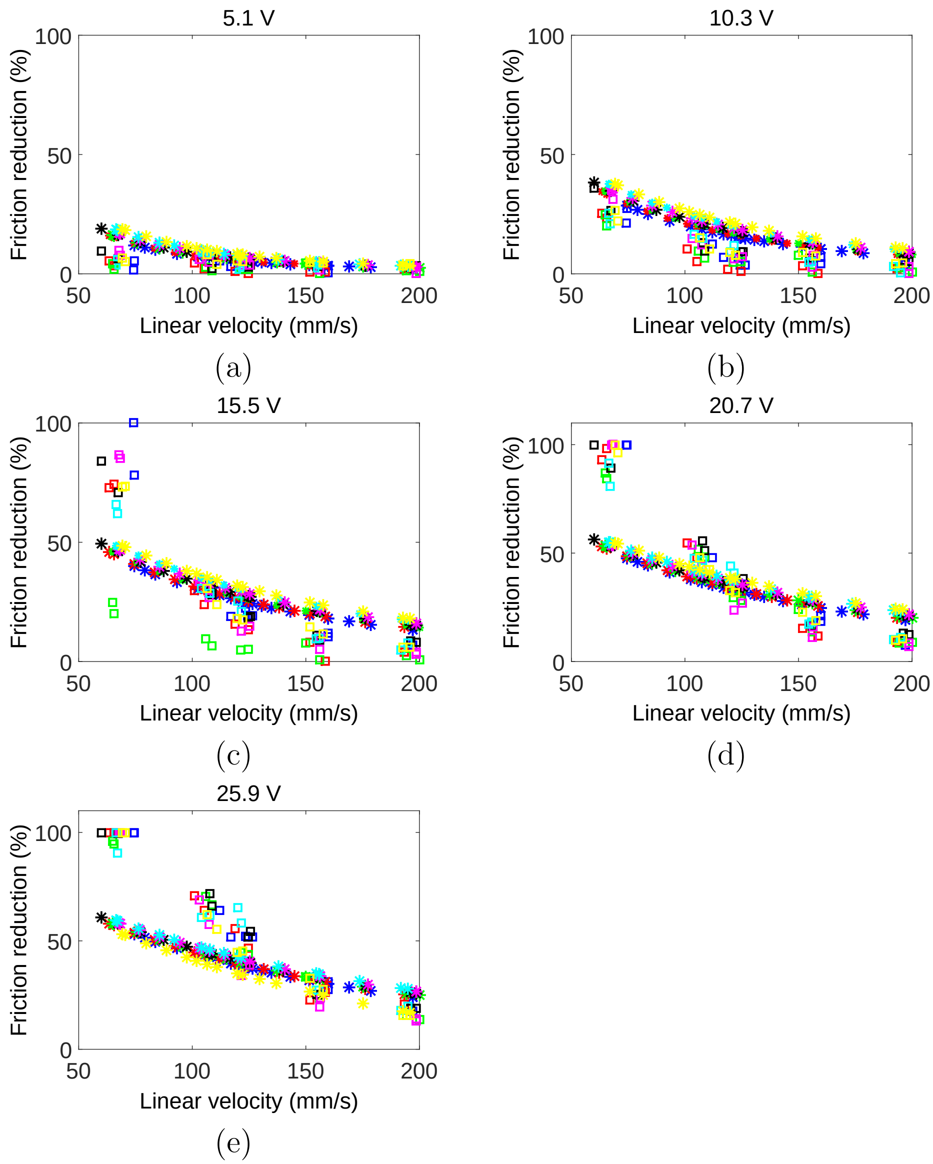

Figure 4.21: Comparison of reduction-velocity relationship between experimental data and model simulation (uncoated steel).

4.1.5 Summary

This section reports on the experimental study between friction reduction and power consumption under various normal stresses and linear velocities. Each test contains measurements of intrinsic friction and friction forces with ultrasonic vibrations applied. Five levels of voltages were applied to the piezoelectric actuator while the normal stress and linear velocity remain unchanged throughout each test. Uncoated and powder-coated steel plates were utilized for tests. Experimental data confirm that friction reduction increases as the power increases, but decreases when the linear velocity increases. The magnitude of normal load/stress does not change the effectiveness of ultrasonic lubrication. Contour maps were created to show the relationship between friction reduction, power consumption, and linear velocity. Wear on both plates was characterized. There was more evident wear created on coated plates than uncoated ones, due to the difference in hardness between the coating and steel.

4.2 Comparison between Lubrication Methods

4.2.1 Introduction

Traditional lubrication methods have been studied and applied extensively [2]. Lubricants include liquid and solid types. It is of great interest to investigate whether ultrasonic lubrication is still effective when traditional lubricants are present.

4.2.2 Experimental Set-up

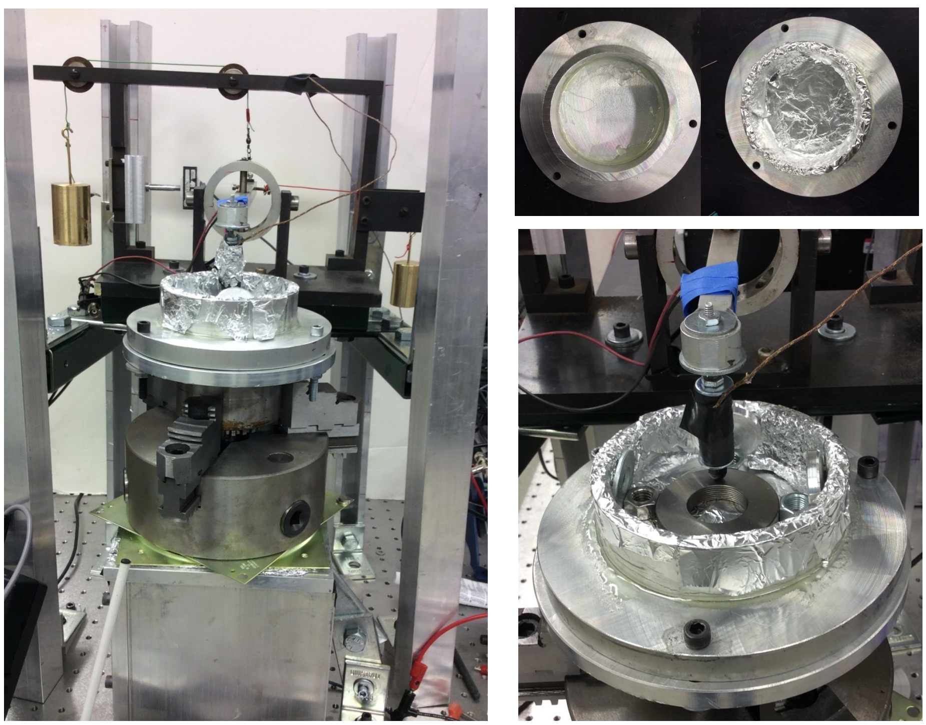

Figure 4.22: Experimental set-up for lubrication comparison.

The experimental set-up is shown in Fig. 4.22. The pin-on-disc tribometer with piezo-actuator was utilized as the platform for this study with a minor modification: the addition of a bowl, onto which the disc was clamped.

Table 4.3: Parameters used in the experiments of lubrication comparison

Parameter	Value
Normal load (N)	3, 6, 9
Estimate nominal contact area (mm^2)	0.126
Nominal normal stress (MPa)	23, 48, 70
Rotational diameter (mm)	28
Linear velocity (mm/s)	60-140
Peak-to-peak Voltage (V)	25.9
Average power consumption of the actuator	5.31
Nominal US amplitude (μm)	2.31
Frequency (kHz)	22
Pin material	Stainless steel
Disc material	M50 tool steel

Parameters used in this experiment are listed in Table 4.1. Normal load was set at 3, 6, and 9 N. Nominal contact area is 0.126 mm^2, which was calculated from the width of the wear grooves. Correspondingly, nominal normal stresses were 23, 48, and 70 MPa. The rotational speed was controlled by the voltage that drives the motor. Rotational diameter was 28 mm. In each test, the linear velocity started at approximately 60 mm/s and increased gradually until 140 mm/s. The pin material was stainless steel and the disc was M50 tool steel.

Intrinsic friction was measured first at all three normal stresses, followed by the testing of friction with ultrasonic vibrations. Figure 4.23 (a) shows the set-up details for those two tests. Next, Molykote was applied onto the disc and pin with a brush (Fig. 4.23 (b)). Friction with Molykote was measured following the same procedures as in the previous two groups (Fig. 4.23 (c)). Finally, friction with both lubrication methods was measured.

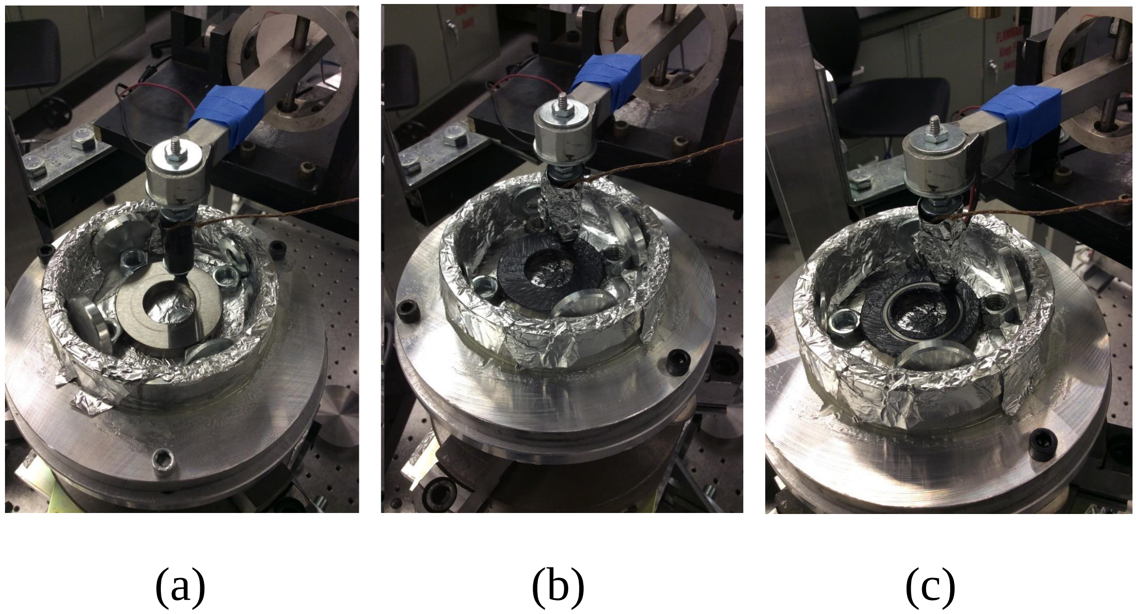

Figure 4.23: Experiments with Molykote: (a) dry surface; (b) surface with Molykote before test; (c) surface with Molykote after test.

4.2.3 Experimental Data

Experimental data obtained under different normal loads (stresses) are plotted in Figure 4.24, 4.25, and 4.26, respectively. There are two plots for each normal load. The top pictures plot the measured friction forces with four lubrication conditions against testing time: intrinsic friction, friction with ultrasonic lubrication, friction with Molykote, and friction with combined lubrication. The bottom figures plot friction coefficients against linear velocity, with error bars representing the standard deviation of the measured data. The linear velocities were calculated from measurements taken by the gaussmeter.

For all three normal loads, there are a few common features in the measurements. Firstly, there was fluctuation in all the measurements. This is due to the wobbling of the plate as it rotates. The wobble causes a small amount of displacement at the contact of the pin and the plate, resulting in an acceleration of the gymbal arm in

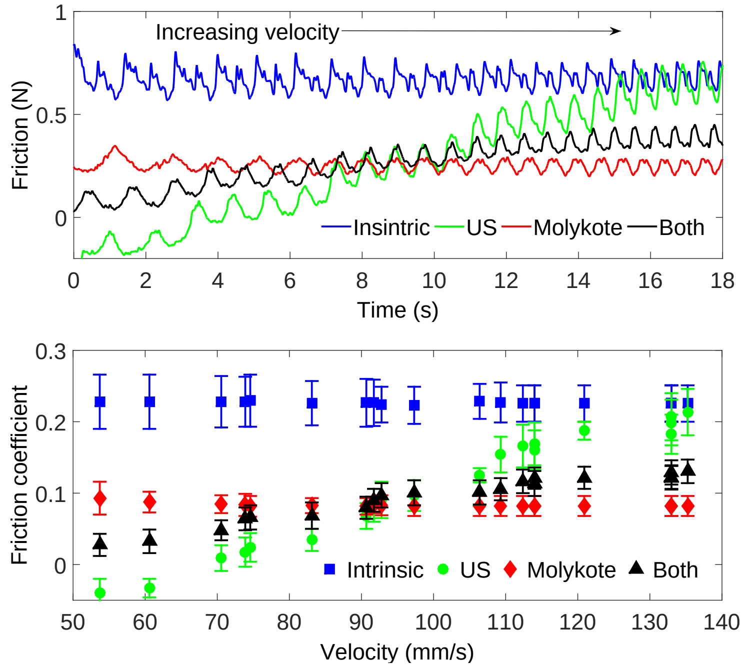

Figure 4.24: Friction and coefficient of friction under 3 N using different lubrication methods

the vertical direction. The normal load varies accordingly, which leads to a variation of measured friction forces. However, the amplitude of the fluctuation is evidently smaller when any type of lubrication is applied as opposed to when at dry surfaces. This is because the vertical acceleration caused by the wobbling was dampened by the lubricants, especially Molykote. Ultrasonic vibrations can also reduce the acceleration, especially at lower linear velocities.

When ultrasonic lubrication was applied by itself, friction increased as the velocity increased. This result is in line with previous studies, including when ultrasonic vibrations are applied longitudinally [34] and vertically [110]. When Molykote alone was applied alone, friction remained constant as the velocity increased. When both

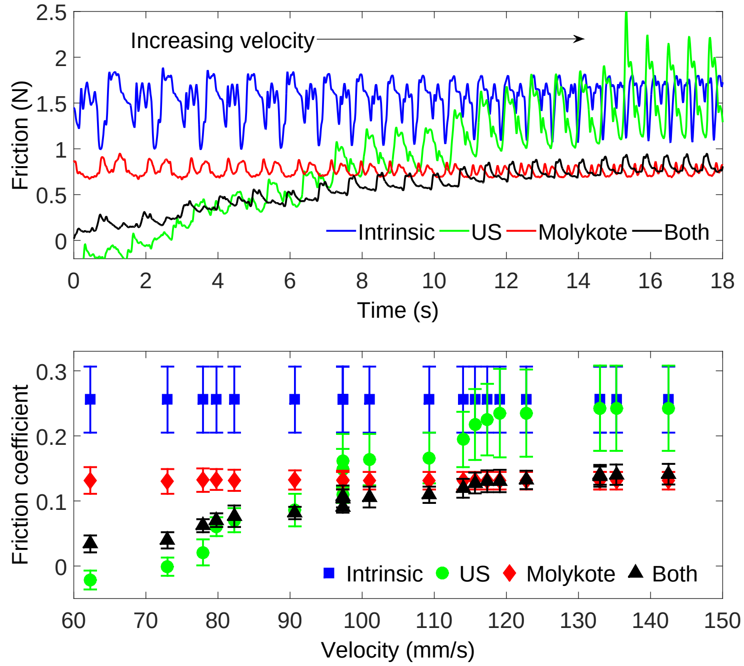

Figure 4.25: Friction and coefficient of friction under 6 N using different lubrication methods

ultrasonic lubrication and Molykote were applied, friction increased as the velocity increased, but with a less steep slope than with ultrasonic lubrication alone.

4.2.4 Discussion

The percentage of friction reduction was calculated from experimental data. Figure 4.27 plots the percentage against the linear velocity for all measurements. The colors represent the lubrication methods, and the shapes of the markers denote the stresses.

The red markers, which represent the friction reduction with Molykote, form three flat lines. The results show that higher normal stress leads to less friction reduction,

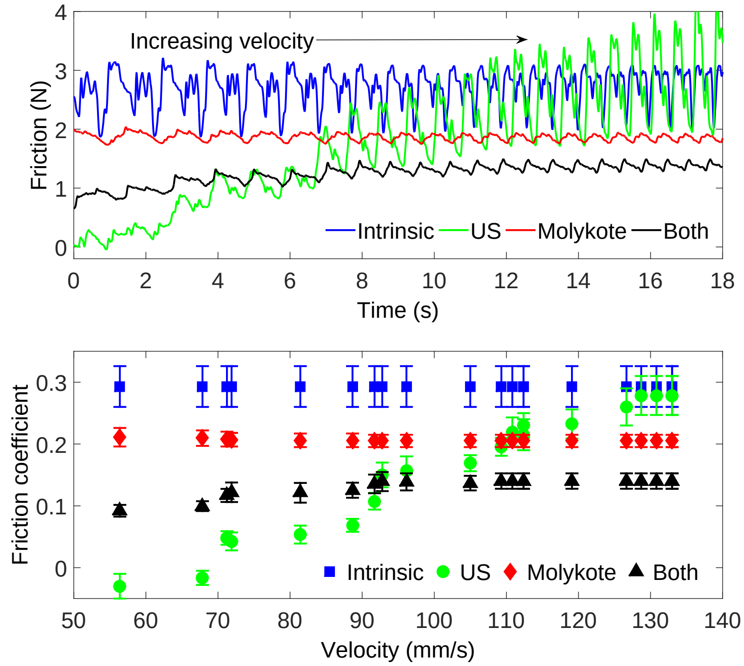

Figure 4.26: Friction and coefficient of friction under 9 N using different lubrication methods

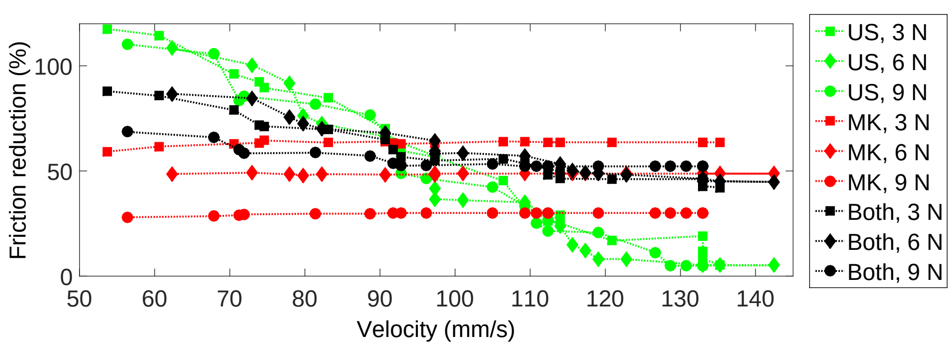

Figure 4.27: Summary of friction reduction using different lubrication methods

and linear velocity has no influence on friction reduction. For the surface lubricated with Molykote, the contact between asperities are not completely eliminated.

Therefore, normal load is shared by both the lubricant and the contacting asperities (Fig. 4.28). The contact between asperities creates more resistance to the relative motion than Molykote, hence, more friction force. As normal stress increases, two surfaces are pushed closer to each other, resulting in more asperities in contact. Friction force increases accordingly.

As the green markers indicate, ultrasonic friction reduction decreases when linear velocity increases. This is in line with previous studies. When both lubrication methods are applied, friction reduction shows little dependence on either velocity or normal stress, as shown by the black markers.

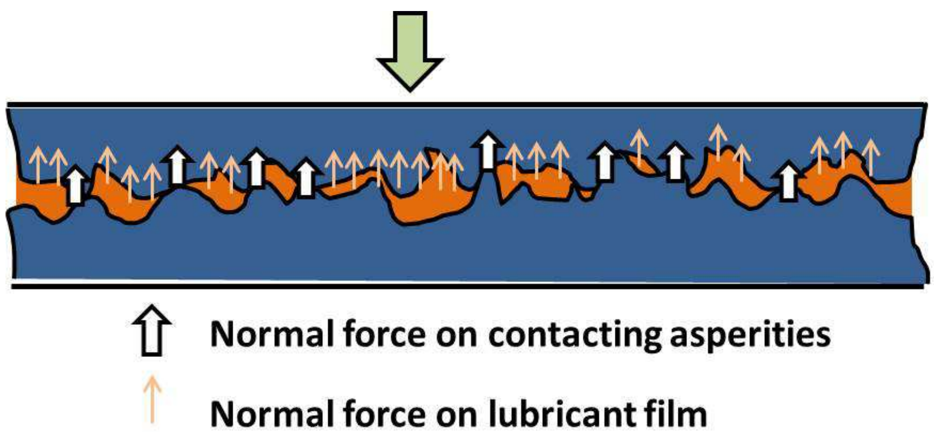

Figure 4.28: Mechanism of boundary lubrication.

Therefore, a simple division of lubrication regimes can be performed using Fig. 4.27. At velocities lower than 90 mm/s, ultrasonic lubrication has the best performance, regardless of the normal load. At velocities higher than 90 mm/s, either the combined lubrication or the Molykote alone could be used, depending on the magnitude of the normal stress. Combined lubrication works better, unless the normal stress is low.

At speeds higher than 110 mm/s, ultrasonic lubrication should not be utilized unless driving power is increased.

4.2.5 Summary

Lubrication methods have been compared experimentally in this study. The cases investigated were intrinsic friction, traditional lubrication with Molykote, ultrasonic lubrication, and combined lubrication of ultrasonic and Molykote. Experimental data show that traditional lubrication depends on normal stress, but not linear velocity, while ultrasonic lubrication depends on linear velocity, but not normal stress. Combined lubrication has little dependence on either factor. Different lubrication regimes were divided based on linear velocity and normal stress, within each of which, one method proved to be better than the others.

4.3 Temperature Change at Ultrasonically-Vibrated Interface

4.3.1 Introduction

It is of great interest to measure the temperature at the interface where friction takes place, especially when ultrasonic vibrations are applied. The factors influencing surface temperature include sliding velocity, normal stress, thermal conductivity of materials in contact, presence of an oxide layer, subsurface temperature, and the nature of surfaces in contact among others [89].

Possible phenomena caused by temperature rise include galling, thermal deformation, thermal instability, thermal stress, and thermal cracking among others [86, 88, 100]. Galling occurs when tips of asperities weld together and are then sheared apart according to weld-junction or adhesion theories [90]. It has been observed that the asperities in contact change geometry at high velocities, leading to thermal deformation [91, 92]. With more heat generation, the deformation of the contact becomes unstable [92, 93]. This is called thermoelastic instability, and can occur even in completely smooth surfaces [87]. Non-uniformities in contact pressure distribution result in more frictional heating and higher surface temperatures in regions of greatest pressure. Thermal expansion is greatest at the hottest locations, resulting in an even greater concentration of contact, and leading to a few hot contact patches. The process is slowed down or stabilized by wear [94].

4.3.2 Methods of Temperature Measurement at Contacts

Several experimental methods on surface temperature measurement have been reported:

- **Embedded thermocouples**: Mounted at a finite depth under the surface, these thermocouples are effective in measuring bulk temperatures but ineffective in measuring flash temperatures [95].

- **Dynamic thermocouples**: Two dissimilar materials in contact can form a thermocouple pair to measure the average temperature at the interface [96]. However, it requires some effort to calibrate the electrical signal with the actual temperature. Also, evident electrical noise exists in the measurements [97].

- **Thin film temperature sensors**: These are fabricated using vapor deposition techniques. Two different metals such as nickel and copper are sandwiched with a layer of hard dielectric material (Al_2O_3) in between. These sensors can be placed on the contact to measure the surface temperature [98].

- **Optical and Infrared photography**: This method utilizes infrared radiation to form images. With careful calibration between radiation density and temperature, the images show the temperature distribution across the surface of the object [99].

4.3.3 Temperature Measurements on Pin-on-Disc Tribometer

To measure the temperature at the pin and disc contact of the modified tribometer, a thermocouple was embedded to the acorn nut and placed in contact with the disc. The temperature was measured directly at the contact point since the thermocouple forms part of the contact. This approach takes advantage of the easy measurements of using a calibrated thermocouple, and avoids the difficult calibration of forming creating a dynamic thermocouple at the pin-on-disc contact.

(a) (b)

Figure 4.29: Measurement set-up: (a) close-up view of the acorn nut; (b) front view of the tribometer.

The acorn nut was machined for the measurement set-up. As shown in Fig. 4.29 (a), two holes were drilled on the acorn nut, one on the tip and the other at a side. The thermocouple wires were inserted from the side hole through the tip hole so that the junction of the thermocouple can pass through the acorn nut tip. Once put in place, the thermocouple was connected to the acorn nut using thermal conductive adhesives. After the adhesives dried and the connection was firm, the acorn nut was then attached and tightened to the piezo-actuator. The junction of the thermocouple was then in contact with the disc (Fig. 4.29 (b)).

Six levels of linear velocities and two levels of normal stresses were chosen for the tests. Each measurement lasted for about 50 seconds with constant linear velocity and normal stress. After 2 seconds, the motor started to rotate and friction was

Table 4.4: Parameters used in temperature measurements.

Parameter	Value
Normal load (N)	3, 6
Estimate nominal contact area (mm^2)	0.115
Nominal normal stress (MPa)	26, 52
Rotational diameter (mm)	28
Linear velocity (mm/s)	36, 67, 110, 145, 182, 220
Peak-to-peak voltage (V)	5.1, 10.3, 15.5, 20.7, 25.9
Nominal vibrational amplitude (μm)	0.45, 0.92, 1.38, 1.85, 2.31
Nominal peak vibrational velocity (mm/s)	63, 127, 191, 255, 319
Average power consumption of the actuator	0-5.31,
Frequency (kHz)	22
Disc material	Coated steel

created between the pin and the disc. During the first 10 seconds of the rotation, no ultrasonic vibrations were applied, which allowed for temperature measurements of intrinsic friction. Starting at 12 seconds, ultrasonic vibrations were applied. Five levels of driving voltages were then applied to drive the actuator, with each level lasting 4 seconds. Afterwards, both the ultrasonic vibrations and motor rotation were turned off. The test lasted another 18 seconds to allow for the temperature to drop. The values of the parameters are listed in Table 4.4.

4.3.4 Measured Data

Measured temperatures are shown in Fig. 4.30. Each figure plots six curves, which represent temperature data at six linear velocities. Without ultrasonic vibrations, temperatures rose rapidly when the relative sliding initiated. Temperatures reached steady states after certain points, and then temperature rises were proportional to the durations of sliding. The temperature at 12 s for all cases were plotted in Fig. 4.31.

The relationship between contact temperature and linear velocity appears linear, however, the slope is greater at higher stress. When rotation stopped, the temperature returned to room temperature rapidly in all measurements.

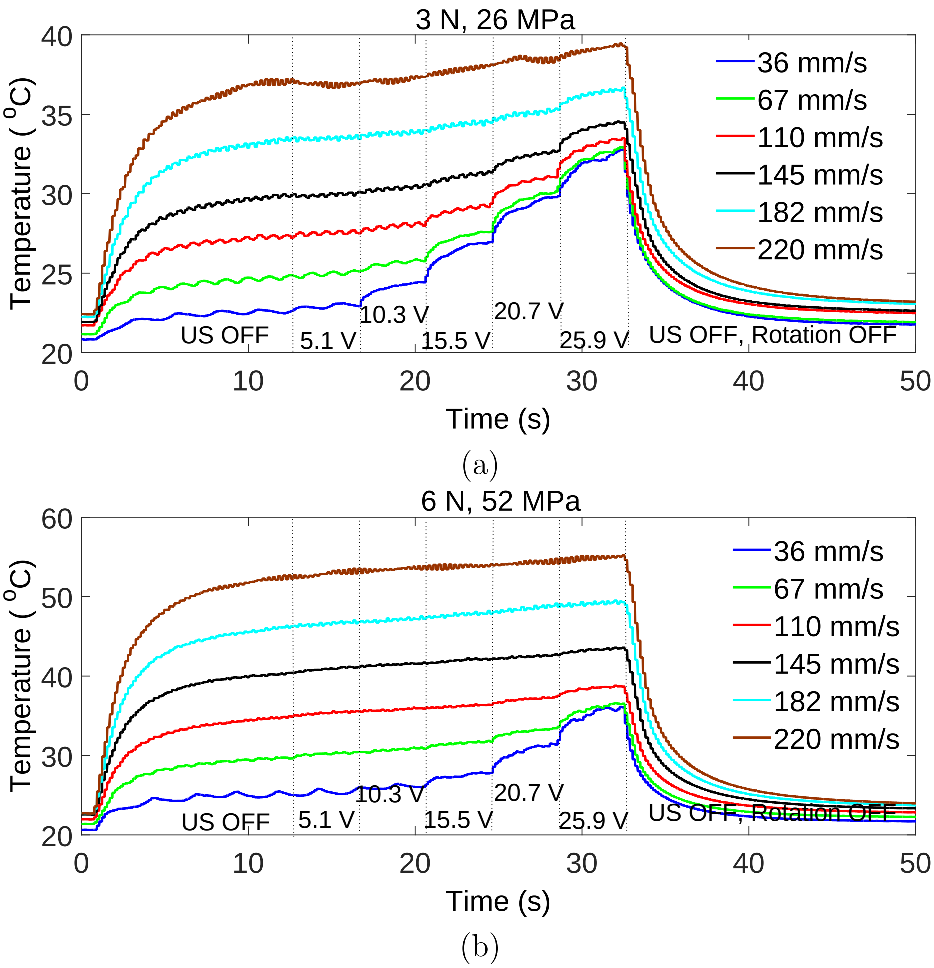

Figure 4.30: Measured temperature: (a) 26 MPa; (b) 52 MPa.

The effect of ultrasonic vibrations on temperature changes can also be observed from Fig. 4.30, especially at low velocities. When ultrasonic vibrations were applied, temperature rises faster than the trend predicted. The higher the voltage, the faster the temperature rise. This is due to fact that, by applying ultrasonic vibration, the

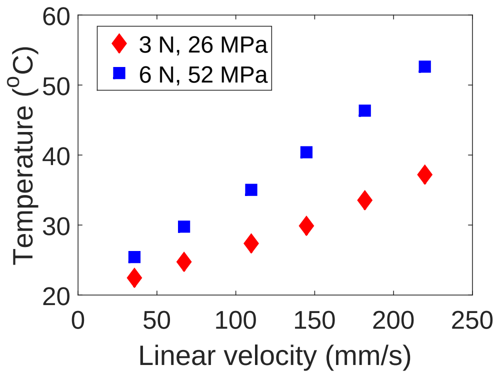

Figure 4.31: Relationship between temperature and linear velocity under different normal stresses.

actual relative velocity is a superimposition of macroscopic velocity and the vibratory velocity. When macroscopic velocity is low (36 mm/s or 67 mm/s), the actual velocity can be increased to around 300 mm/s by applying ultrasonic vibration. Superimposed relative velocities at different voltages are summarized in Table 4.5 and plotted in Fig. 4.32. Higher initial macroscopic velocity results in small changes after superimposition and vice versa. Trends related to changes in velocity are very similar to the trends found with temperature curves.

Table 4.5: Values of superimposed relative velocities.

Voltage (V)	0	5.1	10.3	15.5	20.7	25.9
Peak vibrational velocity (mm/s)	0	63	127	191	255	319
Average vibrational velocity (mm/s)	0	20	40	61	81	101
Superimposed velocity (mm/s)	36	41	54	71	89	108
	67	69	78	91	105	122
	110	110	117	126	137	150
	145	146	151	157	166	177
	182	183	186	192	199	208
	220	221	223	228	235	242

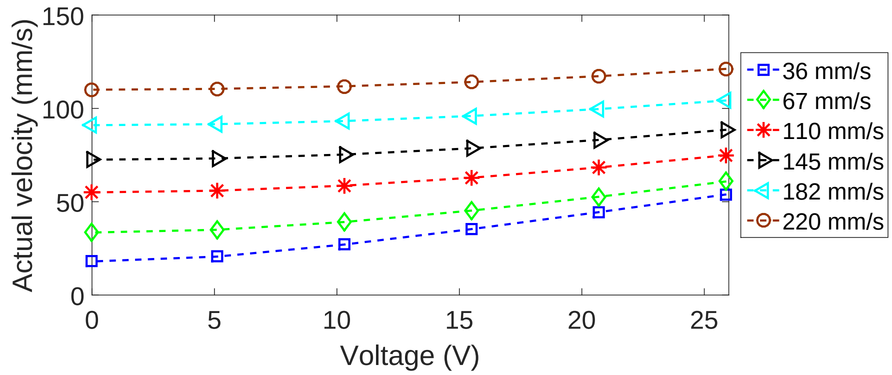

Figure 4.32: Change of actual relative velocity at interfaces when ultrasonic vibrations are applied.

On the other hand, friction forces were reduced by applying ultrasonic vibrations, as shown in Fig. 4.33. The variation of the measurements came from the disc run-out. Lower macroscopic velocity and higher driving voltage resulted in higher friction reduction, which is in line with previous experiments.

The reduction of friction results in the reduction of frictional heat generation, hence, the temperature at the interface. Therefore, by applying ultrasonic vibrations, two factors influencing the temperature change become evident. The introduction of vibrational velocity increases the actual relative velocity, leading to a rise in temperature. The reduction of friction results in a reduction of temperature. The overall temperature change in one particular case is dependent on which factor has a stronger influence than the other.

One example can be found in the case of 220 mm/s under 26 MPa. An additional temperature measurement was repeated under the same condition, but without ultrasonic vibrations applied throughout. The temperature curves with and without ultrasonic vibrations are plotted in Fig. 4.34. Despite the subtleness, it can be seen

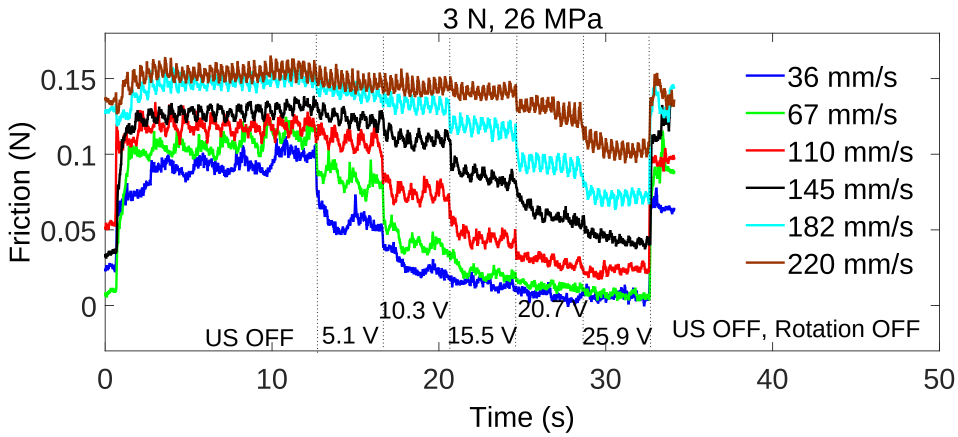

(a)

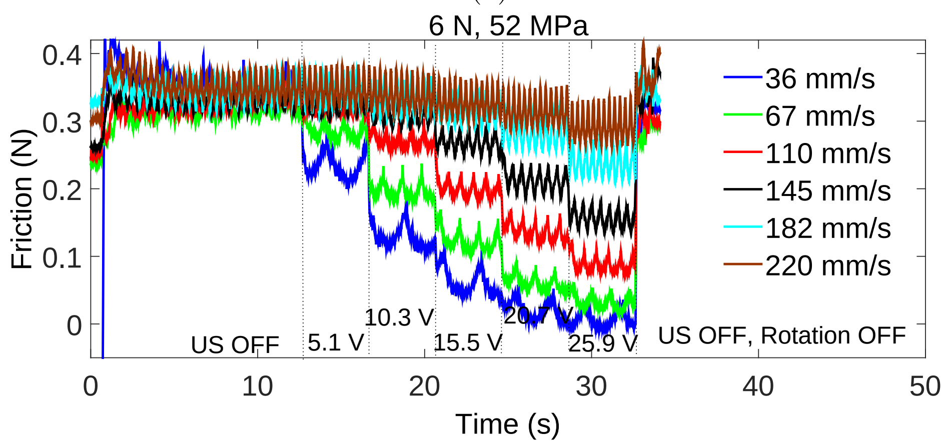

(b)

Figure 4.33: Measured friction: (a) 26 MPa; (b) 52 MPa.

that the temperature was reduced when 5.1 V and 10.3 V was applied to the actuator. At those two stages, friction decreased by 10% (Fig.4.33), but the actual relative velocity only increased by 3 mm/s. Among the two factors, the friction reduction has more influence, which is responsible for a slight decrease of temperature. When voltages increased to 20.7 V and 25.9 V, although friction continued to drop, the actual velocity increased by up to 22 mm/s, eventually causing an increase in temperature.

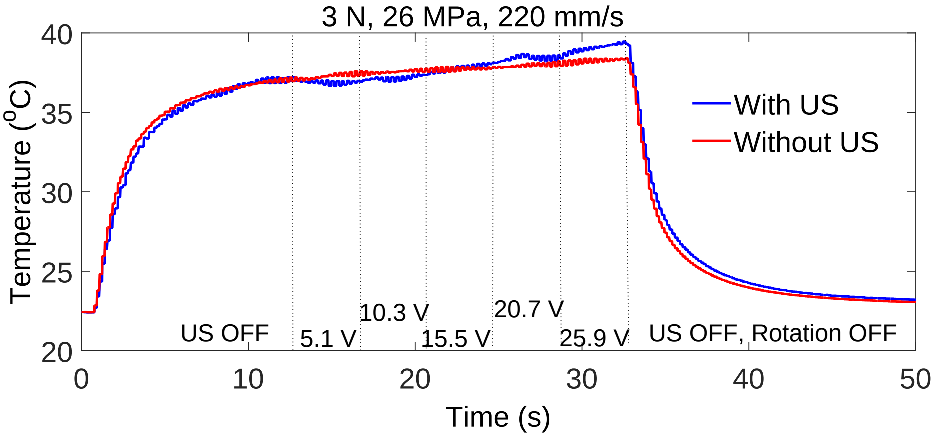

Figure 4.34: A comparison between temperature curves with and without ultrasonic vibrations at 220 mm/s with 26 MPa.

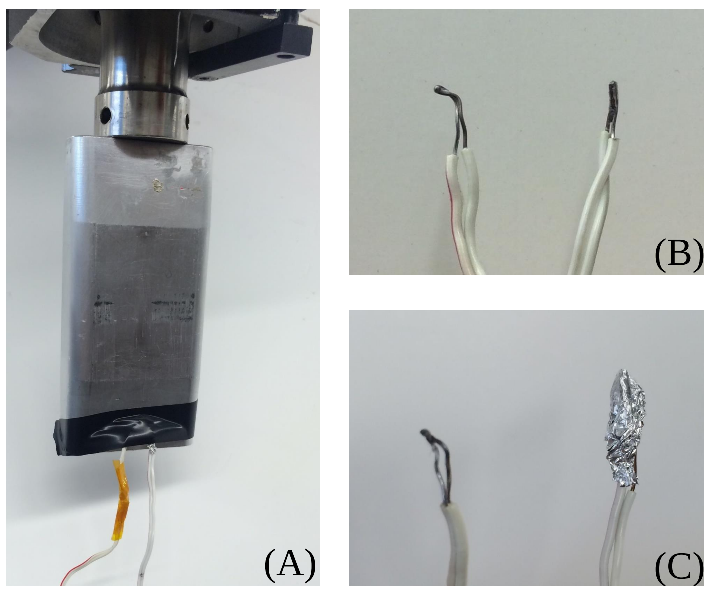

Figure 4.35: Set-up of temperature measurements on the waveguide: (a) overview; (b) thermocouples used in the first measurement; (c) thermocouples used in the second measurement.

4.3.5 Discussion

The temperature rise caused by superimposed velocity was also measured on the waveguide used in the experiments in Chapter 2.1. The set-up is shown in Fig. 4.35 (A). Two thermocouples were used with the tips attached to one side of the waveguide with tape. Temperature was recorded for 70 seconds, with ultrasonic vibrations applied at 20 seconds and lasting for 5 seconds. The temperature records are shown in Fig. 4.36. In the first measurement, both thermocouples are in direct contact with the waveguide. It can be observed in plot (a) that the readings of both thermocouples overlapped each other, demonstrating sharp increases in temperature approximately from 20°C to 80°C when ultrasonic vibrations are applied. As previously explained, these increases are due to the fact that ultrasonic vibrations increase the relative velocity. In fact, the waveguide provides vibrations with 11.24 μm of amplitude, which is much greater than 2.31 μm of the modified tribometer. The velocity of the vibration was higher accordingly, resulting in a much higher peak temperature (80°C versus 53°C).

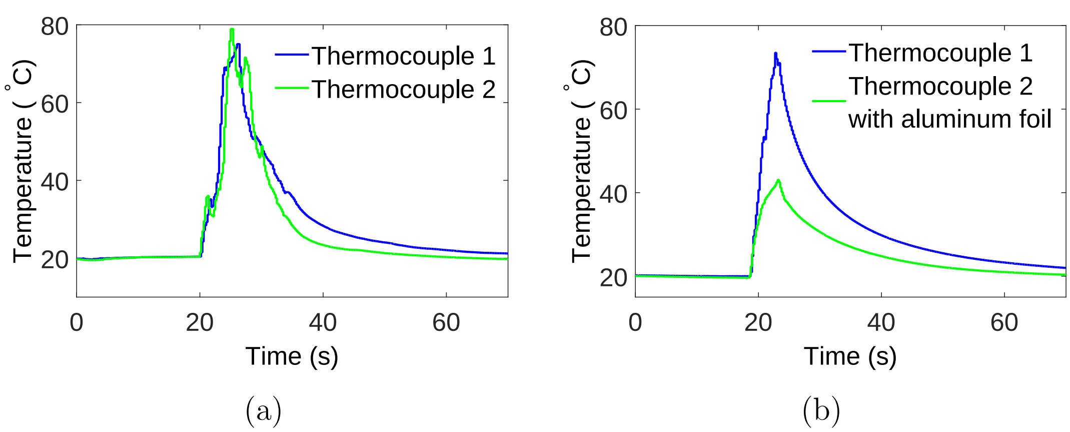

Figure 4.36: Temperature measurements on the waveguide: (a) both thermocouple are in direct contact with the waveguide; (b) one thermocouple is in contact with aluminum foil attached to the waveguide.

An additional measurement was conducted to prove the thermocouple has to be placed directly at the point of contact between two surfaces to measure the actual change in temperature. Any small distance would compromise the precision of the measurement. In this measurement, one thermocouple remained the same as in the first measurement – in direct contact with the waveguide. The second thermocouple was then wrapped with a piece of aluminum foil, which was 0.2 mm thick (Fig. 4.35 (c)). Actual contact took place between the waveguide and the foil so that the thermocouple measurement was not directly at the point of contact. Therefore, the peak temperature was measured at 41°C only.

4.3.6 Summary

Temperature changes were measured at the pin-on-disc contact in the modified tribometer after inserting a thermocouple into the acorn nut and placing it in direct contact with the disc. Measurements were conducted at velocities as high as 220 mm/s and under two levels of normal stresses. It was found that two factors can influence temperature change when ultrasonic vibrations are applied. On one hand, the superimposition of vibratory and macroscopic velocities results in increases in actual relative velocities. This leads to rises in temperature. On the other hand, friction force and related heat generation can be reduced by applying ultrasonic vibrations, resulting in decreases in temperature. Overall temperature change, therefore, is dependent on both factors, which can vary from case to case. Temperature measurements on the waveguide of the plastic welder provided support for the theory of temperature change with ultrasonic vibrations. The data also prove that the thermocouple must be placed directly at the contact point in order to obtain precise temperature measurements.

4.4 Friction Reduction between Metal and Soft Non-metal Materials

4.4.1 Introduction

One of the possible applications of ultrasonic lubrication is in personal health care products. This section shows some preliminary work done in the attempt to reduce friction between a steel part of the product (cutter head) and a replica of human skin. The skin replica is made from a soft, felt-like fabric, that requires miniaturization with water when used.

The majority of past studies in the field of ultrasonic friction and wear reduction have been conducted by with metals and a few hard, non-metal materials such as ceramics. Scant attempts have been made to reduce friction between metal and soft, non-metal materials, such as Teflon and rubber. The results were negative [36]. The major reason can be attributed to the low contact stiffness of the soft materials, which reduce or totally eliminate the separation created by ultrasonic vibrations between the two contacting surfaces .

4.4.2 Experimental Set-up

The modified pin-on-disc is employed for this study with modifications, as shown in Fig. 4.37. The pin consists of a piezoelectric actuator and a weld nut, which the cutter head is glued to (close-up view in Fig. 4.37). The skin replica is slightly stretched and placed on a plate with four sides fixed. The rest of the set-up remained the same as in previous studies. Experimental parameters are shown in Table 4.6. The normal forces were 2, 3, and 4 N of one cutter head. Therefore, total normal loads on the product were 6, 9, 12 N, respectively, which covered the range of interest. The

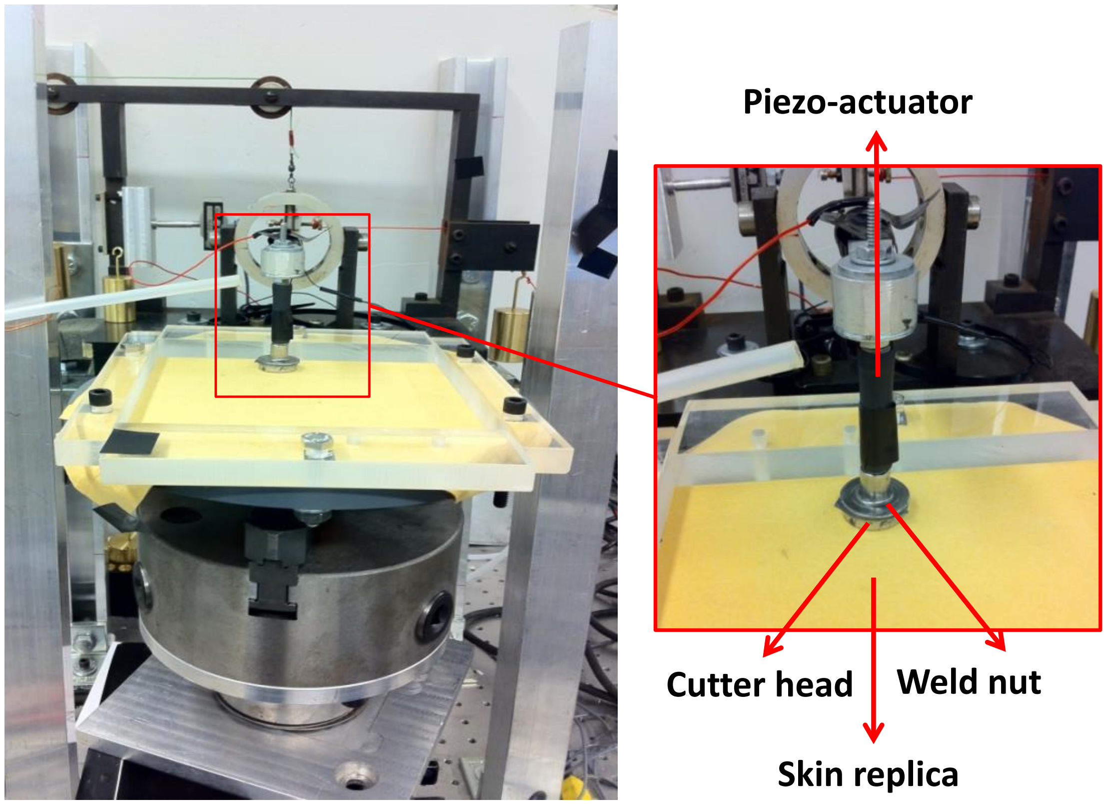

Figure 4.37: Experimental set-up for ultrasonic friction reduction between steel cutter head and skin replica.

Table 4.6: Experimental parameters in ultrasonic friction reduction between steel cutter head and skin replica.

Parameter	Value
Nominal normal force (N)	2, 3, 4
US frequency (kHz)	20
Linear speed (mm/s)	44.3
Nominal diameter of rotation (mm)	112

linear speed (44.3 mm/s) was right in the middle of the bracket of interest. Rotation diameter was measured of the center of the cutter head.

4.4.3 Experimental Data

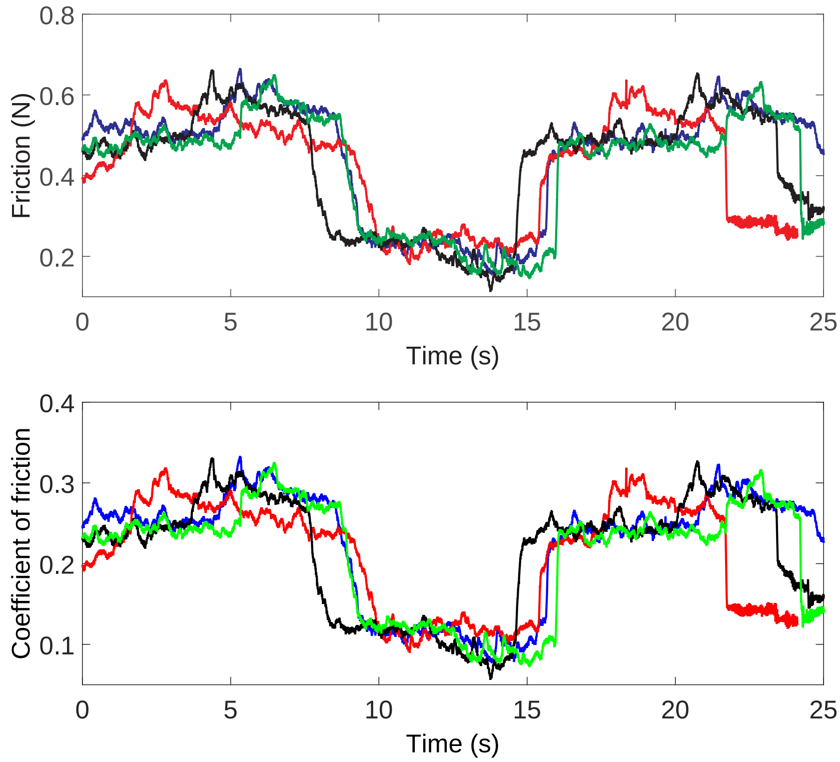

Figure 4.38: Friction force and coefficient of friction under 2 N.

Multiple tests were conducted for each normal load. Time dependent values of friction force and coefficient of friction were recorded and plotted, respectively (Fig. 4.38 to 4.40). In each plot, different colors represent the data from different tests. In each test, friction decreases when ultrasonic vibrations were applied, and coefficient of friction were reduced to close to 0.1 for all three cases.

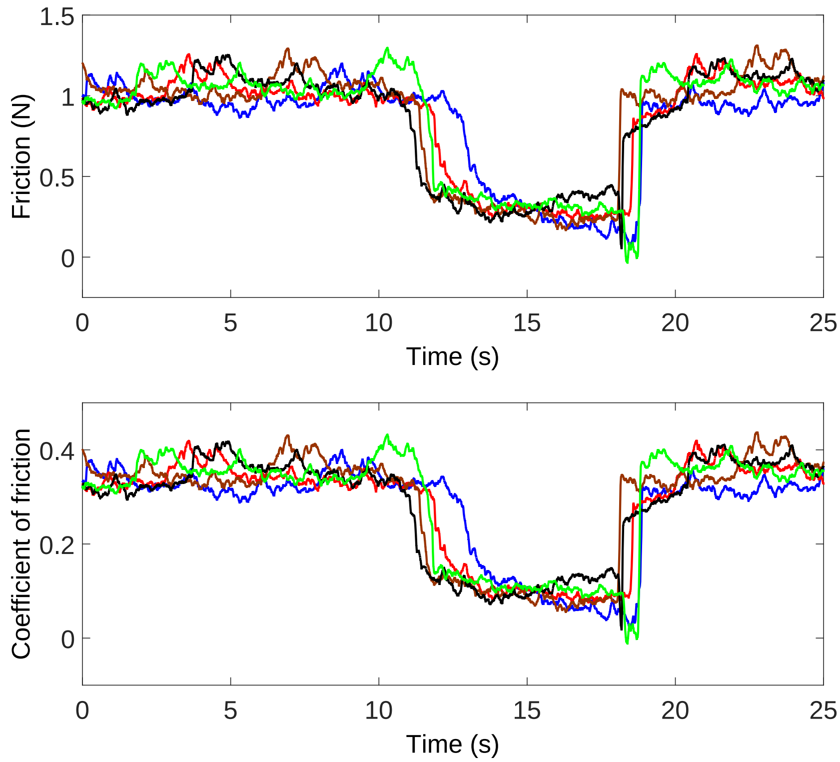

Figure 4.39: Friction force and coefficient of friction under 3 N.

The average value of friction with and without ultrasonic vibrations were calculated. Friction reduction percentages were calculated by dividing the difference of the friction force with and without ultrasonic vibrations by the one without. Under 2 N of normal force, friction force was reduced from 0.57 N (μ=0.29) to 0.21 N (μ=0.105) by 63%. Under 3 N of normal force, friction force was reduced from 1.04 N (μ=0.35) to 0.29 N (μ=0.096) by 72%. Under 4 N of normal force, friction force was reduced from 1.42 N (μ=0.355) to 0.44 N (μ=0.11) by 69%. Ultrasonic vibrations are effective in reducing friction forces under all three normal loads considered.

A second experiment was conducted to study the relationship between friction reduction and the driving voltage. The tests were conducted under 3 N of normal load. The piezo stack was driven at different voltages for different tests. Time-dependent

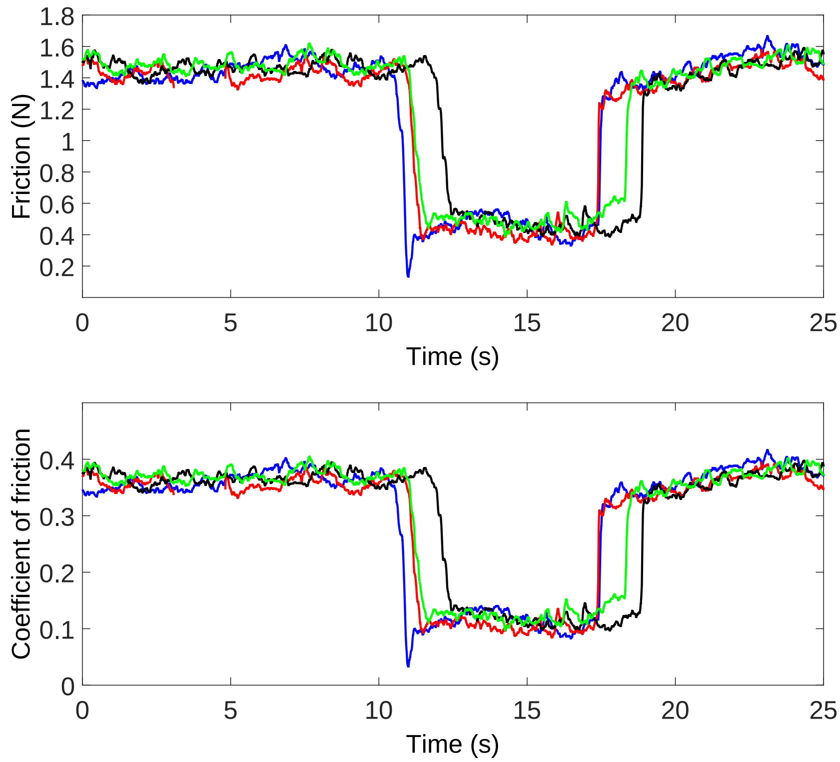

Figure 4.40: Friction force and coefficient of friction under 4 N.

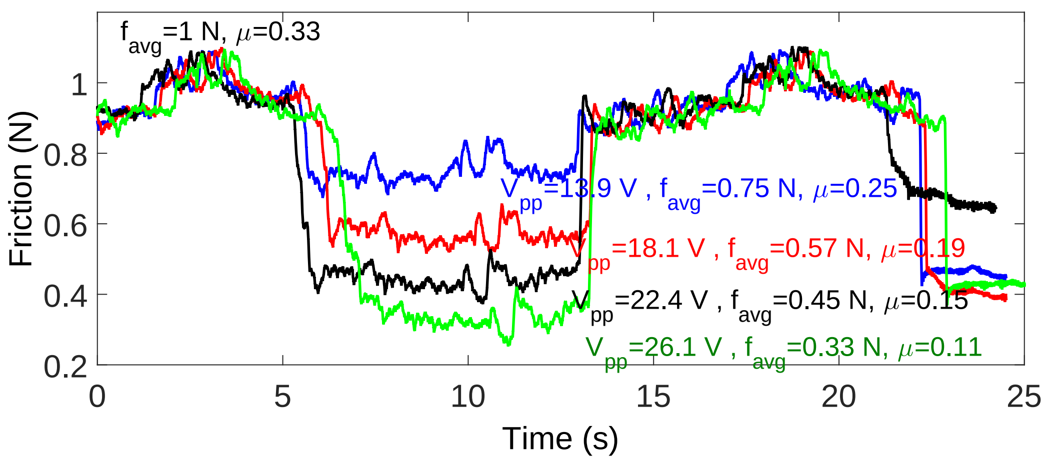

Figure 4.41: Friction reduction under high stress and high velocity.

friction forces were recorded and plotted in Fig. 4.41. Different colors denote different driving peak-to-peak voltages with values labeled in the plot. Intrinsic friction forces were the same for all four cases, while friction was reduced to different levels when different voltages were applied.

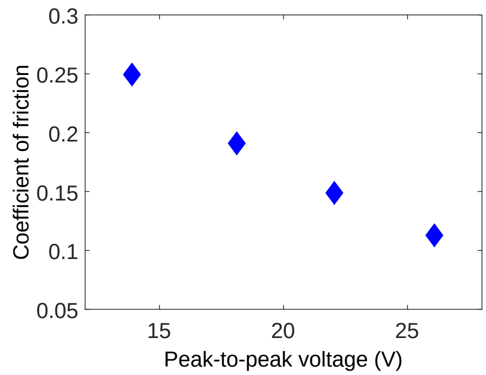

Figure 4.42: Friction reduction under high stress and high velocity.

The relationship between coefficient of friction and driving voltage is plotted in Fig. 4.42. It is evident that higher voltage results in lower coefficient of friction. The trend appears linear within the range of voltages tested, however, based on the multi-scale model of ultrasonic lubrication, the rate of friction reduction should decrease when the driving voltage continues to increase. The decreasing trend of coefficient of friction should decay at even higher voltages.

4.4.4 Discussion

Experimental data show successful reduction of friction between a metal and a soft, non-metal material. The difference from previous failed attempts [36] lies in the vibratory features of the interface. A laser vibrometer was used to study the vibration of the cutter head (Fig. 4.43). The vibration mode shape of the cutter head was obtained from vibrometer measurements (Fig. 4.44). The vibrations at the center and the rim of the head are out-of-phase. Unlike the vibrations between the pin and

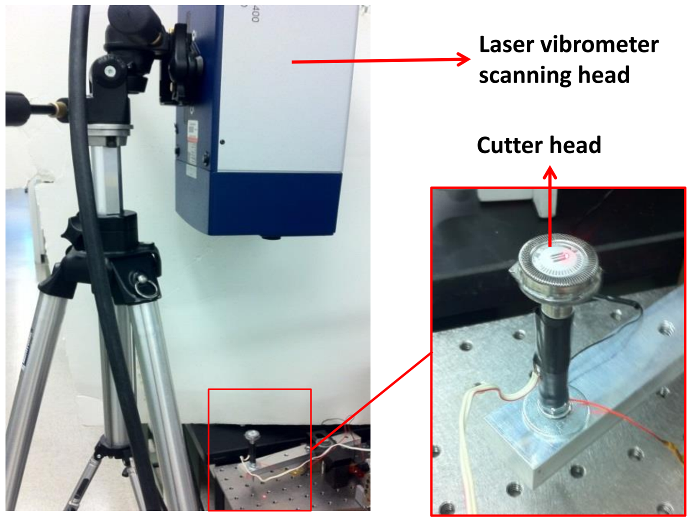

Figure 4.43: Laser vibrometer measurements on cutter head.

disc in previous studies, where the pin moves closer or farther from the disc as a whole, the vibration of the cutter head creates a steady-state reduction in contact. That is to say, a part of the head, either the center or the rim, is always in contact with the skin replica, meaning the other part is always separated from the interface. This supersedes the difficulty of reducing friction on soft materials.

Additionally, the vibration amplitude is critical to the friction reduction effect. A higher amplitude results in greater friction reduction. The relationship between the driving voltage and the vibrational amplitude was studied. The corresponding amplitudes of the vibrations are plotted in Fig. 4.45. Figure 4.46 shows the relationship between the vibrational amplitude and coefficient of friction, as well as the relationship between amplitude and friction reduction. For consumer products, specific requirements of friction coefficients can be met by vibrating the interface at certain amplitudes. By carefully designing the product, the desired amplitude with optimized power consumption can be achieved.

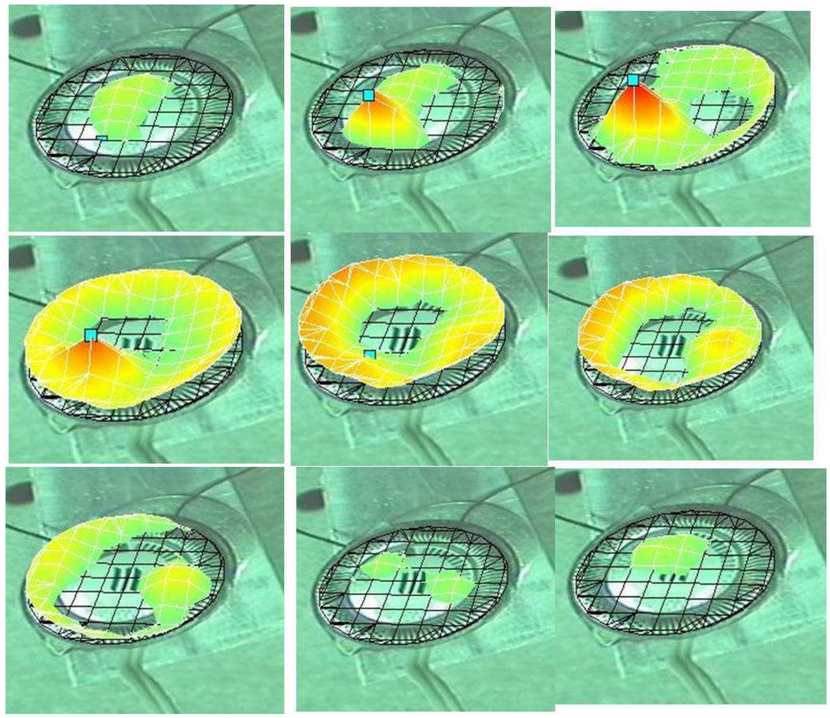

Figure 4.44: Vibrational modes of the cutter head.

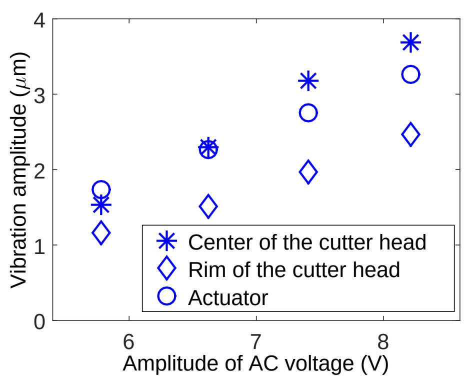

Figure 4.45: Relationship between driving voltage and vibrational amplitudes of the cutter head.

4.4.5 Summary

This section shows preliminary work for reducing friction between a consumer product and human skin. A cutter head and a skin replica were used for testing on

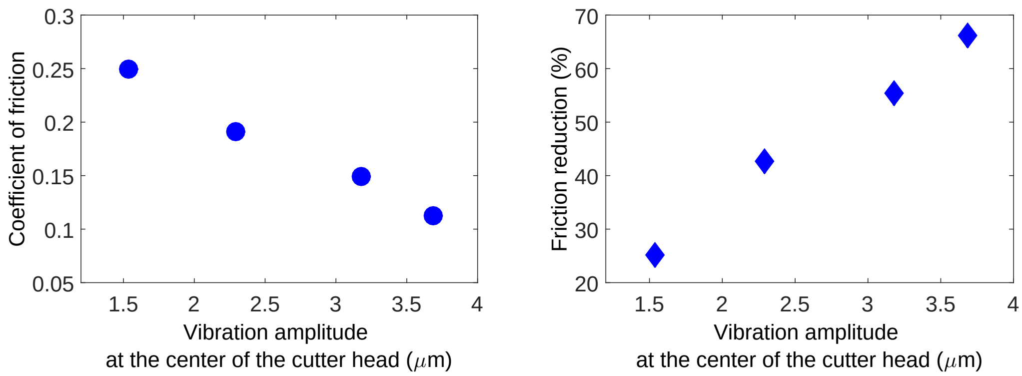

Figure 4.46: Relationship between vibrational amplitude and friction reduction

the modified pin-on-disc tribometer. Friction was reduced to the required friction coefficient under the normal load defined for product usage. By driving the actuator at different voltages, friction can be controlled at different levels. A laser vibrometer was utilized to investigate the vibration features of the cutter head. It was found that the center and the rim of the cutter head vibrate out-of-phase, which creates a constant reduction of contact, leading to successful friction reduction. This is the first time ultrasonic lubrication has proven effective between a metal and a soft, non-metal material.

4.5 Collar Element with Variable Friction

4.5.1 Introduction

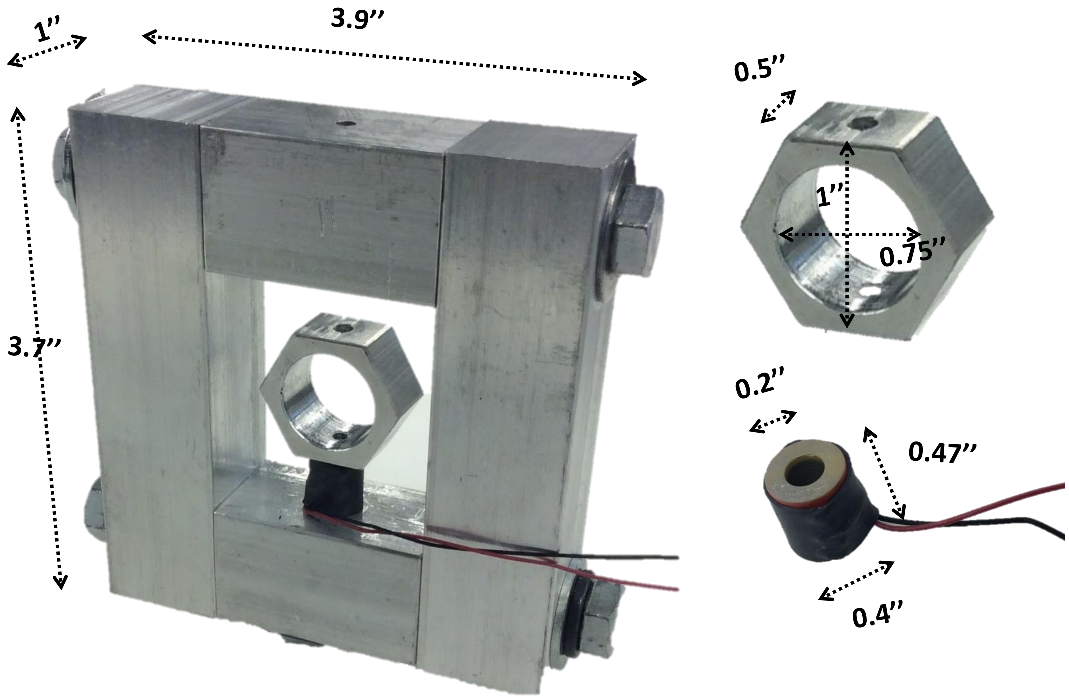

Figure 4.47: Collar element with variable friction.

A collar element with variable friction is proposed to showcase the process of design, analysis, manufacture, and testing of an ultrasonic lubrication device. The collar element can be used in vehicle dampers to mitigate damage from side loading. Side loading is caused by the lateral force produced when on a vehicle changes directions, goes around a curve, or shifts from one lane to another. In MacPherson strut suspensions [102], which are commonly used in the modern vehicles, side loading can lead to excess wear of damper rods, resulting in a decrease in ride performance and overall life of the damper. With the installation of the collar element, the lateral force and friction at the interface of the damper rod, the seal, and piston can be transmitted to the interface of the damper rod and the collar element. Friction force can therefore be reduced by the collar element.

4.5.2 Design of Collar Element

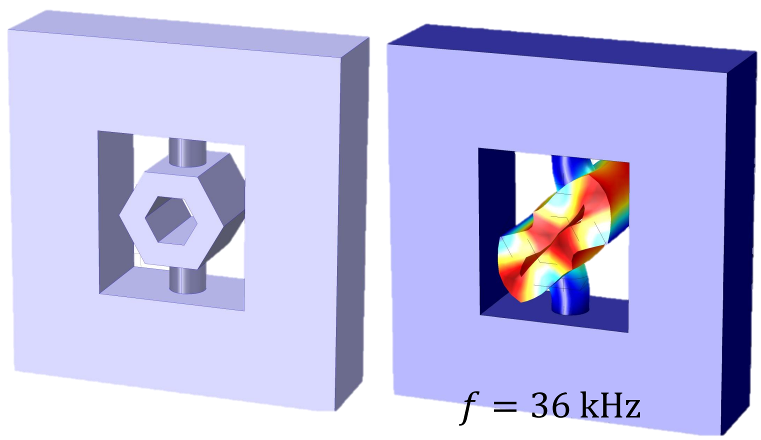

(a) (b)

Figure 4.48: First design of the collar element: (a) design; (b) mode shape at resonance.

The first design of the collar element is shown in Fig. 4.48 (a). There are two rings and two piezoelectric stacks. The outer ring is rectangular in shape with dimensions of 3.7 in. by 3.9 in. by 1 in. The inner ring is hexagonal in shape with a 1 in. outer diameter and 0.5 in. inner diameter. The piezoelectric stack used in the demo is PI Pica P-010.05H and has a ring shape cross-section with a through hole. The specifications of the stack are listed in Table. 4.7. Two through rods connect the actuators to the inner and outer rings. The rods are tightened against the two rings in order to apply compression load to the piezo-actuators.

Table 4.7: Specifications of the piezoelectric stack used in collar element.

Parameter	Value
Length (mm)	12
Outer diameter (mm)	10
Inner diameter (mm)	5
Stiffness (kN/mm)	140
Capacitance (nF)	42
Electromechanical coupling factor	0.69
Piezoelectric coefficient (pm/V)	500
Relative permittivity	2400

The original concept was designed to drive the two symmetrically installed piezo-actuators using in-phase signals of the same amplitude, allowing for the inner ring to vibrate in breathing mode. However, due to the thickness of the inner ring, the resonance frequency of the breathing mode was higher than 40 kHz. A resonance was found at 36 kHz in impedance measurement. The corresponding mode is shown in Fig. 4.48 (b), which is an in-plane torsional mode. A rod was inserted into the inner ring, and the vibrations of the element was tested at 36 kHz. It was found that the rod rotated inside the inner ring, due to the torsional mode.

In order to reduce the resonance frequency of the breathing mode, additional two inner rings were manufactured, of different dimensions. The design was then modified to those shown in Fig. 4.49. These two designs changed the inner hole from hexagonal to round, into which round rods can be securely fit. For both designs, the resonance frequency of the breathing mode was reduced to 27 kHz. However, the torsional mode still existed and the resonance frequency was also close to 27 kHz. It was difficult to separate two modes. Additionally, since the stiffness of the inner rings were greatly reduced due to the smaller thicknesses, the rings deformed easily. When forces were applied to compress the actuators, the inner rings were actually pulled from two ends. The rings deformed so significantly that the round shape was compromised, making it subsequently more difficult to insert the rod through the rings.

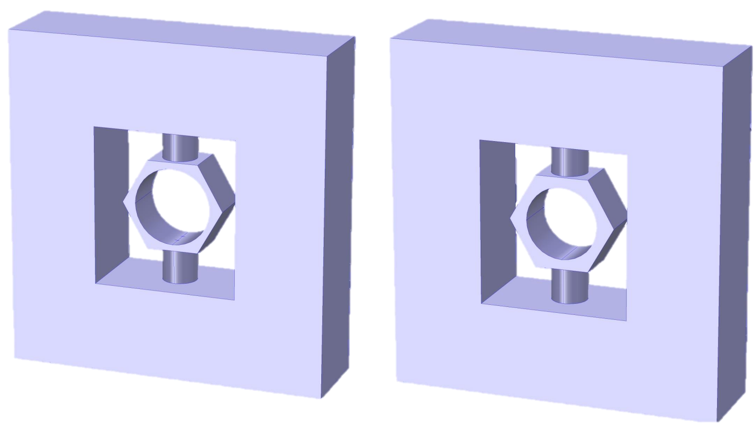

(a) (b)

Figure 4.49: Revised designs of the collar element.

A final modification was made to solve for problems of the inner-ring deformation and the torsional mode. The final version of the element design is shown in Fig. 4.50. Detailed drawings of the parts to assemble the collar element can be found in Appendix C. Only one actuator was retained for the final design. It simplified the vibrational modes of the element. Due to the mass difference of the inner and outer ring, the majority of the vibrations generated by the actuator were distributed to the inner ring, and the outer ring worked as a reaction mass. The impedance of the

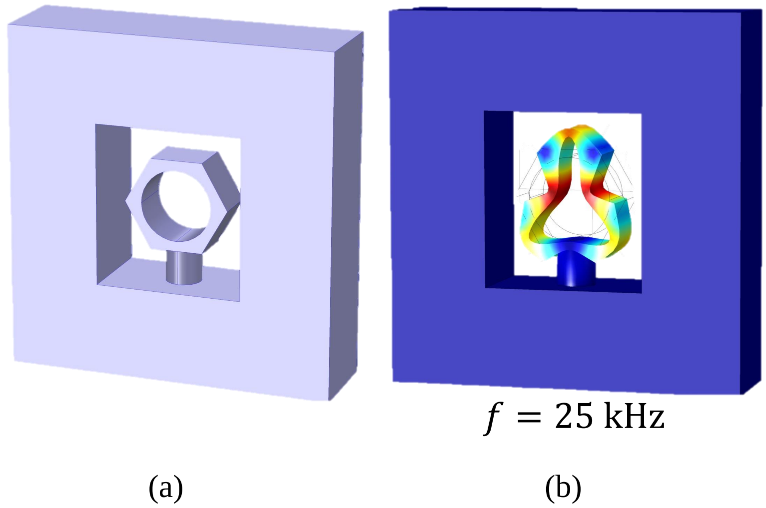

Figure 4.50: Final version of the collar element: (a) design; (b) vibrational mode.

element was measured with two mechanical constraints: clamped and unclamped, as shown in Fig. 4.51. The inner ring has a breathing mode in addition to the motion as a whole, as shown in Fig. 4.50 (b).

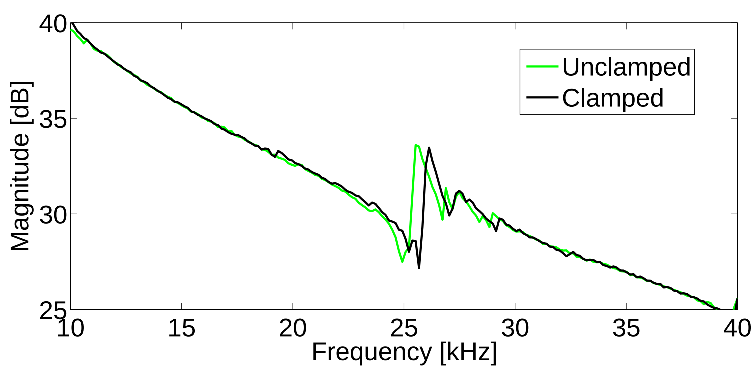

Figure 4.51: Impedance measurements of the collar element.

4.5.3 Laser Vibrometer Measurements

A laser vibrometer was employed to measure the vibrational mode and amplitudes. In order to directly measure the vibration of the inner ring, the top piece of the collar element was removed (Fig 4.52).

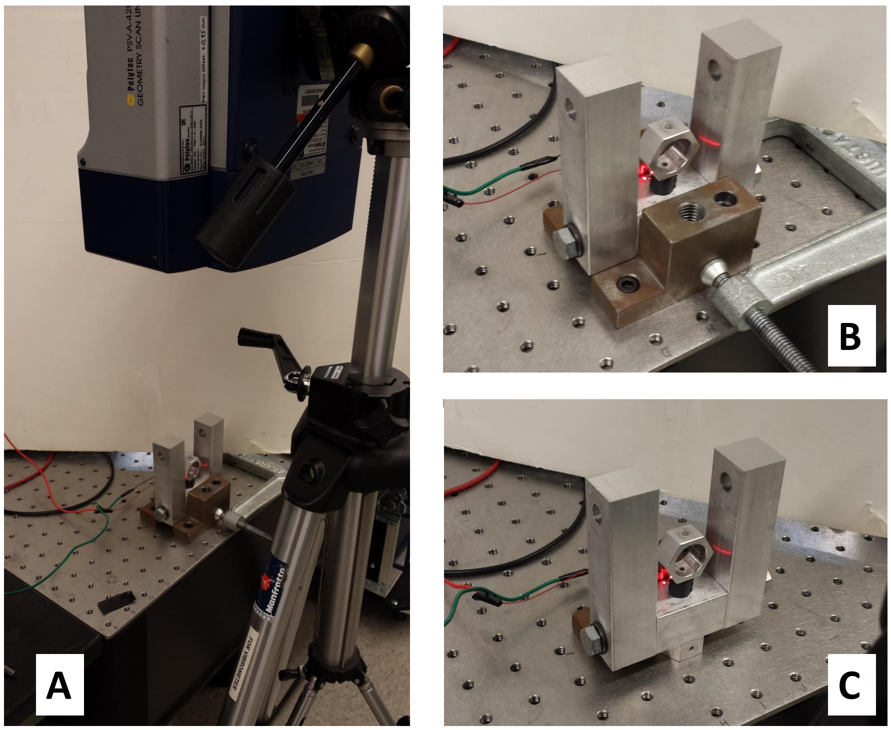

Figure 4.52: Set-up for laser vibrometer measurements on the collar element: (A) Overview; (B) Clamped; (C) Unclamped.

A comparison between the impedance measurements with open and closed top was conducted prior to the vibrometer measurements, ensuring that measured data with the top open can represent those with the top closed. As shown in Fig. 4.53, there is only one pair of resonance and anti-resonance for the closed top, while there are three pairs for the open top. The reason is that, as the top was opened, the outer ring was broken into a base and tow pillars. Additional vibration modes of the

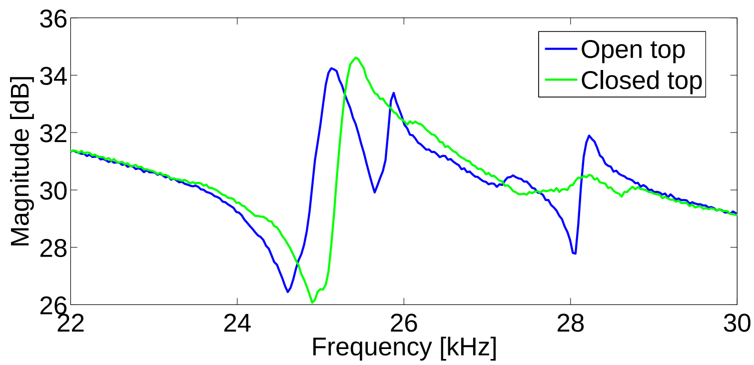

Figure 4.53: Comparison of impedance measurements of the collar with open and closed top.

pillars were generated, both bending or torsional. However, the first mode shifted only slightly from 25 kHz to 24.4 kHz. Therefore, for the purpose of measuring the vibration amplitude of that particular frequency, an open top can be used to represent the closed top.

The set-up of the laser vibrometer measurements is shown in Fig. 4.52.Two mechanical constraints were employed on the collar element: unclamped (free-end) and clamped. A photo taken by the laser vibormeter camera is shown in Fig. 4.54 (a). The top surface of the inner ring and the base of the outer ring were scanned.

Measurements were conducted at 25 kHz for both clamped and unclamped conditions. It could be confirmed that the main vibrational mode at 25 kHz for the top of the inner ring is a superimposition of a vertical motion and a bending motion. This confirms with FEA calculations. The measured vibrations of the top surface of the inner ring are plotted in Fig. 4.54 (b). The red surface represents the highest position in the vertical direction, while the blue one represents the lowest.

The vibrational amplitudes of the top surface of the inner ring and the base of the outer ring, both clamped and unclamped, were measured. As shown in Fig. 4.55,

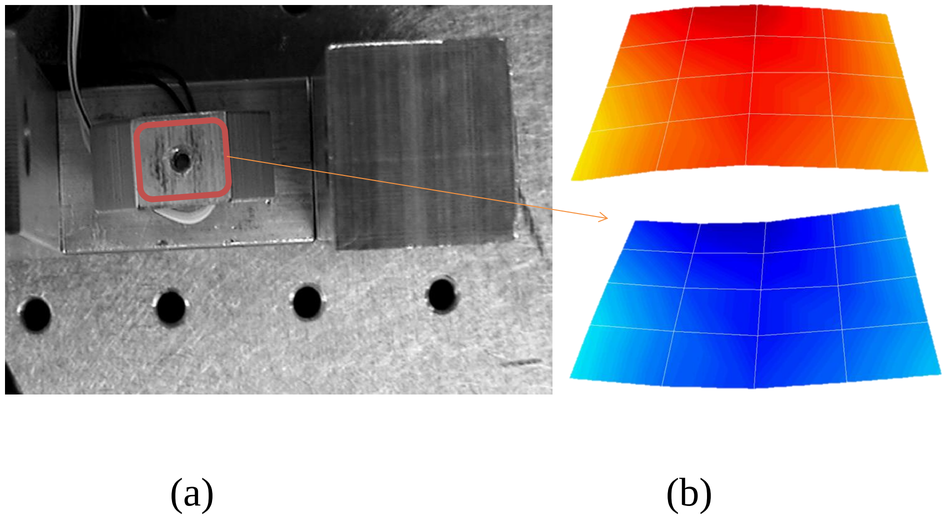

Figure 4.54: Laser vibrometer measurements: (a) scan picture; (b) vibrational mode of the scanned area.

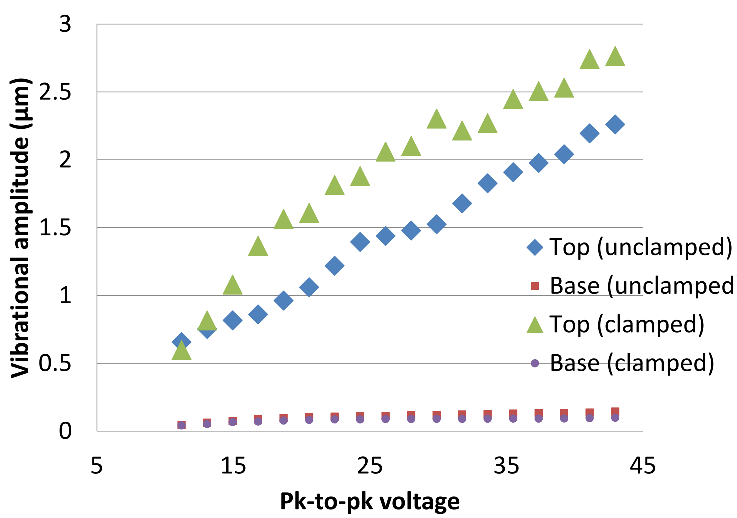

Figure 4.55: Vibrational amplitudes at various voltages.

the vibration of the base was negligible compared to that of the top of the inner ring, regardless whether the base was clamped or not. The vibrational amplitudes of the top are linearly proportional to the driving voltage. The vibrational amplitude of the top face could be significantly increased by clamping the base.

4.5.4 Friction reduction

A simple measurement of friction reduction was conducted and, the schematic is shown in Fig. 4.56. A stainless steel rod with a nominal diameter of 0.75 in. was pulled manually through the ring from one end to the other. The normal force was the weight of the rod, which changed according to the relative position between it and the inner ring. Actual normal force was higher when the ring was in contact with either end of the rod than at the middle. Additionally, irregular spots of tighter and looser fits between the rod and the inner ring exist, due to the manufacturing tolerance in rod diameter.

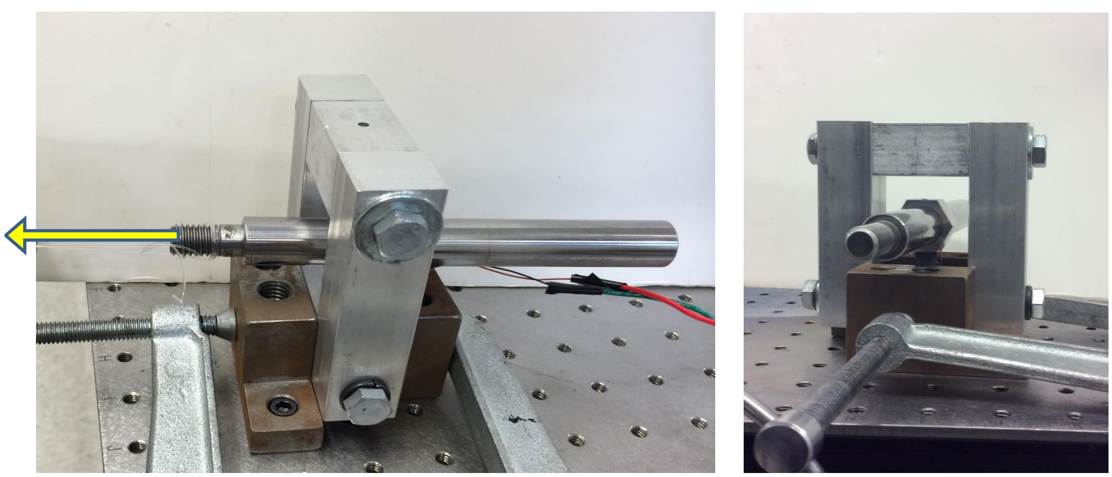

Figure 4.56: Schematic of friction measurements.

Therefore, the measured force was not consistent during pulling. Typical measurements of friction with and without ultrasonic vibrations are as shown in Fig. 4.57 (a). Three stages of friction appeared during the process. The largest friction occurred at the left end, and then dropped to the lowest level when the middle segment of the rod traveled through the ring. Towards the right end, the force picked up again. The error bars of measured friction at all stages are plotted in Fig. 4.57 (b). A sinusoidal signal with 28 V peak-to-peak at 25 kHz was employed to drive the piezo-actuator of the collar element. Friction force was significantly reduced by applying ultrasonic vibrations at all three stages. Of particular interest, the force was virtually eliminated in the middle. The zero-friction state shortened the time that the middle of the rod traveled through the ring, leading to a shorter overall duration for the case with ultrasonic than without.

The percentage of friction reduction varied between 35% to 100% depending on the relative position and fit between the rod and the ring, as shown in Fig. 4.57 (c). Relative velocity between the rod and the inner ring was also inconsistent during the pulling (Fig. 4.57 (d)). Frictional work done in the pulling process is calculated as the product of friction and the corresponding velocity. The friction-velocity curves are plotted in Fig. 4.57 (e), and time-dependent frictional work is plotted in Fig. 4.57 (f). The total frictional work was reduced by 48.9% with the application of ultrasonic vibrations.

4.5.5 Discussion

These simple measurements proved the effectiveness of the collar element in reducing the friction between the rod and the ring. Variable friction can be realized by

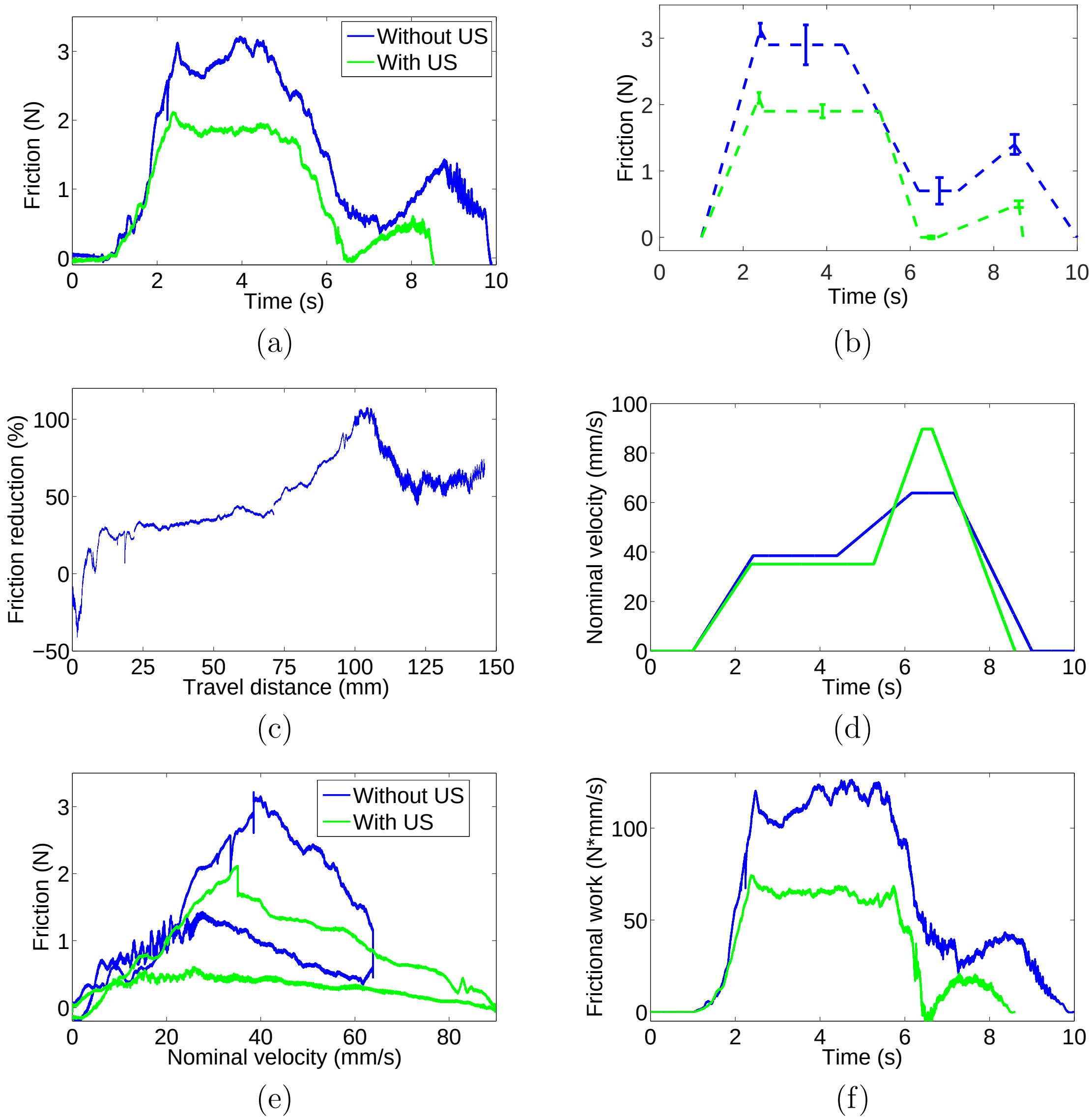

Figure 4.57: Comparison of friction measurements with and without ultrasonic vibrations: (a) friction; (b) error bars of each stage of the measured friction (dashed); (c) friction reduction; (d) nominal velocity; (e) friction-velocity curves; (f) frictional work.

driving the actuator with various voltages. One shortcoming of this design is that the direction of applying normal loads is limited. It is ideal to apply normal force in the axial direction of the piezo-actuator to avoid any bending moment or even tension in piezo-stack. However, small loads is inconsequential, due to the prestress on the piezo stack. At any rate, friction force caused bending moments to the actuator in the pulling direction. However, in order to handle the loads of real-life applications for example, the actual force on damper rods, the design requires further improvements.

4.5.6 Summary

A collar element with variable friction was proposed for damper rod applications. Methods such as impedance measurements, FEA modeling, and trial-and-error testings, were employed to assist the design. The final version of the design included an outer ring, an inner ring, a piezoelectric stack, and fasteners for connection and compression. The outer ring is rectangular in shape, while the inner ring has a hexagonal shape with a round hole in the center to allow for rods to pass through. Impedance measurements found the resonance at 25 kHz. A laser vibrometer measurements were utilized to measure the vibrational mode and amplitude. The vibrational amplitude of the inner ring increased linearly with driving voltage, and the amplitude increased significantly when the collar element was clamped. Friction measurements showed that the collar element can reduce the friction between the ring and the rod between 35% to 100% and the frictional work by 48.9%.

Chapter 5: Conclusions

5.1 Summary of Findings

This research studied friction and wear reduction using ultrasonic lubrication, both experimentally and analytically. Additionally, several practical considerations have been taken into account to asses this technology for real-life applications. The work and main findings of this research are summarized below.

5.1.1 Experiments

In ultrasonic lubrication created by Poisson-effect excitation, the ultrasonic horn was designed to exhibit two distinct regions. In the motor effect regions, the friction forces are fully cancelled by the motor force generated by the ultrasonic vibrations. In the transition region, the friction reduction percentages vary with different material combination and normal loading, in the range from 30% to 60%. The net motor forces increase when the normal load increases and the relationship follows a linear trend.

Using flextensional actuator between two stainless steel plates in a sandwich structure, the friction between the flat surfaces of the actuator and the plates were reduced by up to 70% at different levels of driving power, normal loads, and linear velocities. Higher driving voltage results in higher friction reduction, but the effect saturates due to the fact that peak-to-peak voltage was not increased. Normal force has little effect on friction reduction. Higher linear velocity leads to lower friction reduction. When linear velocity increases close to the vibrational velocity of the actuator, friction reduction diminishes.

A modified pin-on-disc tribometer was built for investigating the effect of ultrasonic vibrations on friction and abrasive wear between stainless steel pins and aluminum discs under a normal load of 3 N. Ultrasonic vibrations generated by a piezoelectric actuator had an amplitude of 2.5 μm and a frequency of 22 kHz. Three different linear speed were considered (20.3 mm/s, 40.6 mm/s, and 87 mm/s) while keeping other parameters unchanged throughout the testing.

The friction measurements show that ultrasonic vibrations reduce the effective friction force up to 62 %. The wear measurements show a consistent reduction in volume loss of up to 49%, with little dependency on velocity at the speeds considered. The SEM images of wear grooves show abrasive mode with small scale features located 3.6 μm apart that appear to be created by a punching action of the pin as it vibrates at 22 kHz over the surface of the disc. Larger scale indentations located approximately 0.9 mm apart appear to be created by stick-slip at a frequency of approximately 100 Hz. The measurements show that stick-slip amplitudes decrease up to 61% when ultrasonic vibrations are applied. However, no clear trend is found in the relationship between stick-slip reduction and linear speeds.

A literature review on the role of ultrasonics in metal forming was conducted. In the related experimental study, ultrasonic friction and wear reduction were investigated with normal stress up to 70 MPa and linear velocity up to 250 mm/s. It was found that stress plays little role in friction reduction but makes a large difference in wear generation. By applying ultrasonic vibrations, friction was reduced up to 51% for both tips, and wear was reduced by 72.6% on round tip.

Ultrasonic wear reduction were tested on various material combinations other than stainless steel on aluminum, which includes stainless steel on titanium, titanium on titanium, ceramic on M50 tool steel, and M50 on M50. Adhesive wear is the primary type at the interfaces of these material combinations. Ultrasonic vibrations were effective in reducing friction for all cases and reduced wear between all material combinations except in cases where titanium was involved. Maximum friction reduction was 73% and wear reduction was 80%. Both results were achieved in the tests between M50 pin and M50 disc.

5.1.2 Modeling

In this work, an cube model is presented which describes ultrasonic lubrication under a range of conditions. Ultrasonic vibrations are projected on three orthogonal directions and the influence of each projection on friction reduction is calculated. An overall reduction result summarizes all three projections. The calculation of contact parameters takes into consideration plastic deformation, which gives smaller distances between two surfaces and larger real contact areas.

The cube model is used to describe the reduction in friction force using parameters from the tests and contact model. These simulations show good agreement with the test results, reflecting average relative errors below 20% despite the fact that small discrepancies exist with normal loads above 160 N. Future work may be able to address this issue by employing a Gaussian distribution for asperity heights instead of an exponential distribution.

The concept of cube model was extended and implemented to describe the wear measurements conducted on the modified pin-on-disc tribometer. Without fundamental modifications, the model describes wear reduction well with errors less than 15%.

A multi-scale dynamic model was proposed in a general form to represent ultrasonic lubrication systems. The model consists of components at different scale levels. A system dynamics model is employed to represent the structure of the lubrication system. An electromechanical model is utilized for the piezoelectric actuator. The contact between two surfaces, of which the friction is aimed to be reduced, is modeled by the "cube" model.

An electrical impedance measurement was taken to identify critical model parameters. The simulation results were validated by the experimental data taken from the modified tribometer tests. The simulations match well with the measurements, with all errors less than 10%.

The influence of driving voltage, macroscopic velocity, driving frequency, and signal waveform on friction reduction is studied. Higher driving voltage results in greater friction reduction. Higher macroscopic velocity leads to a lower reduction of friction. Driving the actuator at its resonant frequency is the most effective solution and requires the least amount of power. When driving at the same peak-to-peak voltages, all waveforms result in friction reduction, and can be ranked in the following order from highest to lowest: square, sinusoid, triangle, and sawtooth.

5.1.3 Applications

The relationship between friction reduction and power consumption under various normal stresses and linear velocities was studied on uncoated and powder-coded plates. It was confirmed that friction reduction increases as the power increases, but decreases when the linear velocity increases. The magnitude of normal load/stress does not change the effectiveness of ultrasonic lubrication. Contour maps were created to show the relationship between friction reduction, power consumption, and linear velocity. Wear on both plates was characterized. There was more evident wear created on coated plates than uncoated ones, due to the difference in hardness between the coating and steel.

Lubrication methods were compared experimentally. The cases investigated were intrinsic friction, traditional lubrication with Molykote, ultrasonic lubrication, and combined lubrication of ultrasonic and Molykote. Experimental data show that traditional lubrication depends on normal stress, but not linear velocity, while ultrasonic lubrication depends on linear velocity, but not normal stress. Combined lubrication has little dependence on either factor. Different lubrication regimes were divided based on linear velocity and normal stress, within each of which, one method proved to be better than the others.

Temperature changes were measured at the pin-on-disc contact in the modified tribometer after inserting a thermocouple into the acorn nut and placing it in direct contact with the disc. Measurements were conducted at velocities as high as 220 mm/s and under two levels of normal stresses. It was found that two factors can influence temperature change when ultrasonic vibrations are applied. On one hand, the superimposition of vibratory and macroscopic velocities results in increases in actual relative velocities. This leads to rises in temperature. On the other hand, friction force and related heat generation can be reduced by applying ultrasonic vibrations, resulting in decreases in temperature. Overall temperature change, therefore, is dependent on both factors, which can vary from case to case.

Preliminary work for reducing friction between a consumer product and human skin was conducted. A cutter head and a skin replica were used for testing on the modified pin-on-disc tribometer. Friction was reduced to the required friction coefficient under the normal load defined for product usage. By driving the actuator at different voltages, friction can be controlled at different levels. A laser vibrometer was utilized to investigate the vibration features of the cutter head. It was found that the center and the rim of the cutter head vibrate out-of-phase, which creates a constant reduction of contact, leading to successful friction reduction. This is the first time ultrasonic lubrication has proven effective between a metal and a soft, non-metal material.

A collar element with variable friction was proposed for damper rod applications. Methods such as impedance measurements, FEA modeling, and trial-and-error testings, were employed to assist the design. The final version of the design included an outer ring, an inner ring, a piezoelectric stack, and fasteners for connection and compression. The outer ring is rectangular in shape, while the inner ring has a hexagonal shape with a round hole in the center to allow for rods to pass through. Friction measurements showed that the collar element can reduce the friction between the ring and the rod between 35% to 100% and the frictional work by 48.9%..

5.2 Contributions

This research advanced the state-of-art of ultrasonic lubrication in multiple ways, which are summarized below:

- Studied ultrasonic friction reduction using vibrations generated by Poisson's effect (paper [107])
- Achieved ultrasonic friction reduction using a flextensional piezoelectric actuator
- Designed and built a modified pin-on-disc tribometer, for concurrent study of ultrasonic friction and wear reduction (paper [108])
- Developed a detailed protocol to conduct ultrasonic lubrication testing and characterize wear properties using optical profilometry
- Formulated an elastic-plastic cube model to explain experimental data on ultrasonic friction and wear reduction (paper [109, 110, 111])
- Proposed a multi-scale model that, for the first time, takes into consideration the system dynamics, electromechanics, and contact properties for ultrasonic lubrication systems
- Investigated the relationship between friction reduction and power consumption under various linear velocities and normal stresses (paper [112])
- Demonstrated, for the first time, the effectiveness of ultrasonic lubrication between a metal and a soft, non-metal material

- Compared different lubrication methods, including ultrasonic, traditional (Molykote), and a traditional-ultrasonic hybrid
- Measured the temperature at the interface where ultrasonic vibrations are applied, and theorized how ultrasonic lubrication influence temperature change
- Created a collar element with various friction, which successfully reduced the friction between the element's inner ring and a damper rod

5.3 Future work

These contributions allow for a range of potential future work:

Experiments

- Create a mechanism to eliminate wobbling of the disc during the tests in the modified tribometer.
- Improve the capability of applying normal loads (in the orders of 100 Ns), and correspondingly, adopt a motor to generate sufficient torque for the rotation.
- Create a mechanism to better adjust the position of the gymbal assembly.
- Measure the interaction in-situ between the asperities of two contacting surfaces when ultrasonic vibrations are applied.
- Measure the temperature of the ultrasonically-vibrated surface with higher normal loads and velocities, to test and develop the theory of temperature change introduced by ultrasonic lubrication
- Investigate the reduction of rolling friction by using ultrasonic lubrication.

- Investigate the ultrasonic reduction of the stick-slip phenomenon in more detail.

Modeling

- Improve the models to better explain experimental data collected under all conditions, especially those from high stress and high velocity.

- Correlate the parameters of the elastic-plastic cube model to the in-situ measurements, especially the real contact area and the cube height.

Applications

- Improve the design of the collar element, so that it can handle higher normal loads that may be applied in any direction.

- Explore other vibrational modes for the inner ring. The attempt to utilize the breathing mode was not successful in this research, but further modifications could make it possible.

- Create ultrasonic lubrication devices for other applications, e.g. seat rails in vehicles for friction control or space mechanisms for wear reduction.

Appendix A: Protocols of Experiments on Modified Pin-on-Disc Tribometer

PROTOCOL:

1. Development of the modified tribometer

   1.1. Install chuck-motor subsystem.

      1.1.1. Level vibration isolation table.

      1.1.2. Place DC motor on the table; level the motor with shims and fix it with struts and bolts.

      1.1.3. Place supporting frame around the motor.

      1.1.4. Connect splined shaft to the motor shaft using a key.

      1.1.5. Put supporting plate on the frame with the splined shaft going through the hole in the plate.

      1.1.6. Set thrust needle-roller bearing on the supporting plate and around the splined shaft.

      1.1.7. Lubricate the bearing.

      1.1.8. Connect the splined shaft to the chuck through an adapter plate, which has a splined shaft coupling on one side and the chucks bolt pattern on the other side.

1.1.9. At this point, the chuck is supported by the frame through the thrust bearing and connected to the motor through the adapter plate.

1.2. Install the gymbal assembly.

1.2.1. Build the supporting frame using U-channel struts, brackets, and bolts. Use four long struts as pillars, and use three shorter ones as cross beams.

1.2.2. Secure the four pillars to the vibration isolation table using brackets and bolts.

1.2.3. Connect the gymbal assembly to the middle cross beam using bolts and nuts.

1.2.4. Install a horizontally-oriented load cell in the gymbal assembly; rigidly connect one side of the load cell to the gymbal assemblys frame, while connecting the other side to the gymbal arm with a wire.

1.3. Assemble the piezoelectric actuator.

1.3.1. Insert 3 in long, fully-threaded rod through the hole of the piezoelectric stack; put one washer and one nut at each end of the stack; leave about 1/8 in of thread protruding from the end of one nut.

1.3.2. Tighten the nuts at both ends to create a preload in the stack.

1.3.3. Connect the long, exposed threads to the gymbal arm using nuts and washers.

1.3.4. Thread acorn nut onto the other end of the piezo-actuator and insert disc in the chuck (this acorn nut and disc are used for set-up purposes, not for testing).

1.3.5. Adjust the height of the gymbal assembly so that the acorn nut is in contact with the top of the disc and the gymbal arm is level.

1.3.6. Adjust the position of the gymbal assembly so that the contact point between the acorn nut and disc is about 25 mm away from the rotational center of the disc.

1.3.7. Tighten all bolts in the set-up to ensure stability.

1.4. Set up signal generation, signal amplification, and data acquisition subsystems.

1.4.1. Connect data acquisition system to a lab computer.

1.4.2. Connect the output of signal generator to the input of an electrical amplifier.

1.4.3. Connect the amplifier output with the input wires of the piezoelectric stack.

1.4.4. Connect the amplifier monitors to the data acquisition system.

1.4.5. Connect the load cell to a signal conditioner, and then connect the output of the signal conditioner to the data acquisition system.

1.5. Additional set-up.

1.5.1. Connect air hose to shop air.

1.5.2. Fix the end of the hose to the frame such that its outlet points at the piezo-actuator.

1.5.3. Tape the tip of thermocouple to the piezo-actuator.

1.5.4. Connect the thermocouple leads to reader; hang the reader on the frame.

2. Pre-test preparation

    2.1. Calibrate the rotational speed of the motor.

        2.1.1. Attach magnet to the rim of the chuck.

        2.1.2. Place Hall-effect probe close to the chuck.

        2.1.3. Connect the output of the Hall-effect probe to gaussmeter that is connected to the data acquisition system.

        2.1.4. Open the data acquisition software and start data acquisition.

        2.1.5. Turn on the motor; turn the speed knob of the motor controller to 10 (the lowest rotational speed the motor provides).

        2.1.6. After the motor rotates for 10 revolutions, turn off the motor.

        2.1.7. End data acquisition.

        2.1.8. Analyze the saved data; the time between two peaks of the output signal from the gaussmeter is the time for the motor to rotate one full revolution.

        2.1.9. Turn the knob from 10 to 100 (the highest rotational speed the motor provides) in increments of 10; repeat steps 2.1.4 to 2.1.8.

    2.2. Place load sensor pad between the acorn nut and the disc to measure the normal force at the interface.

    2.3. Finely machine the surface of testing discs using a lathe.

    2.4. Clean the acorn nut and disc to be tested immediately before test.

        2.4.1. Put on plastic gloves and face mask.

        2.4.2. Prepare pieces of lab wipes; fold them into 1 inch squares.

2.4.3. Spray ethanol on the tissue squares; gently wipe the surface of the acorn nut and disc with them.

2.5. Install the clean acorn nut and disc.

2.5.1. Thread the acorn nut onto the piezo-actuator, tighten it with an open-end wrench.

2.5.2. Insert the disc in the chuck; adjust the position to make sure the tip of the acorn nut is in contact with the disc surface.

2.5.3. Align the top surface of the disc and the gymbal arm.

2.5.4. Tighten the chuck so that the disc is held firmly.

2.6. Measure the runout of the disc rotation.

2.6.1. Install laser displacement sensor in a fixture, and place the fixture next to the tribometer.

2.6.2. Adjust the height and angle of the sensor so that the disc is within the sensors range and the laser beam is normal to the disc.

2.6.3. Connect the sensors output to the data acquisition system.

2.6.4. Start the data acquisition.

2.6.5. Turn on the motor and rotate the disc for 10 revolutions; turn off the motor.

2.6.6. End data acquisition.

3. Perform testing

3.1. Tests with ultrasonic vibrations.

3.1.1. Hang 2 N weight on one hook that connects to the gymbal arm through wire and two pulleys. The weight is used to apply a normal load between the acorn nut and the disc.

3.1.2. Hang another 2 N weight on the other hook that connects to the gymbal arm to provide a horizontal pretension to the load cell.

3.1.3. Set the signal generator to provide a continuous sinusoidal signal with DC offset of 3 V, amplitude of 3 V, and frequency of 22 kHz. Note that the 3 V offset is used to prevent tension in the piezo-actuator.

3.1.4. Start data acquisition.

3.1.5. Turn on the amplifier and turn the gain knob to 15, which corresponds to an actual gain of 4.67 (the numbers on the gain knob are arbitrary).

3.1.6. Turn on the motor; set the rotational speed to 6.67 rpm to provide a linear velocity of 20.3 mm/s.

3.1.7. Run the test for 4 hours.

3.1.8. Turn off the motor and amplifier, and then stop the data acquisition.

3.1.9. Remove the tested acorn nut and disc from the set-up; Repeat steps 2.4 to 2.6 to install new acorn nut and disc.

3.1.10. Repeat steps 3.1.2 to 3.1.9. In step 3.1.6, set the rotational speed to 13.3 rpm and 28.7 rpm to provide linear velocities of 40.6 mm/s and 87 mm/s, respectively; run the tests for 2 and 0.94 hours in step 3.1.7 correspondingly.

3.2. Tests without ultrasonic vibrations.

3.2.1. Repeat step 3.1.9 to change acorn nuts and discs.

3.2.2. Repeat steps 3.1.2 to 3.1.9 with the signal generator and signal amplifier off.

4. Optical profilometer measurements

4.1. Measurement preparation

4.1.1. Clean the discs immediately before measurements using steps 2.4.1 to 2.4.3.

4.1.2. Make eight evenly distributed marks around the rim of the disc.

4.1.3. Open the profilometer software.

4.1.4. Raise the lens so that there is sufficient clearance between the lens and sample platform.

4.1.5. Level the sample platform.

4.1.6. Place a piece of lab wipe on the platform.

4.1.7. Gently place the sample on top of the tissue with one of the eight marks facing the front of the profilometer.

4.2. Measurement settings.

4.2.1. Choose VSI (Vertical-Scanning Interferometry) as the processing type.

4.2.2. Select 5X lens for large field of view and overall shape.

4.2.3. Pick 0.55X magnification for a scan area of 1.8 mm by 2.4 mm.

4.2.4. Choose 1X scan speed.

4.2.5. Set scan range to -100 m to 100 m.

4.2.6. Bring the lens downward toward the sample until there is a blurry image on the screen.

4.2.7. Adjust the height of the lens until the image is clear.

4.2.8. Choose 2 as the number of scans to average for each measurement.

4.2.9. Click the measurement button.

4.3. Post-measurement procedures.

4.3.1. Use the vision recipe that defined in the software to correct the raw image for tilt of the whole sample.

4.3.2. Open the analysis toolbox in the software.

4.3.3. Obtain the measured roughness values from the Basic Stats item.

4.3.4. Obtain the measured volume loss of the wear scar within the scan area from the Volume item.

4.3.5. Save the images of 1D profiles in x and y directions, the 2D profile, the 3D profile, as well as the table of roughness values.

4.3.6. Turn the sample clockwise until the next mark faces the front of the profilometer.

4.4. Repeat steps 4.1.7 to 4.3.6 for the remaining 7 marks.

4.5. Repeat steps 4.1.7 to 4.4 on all six discs.

Appendix B: Additional Contour Plots of Relationship between Friction Reduction, Power Consumption, and Linear Velocity

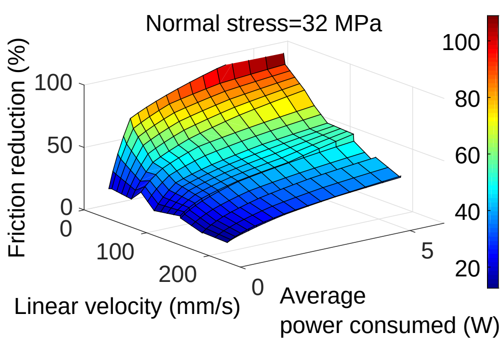

(a)

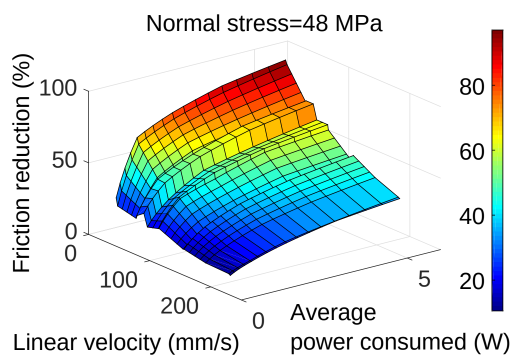

(b)

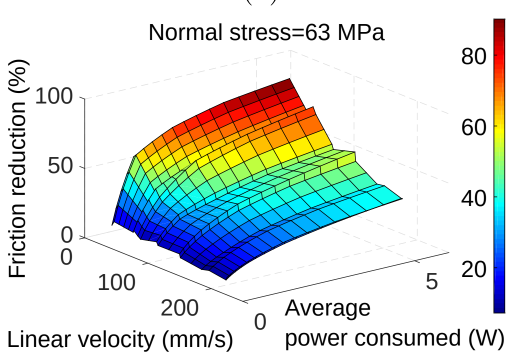

(c)

Figure B.1: Contour plots of friction reduction, linear velocity, and power consumption for seven normal stress levels (uncoated steel).

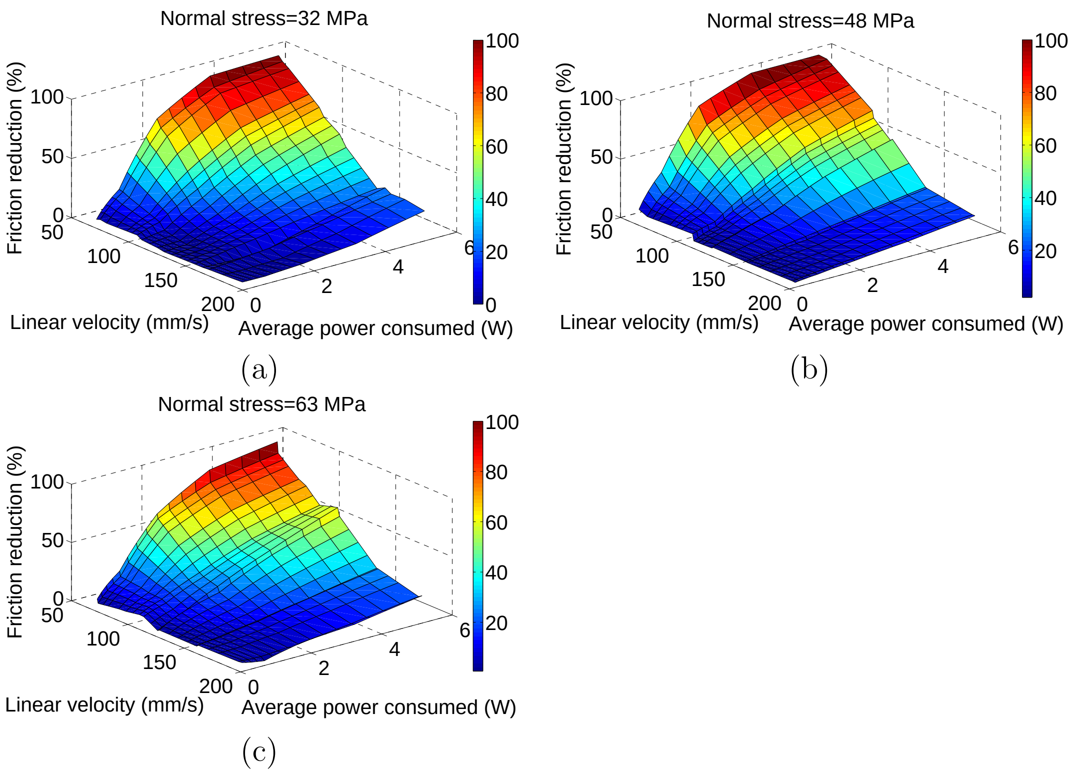

(a) (b) (c)

Figure B.2: Contour plots of friction reduction, linear velocity, and power consumption for seven normal stress levels (uncoated steel).

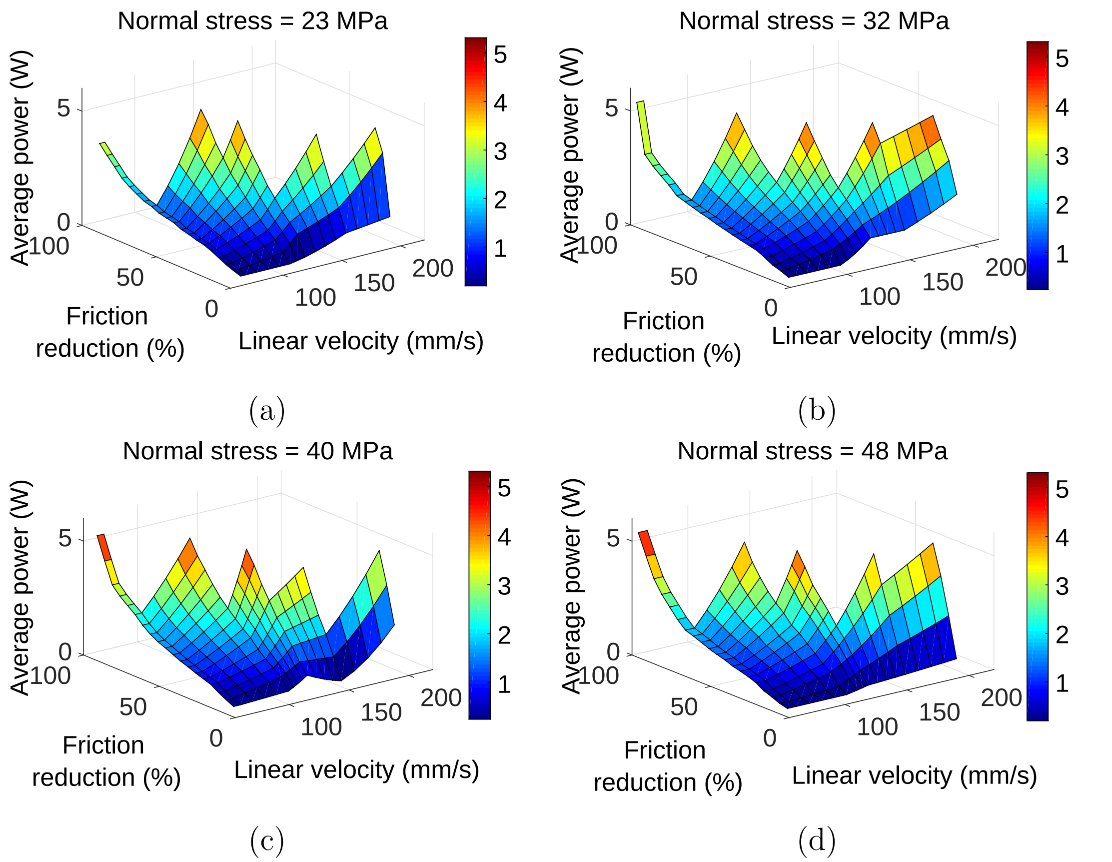

Figure B.3: Contour plots of friction reduction, linear velocity, and power consumption for seven normal stress levels (uncoated steel).

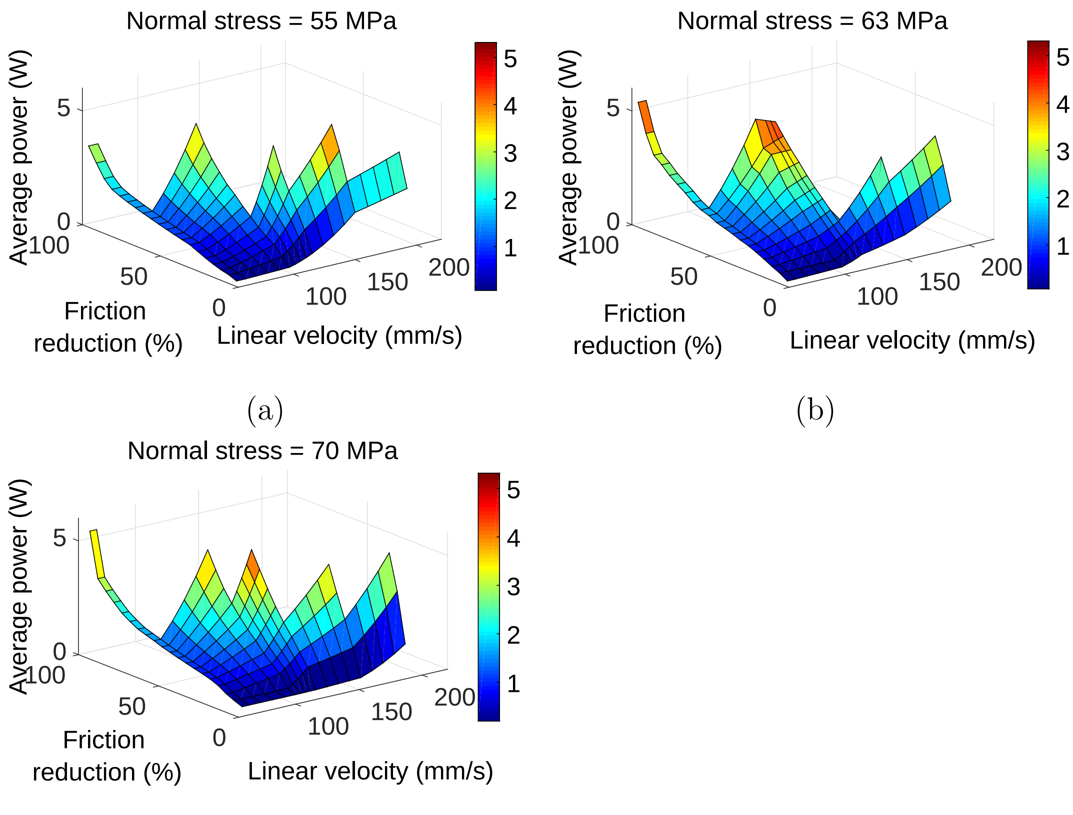

(a) (b)

(c)

Figure B.4: Contour plots of friction reduction, linear velocity, and power consumption for seven normal stress levels (uncoated steel).

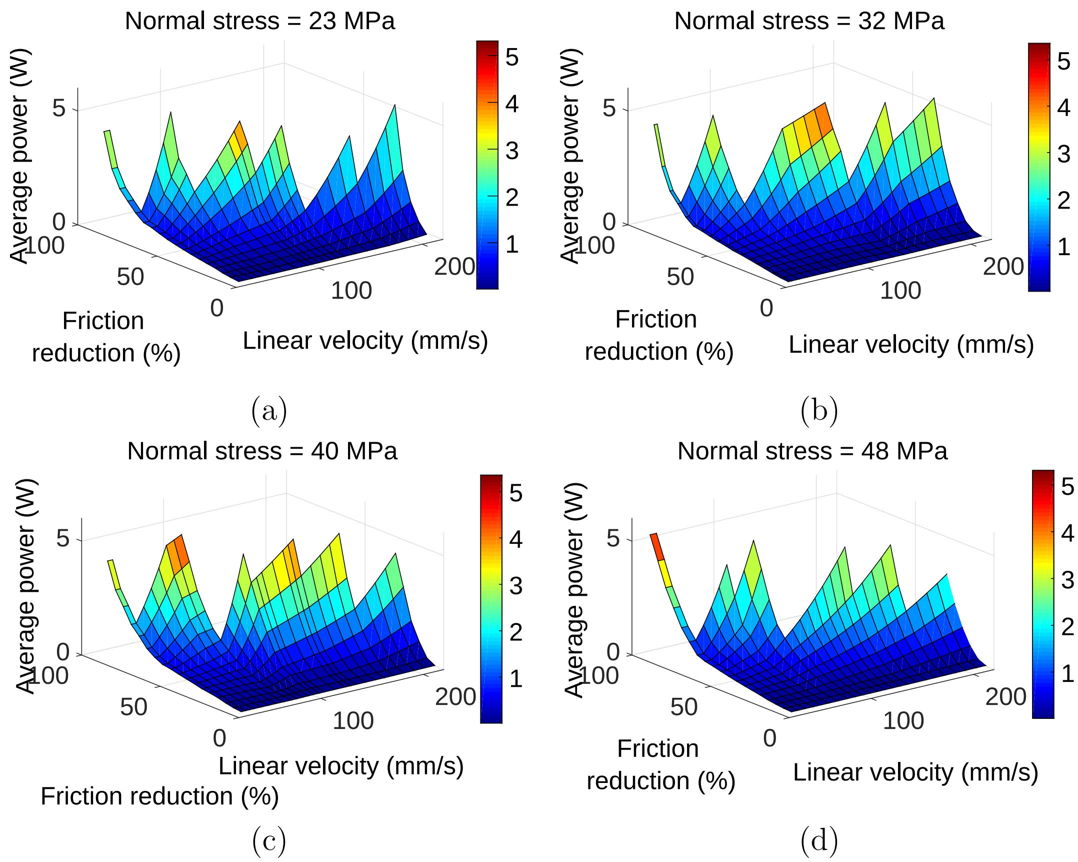

Figure B.5: Contour plots of friction reduction, linear velocity, and power consumption for seven normal stress levels (uncoated steel).

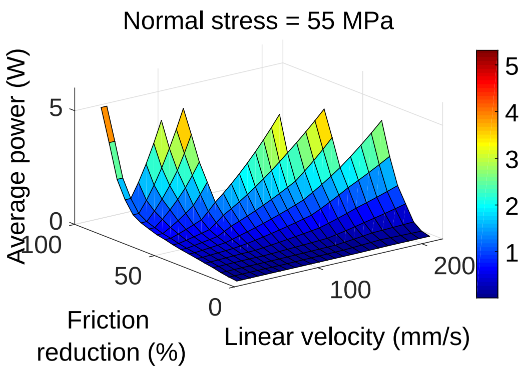

(a)

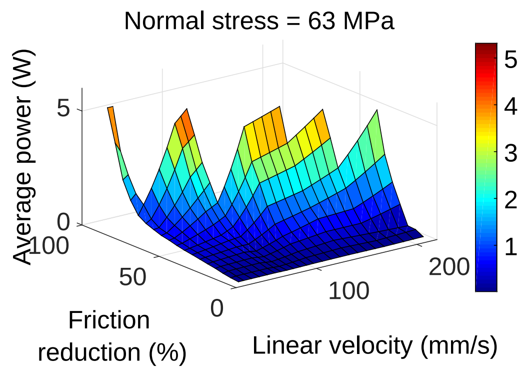

(b)

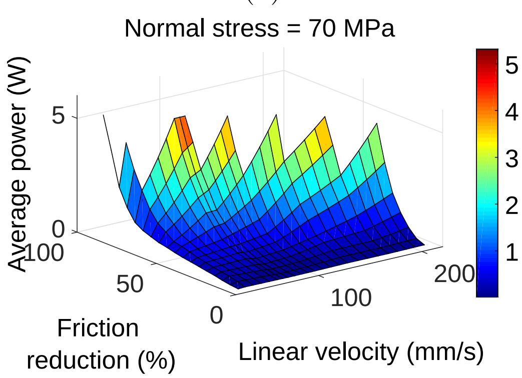

(c)

Figure B.6: Contour plots of friction reduction, linear velocity, and power consumption for seven normal stress levels (uncoated steel).

Appendix C: Drawings of the Collar Element With Various Friction

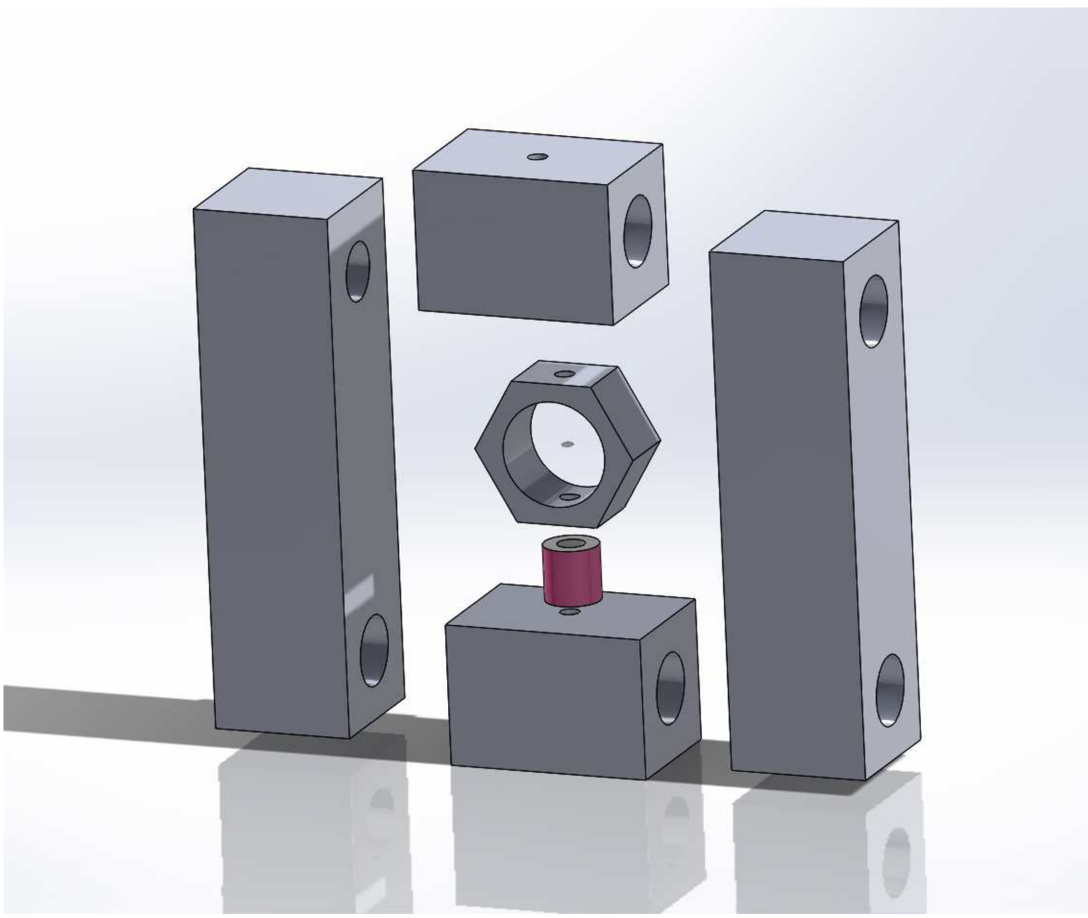

Figure C.1: Diagram of the collar element with various friction.

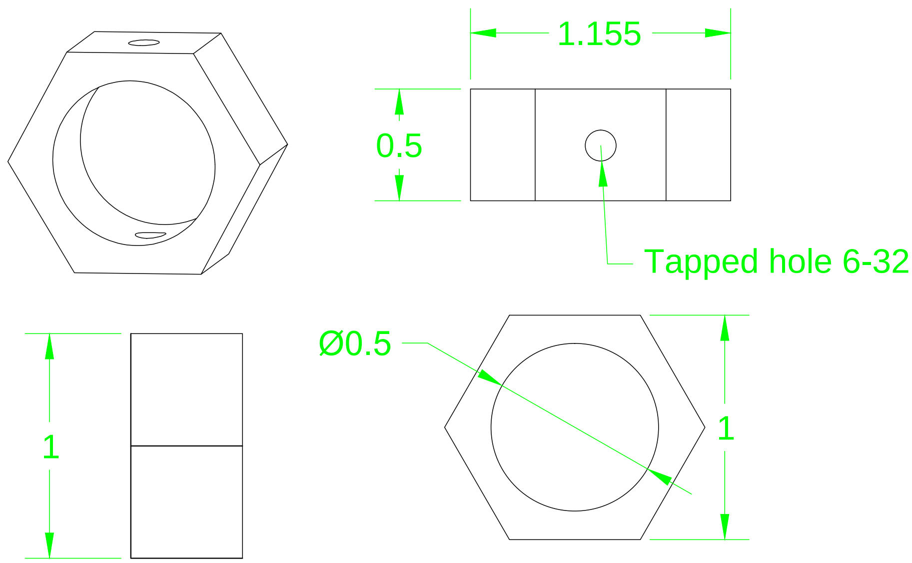

Figure C.2: Schematic of the inner ring. Dimensions in inches.

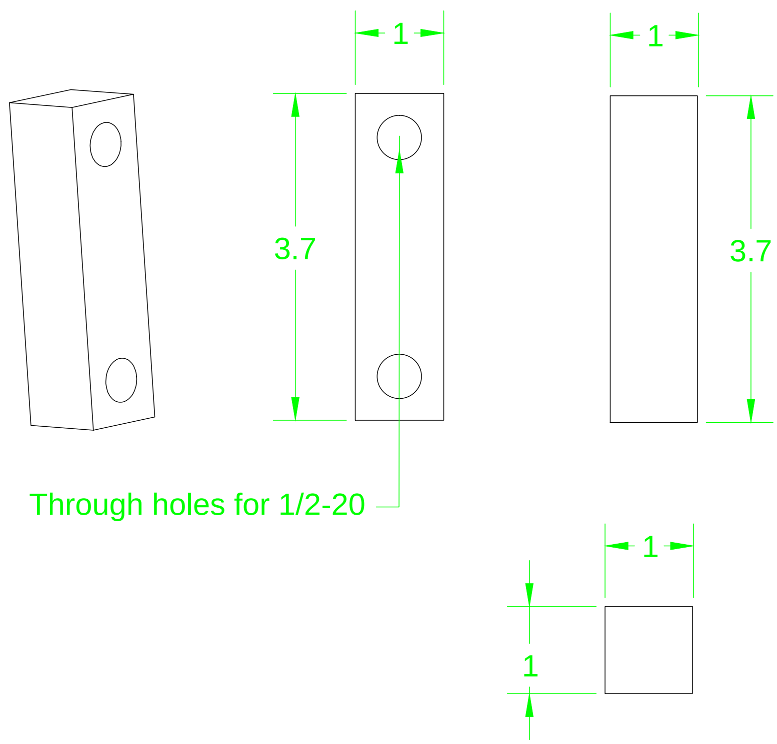

Figure C.3: Schematic of long part of the outer ring. Dimensions in inches.

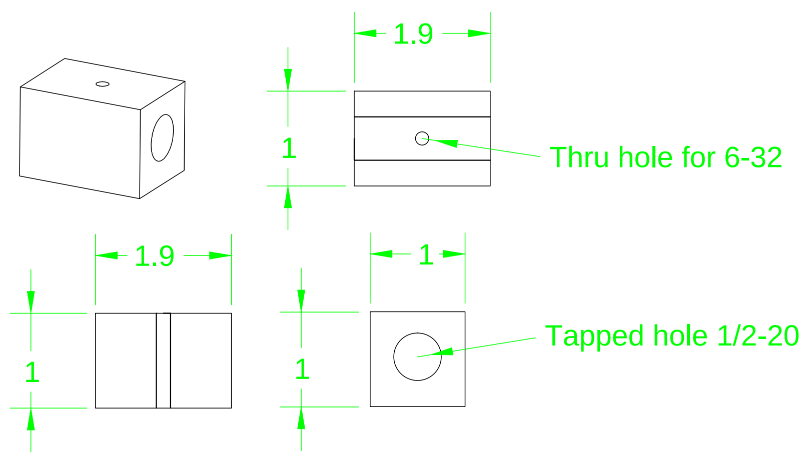

Figure C.4: Schematic of short part of the outer ring. Dimensions in inches.

Bibliography

[1] Bhushan, B., "Introduction to tribology," *John Wiley & Sons*, New York, 2002.

[2] Rabinowicz, E., "Friction and wear of materials," *John Wiley & Sons*, New York, 1965.

[3] Mason, W., "Physical acoustics and the properties of solids,", *Van Nostrand*, Princeton, New Jersey, 1958.

[4] Severdenko, V., Klubovich, V., and Stepanenko, A., "Ultrasonic rolling and drawing of metals," *Consultants Bureau*, New York and London, 1972.

[5] Graff, K., Seaman, J., Ding, J., "Development and applications of the ultrasonic stir welding process," *44th Annual Symposium of Ultrasonic Industry Association*, Washington DC, 2015.

[6] Consumer product, retrieved from: www.thanksmailcarrier.com, 2014.

[7] Space mechanisms, retrieved from: www.grc.nasa.gov, 2014.

[8] Ball joints, retrieved from: www.bizrice.com/products/Ball-Joints-In-A-Car, 2014.

[9] Car powertrain, retrieved from: http://blogs.cas.suffolk.edu, 2014.

[10] Vehicle steering, retrieved from: http://www.howacarworks.com, 2014.

[11] Taylor, R. and Coy, R., "Improved fuel efficiency by lubricant design: a review," *Proceedings of the Institution of Mechanical Engineers, Part J: Journal of Engineering Tribology*, **1**, 1-15, 2000.

[12] Coulomb, C.,"The theory of simple machines (in French)," *Memories of Math and Physics Academy of Science,* **10**, 161–331, 1785.

[13] Bowden, F. and Tabor, D., "The friction and lubrication of solids," *Cleraton Press*, Oxford, 1950.

[14] Greenwood, J. and Williamson, J., "Contact of nominally flat surfaces," *Proceeding of the Royal Society A*, **295**, 300–319, 1966.

[15] Burwell, J. and Rabinowicz, E., "The nature of coefficient of friction," *Journal of Applied Physics*, **24**, 136–139, 1953.

[16] Heslot, F., Baumberger, T., Perrin, B., Caroli, B., and Caroli, C., "Sliding friction: physical principles and applications," *Physical Review E*, **49**, 4973, 1994.

[17] Dahl, P., "A solid friction model," *Aerospace Corp*, 1968.

[18] Stribeck, R., "The key qualities of sliding and roller bearings (in German)," *Zeitschrift des Vereines Seutscher Ingenieure,* **46** (38, 39): 1342–48, 1432–37, 1902.

[19] Khruschov, M., "Principles of abrasive wear," *Wear*, **28** (1), 69–88, 1974.

[20] Burwell, J. and Strang, C., "On the empirical law of adhesive wear," *Journal of Applied Physics*, **23**, 18–28, 1952.

[21] Watson, S., Friedersdorf, F., Madsen, B., and Cramer, S., "Methods of measuring wear-corrosion synergism," *Wear*, **181-183**, Part2, 476–484, 1995.

[22] Bayer, G. and Schumacher, R., "On the significance of surface fatigue in sliding wear," *Wear*, **12**, 173–183, 1968.

[23] Hutchings, I., "Tribology: friction and wear of engineering materials," *CRC Press*, 1992.

[24] Archard, J., "Contact and rubbing of flat surface," *Journal of Applied Physics,* **24** (8), 981–988, 1953.

[25] Milner, D. and Rowe, G., "Fundamentals of solid phase welding," *Metallurgical Review*, **7**, 433–480, 1962.

[26] Ikeda, T., "Fundamentals of piezoelectricity," *Oxford University Press* 1990.

[27] Downey, P. and Dapino, M.,"Extended frequency bandwidth and electrical impedance tuning in hybrid Terfenol-D/PMN-PT transducers in mechanical series configuration," *Journal of Intelligent Material Systems and Structures,* **15**, 2005.

[28] Driesen, W., Bergander, A., Varidel, T., and Breguet, J., "Energy consumption of piezoelectric actuators for inertial drives," *Proceedings of 2003 International Symposium on Micromechatronics and Human Science,* 51–58, 2003.

[29] Graff, K., "A history of ultrasonics," *Acdemic Press*, 1981.

[30] Gallego-Jurez, J. and Graff, K., "Power Ultrasonics: Applications of High-Intensity Ultrasound," *Woodhead Publishing*, 2014.

[31] Hahnlen, R. and Dapino, M.J., "Active metal-matrix composites with embedded smart materials by ultrasonic additive manufacturing" *Proceedings of SPIE*, 2010.

[32] Uchino, K., "Piezoelectric ultrasonic motors: overview," *Smart Materials and Structures*, **7**, 273–285, 1998.

[33] Atherton, M., Mares, C., and Stolarski, T., "Some fundamental aspects of self-levitating sliding contact bearings and their practical implementations," *Proceedings of the Institution of Mechanical Engineers, Part J: Journal of Engineering Tribology*, **0**, 1–12, 2014.

[34] Littmann, W., Storck, H., and Wallaschek, J., "Sliding friction in the presence of ultrasonic oscillations: superposition of longitudinal oscillations," *Archive of Applied Mechanics*, **71,** 549–554, 2001.

[35] Littmann, W., Storck, H., and Wallaschek, J., "Reduction in friction using piezoelectrically excited ultrasonic vibrations," *Proceedings of SPIE*, **4331**, 2001.

[36] Kumar, V. and Hutchings, I. "Reduction of the sliding friction of metals by the application of longitudinal or transverse ultrasonic vibration," *Tribology International*, **37**, 833–840, 2004.

[37] Popov, V., Starcevic, J., and Filippov, A., "Influence of ultrasonic in-plane oscillations on static and sliding friction and intrinsic length scale of dry friction processes," *Tribology Letters*, **39**, 25–30, 2010.

[38] Teidelt, E., Starcevic, J, and Popov, V., "Influence of ultrasonic oscillation on static and sliding friction, " *Tribology Letters*, **1**, 51–62, 2012.

[39] Gutowski, P. and Leus, M., "The effect of longitudinal tangential vibrations on friction and driving forces in sliding motion," *Tribology International*, **55**, 108–118, 2012.

[40] Pohlman, R., Lehfeldt, E., "Influence of ultrasonic vibration on metallic friction," *Ultrasonics*, **4** (4), 178–185, 1966.

[41] Oiwa, T., "Friction control using ultrasonic oscillation for rolling-element linear-motion guide," *Review of Scientific Instruments*, **77**, 016107, 2006.

[42] Tsai, C. and Tseng C. "The effect of friction reduction in the presence of in-plane vibrations," *Archive of Applied Mechanics*, **75**, 164-176, 2005.

[43] Bharadwaj, S. and Dapino, M. J., "Effect of load on active friction control using ultrasonic vibrations," *Proceedings of SPIE*, **7290**, 72900G, 2009.

[44] Bharadwaj, S. and Dapino, M. J., "Friction control in automotive seat belt systems by piezoelectrically generated ultrasonic vibrations," *Proceedings of SPIE*, **7645**, 76450E, 2010.

[45] Bharadwaj, S. and Dapino, M. J., "Characterization of friction reduction with tangential ultrasonic vibrations using a SDOF model," *International Journal of Vehicle Design*, **63** (2/3), 2013.

[46] Chowdhury, M. and Helali, M., "The effect of frequency of vibration and humidity on the wear rate," *Wear*, **262**, 198–203, 2007.

[47] Bryant, M., Tewari, A., and York, D., "Effect of micro (rocking) vibrations and surface waviness on wear and wear debris," *Wear*, **216**, 60–69, 1998.

[48] Bryant, M. and York, D., "Measurements and correlations of slider vibrations and wear," *Journal of Tribology*, **122**, 374–380, 2000.

[49] Goto, H., Ashida, M., and Terauchi, Y., "Effect of ultrasonic vibration on the wear characteristics of a carbon steel: analysis of the wear mechanism," *Wear*, **94**, 13–27, 1984.

[50] Goto, H., Ashida, M., and Terauchi, Y., "Wear behaviour of a carbon steel subjected to an ultrasonic vibration effect superimposed on a static contact load," *Wear*, **110**, 169–181, 1986.

[51] Graff, K. and Short, M., "Thermal stir welding ultrasonic friction reduction test bed," *A technical report to National Aeronautics and Space Administration*, Huntsville, AL, 2009.

[52] Silva, E., Nishiwaki, S., Fonseca, J., "Optimization methods applied to material and flextensional actuator design using the homogenization method," *Computer Methods in Applied Mechanics and Engineering*, **172** (1–4), 241-271, 1999.

[53] ASTM G99-95, ed., "Standard test method for wear testing with a pin on disc apparatus," 1995.

[54] Burwell, J., and Rabinowicz, E., " The nature of the coefficient of friction," *Journal of Applied Physics,* **24**, 136–139, 1953.

[55] Cocks, M., "Interaction of sliding metal surfaces," *Journal of Applied Physics,* **33**, 2152–2161, 1962.

[56] Goddard, J., and Wilman, M. " A Theory of Friction and Wear during the Abrasion of Metals," *Wear,* **5**, 114–135, 1962.

[57] Mulhearn, T., and Samuels, L., "The Abrasion of Metals: A Model of the Process," *Wear,* **5**, 478–498, 1962.

[58] Eaves, A., Smith, A., Waterhouse, W., and Sansome, D., "Review of the application of ultrasonic vibrations to deforming metals," *Ultrasonics*, **13** (4), 162–170, 1975.

[59] Jimma, T., Kasuga, Y., Iwaki, N., Miyazawa, O., Mori, E., Ito, K., and Hatano, H., "An application of ultrasonic vibration to the deep drawing process," *Journal of Materials Processing Technology*, **8081**, 406–412, 1998.

[60] Kirchner, H., Kromp, W., Prinz, F., and Trimmel, P., "Plastic deformation under simultaneous cyclic and unidirectional loading at low and ultrasonic frequencies," *Materials Science and Engineering*, **68**, 2, 197–206, 1985.

[61] Murakawa, M. and Jin, M., "The utility of radially and ultrasonically vibrated dies in the wire drawing process," *Journal of Materials Processing Technology*, **113**, 81–86, 2001.

[62] Siegert, K. and Ulmer, J., "Influencing the Friction in Metal Forming Processes by Superimposing Ultrasonic Waves," *CIRP Annals - Manufacturing Technology,* **50** (1), 195–200, 2001.

[63] Siegert, K. and Ulmer, J., "Superimposing ultrasonic waves on the dies in tube and wire drawing," *Journal of engineering materials and technology*, **123**, 4, 517–523, 2001.

[64] Ashida, Y. and Aoyama, H., "Press forming using ultrasonic vibration," *Journal of Materials Processing Technology*, **187**, 118–122, 2007.

[65] Bunget, C. and Ngaile, G., "Influence of ultrasonic vibration on micro-extrusion," *Ultrasonics*, **51**, 5, 606–616, 2011.

[66] Hung, J., Tsai, Y., and Hung, C., "Frictional effect of ultrasonic-vibration on upsetting," *Ultrasonics*, **46**, 3, 277–284, 2007.

[67] Hayashi, M., Jin, M., Thipprakmas, S., Murakawa, M., Hung, J., Tsai, Y., and Hung, C., "Simulation of ultrasonic-vibration drawing using the finite element method (FEM)," *Journal of Materials Processing Technology*, **140**, 30–35, 2003.

[68] Lucas, M., "Vibration sensitivity in the design of ultrasonic forming dies," *Ultrasonics*, **34** (1), 35–41, 1996.

[69] Blaha, F., and Langenecker, B., "Elongation of zinc monocrystals under ultrasonic action,"*Die Naturwissenschaften*, 1955.

[70] Siddiq, A., Sayed, T., "Ultrasonic-assisted manufacturing processes: Variational model and numerical simulations," *Ultrasonics*, **52** (4), 521–529, 2012.

[71] Biddell, D. and Sansome, D., "The development of oscillatory metal-drawing equipment an engineer's view," *Ultrasonics*, **12** (5), 195–205, 1974.

[72] Daud, Y., Lucas, M., and Huang, Z., "Superimposed ultrasonic oscillations in compression tests of aluminium," *Ultrasonics*, **44**, Supplement, e511-e515, 2006.

[73] Daud, Y., Lucas, M., and Huang, Z., "Modelling the effects of superimposed ultrasonic vibrations on tension and compression tests of aluminium," *Journal of Materials Processing Technology*, **186**, 13, 179–190, 2007.

[74] Lucas, M. and Daud, Y., "A finite element model of ultrasonic extrusion," *Journal of Physics: Conference Series*, **181**, 012027, 2009.

[75] Dinelli, F., Biswas, S., Briggs, G., and Kolosov, O., "Ultrasound induced lubricity in microscopic contact," *Applied Physics Letters*, **71** (9), 1177–1179, 1997.

[76] Siddiq, A., and Ghassemieh, E., "Thermomechanical analyses of ultrasonic welding process using thermal and acoustic softening effects," *Mechanics of Materials*, **40**, 12, 982-1000, 2008.

[77] Donachie, M., "TITANIUM: A Technical Guide," *Metals Park, OH: ASM International,* 1988.

[78] Verhoeven, J., "Steel Metallurgy for the Non-Metallurgist," *ASM International*, 2007.

[79] Oberg, E., Jones, F., McCauley, C., and Heald, R, " Machinery's Handbook (27th ed.)," Industrial Press, 2004.

[80] "Alumina (Aluminium Oxide)–The Different Types of Commercially Available Grades,", *The A to Z of Materials.*

[81] Cohen, D., Kligerman, Y., and Etsion, I., "A Model for contact and static friction of nominally flat rough surfaces under full stick contact condition," *Journal of Tribology*, **130**, 031401, 1–9, 2008.

[82] Shi, X., and Polycarpou, A. A., "Measurement and modeling of normal contact stiffness and contact damping at the meso scale," *Journal of Tribology*, **127**, 52-60, 2005.

[83] Craig, R., "Mechanics of Materials," *John Wiley & Sons*, New York, 2000.

[84] Graff, K., "Wave Motion in Elastic Solids," *Courier Corporation*, 1975.

[85] Sampson, J., Morgan, F., Reed, D., and Muskat, M., "Friction Behavior During the Slip Portion of the Stick-Slip Process," *Journal of Applied Physics,* **14** 689–700, 1943.

[86] Kennedy, F., and Karpe, S., "Thermocracking of a mechanical face seal," *Wear*, **79**, 21–36, 1982.

[87] Dow, T., and Burton, R., "Thermoelastic instability of sliding contact in the absence of wear," *Wear,* **19**, 315–328, 1972.

[88] Mow, V. and Cheng, H., "Thermal stresses in an elastic half-space associated with an arbitrarily distributed heat source," *Zeitschrift fr angewandte Mathematik und Physik ZAMP*, **18**, 500–507, 1967.

[89] Archard, J., "The temperature of rubbing surfaces," *Wear*, **2**, 438 - 455, 1958.

[90] Ling, F., Saibel, E., "Thermal aspects of galling in dry metallic surfaces," *Wear*, **1** (2), 80–91, 1957.

[91] Parker, R., and Marshall, P., "The measurement of the temperature of sliding surfaces with particular reference to railway blocks," *Proceedings of the Institution of Mechanical Engineers*, **158**, 209–229, London, 1948.

[92] Barber, J., "Thermoelastic instabilities in the sliding of conforming solids," *Proceedings of the Royal Society of London. Series A, Mathematical and Physical Sciences*, **312,** (1510), 381–394, 1969.

[93] Barber, J., "The influence of thermal expansion on the friction and wear process," *Wear*, **10**, 155–159, 1967.

[94] Kennedy, F. and Ling, F., "A thermal, thermoelastic, and wear simulation of a high energy sliding contact problem," *Journal of Lubrication Technology*, **96**, 497–508, 1974.

[95] Bhushan, B., "Modern Tribology Handbook," *John Wiley & Sons.*

[96] Cook, N., and Bhushan, B., "Sliding Surface Interface Temperatures," *Journal of Lubrication Technology*, **95** (1), 59-64, 1973.

[97] Furey, M., "Surface Temperatures In Sliding Contact," *ASLE Transaction*, **7**, 133-146, 1964.

[98] Kennedy, F., Frusescu, D., li, J., "Thin Film Thermocouple Arrays For Sliding Surface Temperature Measurement", *Wear*, **207**(1-2), 46–54, 1997.

[99] Quinn, T. and Winer, W., "The Thermal Aspects Of Oxidational Wear," *Wear*, **102** (1-2), 67–80, 1985.

[100] Tseng, M. and Burton, R., "Thermal stress in a two-dimensional (plane stress) half-space for a moving heat input," *Wear*, **79**, 1–9, 1982.

[101] Bowden, F. and Freitag, E., "The friction of solids at very high speeds," *Proceedings of the Royal Society A,* **248** 350–367, 1985.

[102] Fijalkowski, B, "Automotive Mechatronics: Operational and Practical Issues Volume II," *Intelligent systems, Control and Automation: Science and Engineering*, **52**, 2011.

[103] Olsson, H., Astrom, K., Canudas de Wit, C., Gafvert, M., and Lischinsky, P., "Friction models and friction compensation," *European Journal of Control*, **4**, 176-195, 1998.

[104] Polycarpou, A. A., and Etsion, I.,"Analytical approximations in modeling contacting rough surfaces," *Journal of Tribology*, **109**, 257-263, 1999.

[105] Chang, W., Etsion I., and Bogy, D., "An Elastic-Plastic Model for the Contact of Rough Surfaces", *Journal of Tribology*, **109**, 257–263, 1987.

[106] Mason, W., Marfurt, K., Beshers, B, and Kuo, J., "Internal friction in rocks," *The Journal of the Acoustical Society of America,* **63** (5), 1596-1603, 1978.

[107] Dong, S. and Dapino, M.J., "Piezoelectrically-induced ultrasonic lubrication by way of Poisson effect," *Proc. SPIE 8343*, Industrial and Commercial Applications of Smart Structures Technologies, San Diego, CA, March 11–15, 2012.

[108] Dong, S. and Dapino, M.J., "Elastic-plastic cube model for ultrasonic friction reduction via Poisson effect," *Ultrasonics*, **54**, 343-350, 2014.

[109] Dong, S. and Dapino, M.J., "Wear reduction through piezoelectrically-assisted ultrasonic lubrication," *Proc. ASME SMASIS*, Snowbird, UT, September 16–18, 2013.

[110] Dong, S. and Dapino, M.J., "Wear reduction through piezoelectrically-assisted ultrasonic lubrication," *Smart Materials and Structures,* **23**, 104005, 2014.

[111] Dong, S. and Dapino, M.J., "Model for friction and wear reduction through piezoelectrically-assisted ultrasonic lubrication" *Proc. SPIE 9059*, Industrial and Commercial Applications of Smart Structures Technologies, San Diego, CA, March 9–12, 2014.

[112] Dong, S. and Dapino, M.J., "Mapping of power consumption and friction reduction in piezoelectrically-assisted ultrasonic lubrication," *Proc. SPIE 9433*, Industrial and Commercial Applications of Smart Structures Technologies, San Diego, CA, March 8–11, 2015.